NAVAL POSTGRADUATE SCHOOL
Monterey, California

DISSERTATION

VARIATIONAL RETRIEVAL OF EASTERN PACIFIC ATMOSPHERIC BOUNDARY LAYER PARAMETERS USING ATOVS WITH THE COAMPS™ MESOSCALE FORECAST SYSTEM

by

Grant Alexander Cooper IV

September 2002

Dissertation Chair and Co-Advisor:	Philip A. Durkee
Dissertation Co-Advisor:	Nancy L. Baker

Approved for public release; distribution is unlimited

THIS PAGE INTENTIONALLY LEFT BLANK

REPORT DOCUMENTATION PAGE			Form Approved OMB No. 0704-0188
Public reporting burden for this collection of information is estimated to average 1 hour per response, including the time for reviewing instruction, searching existing data sources, gathering and maintaining the data needed, and completing and reviewing the collection of information. Send comments regarding this burden estimate or any other aspect of this collection of information, including suggestions for reducing this burden, to Washington headquarters Services, Directorate for Information Operations and Reports, 1215 Jefferson Davis Highway, Suite 1204, Arlington, VA 22202-4302, and to the Office of Management and Budget, Paperwork Reduction Project (0704-0188) Washington DC 20503.			
1. AGENCY USE ONLY *(Leave blank)*	**2. REPORT DATE** September 2002	**3. REPORT TYPE AND DATES COVERED** Dissertation	
4. TITLE AND SUBTITLE: Title (Mix case letters) Variational Retrieval of Eastern Pacific Atmospheric Boundary Layer Parameters using ATOVS with the COAMPS™ Mesoscale Forecast System			**5. FUNDING NUMBERS**
6. AUTHOR(S) Cooper, Grant Alexander IV			
7. PERFORMING ORGANIZATION NAME(S) AND ADDRESS(ES) Naval Postgraduate School Monterey, CA 93943-5000			**8. PERFORMING ORGANIZATION REPORT NUMBER**
9. SPONSORING / MONITORING AGENCY NAME(S) AND ADDRESS(ES) N/A			**10. SPONSORING / MONITORING AGENCY REPORT NUMBER**
11. SUPPLEMENTARY NOTES The views expressed in this thesis are those of the author and do not reflect the official policy or position of the Department of Defense or the U.S. Government.			
12a. DISTRIBUTION / AVAILABILITY STATEMENT Approved for public release; distribution is unlimited			**12b. DISTRIBUTION CODE**

13. ABSTRACT ***(maximum 200 words)***

A one-dimensional variational (1DVAR) retrieval scheme is used to investigate the ability of the Advanced TIROS Operational Vertical Sounder (ATOVS) to contribute information to a mesoscale NWP system within the summertime Eastern Pacific (EPAC) environment. This system is the Coupled Ocean – Atmosphere Mesoscale Prediction System (COAMPS™) and the Naval Research Laboratory (NRL) Atmospheric Variational Data Assimilation System (NAVDAS). Analyses of information content and retrieval performance show that, when treated optimally, significant humidity and temperature information can be derived from ATOVS retrievals within the clear and cloudy sky summertime EPAC environment. A study of retrieval error sensitivity to representative background state vector elements and associated errors was also conducted to establish the *a priori* elements critical for successful 1DVAR retrievals. 1DVAR profile temperature and humidity retrievals were generated using both simulated and actual ATOVS observations constrained by the COAMPS short-term forecasts and a synoptically relevant background error covariance matrix. The time period of interest coincides with the DYCOMS Phase II field study. The 1DVAR retrieval results indicate that ATOVS observations can provide information that, when used in concert with a COAMPS background field, reduce the retrieval error and adjust the retrieval within the shallow boundary layer toward the designated "true" profile.

14. SUBJECT TERMS Variational Satellite Retrieval, 1DVAR, COAMPS, NAVDAS, ATOVS, HIRS/3, AMSU-A, AMSU-B, DYCOMS II, Information Content, Non-linear Optimal Estimation Theory, Mesoscale Satellite Data Assimilation, Marine Atmospheric Boundary Layer, MABL	**15. NUMBER OF PAGES** 272
	16. PRICE CODE

17. SECURITY CLASSIFICATION OF REPORT	**18. SECURITY CLASSIFICATION OF THIS PAGE**	**19. SECURITY CLASSIFICATION OF ABSTRACT**	**20. LIMITATION OF ABSTRACT**
Unclassified	Unclassified	Unclassified	UL

NSN 7540-01-280-5500 Standard Form 298 (Rev. 2-89)
Prescribed by ANSI Std. 239-18

THIS PAGE INTENTIONALLY LEFT BLANK

Approved for public release; distribution is unlimited

VARIATIONAL RETRIEVAL OF EASTERN PACIFIC ATMOSPHERIC BOUNDARY LAYER PARAMETERS USING ATOVS WITH THE COAMPS™ MESOSCALE FORECAST SYSTEM

Grant A. Cooper IV
Commander, United States Navy
B.S., San Diego State University, 1984
M.S., Naval Postgraduate School, 1992

Submitted in partial fulfillment of the
requirements for the degree of

DOCTOR OF PHILOSOPHY IN METEOROLOGY

from the

NAVAL POSTGRADUATE SCHOOL
September 2002

Author: _____
Grant A. Cooper IV

Approved by:

_____	_____
Philip A. Durkee Professor of Meteorology Committee Chair Dissertation Co-Advisor	Nancy L. Baker Naval Research Laboratory Dissertation Co-Advisor
_____	_____
Carlyle H. Wash Professor of Meteorology	Qing Wang Professor of Meteorology
_____	_____
Douglas K. Miller Professor of Meteorology	Carlos F. Borges Professor of Mathematics

Approved by: _____
Carlyle H. Wash, Chair, Department of Meteorology

Approved by: _____
Carson K. Eoyang, Associate Provost for Academic Affairs

THIS PAGE INTENTIONALLY LEFT BLANK

ABSTRACT

A one-dimensional variational (1DVAR) retrieval scheme has been used to investigate the complex relationship between satellite-derived information and *a priori* constraint. Specifically, this dissertation studies the ability of the Advanced TIROS Operational Vertical Sounder (ATOVS) to contribute information to a mesoscale numerical weather prediction system within the summertime eastern Pacific (EPAC) environment. This system is the Coupled Ocean – Atmosphere Mesoscale Prediction System[1] (COAMPS™) and the Naval Research Laboratory (NRL) Atmospheric Variational Data Assimilation System (NAVDAS).

Analyses of information content and theoretical retrieval performance show that, when treated optimally, significant humidity and temperature information can be derived from ATOVS infrared and microwave retrievals within the clear and cloudy sky summertime EPAC environment. A study of theoretical retrieval error sensitivity to representative EPAC background state vector elements and associated errors was also conducted to establish the *a priori* elements critical for successful 1DVAR retrievals.

1DVAR profile temperature and humidity retrievals were generated using both simulated and actual ATOVS observations constrained by the COAMPS short-term forecasts and a synoptically relevant background error covariance matrix. The time period of interest coincides with the Dynamics and Chemistry of Marine Stratocumulus (DYCOMS) Phase II field study. The 1DVAR results are consistent with the theoretical information content study and indicate that these satellite observations can provide information that, when used in concert with a reasonable first-guess or background (i.e., from COAMPS), reduce the retrieval error and adjust the retrieval within the shallow boundary layer toward the designated "true" profile.

The generally good agreement between theoretical retrieval errors and the error statistics calculated using non-linear Newtonian iteration demonstrates the consistency and reliability of the NRL 1DVAR retrieval scheme.

[1] COAMPS™ is a trademark of the Naval Research Laboratory

THIS PAGE INTENTIONALLY LEFT BLANK

TABLE OF CONTENTS

I. INTRODUCTION 1

II. THEORY AND RESEARCH METHODS 7

A. ATMOSPHERIC SOUNDING THEORY AND ATOVS DESCRIPTION 7

1. Radiative Transfer Equation and Inverse Atmospheric Sounding Theory 7

a. The Radiative Transfer Equation 8

b. Inverse Atmospheric Sounding Theory 9

c. Constraints 10

d. Clouds 12

2. ATOVS Instrument 13

a. Channel Characteristics 13

b. Weighting Functions and Vertical Resolution 16

c. Radiance Bias 19

d. Mesoscale ATOVS Assimilation 19

B. COAMPS MODEL DESCRIPTION 20

C. MARINE ATMOSPHERIC BOUNDARY LAYER 22

1. Description 22

2. Mesoscale Modeling of MABL Parameters 23

3. Alternate Sources of MABL Information 24

D. 1DVAR RETRIEVAL THEORY 25

1. Overview 25

2. NAVDAS and 1DVAR Description 26

3. Radiative Transfer Model (RTTOV-6) 30

E. INFORMATION THEORY AND METHODS 30

1. Information Matrix 31

2. Information Derived from Principal Component Analysis 33

3. Degrees of Freedom and Information Content From R and B Comparison 34

4. Information via Entropy Reduction 35

5. Information Gain Measured by Analysis Error Reduction 36

F. SIMULATED RETRIEVAL METHOD 37

G. MATRIX OPERATIONS 39

III. PRIOR INFORMATION 41

A. BACKGROUND ERROR COVARIANCE MATRIX (B) 41

B. OBSERVATION ERROR COVARIANCE MATRIX (R) 47

C. BACKGROUND STATE VECTORS 49

1. Atmospheric Profiles 49

2. Surface Array 53

3. Cloud Array 53

4. Surface Emissivity Array 53

D. JACOBIAN MATRIX (H) 54

IV. INFORMATION CONTENT STUDY 77
A. INDEPENDENT INFORMATION AND VERTICAL RESOLUTION.. 78
1. Principal Component Analysis of S' 78
2. Singular Value Decomposition of H' 82
3. Averaging Kernel Matrix 84
B. EFFECTIVE BACKGROUND ERROR 87
C. RETRIEVAL ERROR SENSITIVITY 89
1. Background, Background Error, and Inter-Level Correlations of Error 90
2. ATOVS Instrument and AMSU Window Channel Selection 97
3. Observation Error 104
4. Surface Array Errors 108
a. Radiative Skin Temperature Error 108
b. Microwave Surface Emissivity Error 115
c. Surface Pressure and 2m Wind Speed Errors 121
5. Cloud Array Errors 122
a. Cloud-top Pressure Error 122
b. Cloud Fractional Coverage Error 124
6. Profile Array Errors 127
a. Temperature and Log_e Specific Humidity Profile Errors 127
b. Cloud Liquid Water Profile Array Errors 130
D. SUMMARY OF CHAPTER RESULTS 134

V. 1DVAR RETRIEVAL STUDY 137
A. 1DVAR RETRIEVALS WITH SIMULATED BACKGROUND STATE VECTORS AND SIMULATED ATOVS OBSERVATIONS ... 139
1. Simulated Observation Vectors 139
2. Simulated Background State Vectors 139
3. 1DVAR Retrieval Error and Performance for *T* and Log_e *Q* 144
a. Clear Sky T and log_e Q Retrievals 144
b. Cloudy Sky T and Log_e Q Retrievals 151
4. Surface and Cloud Parameter Retrieval Errors 158
5. 1DVAR Simulated *T* and Log_e *Q* Retrievals 159
6. Section Summary 167
B. 1DVAR SIMULATED RETRIEVALS WITH COAMPS BACKGROUND STATE VECTORS AND SIMULATED ATOVS OBSERVATIONS 167
1. Case Study: 0900Z 11 July 2001 169
a. 1DVAR Retrievals with Clear Sky Profiles 176
b. 1DVAR Retrievals with Model CLW Profiles 181
c. 1DVAR Retrievals with Modified CLW Profiles 187
2. Case Study: 1800Z 15 July 2001 192
3. Section Summary 201
C. 1DVAR RETRIEVALS WITH COAMPS BACKGROUND STATE VECTORS AND ATOVS MICROWAVE OBSERVATIONS 202

D. 1DVAR RETRIEVALS USING THE COAMPS / NAVDAS FORECAST SYSTEM AND ATOVS MICROWAVE OBSERVATIONS 210
1. COAMPS Model 210
a. Model Domain 210
b. Model Configuration 211
c. Model Forecast Summary 211
2. AMSU Observations 211
a. Observation Selection and Scene Matching 211
b. Bias Corrections 212
c. Quality Control Procedures 212
3. 1DVAR Retrievals 213
a. Mean Effective Background Error 213
b. T and $\log_e$ Q Retrievals within the COAMPS Domain 214
c. Comparison with a Collocated Dropsonde Observation 215
d. Comparison with a Collocated NESDIS Retrieval 219
E. SUMMARY OF CHAPTER RESULTS 220

VI. DISCUSSION AND RECOMMENDATIONS 223
A. RESEARCH SUMMARY AND DISCUSSION 223
B. RECOMMENDATIONS FOR FUTURE RESEARCH 227

APPENDIX A 231

LIST OF REFERENCES 235

INITIAL DISTRIBUTION LIST 243

THIS PAGE INTENTIONALLY LEFT BLANK

LIST OF FIGURES

Figure. 2.1. Vertical transmittance to space as a function of microwave frequency (GHz). See Table 2.1 for the center frequencies of the corresponding AMSU channels. Regions of the microwave frequency spectrum with large transmittance values are shown as the window "channels." Atmospheric water vapor (H_2O) and oxygen (O_2) are the primary absorbers of MW radiation. [From http: //amsu.cira.colostate.edu.] 15

Figure. 2.2. Example of the scene resolution cells for ATOVS AMSU-A (thin purple circles), AMSU-B (blue dots), and TOVS MSU (thick yellow circles). This comparison shows that the AMSU sounders have the spatial resolution suitable for mesoscale retrieval applications. [From http://amsu.cira.colostate.edu.] 16

Figure 2.3. HIRS/3 sensitivity functions ($d\tau$ / d lnp) for channels 1-19, calculated with respect to U.S. Standard Atmosphere. Channels 16 - 19 are not included in this research. [From Li et al. (2000).] 17

Figure 2.4. Weighting functions for AMSU module A1 (channels 3 – 15), AMSU module A2 (channels 1 – 2), and AMSU-B channels 1 – 5. Calculated with respect to the U.S. Standard Atmosphere for all channels. The sensitivity of AMSU-A2 and AMSU-B channels 1 and 2 to liquid water cloud is also shown. [From http://amsu.cira.colorado.edu.] 18

Figure 3.1. NOGAPS and COAMPS background standard deviations of error $(B_{ii})^{1/2}$ for (a) T, and (b) $\log_e Q$. Globally averaged NOGAPS background errors are used operationally at NRL Monterey for satellite data assimilation and are used in this dissertation as the first-order approximation. The COAMPS background errors are based on the EPAC 6-hr forecast statistics for the period 07 July – 30 September 2001..... 45

Figure 3.2. Representative profiles of T (upper panel) and $\log_e Q$ (lower panel) for the summertime eastern Pacific (EPAC) oceanic environment. Profiles (a,b) are EPAC Profiles 1A and 1B, the clear sky boundary layer cases, and (c,d) are EPAC Profiles 2A and 2B, the cloudy boundary layer cases. In each example, the first profile (red dotted line) is the U.S. Standard Atmosphere. Cloud liquid water profiles are discussed in the text. 50

Figure 3.3. T (left panel) and $\log_e Q$ (right panel) Jacobians for the (a) 15 HIRS/3, (b) 15 AMSU-A, and (c) 5 AMSU-B channels used in this study. Elements of **H** are calculated with respect to Profile 3, the U.S. Standard Atmosphere. 56

Figure 3.4. Clear sky *T* Jacobians for HIRS/3 channels (a) 6, (b) 7, (c) 8, (d) 13 and (e) 14; AMSU-A channels (f) 1, (g) 2, (h) 3, and (i) 15; and AMSU-B channels (i) 1 and (j) 2. Jacobians are compared for H linearized U.S. Standard Atmosphere (Profile 3) and representative clear sky EPAC Profiles 1A and 1B. MABL inversion heights are at 957.44 hPa for Profile 1A and 922.46 hPa for Profile 1B. 57

Figure 3.5. Cloudy sky *T* Jacobians for (a) HIRS/3 channel 8; AMSU-A channels (b) 1, (c) 2, (d) 3, and (e) 15; and AMSU-B channels (e) 1 and (f) 2. Jacobians are compared for the elements of **H** calculated with respect to the representative cloudy sky EPAC Profiles. MABL inversion heights are at 957.44 hPa for Profile 2A and 922.46 hPa for Profile 2B. LWP is varied for each profile with 90 and 190 g m^{-2} for Profiles 2A1 and 2A2, and 145 and 285 g m^{-2} for Profiles 2B1 and 2B2. 63

Figure 3.6. Clear sky $\log_e Q$ Jacobians for (a) HIRS/3 channel 10; AMSU-A channels (b) 1, (c) 2 , (d) 3, and (e) 15; and AMSU-B channels (e) 1, and (f) 2. Jacobians are compared for the elements of **H** calculated with respect to the U.S. Standard Atmosphere (Profile 3) and EPAC Profiles 1A and 1B. MABL inversion heights are at 957.44 hPa for Profile 1A and 922.46 hPa for Profile 1B. 67

Figure 3.7. As in Fig. 3.6, except elements of **H** calculated with respect to cloudy sky EPAC Profiles 2A1, 2A2, 2B1, and 2B2. MABL inversion heights are at 957.44 hPa for Profile 2A and 922.46 hPa for Profile 2B. LWP is varied for each profile with 90 and 190 g m^{-2} for Profiles 2A1 and 2A2, and 145 and 285 g m^{-2} for Profiles 2B1 and 2B2. 70

Figure 3.8. Clear and cloudy sky radiative skin temperature (T_s) Jacobians (i.e., $\partial T_B/\partial T_s$) versus ATOVS channel. HIRS/3 channels are 1-15, AMSU-A are 16-30, and AMSU-B are 31-35. Comparisons are made for H linearized about (a) clear sky background profiles, and (b) cloudy sky background profiles. 74

Figure 3.9. As in Fig. 3.8, except for surface pressure (P_s) Jacobians. 75

Figure 3.10. As in Fig. 3.8b, except for cloud-top pressure (P_{CT}) Jacobians. Comparisons are made for H linearized about cloudy sky EPAC profiles. 76

Figure 3.11. As in Fig. 3.8b, except for cloud fractional coverage (C_{FC}) Jacobians..... 76

Figure 4.1. The 12 significant *T* and $\log_e Q$ eigenvectors of (2.17). Significant is defined as at least 10% of the information for each eigenvector is derived from the satellite observation. Comparison for elements of **H** calculated with respect to clear sky EPAC Profile 1B and U.S. Standard Atmosphere (Profile 3) and the results are calculated using $\mathbf{B_N}$. 79

Figure 4.2. Vertical resolution of theoretical (a,b) T, and (c,d) $\log_e Q$ retrievals calculated as the reciprocal of the diagonal elements of **A**. H linearized about U.S. Standard Atmosphere, EPAC (clear) Profiles 1A, 1B and EPAC (cloudy) Profiles 2A1, 2B2. Results shown for **A** calculated with respect to (a,c) $\mathbf{B_N}$ and (b,d) $\mathbf{B_C}$..... 84

Figure 4.3. Square root of the diagonal elements of effective background error ($\mathbf{H\,B\,H}^T$) and observation error (**R**). Results are calculated with respect to background error covariance (a) $\mathbf{B_N}$, and (b) $\mathbf{B_C}$. HIRS/3 channels are 1-15, AMSU-A channels 1 - 15 are shown as ATOVS channels 16-30, and AMSU-B channels 1 –5 are shown as ATOVS channels 31-35. Comparisons are made for H linearized about profiles described in legend. 88

Figure 4.4. Theoretical T retrieval performance ($P = 100[1-(S_{ii}/B_{ii})]$) as function of background state vector (see legend) and background error covariance matrix (a) $\mathbf{B_N}$, and (b) $\mathbf{B_C}$..... 91

Figure 4.5. As in Fig. 4.4, except for $\log_e Q$ retrieval performance (P)..... 93

Figure 4.6. Theoretical T retrieval performance (P) as a function of surface and atmosphere inter-level correlations of error calculated with respect to $\mathbf{B_C}$ and background state vector (a) U.S. Standard Atmosphere, (b) clear sky EPAC Profile 1A, and (c) cloudy sky EPAC Profile 2B2. The "no coupling" case assumes inter-level correlations of error are zero between $<T_s\ T_{2m}>$, $<T_s\ T>$, and $<T_{2m}\ T>$. The "weakly coupled" case includes the inter-level correlations of error shown in Table 3.1. The "strongly coupled" case assumes a near 1:1 $<T_s\ T_{2m}>$ inter-level correlation of error and large $<T_s\ T>$, $<T_{2m}\ T>$ error correlations..... 96

Figure 4.7. Theoretical T retrieval performance (P) as a function of ATOVS instrument (channels) calculated with respect to $\mathbf{B_N}$ and background state vector (a) U.S. Standard Atmosphere, (b) clear sky EPAC Profile 1A, and (c) cloudy sky EPAC Profile 2B2. The 35-channel curve (solid line) includes the 15 HIRS/3 (dashed), 15 AMSU-A (dotted), and 5 AMSU-B (dash-dot) channels used in this study. 98

Figure 4.8. As in Fig. 4.7, except for theoretical $\log_e Q$ retrieval performance..... 100

Figure 4.9. Theoretical $\log_e Q$ retrieval performance (P) as a function of AMSU-A channels 1-4, 15 and AMSU-B channels 1 and 2. Calculated with respect to $\mathbf{B_N}$ and background state vector (a) U.S. Standard Atmosphere, (b) clear sky EPAC Profile 1A, and (c) clear sky EPAC Profile 1B. 102

Figure 4.10. Theoretical *T* retrieval performance (*P*) as a function of 0.01, 0.10, 1.00, and 10.0 K observation error $(R_{ii})^{1/2}$. Results are calculated with respect to $\mathbf{B_N}$ and background state vector (a) U.S. Standard Atmosphere, (b) clear sky EPAC Profile 1A, and (c) cloudy sky EPAC Profile 2B2. 105

Figure 4.11. As in Fig 4.10, except for theoretical $\log_e Q$ retrieval performance. 107

Figure 4.12. Theoretical *T* and $\log_e Q$ retrieval performance a function of 0.00, 1.57, and 3.14 K radiative skin temperature (T_s) error. Performance is calculated with respect to $\mathbf{B_C}$ (weak surface-atmosphere correlations of error) and background state vector (a) U.S. Standard Atmosphere, (b) clear sky EPAC Profile 1A, (c) clear sky EPAC Profile 1B, (d) cloudy sky EPAC Profile 2A1, and (e) cloudy sky EPAC Profile 2B2. 109

Figure 4.13. As in Fig. 4.12, except for $\log_e Q$ theoretical retrieval performance (*P*) calculated with respect to (a) clear sky EPAC Profile 1A, and (b) cloudy sky EPAC Profile 2B2. 112

Figure 4.14. As in Fig. 4.12b, except theoretical *T* retrieval performance calculated with respect to $\mathbf{B_N}$. 113

Figure 4.15. As in Fig. 4.12, except for *T* theoretical retrieval performance with "strong" surface and atmosphere inter-level correlations of error calculated for (a) clear sky EPAC Profile 1A, and (b) cloudy sky EPAC Profile 2B2. 113

Figure 4.16. Theoretical *T* retrieval performance a function of 0, 1, 2, and 5 % microwave surface emissivity error (ε_m) applied to AMSU window channels. Performance is calculated with respect to $\mathbf{B_C}$ background state vector (a) U.S. Standard Atmosphere, (b) clear sky EPAC Profile 1A, (c) clear sky EPAC Profile 1B, (d) cloudy sky EPAC Profile 2A1, and (e) cloudy sky EPAC Profile 2B2. 115

Figure 4.17. As in Fig. 4.16, except for $\log_e Q$ theoretical retrieval performance (*P*). 118

Figure 4.18. Theoretical *T* retrieval performance (*P*) as a function of 0, 5, 10, 20 and 50 hPa cloud-top pressure (P_{CT}) error calculated with respect to $\mathbf{B_C}$ and (a) cloudy sky EPAC Profile 2A1, and (b) cloudy sky EPAC Profile 2B2. 123

Figure 4.19. As in Fig. 4.18b, except for calculated with respect to $\mathbf{B_N}$ 124

Figure 4.20. Theoretical *T* retrieval performance (*P*) as a function of 0, 10, 50 and 100% cloud fractional coverage (C_{FC}) error calculated with respect to $\mathbf{B_C}$ and (a) cloudy sky EPAC Profile 2A1, and (b) cloudy sky EPAC Profile 2B2. 125

Figure 4.21. As in Fig. 4.20b, except calculated with respect to $\mathbf{B_N}$. 126

Figure 4.22. Theoretical *T* retrieval performance (*P*) as a function of 0, 10, 50 and 100% cloud fractional coverage (C_{FC}) error calculated with respect to $\mathbf{B_C}$ and clear sky EPAC Profile 1A. 126

Figure 4.23. Theoretical (a) *T*, and (b) $\log_e$ *Q* retrieval performance as a function of uniform profile *T* and $\log_e$ *Q* errors applied to all 43 RTTOV-6 levels. Results were calculated with respect to $\mathbf{B_N}$. 128

Figure 4.24. As in Fig. 4.23, except as a function of uniform low-level (a) *T* and (b) $\log_e$ *Q* errors applied to RTTOV-6 levels 34 – 43. 129

Figure 4.25. Theoretical *T* retrieval performance (*P*) as a function of 0.00, 0.05, 0.25, and 0.50 g kg^{-1} cloud liquid water mixing ratio (*CLW*) error and EPAC cloudy sky background state vectors (a) EPAC Profile 2A1, and EPAC Profile 2B2. *P* is calculated using covariance $\mathbf{B_C}$. 131

Figure 4.26. As in Fig. 4.25, except for $\log_e$ *Q* theoretical retrieval performance (*P*). 132

Figure 4.27. As in Fig. 4.26, except with theoretical $\log_e$ *Q* retrieval *P* calculated using clear sky background state vector, EPAC Profile 1A. 133

Figure 5.1. Example of $\log_e$ *Q* Jacobian modification during 1DVAR iteration. Results of the 1st and 7th (final) iteration of $H_i(\mathbf{x}_i)$ for AMSU-A channel 1. The background state vector ($\mathbf{x}_i$) is taken from the set of 1000 simulated profiles and the "true" profile ($\mathbf{x}^t$) is cloudy sky EPAC Profile 2B2. 138

Figure 5.2a. 1000 simulated profile temperature (left panel) and $\log_e$ specific humidity (right panel) background profiles ($\mathbf{x}^b$) calculated by (2.16) with random error perturbations based on $\mathbf{B_C}$. "True" profiles ($\mathbf{x}^t$) shown here is the U.S. Standard Atmosphere. 140

Figure 5.2b. As in Fig. 5.2a, except $\mathbf{x}^t$ is clear sky EPAC Profile 1A. 141

Figure 5.2c. As in Fig. 5.2a, except $\mathbf{x}^t$ is cloudy sky EPAC Profile 2A. 141

Figure 5.2d. As in Fig. 5.2a, except random error perturbations calculated using $\mathbf{B_N}$. The "true" profile is the U.S. Standard Atmosphere (Profile 3). 142

Figure 5.2e. As in Fig. 5.2a, except *T* error set to 5.00 K at RTTOV-6 levels 37 - 43 (839.35 – 1013.25 hPa). The "true" background state vector is EPAC Profile 2A1. 143

Figure 5.3. *T* and $\log_e$ *Q* random error perturbations sum$(\Sigma_i \gamma_i (\lambda_i)^{1/2} \mathbf{C}_i)^2$ normalized by the respective background error for $\mathbf{B_C}$ (left panel) and $\mathbf{B_N}$ (right panel). 143

Figure 5.4a. Absolute T (left panel) and $\log_e Q$ (right panel) background errors $(B_{ii})^{½}$, theoretical retrieval errors $(S_{ii})^{½}$, and simulated retrieval errors (σ_r) calculated with respect to $\mathbf{B_C}$ and the clear sky U.S. Standard Atmosphere as "truth". 146

Figure 5.4b. As in Fig. 5.4a, except for simulated and theoretical retrieval performance... 146

Figure 5.4c. Normalized retrieval bias for T and $\log_e Q$. 146

Figure 5.5a. As in Fig. 5.4a, except errors calculated with respect to $\mathbf{B_N}$. 147

Figure 5.5b. As in Fig. 5.4b, except calculated with respect to $\mathbf{B_N}$. 147

Figure 5.5c. As in Fig. 5.4c, except calculated with respect to $\mathbf{B_N}$. 147

Figure 5.6a. As in Fig. 5.4a, except calculated with respect clear sky EPAC Profile 1A.... 148

Figure 5.6b. As in Fig. 5.4b, except calculated with respect clear sky EPAC Profile 1A... 148

Figure 5.6c. As in Fig. 5.4c, except calculated with respect clear sky EPAC Profile 1A.... 148

Figure 5.7a. As in Figs 5.6a and 5.6b, except for only T retrieval errors and performance calculated with T_s background error of 0.00 K. 149

Figure 5.7b. As in Figs 5.6a and 5.6b, except for only $\log_e Q$ retrieval errors and performance calculated with ε_m background error of 0%. 149

Figure 5.8a. As in Fig. 5.4a, except calculated with respect clear sky EPAC Profile 1B.... 150

Figure 5.8b. As in Fig. 5.4b, except calculated with respect clear sky EPAC Profile 1B... 150

Figure 5.8c. As in Fig. 5.4c, except calculated with respect clear sky EPAC Profile 1B.... 150

Figure 5.9a. Absolute T (left panel) and $\log_e Q$ (right panel) background errors $(B_{ii})^{½}$, theoretical retrieval errors $(S_{ii})^{½}$, and simulated retrieval errors (σ_r) calculated with respect to $\mathbf{B_C}$ and cloudy sky EPAC Profile 2A1 as "truth". C_{FC} set to 0.50 in "truth" and the cloud errors for P_{CT}, C_{FC} and CLW are 20 hPa, 0.50, and 0.25 g kg^{-1}, respectively. 153

Figure 5.9b. As in Fig. 5.9a, except for simulated and theoretical retrieval performance... 153

Figure 5.9c. As in Fig. 5.9a, except for normalized retrieval bias for T and $\log_e Q$. 153

Figure 5.10a. As in Fig. 5.9a, except calculated with respect to cloudy sky EPAC Profile 2B2. 154

Figure 5.10b. As in Fig. 5.9b, except calculated with respect to cloudy sky EPAC profile 2B2. 154

Figure 5.10c. As in Fig. 5.9c, except calculated with respect to cloudy sky EPAC Profile 2B2. 154

Figure 5.11a. Absolute T (left panel) and $\log_e Q$ (right panel) background errors $(B_{ii})^{1/2}$, theoretical retrieval errors $(S_{ii})^{1/2}$, and simulated retrieval errors (σ_r) calculated with respect to $\mathbf{B_C}$ and cloudy sky EPAC Profile 2A1 as "truth". C_{FC} set to 1.00 in "truth" and cloud errors for P_{CT}, C_{FC} and CLW are 20 hPa, 0.00, and 0.25 g kg^{-1}, respectively. 155

Figure 5.11b. As in Fig. 5.11a, except for simulated theoretical retrieval performance..... 155

Figure 5.11c. As in Fig. 5.11a, except for normalized retrieval bias. 155

Figure 5.12a. As in Fig. 5.11a, except calculated with respect to cloudy sky EPAC Profile 2B2. 156

Figure 5.12b. As in Fig. 5.11b, except calculated with respect to cloudy sky EPAC Profile 2B2. 156

Figure 5.12b. As in Fig. 5.11c, except calculated with respect to cloudy sky EPAC Profile 2B2. 156

Figure 5.13a. As in Fig. 5.11a, except background T errors set to 5.00 K at levels 37-43 (839.95 – 1013.25 hPa). 157

Figure 5.13b. As in Fig. 5.11b, except background T errors set to 5.00 K at levels 37-43... 157

Figure 5.13c. As in Fig. 5.11c, except background T errors set to 5.00 K at levels 37-43.. 157

Figure 5.14. As in Figs. 5.11a-b, except for $\log_e Q$ retrieval errors (left panel) and performance (right panel) were the CLW background errors were set to 0.00 g kg^{-1}. 158

Figure 5.15. Example of a "successful" (a) T and (c) $\log_e Q$ simulated retrieval with clear sky EPAC Profile 1A. Convergence was achieved in 2 iterations. An expanded view of the lower atmosphere for (a) and (c) is provided in (b) and (d), respectively..... 161

Figure 5.16. As in Fig. 5.15, except for cloudy sky EPAC Profile 2A1. 163

Figure 5.17. As in Fig. 5.16, except is an example of retrieval that failed to converge in 10 iterations or less. 165

Figure 5.18. GOES-10 channel 2 image 20010711 0900Z of DYCOMS II area. [After http://www.joss.ucar.edu.] The box indicates the approximate geographic extent of the 360 x 288 km COAMPS 3rd nested grid and locations of the COAMPS reference profiles (Fig. 5.18). Reference grid point (1,1) is at 30.15 N, 123.19 W. 169

Figure 5.19. ECMWF "true" profile representing the averaged values for the area 30.0 – 32.5 N, 120.0 – 124.5 W, and selected COAMPS 9-hr forecast (a) T, (c) $\log_e Q$, and (e) CLW profiles from the 3rd nest (6 km horizontal grid spacing) interpolated to the 43 RTTOV-6 pressure levels. Expanded view of (a), (c), and (e) is provided in (b), (d), and (f), respectively. 170

Figure 5.20. Horizontal cross-section at 500 m of cloud mixing ratio (g kg^{-1}) for DYCOMS II COAMPS 6 km grid. The 9-hr forecast valid time is 0900Z 11 July 2001. [From http://www.joss.ucar.edu.] The maximum observed values for 11 July were near 0.6 g kg^{-1} (Stevens et al. 2002)..... 173

Figure 5.21. High-resolution dropsonde observation of (a) T, (b) $\log_e Q$, and (c) RH for 11 July 2001. Drop time was 0815Z at 32.135 N 121.673 W. [After http://www.joss.ucar.edu.] The collocated, vertically uninterpolated ECWMF and COAMPS (grid point 30-25) forecast profiles are also shown. .. 175

Figure 5.22a. Background, and theoretical retrieval T (left panel) and $\log_e Q$ (right panel) errors. CLW set to zero to simulate clear sky conditions. Background state vectors are DYCOMS II COAMPS 9-hr forecasts VT 20010711 0900Z. 177

Figure 5.22b. As in Fig. 5.22a, except for theoretical T and $\log_e Q$ retrieval performance ($P = 100[1- (S_{ii}/B_{ii})]$)..... 177

Figure 5.23. 1DVAR (a) T, and (c) $\log_e Q$ simulated clear sky retrievals with CLW profiles set to zero in $\mathbf{x}^b$ and $\mathbf{x}^t$. DYCOMS II COAMPS 9-hr forecasts VT 20010711 0900Z from the set of background state vectors ($\mathbf{x}^b$) and the simulated observations are calculated from the collocated ECMWF "true" forecast profile ($\mathbf{x}^t$). Background and retrieved profiles represent the averaged values over all successful retrievals. Lower panels are expanded views of the lower atmosphere from surface to 800 hPa. Expanded view of (a) and (c) are provided in (b) and (d), respectively. 179

Figure 5.24. As in Fig. 5.23b, except T_s error set to zero. 181

Figure 5.25a. Background, and theoretical retrieval T (left panel) and $\log_e Q$ (right panel) errors for cloudy sky 1DVAR simulated retrievals calculated using model CLW profiles. Cloud background errors are 20 hPa, 0.50, and 0.10 g kg^{-1} for P_{CT}, C_{FC} and CLW, respectively..... 182

Figure 5.25b. As in Fig. 5.25a, except for theoretical T and $\log_e Q$ retrieval performance. 182

Figure 5.26. As in Fig. 5.23, except for cloudy sky simulated retrievals with P_{CT}, C_{FC} and CLW errors of 20 hPa, 0.50, and 0.10 g kg^{-1}, respectively. The model CLW values were used for these simulations. 184

Figure 5.27. As in Figs. 5.26a-b, except for P_{CT} background error of 60 hPa and T errors within the lowest seven RTTOV-6 pressure levels (839.95 – 1013.25 hPa) set to 5.00 K..... 186

Figure 5.28a. Background, and theoretical retrieval T (left panel) and $\log_e Q$ (right panel) errors for cloudy sky 1DVAR simulated retrievals calculated using modified $\mathbf{x}^t$ and $\mathbf{x}^b$ CLW profiles. Cloud background errors are 20 hPa, 0.00, and 0.10 g kg^{-1} for P_{CT}, C_{FC} and CLW, respectively. 187

Figure 5.28b. As in Fig. 5.28a, except for theoretical T and $\log_e Q$ retrieval performance. 188

Figure 5.29. As in Fig. 5.23, except for cloudy sky simulated retrievals with modified CLW profiles. P_{CT}, C_{FC} and CLW errors are 20 hPa, 0.00, and 0.10 g kg^{-1}, respectively. 189

Figure 5.30. As in Fig. 5.29a and Fig. 5.29d, except P_{CT} background error set to 60 hPa. . 191

Figure 5.31. As in Fig. 5.18, except for GOES-10 channel 1 image for 1800Z 15 July 2001..... 192

Figure 5.32. As in Fig. 5.19, except for 6-hr forecast valid time of 1800Z 15 July 2001.... 193

Figure 5.33. Horizontal cross-section at 500 m of cloud mixing ratio (g kg^{-1}) for DYCOMS II COAMPS 6 km grid. The 6-hr forecast valid time is 1800Z 15 July 2001. [From http://www.joss.ucar.edu.]..... 196

Figure 5.34a. Background, and theoretical retrieval T (left panel) and $\log_e Q$ (right panel) errors for cloudy sky 1DVAR simulated retrievals. Cloud background errors are 20 hPa, 0.20, and 0.10 g kg^{-1} for P_{CT}, C_{FC} and CLW, respectively. 198

Figure 5.34b. As in Fig. 5.34a, except for theoretical T and $\log_e Q$ retrieval performance. 198

Figure 5.35. 1DVAR (a) T, and (c) $\log_e Q$ simulated cloudy sky retrievals using the DYCOMS II COAMPS 6-hr forecasts valid at 20010715 1800Z as background state vectors ($\mathbf{x}^b$) and simulated observations calculated from the collocated ECMWF "true" forecast profile. Cloud element background errors for P_{CT}, C_{FC}, and CLW set to 20 hPa, 0.20, and 0.10 g kg^{-1}, respectively. Background and retrieved profiles represent the averaged values over all successful retrievals. Expanded view of (a) and (c) provided in (b) and (d), respectively. 199

Figure 5.36. 1DVAR (a) T, and (b) $\log_e Q$ retrievals using the AMSU-A and B observations listed in Table 5.5 and COAMPS 9-hr forecast fields (valid at 0900Z 11 July 2001) from the DYCOMS II data set. Standard deviations of error for P_{CT}, C_{FC} and CLW set to 60 hPa, 0.50, and 0.03 g kg^{-1}. Retrievals are compared to collocated high-resolution dropsonde observation of 0815 Z and are shown for the lower atmosphere only. 204

Figure 5.37. As in Fig. 5.36b, except for $\log_e Q$ with CLW background error increased to 0.10 g kg^{-1}. 206

Figure 5.38. As in Fig. 5.36b, except for $\log_e Q$ with emissivity error of 0.05 for the AMSU surface sensitive channels..... 207

Figure 5.39. As in Fig. 5.36a, except T_s error increased from 1.57 to 3.14 K. 208

Figure 5.40. As in Fig. 5.36, except COAMPS CLW increased by a factor of ten. 209

Figure 5.41. Square root of the diagonal elements of the mean effective background error ($\mathbf{H}\,\mathbf{B_C}\,\mathbf{H}^T$) and observation error ($\mathbf{R}$) ATOVS channels 16 – 35 are AMSU-A channels 1 – 15 and ATOVS channels 31 –35 are AMSU-B channels 1 - 5. $\mathbf{H}$ was calculated at the final iteration for each of the 4,550 successful retrievals. $\mathbf{B_C}$ is the COAMPS specific background error covariance matrix. .. 214

Figure 5.42. GOES-10 channel 1 satellite image for 1430Z 11 July 2001. [From http://www.joss.ucar.edu.] The star near 31.7 N 121.1 W indicates the approximate release position of the 1432Z high-resolution dropsonde observation. 215

Figure 5.43. 1DVAR (a) T, and (c) $\log_e Q$ retrieval located near 31.7 N 121.1 W. These retrieval used AMSU-A and B observations and a COAMPS / NAVDAS 6-hr forecast valid at 12Z 11 July 2001. Expanded view of (a) and (c) from 800 hPa to the surface are shown in (b) and (c), respectively, along with the collocated 1423Z high-resolution dropsonde observation from the DYCOMS II data set. Release altitude for the in-situ observation was 2517 m..... 217

Figure 5.44. As in Figs. 5.43b and 5.43c, except the (a) T, and (b) $\log_e Q$ 1DVAR retrieval is compared with the adjacent NESDIS retrieval at 31.9N 121.0 W... 219

Figure A.1. Simulated 1DVAR *T* retrieval (dashed line) calculated with respect to diagonal **B** matrix with *T* background standard deviations of error set to 10 K. The background standard deviations of error for T_{2m} and T_s were set to 10 K. Simulated clear sky ATOVS observations were calculated from the 0900Z 11 July 2001 ECMWF "true" ($\mathbf{x}^t$) forecast profile (dashed-dotted line) shown in Fig. 5.19. The background profile (dotted line) is a representation of $\mathbf{x}^t$ without the MABL temperature inversion. 232

Figure A.2. As in Fig. A.1, except the retrieval was calculated using the diagonal **B** matrix with surface and atmosphere coupled inter-level correlations of error listed Table 3.1. 233

Figure A.3. As in Fig. A.1, except the retrieval was calculated using the COAMPS EPAC specific background error covariance ($\mathbf{B_C}$). 233

THIS PAGE INTENTIONALLY LEFT BLANK

LIST OF TABLES

Table 2.1. ATOVS channel characteristics and corresponding individual instrument channels. HIRS/3 channels 16-20 are not used in this dissertation. [After Li et al. (2000).] 14

Table 3.1 Inter-level correlations of error (x 100). [T and $\log_e Q$ after Franke 1999]. 42

Table 3.2. Standard deviations of error associated with the diagonal elements of the NOGAPS and summertime COAMPS EPAC background error covariance matrices ($\mathbf{B_N}$ and $\mathbf{B_C}$) for atmospheric profile parameters [temperature (T), log specific humidity ($\log_e Q$), ozone (O_3), and cloud liquid water mixing ratio (CLW)]. Cloud errors are discussed in Chapters IV and V..... 44

Table 3.3. As in Table 3.3, except for surface and cloud parameters. Cloud and emissivity errors are discussed in Chapters IV and V. 45

Table 3.4. Standard deviations associated with the diagonal elements of the ATOVS instrument error (**O**), RTTOV-6 forward model error (**F**), and combined observation error (**R**) covariance matrices. See text for data sources..... 48

Table 3.5. Summary of cloud and surface characteristics of the representative clear and cloudy sky EPAC background state vectors (1A, 1B, 2A1, 2A2, 2B1, and 2B2) and the clear sky U.S. Standard Atmosphere (Profile 3). 54

Table 4.1. Significant eigenvalues from the principal component analysis of (2.17) for the 35 ATOVS channels. H has been linearized about the clear sky EPAC Profile 1B background and U.S. Standard Atmosphere (Profile 3). Profile temperature (T) and $\log_e$ specific humidity ($\log_e Q$) contributions are shown as a percentage of each eigenvector. Results are calculated with respect to $\mathbf{B_N}$. 81

Table 4.2. First 10 singular values (λ_i) of (2.18) and associated degrees of freedom (ds_i) and information content (H) for clear sky EPAC Profile 1B and U.S. Standard Atmosphere (Profile 3). Totals are for all 35 singular values. Results for full and diagonal covariance $\mathbf{B_N}$ are shown. 83

Table 4.3. Background $(B_{ii})^{1/2}$ and theoretical retrieval $(S_{ii})^{1/2}$ errors and percent improvement (P) for surface pressure (P_s) and radiative skin temperature (T_s) as a function of selected background statevectors. Background profiles are shown in Fig. 3.2 and described in the text. Results were calculated with cloud errors set to zero in $\mathbf{B_N}$. 95

Table 5.1. Background errors $(B_{ii})^{1/2}$, simulated retrieval errors (σ_r) and biases for surface pressure (P_s), radiative skin temperature (T_s), cloud-top pressure (P_{CT}), and cloud liquid water mixing ratio (*CLW*). Cloud errors are 25 hPa for P_{CT}, 0.50 for C_{FC}, and 0.25 g kg^{-1} for *CLW*. Results are calculated with respect to $\mathbf{B}_C$ and for cloudy sky EPAC Profiles 2A1 and 2B2. Theoretical retrieval errors are shown for comparison. 159

Table 5.3. Surface parameters for ECMWF "true" profile ($\mathbf{x}^t$) and averaged COAMPS background state vectors ($\mathbf{x}^b$). Forecast valid time of 0900Z 11 July 2001..... 173

Table 5.4. As in Table 5.3, except for 6-hr forecast valid time of 1800Z 15 July 2001. 197

Table 5.5. NOAA-16 AMSU-A and -B observations averaged over area 30.0 – 33.0 N, 119.5 – 123.5 W. Orbit start time is 1010Z 11 July 2001..... 203

ACKNOWLEDGMENTS

I would first like to thank my co-advisors, Dr. Nancy Baker and Professor Philip Durkee for their mentorship during this academic odyssey. Dr. Baker dedicated many hours supervising this research and she provided invaluable technical guidance. Additionally, the expert insights provided by my other committee members, Professor Carlyle Wash, Professor Qing Wang, Professor Douglas Miller, and Professor Carlos Borges, are gratefully acknowledged.

I would also like to thank my M.S. thesis advisor Professor Tom Murphree for supporting my desire to pursue this degree. The technical assistance provided by Mr. Robert Creasey and Mr. Kurt Nielsen of Naval Postgraduate School was invaluable and greatly appreciated.

I have thoroughly enjoyed my association with the scientific professionals of Naval Research Laboratory, Monterey. In particular, I would like to thank Dr. Keith Sashegyi for his help with the COAMPS / NAVDAS code and Dr. Jason Nachamkin for providing the COAMPS error statistics. Dr. Bill Campbell and Dr. Clay Blankenship's expertise in satellite data assimilation was extremely valuable and Mr. Steve Swadley provided the ATOVS data for this research.

I could not have completed this Ph.D. program without the love and full support of my remarkable wife, Katie. She offered continual encouragement while at the same time raising our twin toddlers, Ryan and Marisa. In proper Navy fashion, her reward will be an extended overseas tour to the Middle East.

THIS PAGE INTENTIONALLY LEFT BLANK

I. INTRODUCTION

The theoretical and applied research presented in this dissertation is a rigorous study of the variational satellite retrieval problem. Specifically, it investigates the ability of a combined infrared and microwave atmospheric sounding system to contribute information to a mesoscale numerical weather prediction (NWP) system within the summertime eastern Pacific (EPAC) environment. This dissertation has direct application to on-going, and future Navy relevant research, e.g., mesoscale satellite data assimilation efforts at Navy Research Laboratory (NRL) Monterey, CA.

Non-linear optimal estimation theory is used to evaluate the information content and retrieval error sensitivity of Advanced TIROS (Television and Infrared Observation Satellite) Observational Vertical Sounder (ATOVS) retrievals with respect to mesoscale *a priori* constraints. Based upon these results, simulated ATOVS retrievals using representative EPAC background state vectors and a synoptically relevant background error covariance matrix are conducted in order to validate the NRL one-dimensional variational (1DVAR) retrieval algorithm. Simulated and actual ATOVS retrievals are then generated using the U.S. Navy's Coupled Ocean – Atmosphere Mesoscale Prediction System[2] (COAMPS™; Hodur 1997) as background. A three dimensional analysis of ATOVS retrievals is also conducted using COAMPS with the NRL Atmospheric Variational Data Assimilation System (NAVDAS; Daley and Barker 2000).

Motivation for this research is that naval forces primarily operate within the marine atmospheric boundary layer (MABL) environment. The safety and combat effectiveness of ship and aircraft operations depend on the accurate nowcasting and forecasting of sensible weather elements such as cloud ceiling, visibility, and winds, all of which are directly influenced by the MABL. Performance of electromagnetic (EM) - based surveillance and weapons systems can be affected to varying degrees by small-scale vertical and horizontal changes in MABL humidity and temperature. Various research programs, sponsored by Office of Naval Research (ONR) and other Department

[2] COAMPS™ is a trademark of Naval Research Laboratory

of Defense activities, are attempting to address these issues by working to improve mesoscale NWP cloud initialization, satellite data assimilation, nowcasting, cloud microphysical retrievals, and mesoscale modeling of atmospheric refractivity (e.g., see Mozer and Ayer 1998; Ruggiero et al. 1999; Cook et al. 2000; Haack and Burk 2000; Wetzel et al. 2001). The U.S. Navy meteorology and oceanography (METOC) community is also actively pursuing remote sensing and NWP techniques that will provide (near) real-time volumetric environmental battlespace characterization. Furthermore, these methods must succeed in data denied areas, or where in-situ observations are limited.

Assimilation of temperature and humidity retrievals and/or radiances from various satellite atmospheric sounders is performed at all major NWP centers and has improved overall model skill (Ghil et al. 1979; Cram and Kaplan 1985; Filiberti and Eymard 1994; Powers and Gao 2000). Fleet Numerical Meteorology and Oceanography Center (FNMOC) / NRL Monterey currently assimilate ATOVS temperature retrievals into the Navy Operational Global Atmospheric Prediction System (NOGAPS; Hogan and Rosmond 1991). NRL Monterey, in collaboration with this dissertation, is investigating assimilation of ATOVS observations with COAMPS / NAVDAS. NAVDAS, a three-dimensional variational (3DVAR) scheme, is the replacement for multivariate optimum interpolation (MVOI) analysis. Other NWP centers, e.g. United Kingdom Meteorological Office (English et al. 2002), are also focusing resources on the mesoscale satellite data (AMSU-A and B) assimilation efforts.

In many instances satellites are the only means in which to collect METOC observations within these data sparse / denied areas. However, current satellite-borne sounding instruments (e.g., ATOVS) alone cannot provide the required vertical resolution to detect low-level temperature and humidity gradients (Thompson and Hou 1990; Kidder and Vonder Haar 1995) and it is uncertain whether emergent systems, such as the Advanced Infrared Sounder (AIRS) will be able to independently resolve the MABL inversion problem (Garand 2000).

With respect to the MABL retrieval problem, the general structure of the low-level temperature gradient represented in a satellite sounding is an artifact of the *a priori* constraint (e.g., Eyre et al. 1993; Kidder and Vonder Haar 1995; Daley and Barker 2000). The inverse sounding or retrieval problem is ill-posed and satellite data provide relatively limited independent information over *a priori* constraints, i.e., a background profile (Smith 1972; Rodgers 1976; Thompson et al. 1986; Rodgers 2000). For most applications, such as NWP data assimilation, this *a priori* constraint is a short-term forecast profile. As a consequence, the quality of a satellite retrieval depends on the accuracy of this background profile. COAMPS has demonstrated skill in forecasting the three-dimensional structure of the EPAC boundary-layer structure (e.g., Haack and Burk 2000). This suggests that it should be a suitable background for mesoscale applications. However, all NWP models are subject to some degree of error and uncertainty due to treatment of model physics and lack of in-situ observations for providing accurate initial conditions. Information from satellite observations is therefore still required.

Non-linear optimal estimation theory is applied in this research to advance our knowledge of the complex temperature and humidity structure of the marine environment. This theory uses the principle of Bayes' theorem to find the most probable state of the atmosphere, given a set of satellite measurements, by constraining the satellite observations with a short-term NWP forecast and statistically derived background error covariances. Although the general structure of the shallow temperature inversion is derived from the background, satellite soundings when treated optimally have been shown to improve aspects of the retrieval. For example, Eyre (1989a) showed that the effects of mid-level cloud on infrared radiances can theoretically improve the temperature retrieval above the cloud top. Previous research using non-linear optimal estimation techniques investigated the capabilities of satellite sounders based upon global scale *a priori* constraints (e.g. Rodgers 1976; Eyre 1986a, 1986b, 1990; Prunet et al. 1998; English 1999; Garand 2000).

Information theory is used to thoroughly evaluate the information content of ATOVS retrievals and to test retrieval (or analysis) error sensitivity. This research focuses on both the cloud-free, and stratus- / stratocumulus-topped MABL environments

under strong subsidence inversions, specifically, summertime conditions in the vicinity of coastal California. COAMPS specific forecast errors for the summertime EPAC regime are used to construct a synoptically relevant background error covariance matrix. Additionally, this error covariance matrix couples the surface and profile errors for temperature. Results are then compared with those calculated using globally averaged NOGAPS background errors, which are used as the appropriate first-order approximation. Total information content is not expected to differ significantly between background profile types; however, the vertical distribution of information is more germane; particularly the effects of a strong low-level water vapor gradient.

Within the framework of this ATOVS retrieval problem, an objective of this research is to establish which parameters within the EPAC background state vector need to be accurately known for successful variational retrievals. Requirements for additional observations (e.g. from collocated satellites) and prioritization of future improvements in model background (e.g. COAMPS) can then be established. Retrieval error sensitivity and retrieval performance are evaluated in this dissertation for various clear and cloudy sky EPAC background state vectors and associated errors. These additional MABL observations from satellite imagers (e.g., Advanced Very High Resolution Radiometer (AVHRR), Geostationary Operational Environmental Satellite (GOES), and Special Sensor Microwave Imager (SSM/I)) include, but are not limited to, cloud-top temperature, sea surface temperature, cloud optical depth, column integrated water vapor, and surface wind speed. Additionally, retrieval methods to determine the height of both clear, and stratocumulus-topped MABL's have been studied by numerous researchers (e.g., Kren 1987; Minnis et al. 1992; Betts et al. 1992; McBride 2000). The techniques developed by Kren (1987) and McBride (2000) are independent of a background NWP model, but all these methods combine a thermodynamic boundary layer model with satellite retrievals of MABL parameters such as cloud-top temperature and sea surface temperature. Also, researchers at Desert Research Institute (DRI) and NRL Monterey are developing improved retrieval techniques for cloud liquid water and boundary layer height (M. Wetzel and T. Haack, personal communication).

To complement the extensive theoretical information content and retrieval error sensitivity study and to validate the NRL Monterey's 1DVAR retrieval algorithm, a statistically significant number of simulated ATOVS retrievals are calculated for representative summertime clear and cloudy sky EPAC conditions. This 1DVAR scheme, developed by N. Baker and R. Daley (NRL Monterey), is available as an off-line satellite retrieval algorithm for NAVDAS. In this non-linear Newtonian iterative scheme, the fast radiative transfer model RTTOV-6 is used to calculate the top of the atmosphere radiances (Saunders et al. 1999; Saunders 2000). By comparing the theoretically derived retrieval errors and those calculated from the 1DVAR retrieval for various EPAC profile types and *a priori* errors, the validity of the NRL 1DVAR retrieval algorithm for this mesoscale application can be assessed.

1DVAR retrievals are then computed using ATOVS simulated observations and a set of COAMPS short-term forecasts from the Dynamics and Chemistry of Marine Stratocumulus (DYCOMS) Phase II field study (see Bjorn et al. 2002). This phase of research investigates the ability of this 1DVAR technique to use the satellite derived information to adjust the background, especially within the MABL, toward the designated true profile. Temperature and humidity retrievals are then generated using ATOVS microwave sounder data (i.e., AMSU-A and B) and the same set of DYCOMS II COAMPS short-term forecasts. Temperature and humidity retrievals are evaluated against an in-situ observation.

This research employs information theory and non-linear optimal estimation techniques to study the complex relationship between satellite atmospheric soundings and *a priori* constraint. Specifically, this dissertation is a study of ATOVS infrared and microwave retrievals within the summertime EPAC MABL environment. Chapter II reviews relevant theory and outlines the research methods used in this dissertation. The theoretical discussion is not intended as comprehensive review, but provides a basic overview of satellite inverse theory, marine atmospheric boundary layer (MABL) structure and modeling, the COAMPS model, information theory and methods, and simulated retrieval methods. Chapter III describes the specific prior information used in this dissertation. These include the background and observation error covariance

matrices, idealized (clear and cloudy) summertime EPAC atmospheric background state vectors, and Jacobians. Chapter IV presents the results of the information content and retrieval error sensitivity study. Chapter V presents the results of 1DVAR retrievals based upon simulated ATOVS observations and both simulated background state vectors, and COAMPS short-term forecasts from the DYCOMS II field experiment. 1DVAR retrievals conducted using ATOVS observations and COAMPS short-term forecasts for DYCOMS II are presented in Chapter VI. Conclusions and recommendations are presented in Chapter VII.

II. THEORY AND RESEARCH METHODS

This chapter reviews the fundamental theoretical principles applied in this research and outlines the methods used to calculate information content and one-dimensional variational (1DVAR) retrievals. The first section briefly introduces the radiative transfer equation and reviews basic atmospheric sounding theory. A description of the ATOVS system and a review of its retrieval applications are also provided in Section II.A. The COAMPS model, which is used in this dissertation as *a priori* constraint, is described in Section II.B. Section II.C summaries the general structure of the marine atmospheric boundary layer (MABL) and includes discussions of current mesoscale modeling efforts and satellite-based capabilities to retrieve boundary layer parameters. 1DVAR retrieval theory and information theory are thoroughly discussed in Sections II.D and II.E. The techniques used to calculate simulated atmospheric retrievals are described in Section II.F.

A. ATMOSPHERIC SOUNDING THEORY AND ATOVS DESCRIPTION

1. Radiative Transfer Equation and Inverse Atmospheric Sounding Theory

The following discussion is intended as an overview of the radiative transfer equation and the inverse atmospheric sounding problem. A comprehensive review of satellite remote sensing theory and applications can be found in Kidder and Vonder Haar (1995) and satellite inversion theory is rigorously addressed in Smith (1972), Rodgers (1976), Eyre (1991), Bouttier and Courtier (1999), and Rodgers (2000). Techniques for the retrieval of atmospheric water vapor, cloud liquid water and cloud optical depth by complimentary satellite systems (e.g., AVHRR, DMSP SSM/I, etc.) are discussed in Hansen and Travis (1974), Stephens (1978), McMillin and Crosby (1984), Dalu (1986), Durkee et al. (1986;1991), Wetzel and Vonder Haar (1991), Kuji et al. (2000), and Simpson et al. (2000).

a. The Radiative Transfer Equation

The non-scattering, general form of the radiative transfer equation (RTE), or Schwartzchild's equation, is a good approximation for passive infrared (IR) and microwave (MW) satellite measurements (Kidder and Vonder Haar 1995). This form of the RTE can be written as

$$L_t(\lambda,\theta,\varphi) = \varepsilon_s(\lambda,\theta)B(\lambda,T_s)\tau_d(\lambda) + \int_{p_0}^{0} B(\lambda,T(p))\frac{d\tau_d(\lambda,p)}{dp}dp\,, \qquad (2.1)$$

where L_t (λ,θ,φ) is spectral radiance (Wm^{-2} sr^{-1} μm^{-1}) that reaches the top of the atmosphere and is function of wavelength λ, zenith angle θ, and azimuth angle φ. Note that all terms in the equation are wavelength dependent. The first term on the right hand side of the equation is the surface source term. It is composed of surface emissivity $\varepsilon_s(\lambda,\theta)$, Planck function $B(\lambda,T_s)$, which is surface temperature T_s dependent, and $\tau_d(\lambda)$, the direct transmittance from the surface to the top of the atmosphere. The second term represents the contribution from atmospheric path radiance and is integrated from pressure level p_0 to the top of the atmosphere. $B(\lambda,T(p))$ is the Planck blackbody radiance profile and is function of atmospheric temperature at a given pressure level. The Planck function is weighted by the derivative of the pressure level dependent direct transmittance, $\tau_d(\lambda,p)$. This weighting function determines the vertical level within the atmosphere that contributes the most to $L_t(\lambda,\theta,\varphi)$.

Equation (2.1) assumes that there is no reflection of radiation from the earth's surface. Kidder and Vonder Haar (1995) also present alternate forms of the RTE. This example deals only with monochromatic radiation and in practice the RTE must be integrated over multiple wavelengths.

The Planck function describes the radiance emitted by a blackbody and can be expressed as $B(\lambda,T) = c_1\lambda^{-5}\Big/\left(e^{(c_2/\lambda T)}-1\right)$, where λ is the wavelength at which the radiation is emitted, and c_1 and c_2 are first and second radiation constants, and T is the temperature in Kelvin. For microwave applications, the Rayleigh-Jeans approximation

can be applied, since for earth and atmospheric temperatures, $c_2 / \lambda T << 1$ and therefore, we can make the approximation $e^{(c_2/\lambda T)} \approx 1 + c_2/\lambda T$. The Planck function then becomes a linear function of temperature $B(\lambda, T) = (c_1/c_2)\lambda^{-5} T$.

b. Inverse Atmospheric Sounding Theory

The inverse atmospheric sounding problem involves inverting the RTE to express the Planck function profile in terms of the measured satellite radiances. Following Rodgers (1976; 2000) the simple solution to inverse problem, as function of wavenumber (ν), is obtained from the linearized form of the RTE

$$L(\nu) = \int_0^\infty B[\nu, T(z)] \frac{d\tau(\nu, z)}{dz} dz \,, \tag{2.2}$$

where $L(\nu)$ is the upward radiance at the top of the atmosphere, $B[\nu, T(z)]$ is the blackbody radiance at temperature T and height z and, and $\tau(\nu, z)$ is the transmittance from height z to the satellite. This simplified RTE assumes the atmospheric optical depth is so large that the transmittance from the surface to the satellite is zero.

By making m measurements of $L(\nu)$ for a set of narrowly spaced ν, the frequency dependence of $B[\nu, T(z)]$ can be ignored. Equation (2.2) can then be written for a representative wavenumber ($\bar{\nu}$) as

$$L_i = L(\nu_i) = \int_0^\infty B\left\{\bar{\nu}, T(z)\right\} K_i(z) dz \,, \tag{2.3}$$

where $i = 1 \ldots m$, and the weighting function $K_i(z) = d\tau(\nu, z)/dz$. The problem is now linear with respect to the unknown Planck function profile and $L(\nu_i)$ is simply the weighted mean of $B\left\{\bar{\nu}, T(z)\right\}$. However, solutions to the Planck function profile and hence, T(z) are rather problematic. Equation (2.3) is under-constrained, or ill-posed, since it attempts to represent an unknown continuous profile with a limited set of

measurements. By converting (2.3) to its discrete form, the solution to the RTE can be written as

$$B(\overline{\nu},T(z)) = \sum_{i,j} W_j(z) C_{ji}^{-1} L(\nu_i) = \sum_i G_i(z) L(\nu_i) \quad , \tag{2.4}$$

where $W_j(z)$ is a set of functions representing the profile, j is the number of functions, C_{ji}^{-1} is the ji^{th} component of the known inverse matrix $\mathbf{C}^{-1}$, $G_i(z)$ are the contribution functions, and $G_i(z)L_i$ is the contribution to the solution profile due to the measure radiance L_i. The square matrix $\mathbf{C}$ has elements $C_{ij} = \int_0^\infty W_j(z) K_i(z) dz$. This solution gives back exactly the measured radiance when inserted in measurement equation [2.3], and can therefore be termed exact (Rodgers 2000). However, in practice the problem is still ill-conditioned, since any error (ε_i) in L_i will result in corresponding error of $G_i(z)\varepsilon_i$ in the solution profile.

As described above, the inverse problem is ill-posed and requires application of estimation theory to determine the appropriate solution (Rodgers 1976). This research employs a variational approach to the inverse problem, which is fully described in Section II.E.

c. Constraints

The first-guess profiles can be derived using a regression technique with a global radiosonde data set, climatological mean, adiabatic lapse rate, and/or NWP forecast model (e.g., Li et al. 2000; Kidder and Vonder Haar 1995; Peckham and Grippa 2000; and Smith et. al. 1972, respectively). As mentioned above, the retrieval of atmospheric variables (e.g., temperature and humidity) from measured spectral radiances is an ill-posed, or under-constrained problem, that results from representing a continuous function of height with a finite number of noise contaminated measurements. Each retrieval, or inverse solution, produces an infinite set of thermal profiles that satisfy the

measurements within a given error envelope (Thompson et al. 1986). The solution, therefore, depends on imposing additional constraints to find temperature profiles that are consistent with brightness temperatures computed using the radiative transfer equation and that closely represent the true atmosphere (Rodgers 1976; Eyre 1990; Kidder and Vonder Haar 1995; Rodgers 2000).

Smith et al. (1972) first described a method to retrieve vertical atmospheric temperature profiles from satellite (NIMBUS IV Satellite Infrared Spectrometer) measured spectral radiances and a NWP first-guess. Follow-on research by Lipton and Vonder Haar (1990) showed that vertical resolution for the VISSR Atmospheric Sounder (VAS) retrieval was improved when a numerical model provided the initial guess profile. Even though Thompson and Trippuit (1994) cautioned against this "interactive" satellite retrieval scheme because of the possible adverse influence of systematic model errors on the satellite retrieval, Ruggiero et al. (1999) successfully demonstrated forecast improvement over independent stand-alone retrievals using this coupled model-satellite concept.

Several studies have demonstrated NWP forecast improvement by assimilating satellite-derived temperature and moisture profiles (e.g., Ghil et al. 1979; Cram and Kaplan 1985; Filiberti and Eymard 1994; Powers and Gao 2000). Eyre et al. (1993) argued that assimilation of retrieved products constitutes a suboptimal use of the data, because it disregards the cross-covariances between the background and retrieval errors. Many of the major NWP centers (e.g., European Centre for Medium-Range Weather Forecasts (ECMWF), National Center for Environmental Prediction (NCEP) and United Kingdom Meteorology Office (UKMO)) have transitioned to directly assimilating radiances using variational methods, vice assimilating retrievals (geophysical products) derived from the global radiance measurements. Efforts are currently underway at NRL Monterey to assimilate selected ATOVS-derived radiances into NOGAPS via a three-dimensional variational (3DVAR) scheme.

d. Clouds

Clouds make the IR retrieval problem nonlinear. Not only do opaque clouds prevent sounders from measuring the upwelling IR radiation from below cloud level, but the shape of the weighting functions change radically at cloud top.

Microwave sounding channels are virtually insensitive to cloud liquid water path less than 100 g m^{-2}; however, the surface sensitive channels are highly sensitive to liquid water path (English 1999). With the presence of cloud liquid water, three effects on the sensitivity of microwave radiances must be addressed: 1) the possibility of cloud liquid water must be included in the background state vector; 2) sensitivity to the atmosphere below the cloud will be reduced by absorption within the cloud; and 3) forward model errors will most likely be larger in cloudy scenes due to increased scattering, heterogeneity, and errors in the dielectric model (English 1999). Random errors in the forward model increase as the clouds become deeper.

In general, three approaches can be used to eliminate, or minimize cloud contamination. The first method uses passive microwave sensors; the second screens data through various cloud-clearing techniques; and the third method performs the inversion directly from the cloudy radiances (Eyre 1989a,1991; Kidder and Vonder Haar 1995). Each method has distinct advantages and disadvantages. Microwave channels exploit frequencies nearly transparent to non-precipitating clouds, and with the considerations discussed in the previous paragraph, has the obvious advantage of allowing for data collection below cloud level. However, significant upper-air temperature profile information may be lost by IR channel deselection, especially for the low cloud environment. Cloud-clearing techniques eliminate most of the uncertainty with respect to clouds, but require additional data processing and may exclude geographical areas of interest. Atmospheric temperature and constituent retrievals using cloud-cleared radiances often contain large, non-Gaussian errors with inter-channel error correlations (Eyre 1989a). The third method is the most complex since it requires solutions to the nonlinear retrieval problem. However, this method has the potential to provide the most information from the radiances and avoids the requirement for cloud-

clearing. This dissertation uses a non-linear optimal estimation approach. Effects of cloud on IR radiances can, if treated optimally, improve aspects of the retrieval, such as the air temperature above cloud top (Eyre 1989a).

2. ATOVS Instrument

The Advanced Television and Infrared Observation Satellite (TIROS) Observational Vertical Sounder (ATOVS) package was chosen for this study because it is: 1) a combined infrared (IR) and microwave (MW) sounding system; 2) currently operational; and 3) the current focus of NRL Monterey satellite data assimilation efforts. ATOVS consists of the High-resolution Infrared Radiation Sounder (HIRS/3), Advanced Microwave Sounding Unit-A (AMSU-A), and the Advanced Microwave Sounding Unit-B (AMSU-B).

a. Channel Characteristics

The basic characteristics of the selected 35 ATOVS channels used for this study are listed in Table 2.1. See Li et al. (2000) and NOAA KLM User's Guide (2001) for detailed instrument characteristics. The microwave frequency spectrum as a function of vertical transmittance to space is shown for reference in Fig. 2.1. The regions of the microwave frequency spectrum with large transmittance values correspond to the atmospheric window channels, such as 31.4 and 89.0 GHz. Low values of vertical transmittance is associated with the frequencies affected by atmospheric water vapor (H_2O_v) and oxygen (O_2) absorption. Detailed diagrams of the IR spectrum can be found in Kidder and Vonder Haar (1995). The primary atmospheric absorbers of IR radiation are carbon dioxide (CO_2), H_2O_v, and ozone (O_3).

The 20-channel HIRS/3 instrument has one visible (0.69 μm), seven shortwave IR (3.7 – 4.6 μm), and 12 longwave IR (6.5 – 15 μm) channels. Temperature profile information is derived primarily from CO_2 sounding channels 1 – 7 and 13 – 16. Humidity information is derived primarily from water vapor channels 10 - 12 and surface temperature is derived from channels 8, 18, and 19. Channels 9 and 17 provide total atmospheric O_3 and nitrogen (N_2) temperatures, respectively. The visible channel (channel 20) can be used for cloud detection. This study uses only HIRS/3 channels 1 - 15 to exclude the possibility of solar contamination. In an optimal sense, Eyre (1989a)

showed that HIRS/3 surface sensitive channels 18 and 19 contributed to minimal improvement in profile retrieval performance; however, these channels can improve retrieval of radiative skin temperature and low-level cloud parameters. The HIRS/3 instantaneous field-of-view (IFOV) encompasses approximately 20 km at nadir (20.3 km for visible and shortwave IR and 18.9 km for longwave IR).

Table 2.1. ATOVS channel characteristics and corresponding individual instrument channels. HIRS/3 channels 16-20 are not used in this dissertation. [After Li et al. (2000).]

ATOVS channel	instrument channel	central wavelength (μm)	ATOVS channel	instrument channel	central frequency f_o (GHz)
	HIRS/3			AMSU-A	
1	1	14.95	16	1	23.8
2	2	14.71	17	2	31.4
3	3	14.49	18	3	50.3
4	4	14.22	19	4	52.8
5	5	13.97	20	5	53.6
6	6	13.64	21	6	54.4
7	7	13.35	22	7	54.9
8	8	11.11	23	8	55.5
9	9	9.71	24	9	f_o= 57.29
10	10	12.47	25	10	f_o +/- .217
11	11	7.33	26	11	f_o +/- .332 +/- .048
12	12	6.52	27	12	f_o +/- .332 +/- .022
13	13	4.57	28	13	f_o +/- .332 +/- .010
14	14	4.52	29	14	f_o +/- .332 +/- .0045
15	15	4.47	30	15	89.0
				AMSU-B	
			31	1	89.0
			32	2	150.0
			33	3	183.3 +/- 1.0
			34	4	183.3 +/- 3.0
			35	5	183.3 +/- 7.0

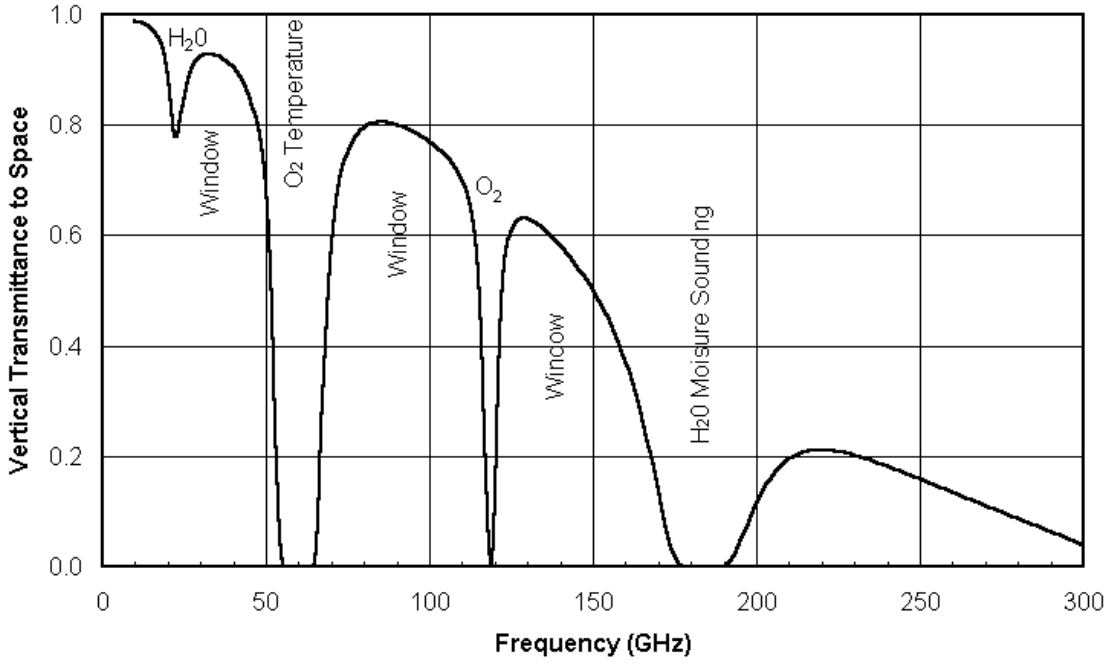

Figure. 2.1. Vertical transmittance to space as a function of microwave frequency (GHz). See Table 2.1 for the center frequencies of the corresponding AMSU channels. Regions of the microwave frequency spectrum with large transmittance values are shown as the window "channels." Atmospheric water vapor (H_2O) and oxygen (O_2) are the primary absorbers of MW radiation. [From http: //amsu.cira.colostate.edu.]

AMSU-A, a 15-channel microwave radiometer, is divided into two separate modules. AMSU-A1 (channels 3 – 15) measures global temperature profiles by exploiting the O_2 temperature bands and AMSU-A2 uses the two lowest frequencies at 23.8 and 31.4 GHz (i.e., channels 1 and 2) to provide information on atmospheric water vapor and cloud liquid water. AMSU-A1 channel 15 is the 89.0 GHz window channel and can be used to measure near-surface humidity and cloud information. Nominal resolution for this instrument is approximately 50 km at nadir. AMSU-B is a 5-channel microwave radiometer originally designed to obtain global humidity profile data. Sounding channels 3, 4 and 5 cover the strongly opaque 183 GHz water vapor absorption line while channels 1 and 2 provide near-surface humidity and cloud information. This instrument's scene resolution cells are approximately 16 km in diameter at nadir.

An example of the size and spatial orientation of the AMSU-A scene resolution cells is shown (as purple circles) in Fig. 2.2. These MW sounders provide nearly full coverage under the satellite path with approximately nine AMSU-B cells (as indicated by the blue center dots) per AMSU-A scene. The coverage for the older TOVS Microwave Sounding Unit (MSU) is also shown (as yellow circles) and demonstrates the significant improvement in spatial coverage provided by AMSU. This comparison indicates that these new MW sounders should be suitable for mesoscale retrieval applications.

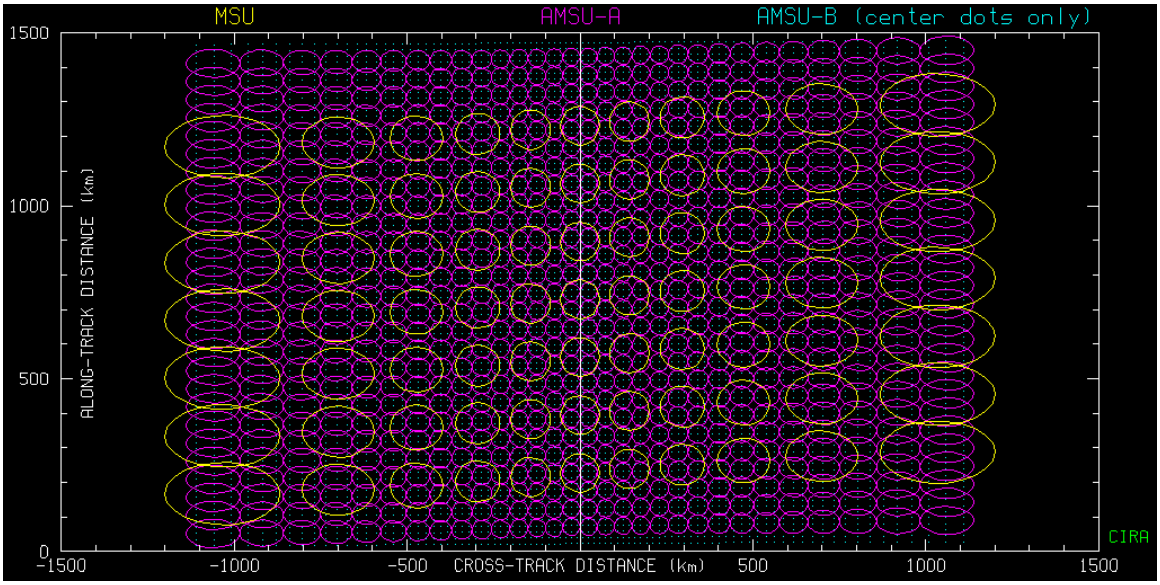

Figure. 2.2. Example of the scene resolution cells for ATOVS AMSU-A (thin purple circles), AMSU-B (blue dots), and TOVS MSU (thick yellow circles). This comparison shows that the AMSU sounders have the spatial resolution suitable for mesoscale retrieval applications. [From http://amsu.cira.colostate.edu.]

b. Weighting Functions and Vertical Resolution

The HIRS/3 and AMSU channel weighting functions for U.S. Standard Atmosphere background are shown in Figs. 2.3 and 2.4. These functions specify contributions from each layer of the atmosphere to the observed radiances. Unfortunately, individual weighting functions of current operational sounders (e.g., AMSU-A) can be very broad at their inflection point (~ 20 km). The combined vertical

resolution of the sounder system depends on the number and sharpness of the weighting function inflection, and how closely the individual channels overlap. Smith and Woolf (1978) and Chesters et al. (1983) describe how the broadness of the spectral weighting functions for temperature and moisture retrieval schemes limit vertical resolution. Though there have been improvements in sounding system technology (e.g., ATOVS and GOES High Resolution Interferometer Sounder (GHIS)), they cannot independently resolve, to a necessary degree of fidelity, the temperature and moisture structure of the atmospheric boundary layer. For example, sounders have difficulty resolving the surface layer inversion where the lapse rate abruptly changes with height (Kidder and Vonder Haar 1995). Retrieval validation performed by Li et al. (2000) shows ATOVS retrieved global profiles are accurate to 2 K r.m.s. error for temperature at 1 km vertical resolution and 3 - 6 K r.m.s. error for humidity at 2 km vertical resolution.

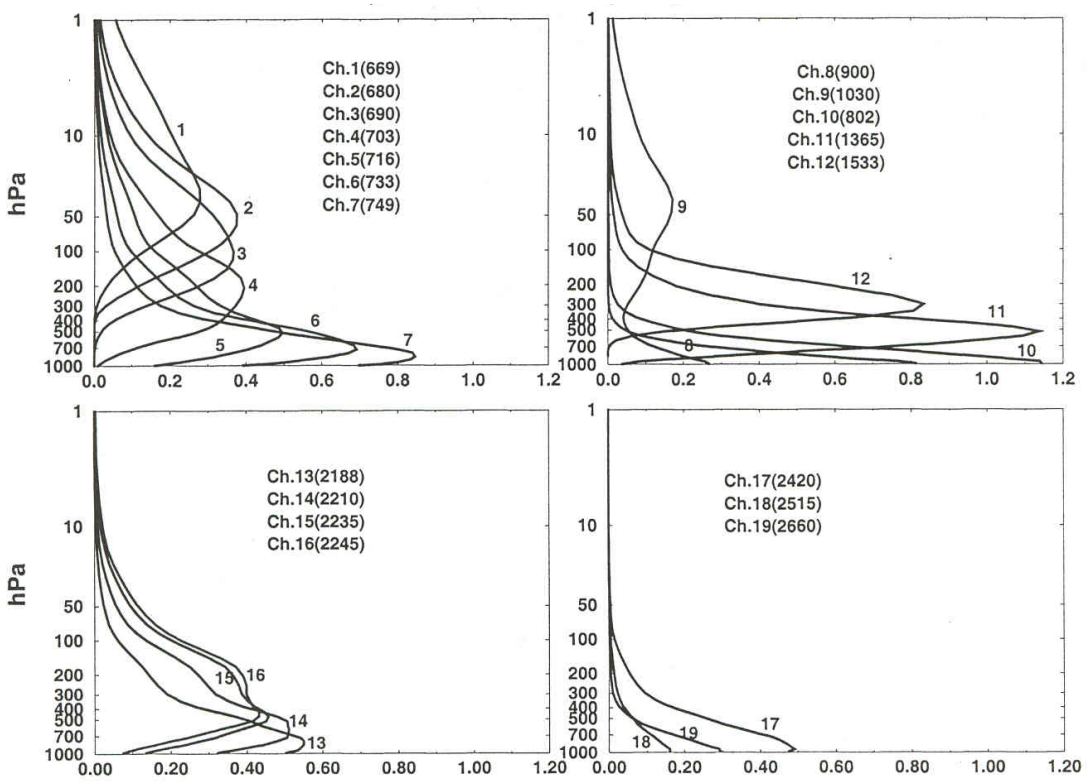

Figure 2.3. HIRS/3 sensitivity functions ($d\tau$ / d lnp) for channels 1-19, calculated with respect to U.S. Standard Atmosphere. Channels 16 - 19 are not included in this research. [From Li et al. (2000).]

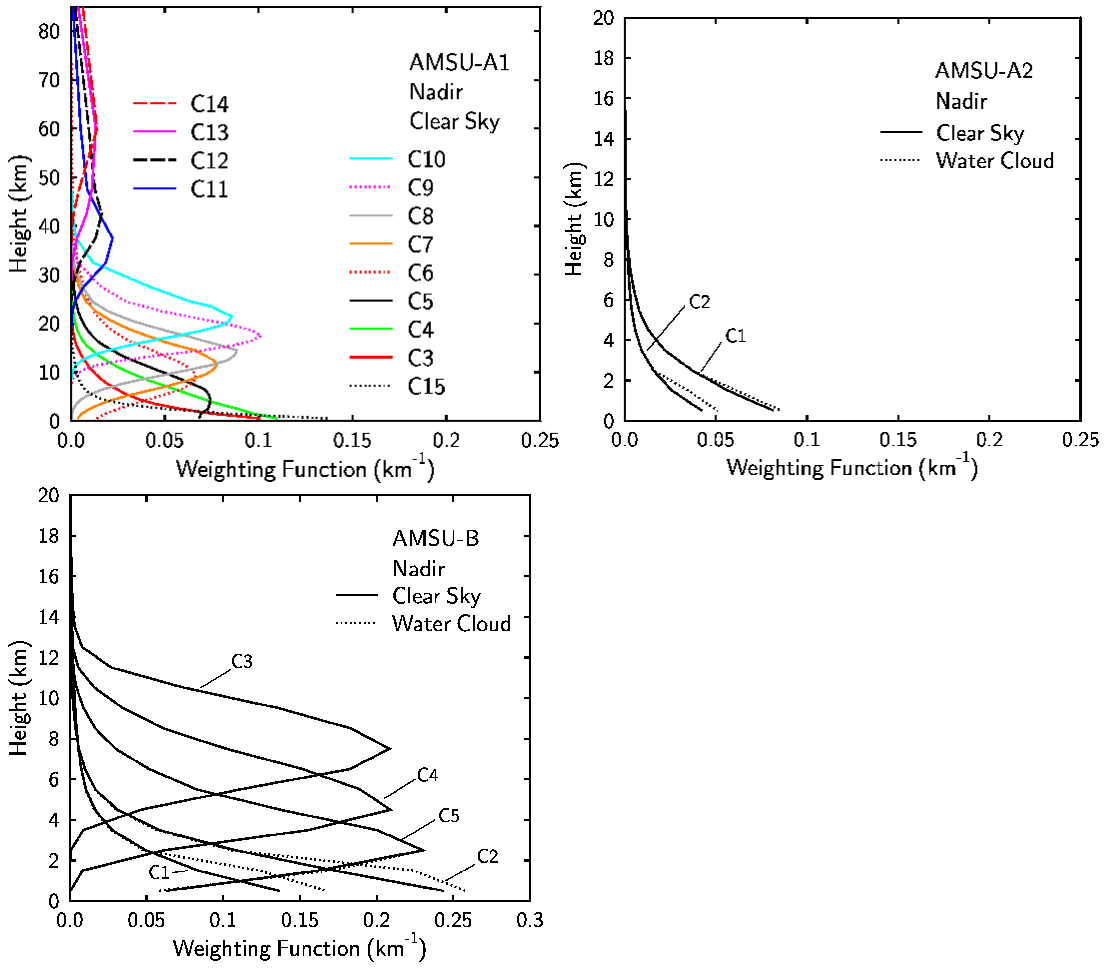

Figure 2.4. Weighting functions for AMSU module A1 (channels 3 – 15), AMSU module A2 (channels 1 – 2), and AMSU-B channels 1 – 5. Calculated with respect to the U.S. Standard Atmosphere for all channels. The sensitivity of AMSU-A2 and AMSU-B channels 1 and 2 to liquid water cloud is also shown. [From http://amsu.cira.colorado.edu.]

By using instruments with greater spectral resolution, Eyre (1991) states that it is possible to closely match the widths of the atmospheric absorption lines, thereby narrowing the weighting function width and improving vertical resolution within the free atmosphere. However, even the much anticipated next generation sounders will probably not be able to independently resolve the MABL inversion structure (Garand 2000). These sounders include NASA's Atmospheric Infrared Sounder (AIRS), EUMETSAT's Infrared Atmospheric Sounding Interferometer (IASI), and the NASA-ONR sponsored

Geosynchronous Imaging Fourier Transform Spectrometer (GIFTS) – Indian Ocean METOC Imager (IOMI). An obvious, but non-trivial point is that these impressive IR sounders cannot "see" through opaque clouds.

c. Radiance Bias

In practice, bias corrections are required to obtain the most useful information from satellite sounders. Sources of bias include the conversion from antenna temperature to brightness temperature, forward model error, forecast model error, and data preprocessing. The bias is defined here as the preprocessed observed brightness temperatures minus the equivalent brightness temperature calculated from model background profile. All major NWP centers monitor the biases with respect to their global model. For example, a one-year time series that includes both clear and cloudy sky conditions may show standard deviations of global brightness temperature bias approaching 20 K for the AMSU-A surface sensitive channels and 15 K for HIRS/3 channel 8. Clear sky biases are generally smaller. These issues as related to AMSU are currently being addressed at NRL Monterey (B. Campbell, personal communication).

d. Mesoscale ATOVS Assimilation

Most efforts by the major forecast centers has focused on assimilating ATOVS observations into global NWP models. For example, NRL Monterey is currently developing techniques to assimilate AMSU-A channels 4 – 10 radiances in NOGAPS via 3DVAR and AMSU-B channels 3 – 5 into NOGAPS using a 1DVAR scheme. Efforts are now shifting to assimilate these sounder data in mesoscale NWP models.

In this dissertation, and in collaboration with NRL Monterey, the assimilation of ATOVS 1DVAR retrievals is being investigated for the COAMPS model. In addition to the work at NRL Monterey, the UKMO (English et al. 2002) is researching the assimilation of AMSU-A channels 4 – 9, and AMSU-B channels 3 - 5 direct broadcast radiances from NOAA-15, and -16 into their mesoscale (limited area) model. HIR/3 radiances are not included. For mesoscale NWP applications, they have reduced the satellite-data assimilation window from three to ±1.5 hr and thinned the AMSU observations to 0.4^{o}. UKMO also uses smaller observation errors of 2 K for mesoscale applications vice the nominal global error values of 4 K.

B. COAMPS MODEL DESCRIPTION

The U.S. Navy's Coupled Ocean-Atmosphere Mesoscale Prediction System (COAMPS; Hodur 1997), developed at NRL Monterey is non-hydrostatic atmospheric regional forecast model. Efforts are currently ongoing to couple the atmospheric model with a hydrostatic ocean model. This multi-nested, globally relocatable atmospheric model is capable of predicting meso-β scale phenomena. The model's prognostic variables are specified on a horizontally staggered Arakawa C grid and vertical terrain-following sigma-*z* coordinate system. Operationally, COAMPS is run using 30 vertical levels, but up to 300 sigma levels are possible. Grids are commonly triple nested with a required 3:1 grid ratio.

Kain and Fritsch (1993) cumulus parameterization is designed specifically for mesoscale models to represent cumulus convection explicitly in terms of modeled grid-scale resolvables. For grid resolution less than a specified value (e.g., 10 km), the COAMPS model follows the explicit moist physics scheme of Rutledge and Hobbs (1983). The cloud no cloud decision is based on the amount of heating or cooling due to condensation or evaporation at a model grid point.

Subgrid scale turbulence is modeled using the 1.5 order (i.e., prognostic equation for turbulent kinetic energy (TKE) with 1st order closure for other second order moment quantities), level 2.5 closure scheme of Mellor and Yamada (1974; 1982). Unlike traditional K theory, the COAMPS model includes a counter-gradient term in the temperature equation to allow for non-local turbulent transport. Turbulent length scale calculation uses the height, von Karaman constant, and an asymptotic value dependent on TKE vertical distribution. Boundary layer depth is diagnosed in the COAMPS model as the lowest elevation at which the flux Richardson number (i.e., ratio of buoyant production/consumption of TKE to shear production of TKE) is less than or equal to 0.50. The Eddy diffusivity formulation is a polynomial function of flux Richardson number multiplied by the length scale and square-root of the TKE.

The surface layer is defined as the bottom portion of the boundary layer in which the turbulent fluxes vary by less than 10% of their magnitude (Haltiner and Martin 1957). Surface layer parameterizations in COAMPS are based on Louis (1979), which was designed as a simple, computationally effective method to include surface fluxes in global models. This scheme uses polynomial expressions, based on the bulk Richardson number, for the stability functions in order to calculate friction velocity and temperature scale directly.

Short and long wave radiative transfer parameterizations follow Harshvardhan et al. (1987). Shortwave, solar radiation is absorbed above cloud top by O_3 for frequencies less than 0.9 μm and by cloud liquid water for frequencies greater than 0.9 μm. Solar radiation is reflected by the surface, clouds, and (diffusely) by air molecules. Surface albedo for land is derived from climatology and is assigned a constant value for open water (0.09) and ice surfaces (0.6). Absorption and emission of longwave radiation is by H_2O, CO_2 and O_3 with broadband parameterization from 3.3 μm to infinity. Clouds are considered blackbodies for longwave radiation with diagnosis for cumulus and stratiform fractional cloud amounts.

The NOGAPS model provides the lateral boundary conditions for the COAMPS model outer grid. Sea surface temperature fields are provided by the U.S. Navy's Fleet Numerical Meteorology and Oceanography Center's (FNMOC) global analysis and the source of the 1 km terrain data is National Imaging and Mapping Agency's Digital Terrain Elevation Data Base (DTED) level 1.

The COAMPS model can either be run in a continuous update cycle (i.e., warm start) where the analysis background fields are derived from the previous COAMPS forecast, or in cold start mode where the background field is a NOGAPS forecast. After quality control algorithms (Baker 1992) screen the observations, a multivariate optimum interpolation (MVOI) analysis (Lorenc 1986) step combines the observations with the analysis background. The observations and background are weighted by their respective

error covariances according to linear estimation theory. Transition of the COAMPS analysis from MVOI to NAVDAS is expected by Fall 2002 (N. Baker and K. Sashegyi, personal communication).

C. MARINE ATMOSPHERIC BOUNDARY LAYER

In this section a brief description of the marine atmospheric boundary layer (MABL) is followed by a summary of MABL modeling and satellite-based retrieval capabilities. A stated goal of this research is to determine how accurately the individual MABL background elements (e.g., cloud-top height, cloud liquid water content, radiative skin temperature, etc.) must be known *a priori* to generate the best 1DVAR ATOVS retrieval. As previously discussed, ATOVS soundings lack the vertical resolution to independently resolve the MABL temperature inversion and the retrieved structure of this feature is determined primarily by the background field. Therefore, the MABL elements that cannot be measured by the sounder must be accurately represented in the model background field or be derived by other methods. These alternate sources of MABL information include collocated satellite imagery and independent thermodynamic boundary models.

1. Description

The marine atmospheric boundary layer (MABL) is the lower 10% of the troposphere that is directly affected by the ocean surface properties and responds to surface forcing with a time scale of approximately one-hour (Stull 1997). The depth of the MABL is determined by free atmosphere subsidence and entrainment through the top of the MABL.

The MABL top, often referred to as the inversion, is marked by an abrupt increase in temperature, and decrease in humidity with height. Air above the inversion is relatively dry and warm compared to the underlying moist air. Below the inversion (or also known as the entrainment zone) the MABL can, in general, be divided into three sub-layers. Immediately above the ocean surface is the very thin viscous layer, which is determined by surface roughness. Next, the surface layer accounts for approximately the lowest 10% of the MABL and is where turbulent fluxes vary by less than 10% of their magnitude. The remainder of the MABL is usually termed the outer layer and is

dominated by turbulent mixing. Turbulent eddies within the MABL act to erode the inversion by entraining dry air from above. When the MABL is well-mixed and cloud free, potential temperature and humidity tend to be constant with height.

Strong subsidence inversions are typical features over eastern subtropical oceans, such as the North East Pacific basin, during the summer months. For strong subsidence inversion regimes, such as the subtropical California coast, Rosenthal et al. (1997) show a strong correlation between MABL height (corresponding to electro-magnetic (EM) duct height) and cloud-top temperature. Extensive marine stratiform clouds typically cap the boundary layer during this time of year and complicate the dynamics of the MABL. In addition to shear-generated turbulence, cloud-top radiative cooling and cloud-base radiative heating have important roles in maintaining turbulent mixing in the boundary layer (Stull 1997). Stratocumulus-topped MABL's can become decoupled from the lower portion of the MABL through diurnal temperature changes and precipitation. As a result of the decoupling, liquid water potential temperature and total water are no longer constant with height.

In their summer 1996 study of the EPAC, Dorman et al. (2000) found the MABL inversion base height to be lowest off the north-central California coast (195 m) and highest off southern California (416 m). An inversion strength of 10.8 C over a few hundred meters was observed off central California. The boundary layer depth increased off shore to near 800 m at distances of 80 – 100 km from the coast. More information on the structure of the EPAC boundary layer may be found in Dorman and Winant (2000) and Burk and Thompson (1996).

2. Mesoscale Modeling of MABL Parameters

Studies have shown that mesoscale models are able to represent the MABL properties, such as low-level winds, boundary layer height, atmospheric refractivity gradients, and cloud microphysics. Burk and Thompson (1982) were moderately successful in modeling refractivity profiles within the atmospheric boundary layer using a one-dimensional boundary layer model and a coarse-resolution hemispheric model. Sharp vertical gradients of humidity and temperature found at the top of a well-mixed MABL can affect the propagation of microwave energy from radar and communications system. Using the U.S. Navy Operational Regional Atmospheric Prediction System

(NORAPS; Hodur 1987), Burk and Thompson (1996,1997) demonstrated the model's ability to represent and forecast MABL structure associated with the summertime low-level jet along the California coast and height of the microwave trapping layer. Haack and Burk (2000) compared observational data from the Variability of Coastal Atmospheric Refractivity (VOCAR) and Coastal Waves 1996 experiments with COAMPS forecasts. They determined that COAMPS "captures much of the observed MABL vertical structure and horizontal variability," associated with refractivity and surface-based EM ducting. In addition, Dorman et al. (2000) demonstrated the COAMPS model's ability to forecast MABL depth and wind stress maxima off the California coast.

Wetzel et al. (2001) evaluated mesoscale model forecasts of coastal stratus, offshore of central Oregon, using satellite microphysical retrievals and aircraft measurements. COAMPS forecasts, and satellite derived cloud optical depth, droplet effective radius and cloud liquid water path were verified by aircraft measurements during the COAMPS Operational Satellite and Aircraft Test (COSAT) field program. This data set includes multispectral radiances from NOAA AVHRR and GOES imagers, and corresponding aircraft observations and COAMPS model fields. The data inter-comparisons show good agreement between model forecasts and satellite observed cloud distribution; however, the Rutledge and Hobbs (1983) microphysical parameterization was shown to over predict cloud liquid water path.

3. Alternate Sources of MABL Information

Though not directly used in this dissertation, previous research has demonstrated success in retrieving cloud free, and stratocumulus-topped boundary layer height from infrared and visible satellite imagers (e.g., AVHRR) and thermodynamic models. This discussion is included here since these observation types and derived products could be used to either assign confidence to COAMPS background field or as additional observations or constraints to a variational retrieval scheme.

Scientists at the Desert Research Institute (M. Wetzel, personal communication) are working to improve satellite retrievals of EPAC MABL parameters. These techniques exploit both visible and infrared imagers to determine cloud-top height, cloud fraction, cloud liquid water path, and sea surface temperature.

There are numerous established methods to calculate the depth of the MABL. Betts et al. (1992) suggested that a simple equilibrium model might improve the retrieval of detailed boundary layer structure. To improve the boundary layer definition, Betts et al. (1992) used a mixing-line boundary layer model to determine convective boundary layer height from National Meteorological Center gridded analyses, satellite derived monthly mean cloud top temperatures and cloud fraction, and Comprehensive Ocean and Atmosphere Data Set (CODA) sea surface temperatures.

Following a similar approach of Minnis et al. (1992) and Betts et al. (1992), McBride (2000) developed a near-real time technique to determine the height of the stratocumulus-topped MABL based on satellite derived cloud top temperatures, sea surface temperatures, assumed cloud fraction and dry/moist adiabatic lapse rate. The McBride (2000) technique has the advantage of being independent of a background model field. Minnis et al. (1992) and Betts et al. (1992) combined a thermodynamic boundary layer model with independent satellite retrievals of cloud-top temperature and sea surface temperature. Betts et al. (1992) compared the constant-lapse-rate method of Minnis et al. (1992) and a mixing-line method to determine boundary layer structure over the ocean. Kren (1987) developed an iterative technique to estimate the depth of the cloud-free MABL and parameterized relative humidity profile from satellite derived aerosol optical depth, total water vapor and sea surface temperature. An important assumption of this technique is that optical depth and total water vapor are confined within a well-mixed MABL.

D. 1DVAR RETRIEVAL THEORY

1. Overview

A 1DVAR scheme for TOVS became operational at the European Centre for Medium-Range Weather Forecasts (ECMWF) in 1992 and demonstrated a positive impact on forecast skill especially in the tropics and southern hemisphere (Eyre et al. 1993). Phalippou (1996) showed that variational methods provide a simple optimal method of retrieving the humidity profile, surface wind speed and cloud liquid water from SSM/I marine observations. McNally and Vesperini (1996) showed that assimilation of TOVS radiance data using a 1DVAR approach improved some aspects of the ECMWF global model hydrological cycle. Deblonde (1999, 2000) was successful in

directly assimilating SSM/I and SSM/T-2 brightness temperatures in a 1DVAR assimilation system for both clear and cloudy sky conditions. NRL Monterey currently developing 1DVAR techniques for assimilation of certain satellite data into the NOGAPS model. Variational methods are further discussed in Lorenc (1986), Daley (1991), Courtier et al. (1993), Eyre (1995), and Rodgers (2000).

2. NAVDAS and 1DVAR Description

This discussion provides a brief description of the 1DVAR algorithm as applied to NAVDAS (a 3DVAR scheme) following Eyre et al. (1993) and Daley and Barker (2000). Unlike the multivariate optimal interpolation (MVOI) technique, 3DVAR can directly assimilate radiances from polar orbiting satellite sounders and formulate more realistic error covariances. NAVDAS allows three options for assimilating sounder data: 1) retrieved temperature and humidity data provided by National Environmental Satellite, Data, and Information Service (NESDIS) are assimilated in a manner similar to radiosondes; 2) assimilate temperature and humidity data produced via 1DVAR; or 3) assimilate radiances directly into 3DVAR.

Although in general 3DVAR is non-linear, NAVDAS has been implemented as a linear scheme except in its treatment of SSM/I winds. In NAVDAS, the observed radiances are used to change only the (linear) temperature profile and the background information is derived from the NWP model forecast. NESDIS retrievals, or climatology, are used to provide information above model top. Currently NAVDAS with the COAMPS model does not directly assimilate nonlinear cloud parameters and only cloud-free, or cloud-cleared radiances are currently used (N. Baker, personal communication).

The NRL 1DVAR algorithm developed by N. Baker and R. Daley (NRL Monterey) is used to retrieve temperature and humidity profiles from (A)TOVS measured radiances. Unlike the current version of NAVDAS, the 1DVAR algorithm includes nonlinear iteration, which is important for modeling the effects of clouds and water vapor. The retrieved temperature and non-linear humidity data can be ingested into 3DVAR if direct radiance assimilation is not desired. Even with direct assimilation of radiances, retrieval of temperature and winds are performed for quality control and to obtain a better state estimate above the model top and for surface skin temperature.

As discussed in Section II.A, the inverse problem is ill-posed and requires the use of some type of estimation technique in order to find the best solution that is consistent with the observations. One approach to finding realistic solutions describes the variables in terms of a probability density function (PDF), which can be written in general form as

$$P(\mathbf{x}) \approx \exp(-½\,[\mathbf{x} - \mathbf{x}_o]^T\, \mathbf{E}^{-1}\, [\mathbf{x} - \mathbf{x}_o]), \tag{2.5}$$

where $P(\mathbf{x})$ is the probability that a scalar will have a value of $\mathbf{x}$. The estimates of $\mathbf{x}$ have mean value $\mathbf{x}_o$ and normally distributed errors with covariance $\mathbf{E}$. The matrix transpose and inverse are denoted by ^{T} and $^{-1}$, respectively.

1DVAR applies the principle of Bayes' theorem (see Rodgers 2000) to find the most probable state of the atmosphere $\mathbf{x}$ (e.g., vertical temperature profile) given satellite measurements $\mathbf{y}^o$ (e.g., radiances). For this variational scheme, the maximum conditional probability or likelihood is expressed as

$$P(\mathbf{x}|\mathbf{y}^o) \approx P(\mathbf{y}^o|\mathbf{x})P(\mathbf{x}), \tag{2.6}$$

where $P(\mathbf{y}^o|\mathbf{x})$ is the probability that measurement $\mathbf{y}^o$ will be made when the atmospheric state is $\mathbf{x}$ and $P(\mathbf{x})$ is the prior probability of $\mathbf{x}$ before making any measurements. In an error free environment $P(\mathbf{y}^o|\mathbf{x})$ is a delta function at $\mathbf{y}^o = H(\mathbf{x})$, where $H(\mathbf{x})$ is the generalized forward model. However, measurements are not error free. Assuming the errors are Gaussian with covariance $\mathbf{R}$, (2.5) can be written as

$$P(\mathbf{y}^o|\mathbf{x}) \approx \exp(-0.5\,[\mathbf{y}^o - H(\mathbf{x})]^T\, \mathbf{R}^{-1}\, [\mathbf{y}^o - H(\mathbf{x})]). \tag{2.7}$$

Information regarding $P(\mathbf{x})$ is derived from the background information and error characteristics. For normally distributed background errors with background profile $\mathbf{x}^b$ and error covariance $\mathbf{B}$, (2.5) can be written as

$$P(\mathbf{x}) \approx \exp(-0.5\,[\mathbf{x} - \mathbf{x}^b]^T\,\mathbf{B}^{-1}\,[\mathbf{x} - \mathbf{x}^b]), \quad (2.8)$$

The variational approach to the inversion problem is accomplished by maximizing the conditional probability (i.e., minimizing $-\log_e P(\mathbf{x}|\mathbf{y}^o)$) to yield a scalar cost (penalty) function $J(\mathbf{x})$, which is a measure of the fit between the observed radiances and the background information, other observations, and physical or dynamical constraints. To assimilate radiances via a variational approach, $J(\mathbf{x})$ is minimized with respect to the atmospheric state $\mathbf{x}$. Assuming the errors are normally distributed, then following Daley and Barker (2000) the optimal cost function may be written as a sum of quadratic terms

$$J(\mathbf{x}) = 0.5[\mathbf{y}^o - H(\mathbf{x})]^T\,\mathbf{R}^{-1}\,[\mathbf{y}^o - H(\mathbf{x})] + 0.5\,[\mathbf{x} - \mathbf{x}^b]^T\,\mathbf{B}^{-1}\,[\mathbf{x} - \mathbf{x}^b] + \mathbf{J}_0 + \mathbf{J}_c, \quad (2.9)$$

where $\mathbf{x}$ is a vector (length n) containing the atmospheric state, $\mathbf{x}^b$ is a vector (length n) containing the background (e.g., short-term forecast) values, $\mathbf{y}^o$ is a vector (length m) of measured radiances, H represents the forward radiative transfer model from the atmospheric state $\mathbf{x}$ to observed radiances $\mathbf{y}^o$, $\mathbf{R}$ is the m x m observation error covariance matrix and includes the covariance of the instrument errors ($\mathbf{O}$) and the forward model error covariance ($\mathbf{F}$), $\mathbf{B}$ is the n x n background error covariance matrix, and $\mathbf{J}_0$ and $\mathbf{J}_c$ represent the cost for other observations and constraints. The TOVS 1DVAR algorithm (Eyre et al. 1993) uses non-linear Newtonian iteration to minimize $J(\mathbf{x})$. The i^{th} estimate of $\mathbf{x}$ is updated by

$$\mathbf{x}_{i+1} = \mathbf{x}_i - [\nabla^2_x\, J(\mathbf{x})]^{-1}\,\nabla_x\, J(\mathbf{x}), \quad (2.10)$$

where the gradient of $J(\mathbf{x})$ is

$$\nabla_x\, J(\mathbf{x}) = \mathbf{H}^T\,\mathbf{R}^{-1}\,[H(\mathbf{x}) - \mathbf{y}^o] + \mathbf{B}^{-1}\,[\mathbf{x} - \mathbf{x}^b]. \quad (2.11)$$

H is the *m* x *n* Jacobian matrix (also known as the tangent linear operator) corresponding to the forward operator H(**x**) linearized about the atmospheric state vector. $\mathbf{H}^T$ is the adjoint operator. If linear, then H = **H**. If H is nonlinear, then $\mathbf{H} = \partial H(\mathbf{x})/\partial \mathbf{x}$ evaluated at $\mathbf{x} = \mathbf{x}_b$. Therefore, **H** maps the solution from physical (state vector) space to radiance (brightness temperature) space and $\mathbf{H}^T$ maps the solution back to physical space (i.e., brightness temperatures back to the state vector). Errico et al. (1993) and Errico (1997) give in depth descriptions of the tangent linear and adjoint models. The square (*n* x *n*) Hessian matrix

$$\nabla^2_x J(\mathbf{x}) = 2(\mathbf{B}^{-1} + \mathbf{H}^T \mathbf{R}^{-1} \mathbf{H}), \tag{2.12}$$

is obtained by differentiating (2.11) with respect to **x**. The Hessian is a measure of the convexity of the cost function J(**x**) and indicates the sharpness of the analysis PDF. A sharper PDF corresponds to a more accurate analysis and a higher probability that the estimated state is closer to the true state (Bouttier and Courtier 1999). The Hessian of the cost function is equal to twice the inverse of the analysis (expected) error covariance matrix and as discussed later, is related to the information content of the retrieval. Note the gradient of **H**, and the optional $\mathbf{J}_o$ and $\mathbf{J}_c$ terms have been omitted in (2.12). The Newtonian iteration can then be expressed as:

$$\mathbf{x}_{i+1} = \mathbf{x}^b + \mathbf{K}_i [\mathbf{y}^o - H(\mathbf{x}_i) - \mathbf{H}_i (\mathbf{x}^b - \mathbf{x}_i)], \tag{2.13}$$

where $\mathbf{K}_i = \mathbf{B}\ \mathbf{H}_i^T\ [\mathbf{H}_i\ \mathbf{B}\ \mathbf{H}_i^T + \mathbf{R}]^{-1}$, and is the weight (or Kalman gain) matrix. Expanding (2.13), NRL Monterey's version of the 1DVAR algorithm converts measured brightness temperatures into retrieved temperature and humidity profiles using the following nonlinear Newtonian iterative procedure:

$$\mathbf{x}_{i+1} = \mathbf{x}_i + \mathbf{B}\ \mathbf{H}_i^T\ [\mathbf{H}_i\ \mathbf{B}\ \mathbf{H}_i^T + \mathbf{R}]^{-1}\ [\mathbf{y}^o - H(\mathbf{x}_i) + \mathbf{H}_i\ \mathbf{x}_i - \mathbf{H}_i\ \mathbf{x}^b], \tag{2.14}$$

where $\mathbf{x}_0$, $\mathbf{x}_1$,…$\mathbf{x}_i$ are state estimate vectors. This procedure starts with an initial guess for $\mathbf{x}_0$ (usually $\mathbf{x}^b$) and continues until convergence, i.e., $\mathbf{x}_i \approx \mathbf{x}_{i+1}$. As mentioned earlier, 1DVAR allows for nonlinear iteration, which is important when including the effects of clouds and humidity. Since this is a nonlinear problem, the convergent solution (if it exists) may not be unique and the minimum of the cost function depends on selection of $\mathbf{x}_0$. An accurate first guess will speed convergence. Convergence criteria used in this dissertation are discussed in Chapter V.

3. Radiative Transfer Model (RTTOV-6)

The forward model H, the *m x n* tangent linear operator (Jacobian) **H**, and the *n x m* adjoint operator $\mathbf{H}^T$ used in the 1DVAR scheme are derived from the fast radiative transfer (RT) TOVS model (RTTOV-6; Saunders et al. 1999; Saunders 2000). This RT model calculates top of the atmosphere radiances for a given background state vector ($\mathbf{x}^b$) that includes four atmospheric profiles, six surface array elements, two cloud array elements, and a surface emissivity array. The atmospheric profile elements are at 43 fixed pressure levels and include air temperature, specific humidity, ozone and cloud liquid water concentration. Surface array elements include 2 m air temperature, 2 m specific humidity, surface pressure, vector wind speeds, and radiative skin temperature. The cloud elements are cloud-top pressure and cloud fractional coverage. Surface emissivity is calculated using the vector wind speeds described in Chapter III.A.

The elements of **H** are calculated by differentiating the discrete form of the RTE by elements of $\mathbf{x}^b$ (see Eyre 1989a). Naval Postgraduate School is a licensed user of the RTTOV-6 software (M. Manoussakis, personal communication).

E. INFORMATION THEORY AND METHODS

Analysis of the information content of satellite sounder data allows for a quantitative examination of these systems' ability to improve upon the background information. In addition, the sensitivity of the retrieval to changes in background profile structure (e.g., U.S. Standard Atmosphere reference profile versus NWP background) and to the MABL parameters can be evaluated. The information content of satellite sounder data has been studied by numerous researchers (e.g., Rodgers 1976; Eyre 1990; Thépaut

and Moll 1990; Prunet et al. 1998; English 1999; Garand 2000). Specifically, they examined the ability of infrared (IR) and/or microwave (MW) sounder(s) to contribute information to a global NWP system.

Nearly 10 years prior to launch of ATOVS, Eyre (1990) conducted a simulation study to determine the information content of TOVS and ATOVS retrievals. The retrieval error covariances associated with an optimal nonlinear inversion scheme was calculated and compared with the assumed background (i.e., prior information) error covariance. Retrieval performance was assessed for combinations of sensors and different assumed conditions, such as atmospheric profile, cloud conditions, surface types, etc. His early study showed that ATOVS data has limited ability to improve global NWP temperature and humidity analyses, even through it can improve the analysis of layer quantities. This is a promising result, which may indicate the ability to derive independent low-level information from ATOVS.

As discussed previously, the radiance inversion problem is ill-posed and therefore, an optimal solution can only be obtained through use of prior information or other constraints. One of the challenges of this study is to quantify the extent to which ATOVS temperature and humidity sounder data can improve our knowledge of the eastern Pacific (EPAC) boundary layer environment. One purpose of this dissertation is to evaluate if ATOVS can provide sufficient information via a 1DVAR scheme to adjust the background toward the designated true atmospheric state. Results are presented in Chapter IV.

1. Information Matrix

For the Gaussian linear case, (2.12) is proportional to the inverse of the retrieval (analysis) error covariance matrix, $\mathbf{S}(\mathbf{x})$, or

$$0.5\nabla^2_x J(\mathbf{x}) = \mathbf{S}(\mathbf{x})^{-1} = \mathbf{B}^{-1} + \mathbf{H}^T \mathbf{R}^{-1} \mathbf{H}, \tag{2.15}$$

where $\mathbf{H}^T\mathbf{R}^{-1}\mathbf{H}$ is the radiance error covariance matrix projected into n x n analysis space. According to (2.15), small errors in $\mathbf{B}$ and/or $\mathbf{R}$ result in larger $\mathbf{S}(\mathbf{x})^{-1}$ and greater information content since the analysis error covariance $\mathbf{S}(\mathbf{x})$ becomes smaller. Now let

$\mathbf{S}(\mathbf{x}) = \mathbf{S}$ and, as shown by Rodgers (1976) and Eyre (1990), but with slight notation change, **S** can be written

$$\mathbf{S} = \mathbf{B} - \mathbf{B}\,\mathbf{H}^{\mathrm{T}}\,[\mathbf{H}\,\mathbf{B}\,\mathbf{H}^{\mathrm{T}} + \mathbf{R}]^{-1}\,\mathbf{H}\,\mathbf{B}. \tag{2.16}$$

The $\mathbf{H}\,\mathbf{B}\,\mathbf{H}^{\mathrm{T}}$ matrix in (2.16) is the projection of **B** into *m* x *m* radiance space. This covariance matrix is also known as the effective background error. For smaller **S** we again need smaller errors in **B** and **R** to make the $\mathbf{B}\,\mathbf{H}^{\mathrm{T}}\,[\mathbf{H}\,\mathbf{B}\,\mathbf{H}^{\mathrm{T}} + \mathbf{R}]^{-1}\,\mathbf{H}\,\mathbf{B}$ matrix large. Theoretical values of **S** calculated in Chapters IV are calculated at the first iteration only, i.e., $\mathbf{S}_{i=1}$. In (2.14), **H** is recalculated for each $\mathbf{x}_i$ until convergence.

For the linear case where **H** is linearized about $\mathbf{x}^{\mathrm{b}}$, **S** equals the expected error covariance of the optimal retrieval. For the weakly nonlinear case, **S** is a good approximation if it varies slowly with **x**. Performance assessment requires the calculation of the gradient of the forward model (i.e., $\mathbf{H} = \partial \mathrm{H}(\mathbf{x})/\,\partial \mathbf{x}$) and evaluation of **S** over a number of iterations. It is then possible to determine what information can be extracted from the sounding data for the assumed conditions. Humidity retrievals should be considered as at least weakly non-linear and clouds as highly non-linear. Unlike the current NAVDAS implementation, the NRL 1DVAR scheme allows for non-linear iteration, which should provide better estimates of these parameters.

Reduction in retrieval error, in terms of root mean square (r.m.s.) error, can be determined from the square roots of the diagonal elements of (2.16). Improvement over the background can be assessed by comparing the principal diagonal elements (variances) of **S** and **B**. If the ratio S_{ii} / B_{ii} is much less than unity, then the retrieval is nearly independent of the background state vector. The satellite sensor adds little or no information if this ratio is near unity (Eyre 1989a). This method does not; however, compare the covariance information, since it only considers the diagonal elements.

The following sub-sections provides an overview of the techniques used in this study to determine information content and degrees of freedom for signal and follows the works of Rodgers (1976), Thépaut and Moll (1990) and Prunet et al. (1998), English

(1999) and Rodgers (2000). Unlike these previous works, this dissertation addresses the information content of a combined IR and MW system for the specific mesoscale case of the summertime EPAC boundary layer regime.

2. Information Derived from Principal Component Analysis

The principal component analysis (PCA) technique described by Thépaut and Moll (1990) and Prunet et al. (1998) is used to provide an estimate of observation gain over background information, or

$$\mathbf{S}' = \mathbf{B}^{-½}\,\mathbf{S}\,\mathbf{B}^{-½}. \tag{2.17}$$

S is normalized by the background error covariance by pre- and post-multiplying by $\mathbf{B}^{-½}$, where the inverse of the matrix square root is calculated using eigenvector decomposition, $\mathbf{B}^{-½} = \mathbf{L}\,\mathbf{\Lambda}^{-½}\,\mathbf{L}^{T}$. **L** is the *n* x *n* eigenvector matrix of symmetric positive-definite **B** and **Λ** is the diagonal eigenvalue matrix (positive for positive-definite **B**). The significant eigenvalues of (2.17), as defined by Thépaut and Moll (1990), are those less than or equal to 0.9, indicating at least 10% of the information is derived from the satellite radiances. Prunet et al. (1998) used this criterion to compare the IR instruments HIRS/2 and IASI. Their case study showed HIRS/2 to have 6 significant eigenvectors for temperature and humidity as compared to 19 for IASI.

In the case where **B** is diagonal, the eigenvectors of (2.17) are the same as the radiance error in analysis space covariance matrix, $\mathbf{H}^{T}\mathbf{R}^{-1}\mathbf{H}$. Daley and Barker (2000) calculated the eigenmodes of $\mathbf{H}^{T}\mathbf{R}^{-1}\mathbf{H}$ for the TOVS instrument. Their example shows that the gravest vertical modes are associated with the largest eigenvalues and the most favorable signal-to-noise ratio (SNR), i.e., $\mathrm{SNR} = [(1 - \lambda_a{}^n) / \lambda_a{}^n] = \varepsilon_b[\lambda_r{}^n]^{1/2}$, where ε_b is the background error standard deviation and $\lambda_a{}^n$ and $\lambda_r{}^n$ are the nth eigenvalues of (2.17) and $\mathbf{H}^{T}\mathbf{R}^{-1}\mathbf{H}$. The eigenstructure of $\mathbf{H}^{T}\mathbf{R}^{-1}\mathbf{H}$ demonstrates that the TOVS instrument cannot independently resolve the MABL, or other abrupt vertical temperature changes, such as the tropopause. As discussed in Chapter I, low-level features present in a TOVS retrieval are artifacts of the background information.

The results of the PCA analysis are presented in Chapter IV.A. Again, it is not suggested that ATOVS can independently resolve the shallow summertime EPAC MABL temperature inversion. The purpose of using this PCA technique is to determine if ATOVS can provide significant low-level profile temperature and humidity information to a 1DVAR scheme.

3. Degrees of Freedom and Information Content From R and B Comparison

The effective row space, and hence the number of independent pieces of information, can be determined by comparing the observation error covariance **R** with the background error covariance **B**. Elements outside the effective row space cannot be measured since their natural variability is less than the observation error. Rodgers (2000) transforms **H** to **H**' by

$$\mathbf{H}' = \mathbf{R}^{-½}\,\mathbf{H}\,\mathbf{B}^{½}, \tag{2.18}$$

and states, "the number of independent measurements made to better than measurement error, the effective rank of the problem, is the number of singular values of [**H**'] which are greater than about unity." In this study, (2.18) was calculated using an upper triangular Cholesky decomposition.

The degrees of freedom for signal is expressed as

$$d_s = \sum_i \lambda^2_i /(1 + \lambda^2_i) = \mathrm{tr}(\mathbf{A}), \tag{2.19}$$

where λ_i are the singular values of **H**', and **A** is the averaging kernel, or model resolution matrix, given by

$$\mathbf{A} = \mathbf{KH} = \mathbf{BH}^{\mathrm{T}}\,(\mathbf{HBH}^{\mathrm{T}} + \mathbf{R})^{-1}\,\mathbf{H}, \tag{2.20}$$

where **K** is the Kalman gain (or contribution function) matrix. Information content (*H*), expressed in bits, is calculated using

$$H = 0.5\sum_i \log_e (1 + \lambda^2_i) = -0.5 \log_e | \mathbf{I}_n - \mathbf{A}|, \quad (2.21)$$

where $\mathbf{I}_n$ is the n x n Identity matrix. The results in Chapter IV show greater information content when the full covariance (non-diagonal) **B** matrix is used. According to Rodgers (2000), one would at first glance expect the "*a priori*" to be more tightly constrained for the non-diagonal covariance with fewer degrees of freedom and information content. However, this is not the case. The "paradox" arises because the weighting functions only observe the large-scale structure and at these scales the non-diagonal covariance has larger variance than at smaller scales. The diagonal case has equal variance at all scales. "Thus at the scale of the width and spacing of the weighting functions, the non-diagonal *a priori* is less constrained, while it is more constrained at scales which cannot be measured."

As shown by (2.19) the trace of **A** is the number of degrees of freedom for signal. The diagonal elements of **A** are the number of degrees of freedom per model level and the reciprocal, the number of levels per degree of freedom, is a rough measure of vertical resolution. Purser and Huang (1993) regard the diagonal elements of **A** as an approximate measure of effective data quantity, i.e., information.

The results of the **H'** analysis is presented in Chapter IV.A. Used in conjunction with the mathematically related PCA, this technique calculates the total quantity of independently derived information from ATOVS with respect to the summertime EPAC environment. The diagonal elements of **A** calculated for this mesoscale application are also presented in Chapter IV.A.

4. Information via Entropy Reduction

An alternate method to assess performance is through the analysis of information content of the retrieval compared to the background. Rodgers (1976) defined information content as the entropy of the probability function describing the state vector. The increase in information is related to a decrease in entropy. An advantage to using the entropy representation is that it expresses the retrieval performance for the entire profile as one value. The information gain (units of bits) is expressed as

$$\Delta H = \log_2 |\mathbf{B}| - \log_2 |\mathbf{S}|. \quad (2.22)$$

where the determinates of **S** and **B** are calculated using T and $\log_e Q$ sub-matrices. However, **S** is calculated using full 215 element background state vector in (2.16).

5. Information Gain Measured by Analysis Error Reduction

Theoretical retrieval performance (P), or percent improvement over background, can be calculated using

$$P = 100[1 - (S_{ii} / B_{ii})], \quad (2.23)$$

where S_{ii} and B_{ii} are the diagonal elements (variances) of **S** and **B** error covariance matrices. As the ratio $S_{ii} / B_{ii} \rightarrow 0$ ($P \rightarrow 100\%$) the retrieval is determined increasingly by the satellite observation. If $S_{ii} / B_{ii} \rightarrow$ unity then the satellite observation contributes no information to the retrieval. English (1999) used (2.23) to show that significant temperature and humidity profile information could be obtained from microwave sounders AMSU-A, and -B over non-ocean surfaces (i.e., forest, snow-ice free, and desert). In his theoretical study, results for rough ocean surface were included since they are germane to this dissertation. The sensitivity of temperature and humidity retrieval accuracy was studied by varying both the background skin temperature error and emissivity forward model error. Results were then compared for H linearized about three representative mean atmospheric profiles (arctic, mid-latitude, and tropical).

English (1999) found that temperature profile retrieval information is virtually insensitive to emissivity and emissivity model error if there is *a priori* knowledge of cloud liquid water path less than 100 g m^{-2}. However, the sensitivity increases for even small amounts of cloud liquid water if there is no prior information. In contrast, humidity information is sensitive to emissivity and emissivity model error for clear and thin cloud (< 500 g m^{-2}) conditions. Humidity retrieval error becomes less sensitive to emissivity for larger amounts of cloud liquid water where the atmosphere becomes optically thick for AMSU-B channels 3, 4 and 5.

Near surface temperature retrieval performance is strongly dependent on *a priori* knowledge of skin temperature error for both clear and cloudy conditions, whereas humidity retrieval performance is only weakly sensitive to background skin temperature error for each case. As cloud LWP increases, both near surface temperature and humidity information decrease. Skin temperature retrieval performance decreases as cloud liquid water path increases. Cloud liquid water retrieval performance is nearly insensitive to changes in liquid water path over ocean surfaces.

In this dissertation (2.23) is used to examine the sensitivity of the theoretical atmospheric temperature and humidity retrieval to changes in ocean surface, cloud, and profile *a priori* information. The purpose is to establish which parameters within the EPAC background state vector need to be accurately known. Requirements for additional observations (e.g. from collocated satellites) and prioritization of future improvements in model background (e.g. COAMPS) can then be established. Results of these sensitivity analyses are presented in Chapter IV.C.

F. SIMULATED RETRIEVAL METHOD

Techniques used in this study to derive simulated observations and background profiles follows Eyre (1989a), Healy and Eyre (2000), and Palmer et al. (2000). The latter two studies are specific to radio occultation retrievals, but the techniques are germane to this dissertation. In this research, "true" profiles ($\mathbf{x}^t$) are derived from the set of representative EPAC profiles discussed in Chapter III.C. The associated background profiles $\mathbf{x}^b$ are then calculated by superimposing a random combination of the eigenvectors of $\mathbf{B}$ onto $\mathbf{x}^t$. This method ensures the perturbations are consistent with the errors in $\mathbf{B}$. $\mathbf{x}^b$ is determined by

$$\mathbf{x}^b = \mathbf{x}^t + \Sigma_i \, \gamma_i \, (\lambda_i)^{1/2} \, \mathbf{C}_i \,, \tag{2.24}$$

where γ_i is a random Gaussian number (randn in MATLAB®) and λ_i and $\mathbf{C}_i$ are the i^{th} eigenvalue and eigenvector of $\mathbf{B}$.

"True" radiances and brightness temperature are calculated from $\mathbf{x}^t$ using the RTTOV-6 forward radiative transfer model, $H(\mathbf{x}^t)$. Simulated observation vectors are computed as

$$\mathbf{y}_s{}^o = H(\mathbf{x}^t) + \varepsilon, \tag{2.25}$$

where $\varepsilon = \Sigma_j \gamma_j (\lambda_j)^{1/2} \mathbf{D}_j$. As before, γ_j is a normally distributed random number and λ_j and $\mathbf{D}_j$ are the j^{th} eigenvalue and eigenvector of $\mathbf{R}$. The simulated observation vector is then used in (2.14) to find the most probable solution of the atmospheric state, $\mathbf{x}$.

A statistically significant number of "background" profiles $\mathbf{x}^b$ and error vectors ε are required to calculate the retrieval mean

$$\mu_r = \overline{(\mathbf{x} - \mathbf{x}^t)}, \tag{2.26}$$

and retrieval standard deviation

$$\sigma_r = [\overline{(\mathbf{x} - \mathbf{x}^t)^2} - \mu^2]^{1/2}. \tag{2.27}$$

Healy and Eyre (2000) used 1000, and Palmer et al. (2000) used 500 simulated background profiles and error vectors. The mean (μ_r) quantifies any biases within the retrieval and the standard deviation (σ_r) is compared with the square root of the principal diagonal elements of

$$\mathbf{S}_i = \mathbf{B} - \mathbf{B}\,\mathbf{H}^T{}_i\,[\mathbf{H}_i\,\mathbf{B}\,\mathbf{H}^T{}_i + \mathbf{R}]^{-1}\,\mathbf{H}_i\,\mathbf{B}, \tag{2.28}$$

which is the iterated version of (2.16). Results are presented in Chapter V.

G. MATRIX OPERATIONS

Many of the equations discussed above require operating on large matrices. This poses a challenge since some effort is required to ensure they are non-singular (or at best near non-singular) and positive definite (see Golub and Van Loan 1996). In this research the matrix rank was calculated to determine the proper method to calculate **S**. For example the information matrix $\mathbf{S}^{-1}$ from (2.15) is size *215* x *215*, but is singular with rank 70 and therefore, cannot be directly inverted (Rodgers 1976). Since profile temperature(T) and $\log_e$ specific humidity ($\log_e Q$) are mutually uncorrelated, these matrices can be reduced to their respective non-singular *43* x *43* submatrices prior to calculating the inverse; however, this will result in loss of information derived from the surface and cloud elements. In contrast, the *215* x *215* **S** matrix calculation in (2.16) only requires the inversion of the non-singular (or nearly non-singular) radiance space $(\mathbf{H}\,\mathbf{B}\,\mathbf{H}^{T} + \mathbf{R})^{-1}$ matrix. This dissertation calculates the full *215* x *215* **S** matrix using equation (2.16) to preserve the errors associated with the total background state vector.

THIS PAGE INTENTIONALLY LEFT BLANK

III. PRIOR INFORMATION

This chapter describes the prior information used for the information content analyses of Chapter IV and 1DVAR retrievals of Chapter V. Prior information includes assumed errors in the background field; instrument and forward model errors associated with the satellite sounder and radiative transfer model; and the 215 element background state vector used to calculated the Jacobian matrix.

A. BACKGROUND ERROR COVARIANCE MATRIX (B)

The *215* x *215* (*n* x *n* analysis space) background error covariance matrix **B** models the vertical structure of errors in the background (first-guess) profile. **B** is constructed from the inter-level correlations of error and standard deviations of error associated with the uncertainty in the background state vector. This research is the first to use COAMPS forecast errors specific to the mesoscale summertime EPAC environment. The 215 elements within the RTTOV-6 background state vector ($\mathbf{x}^b$) include profile arrays of atmospheric temperature (T), $\log_e$ specific humidity ($\log_e Q$), ozone (O_3), and cloud liquid water mixing ratio (CLW); surface array of 2 m air temperature (T_{2m}), 2 m $\log_e$ specific humidity ($\log_e Q_{2m}$), surface pressure (P_s), 2 m vector wind speeds (u_{2m}, v_{2m}), and radiative skin temperature (T_s); cloud array of cloud-top pressure (P_{CT}) and cloud fractional coverage (C_{FC}); and surface emissivity (ε) for each channel.

Following Franke (1999) the inter-level correlations of error for T and profile $\log_e Q$ were calculated and are shown in Table 3.1. These vertical correlations of error were calculated for the NOGAPS model and were approximated using a combination of functional fitting and transformation of the pressure levels. As shown by Eyre (1989a), the variational retrieval of profile elements is highly sensitive to the strength of inter-level correlations of error. T and $\log_e Q$ errors are assumed here to be mutually uncorrelated, which is most likely an oversimplification. This dissertation includes non-zero error correlations between the T_{2m}, T_s error, and T when using the COAMPS forecast errors. As discussed in Chapter II.C, boundary layer conditions will determine the magnitude of the surface and atmosphere coupling, e.g., T_s and T_{2m}. However, this

Table 3.1 Inter-level correlations of error (x 100). [T and $\log_e Q$ after Franke 1999].

Temperature

P (hPa)	level	1	2	3	4	5	6	7	8	9	10	11	12	13	14	15	16	17	18	19	20	21	22	23	24	25	26	27	28	29	30	31	32	33	34	35	36	37	38	39	40	41	42	43
0.1	1	100																																										
0.29	2	-34	100																																										
0.69	3	-11	-35	100																																								
1.42	4	-2	-15	-28	100																																							
2.61	5	0	-3	-19	-20	100																																						
4.41	6	0	-1	-6	-22	-12	100																																					
6.95	7	0	0	-2	-9	-24	-5	100																																				
10.37	8	0	0	-1	-3	-12	-25	2	100																																			
14.81	9	0	0	0	-1	-5	-15	-25	8	100																																		
20.4	10	0	0	0	0	-1	-3	-8	-18	-25	14	100																																	
27.26	11	0	0	0	0	0	-1	-4	-11	-21	-23	19	100																																
35.51	12	0	0	0	0	0	-1	-2	-6	-14	-22	-20	26	100																															
45.29	13	0	0	0	0	0	0	-1	-3	-8	-14	-20	-12	34	100																														
56.73	14	0	0	0	0	0	0	-1	-2	-5	-9	-15	-17	-6	34	100																													
69.97	15	0	0	0	0	0	0	0	-1	-3	-6	-10	-14	-14	-6	39	100																												
85.18	16	0	0	0	0	0	0	0	-1	-2	-4	-7	-10	-13	-16	-3	40	100																											
102.05	17	0	0	0	0	0	0	0	0	-1	-2	-4	-7	-10	-16	-15	-3	42	100																										
122.04	18	0	0	0	0	0	0	0	0	-1	-1	-3	-5	-8	-13	-16	-17	-3	40	100																									
143.84	19	0	0	0	0	0	0	0	0	0	-1	-2	-3	-5	-10	-13	-18	-17	-5	41	100																								
167.95	20	0	0	0	0	0	0	0	0	0	-1	-1	-2	-4	-7	-10	-15	-18	-17	-2	44	100																						
194.36	21	0	0	0	0	0	0	0	0	0	0	-1	-1	-2	-5	-7	-11	-15	-18	-16	-1	46	100																					
222.94	22	0	0	0	0	0	0	0	0	0	0	-1	-1	-2	-3	-5	-9	-12	-16	-18	-14	4	49	100																			
253.71	23	0	0	0	0	0	0	0	0	0	0	0	-1	-1	-2	-4	-6	-9	-13	-17	-18	-13	6	51	100																		
286.6	24	0	0	0	0	0	0	0	0	0	0	0	0	-1	-2	-3	-5	-7	-10	-14	-18	-18	-12	9	53	100																	
321.5	25	0	0	0	0	0	0	0	0	0	0	0	0	-1	-1	-2	-4	-5	-8	-12	-16	-18	-18	-10	12	56	100																
358.28	26	0	0	0	0	0	0	0	0	0	0	0	0	-1	-2	-3	-4	-6	-10	-13	-17	-19	-17	-8	14	58	100																
396.81	27	0	0	0	0	0	0	0	0	0	0	0	0	-1	-1	-2	-3	-5	-8	-11	-15	-18	-20	-17	-6	17	60	100															
436.95	28	0	0	0	0	0	0	0	0	0	0	0	0	-1	-1	-2	-3	-4	-6	-9	-13	-16	-19	-20	-16	-4	20	62	100														
478.54	29	0	0	0	0	0	0	0	0	0	0	0	0	0	-1	-1	-2	-3	-5	-8	-11	-14	-18	-20	-19	-14	-1	24	64	100													
521.46	30	0	0	0	0	0	0	0	0	0	0	0	0	0	-1	-1	-1	-3	-4	-6	-9	-12	-16	-19	-20	-19	-12	2	27	66	100												
565.54	31	0	0	0	0	0	0	0	0	0	0	0	0	0	0	-1	-1	-2	-3	-5	-7	-10	-13	-16	-19	-19	-16	-8	6	31	68	100											
610.6	32	0	0	0	0	0	0	0	0	0	0	0	0	0	0	-1	-1	-2	-3	-4	-6	-8	-11	-14	-16	-18	-18	-14	-6	9	32	66	100										
656.43	33	0	0	0	0	0	0	0	0	0	0	0	0	0	0	0	-1	-1	-2	-3	-5	-7	-9	-11	-14	-16	-17	-16	-12	-5	9	28	64	100									
702.73	34	0	0	0	0	0	0	0	0	0	0	0	0	0	0	0	-1	-1	-1	-2	-4	-5	-7	-9	-12	-14	-16	-16	-15	-11	-4	6	25	62	100								
749.12	35	0	0	0	0	0	0	0	0	0	0	0	0	0	0	0	0	-1	-1	-2	-3	-4	-5	-7	-9	-11	-13	-14	-15	-14	-10	-6	4	24	61	100							
795.09	36	0	0	0	0	0	0	0	0	0	0	0	0	0	0	0	0	-1	-1	-1	-2	-3	-4	-6	-7	-9	-11	-12	-13	-14	-12	-11	-8	2	22	60	100						
839.95	37	0	0	0	0	0	0	0	0	0	0	0	0	0	0	0	0	0	-1	-1	-1	-2	-3	-4	-6	-7	-9	-10	-11	-12	-12	-13	-13	-9	-1	18	56	100					
882.8	38	0	0	0	0	0	0	0	0	0	0	0	0	0	0	0	0	0	0	-1	-1	-2	-2	-3	-4	-5	-7	-8	-9	-10	-11	-13	-14	-14	-12	-5	12	52	100				
922.46	39	0	0	0	0	0	0	0	0	0	0	0	0	0	0	0	0	0	0	0	-1	-1	-2	-2	-3	-4	-5	-6	-7	-8	-9	-11	-13	-14	-15	-14	-8	8	51	100			
957.44	40	0	0	0	0	0	0	0	0	0	0	0	0	0	0	0	0	0	0	0	0	-1	-1	-2	-2	-3	-4	-4	-5	-6	-7	-9	-11	-13	-15	-16	-15	-10	10	55	100		
985.88	41	0	0	0	0	0	0	0	0	0	0	0	0	0	0	0	0	0	0	0	0	-1	-1	-1	-2	-2	-3	-3	-4	-5	-6	-7	-9	-11	-13	-15	-16	-15	-6	18	62	100	
1005.43	42	0	0	0	0	0	0	0	0	0	0	0	0	0	0	0	0	0	0	0	0	0	-1	-1	-1	-1	-2	-2	-3	-3	-4	-5	-6	-7	-9	-11	-13	-15	-16	-12	3	31	71	100
1013.25	43	0	0	0	0	0	0	0	0	0	0	0	0	0	0	0	0	0	0	0	0	0	-1	-1	-1	-1	-2	-2	-3	-3	-4	-5	-6	-8	-9	-11	-14	-15	-13	-2	19	50	83	100
T2m		0	0	0	0	0	0	0	0	0	0	0	0	0	0	0	0	0	0	0	0	0	0	0	0	0	-1	-2	-3	-3	-4	-5	-6	-8	-10	-13	-15	-18	-19	-14	1	22	47	64	100
Tskin		0	0	0	0	0	0	0	0	0	0	0	0	0	0	0	0	0	0	0	0	0	0	0	0	0	-1	-1	-2	-2	-3	-4	-5	-7	-8	-10	-13	-16	-15	-10	-2	9	16	57	100

$\log_e$ Specific Humidity

P (hPa)	level	1	2	3	4	5	6	7	8	9	10	11	12	13	14	15	16	17	18	19	20	21	22	23	24	25	26	27	28	29	30	31	32	33	34	35	36	37	38	39	40	41	42	43
0.1	1	100																																										
0.29	2	0	100																																										
0.69	3	0	0	100																																								
1.42	4	0	0	0	100																																							
2.61	5	0	0	0	0	100																																						
4.41	6	0	0	0	0	0	100																																					
6.95	7	0	0	0	0	0	0	100																																				
10.37	8	0	0	0	0	0	0	0	100																																			
14.81	9	0	0	0	0	0	0	0	0	100																																		
20.4	10	0	0	0	0	0	0	0	0	1	100																																	
27.26	11	0	0	0	0	0	0	0	0	0	2	100																																	
35.51	12	0	0	0	0	0	0	0	0	0	0	3	100																																
45.29	13	0	0	0	0	0	0	0	0	0	0	0	4	100																															
56.73	14	0	0	0	0	0	0	0	0	0	0	0	0	5	100																														
69.97	15	0	0	0	0	0	0	0	0	0	0	0	0	0	7	100																													
85.18	16	0	0	0	0	0	0	0	0	0	0	0	0	0	0	9	100																												
102.05	17	0	0	0	0	0	0	0	0	0	0	0	0	0	0	0	11	100																											
122.04	18	0	0	0	0	0	0	0	0	0	0	0	0	0	0	0	1	13	100																										
143.84	19	0	0	0	0	0	0	0	0	0	0	0	0	0	0	0	0	1	14	100																									
167.95	20	0	0	0	0	0	0	0	0	0	0	0	0	0	0	0	0	0	1	17	100																								
194.36	21	0	0	0	0	0	0	0	0	0	0	0	0	0	0	0	0	0	0	1	20	100																						
222.94	22	0	0	0	0	0	0	0	0	0	0	0	0	0	0	0	0	0	0	0	2	22	100																					
253.71	23	0	0	0	0	0	0	0	0	0	0	0	0	0	0	0	0	0	0	0	0	3	26	100																			
286.6	24	0	0	0	0	0	0	0	0	0	0	0	0	0	0	0	0	0	0	0	0	3	29	100																			
321.5	25	0	0	0	0	0	0	0	0	0	0	0	0	0	0	0	0	0	0	0	0	0	4	32	100																		
358.28	26	0	0	0	0	0	0	0	0	0	0	0	0	0	0	0	0	0	0	0	0	0	1	6	35	100																	
396.81	27	0	0	0	0	0	0	0	0	0	0	0	0	0	0	0	0	0	0	0	0	0	0	1	7	38	100																
436.95	28	0	0	0	0	0	0	0	0	0	0	0	0	0	0	0	0	0	0	0	0	0	0	0	1	9	41	100															
478.54	29	0	0	0	0	0	0	0	0	0	0	0	0	0	0	0	0	0	0	0	0	0	0	0	0	2	10	44	100														
521.46	30	0	0	0	0	0	0	0	0	0	0	0	0	0	0	0	0	0	0	0	0	0	0	0	0	0	2	12	47	100													
565.54	31	0	0	0	0	0	0	0	0	0	0	0	0	0	0	0	0	0	0	0	0	0	0	0	0	0	1	3	14	50	100												
610.6	32	0	0	0	0	0	0	0	0	0	0	0	0	0	0	0	0	0	0	0	0	0	0	0	0	0	0	1	4	17	53	100											
656.43	33	0	0	0	0	0	0	0	0	0	0	0	0	0	0	0	0	0	0	0	0	0	0	0	0	0	0	0	1	5	19	56	100										
702.73	34	0	0	0	0	0	0	0	0	0	0	0	0	0	0	0	0	0	0	0	0	0	0	0	0	0	0	0	0	2	6	22	59	100									
749.12	35	0	0	0	0	0	0	0	0	0	0	0	0	0	0	0	0	0	0	0	0	0	0	0	0	0	0	0	0	0	2	8	24	62	100								
795.09	36	0	0	0	0	0	0	0	0	0	0	0	0	0	0	0	0	0	0	0	0	0	0	0	0	0	0	0	0	0	1	3	9	28	65	100							
839.95	37	0	0	0	0	0	0	0	0	0	0	0	0	0	0	0	0	0	0	0	0	0	0	0	0	0	0	0	0	0	0	1	4	12	31	68	100						
882.8	38	0	0	0	0	0	0	0	0	0	0	0	0	0	0	0	0	0	0	0	0	0	0	0	0	0	0	0	0	0	0	0	2	5	14	36	72	100					
922.46	39	0	0	0	0	0	0	0	0	0	0	0	0	0	0	0	0	0	0	0	0	0	0	0	0	0	0	0	0	0	0	0	1	2	7	18	41	76	100				
957.44	40	0	0	0	0	0	0	0	0	0	0	0	0	0	0	0	0	0	0	0	0	0	0	0	0	0	0	0	0	0	0	0	0	1	4	10	23	48	80	100			
985.88	41	0	0	0	0	0	0	0	0	0	0	0	0	0	0	0	0	0	0	0	0	0	0	0	0	0	0	0	0	0	0	0	0	1	2	6	14	31	57	86	100		
1005.43	42	0	0	0	0	0	0	0	0	0	0	0	0	0	0	0	0	0	0	0	0	0	0	0	0	0	0	0	0	0	0	0	0	0	1	4	10	21	42	68	91	100	
1013.25	43	0	0	0	0	0	0	0	0	0	0	0	0	0	0	0	0	0	0	0	0	0	0	0	0	0	0	0	0	0	0	0	0	0	1	3	8	17	35	58	82	97	100

coupling of environmental parameters may not directly correspond to the correlation of their respective forecast errors. In any event, this dissertation assumes no boundary layer decoupling and the RTTOV-6 pressure level 43 (1013.25 hPa) is within the surface layer. Inter-level correlations of error for $<T_s\ T_{2m}>$, $<T_s\ T>$, and $<T_{2m}\ T>$ apply only to the COAMPS specific background error covariance matrix. All other elements are assumed to be mutually uncorrelated. Globally averaged background errors are used operationally at NRL Monterey for NOGAPS satellite data assimilation (N. Baker, personal communication). This globally averaged covariance matrix, hereby designated $\mathbf{B_N}$, is used as a first approximation in this dissertation. Forecast errors are not homogeneous and vary depending on geographical location and synoptic situation (Eyre 1989a; Healy and Eyre 2000). In practice, NAVDAS does allow for some latitudinal variation of the background errors and assigns different values for land and ocean surfaces. In $\mathbf{B_N}$, the surface and profile errors are mutually uncorrelated. As described in the following paragraphs, the globally averaged NOGAPS background errors used by the NRL Monterey 1DVAR scheme have been slightly modified for this research.

A new background error covariance matrix, hereby-designated $\mathbf{B_C}$, specific to EPAC summertime conditions was developed for this research. $\mathbf{B_C}$ includes the surface and profile error correlations discussed above. COAMPS background error statistics were provided by NRL Monterey (J. Nachamkin, personal communication). These T, $\log_e Q$ and surface wind speed background errors are based on Fleet Numerical Meteorology and Oceanography Center's (FNMOC) 27 km COAMPS operational runs for the period 07 July – 30 September 2001. A longer data set was not available at the time of this research. Errors are based on model forecast minus radiosonde observation (see Nachamkin and Hodur 2001). The standard deviation of the 6-hr forecast error is used in this study and was estimated by interpolating between the averaged 00-, and 12-hr forecast errors. The 6-hr COAMPS errors at 16 pressure levels were then interpolated to the 43 RTTOV-6 pressure levels.

The diagonal elements of the background error covariance matrices $\mathbf{B_N}$ and $\mathbf{B_C}$ are the square of the respective standard deviations of error ($(B_{ii})^{1/2}$) listed in Tables 3.2 and 3.3. The $(B_{ii})^{1/2}$ values for T and $\log_e Q$ are also compared in Fig. 3.1.

Table 3.2. Standard deviations of error associated with the diagonal elements of the NOGAPS and summertime COAMPS EPAC background error covariance matrices ($\mathbf{B_N}$ and $\mathbf{B_C}$) for atmospheric profile parameters [temperature (T), log specific humidity ($\log_e Q$), ozone (O_3), and cloud liquid water mixing ratio (CLW)]. Cloud errors are discussed in Chapters IV and V.

Profile parameters		Standard deviation of error $[B_{ii}]^{1/2}$					
		NOGAPS	COAMPS EPAC	NOGAPS	COAMPS EPAC		
Level	P (hPa)	T (K)		$\log_e Q$ (g kg^{-1})		O_3 (g kg^{-1})	CLW (g kg^{-1})
1	0.10	3.00	3.00	0.35	1.00	0.00	0.00
2	0.29	3.00	3.00	0.35	1.00	0.00	0.00
3	0.69	3.00	3.00	0.35	1.00	0.00	0.00
4	1.42	3.00	3.00	0.35	1.00	0.00	0.00
5	2.61	3.00	3.00	0.35	1.00	0.00	0.00
6	4.41	3.00	3.00	0.35	1.00	0.00	0.00
7	6.95	3.00	3.00	0.35	1.00	0.00	0.00
8	10.37	3.00	1.80	0.35	1.00	0.00	0.00
9	14.81	3.00	1.62	0.35	1.02	0.00	0.00
10	20.40	3.00	1.39	0.35	1.05	0.00	0.00
11	27.26	2.50	1.33	0.35	1.13	0.00	0.00
12	35.51	1.95	1.25	0.35	1.14	0.00	0.00
13	45.29	1.60	1.15	0.35	1.10	0.00	0.00
14	56.73	1.60	1.11	0.35	1.09	0.00	0.00
15	69.97	1.60	1.14	0.35	1.11	0.00	0.00
16	85.18	1.30	1.15	0.35	1.01	0.00	0.00
17	102.05	1.30	1.16	0.35	0.92	0.00	0.00
18	122.04	1.30	1.15	0.35	0.93	0.00	0.00
19	143.84	1.30	1.15	0.35	0.96	0.00	0.00
20	167.95	1.30	1.29	0.35	0.89	0.00	0.00
21	194.36	1.43	1.50	0.35	0.79	0.00	0.00
22	222.94	1.37	1.40	0.35	0.66	0.00	0.00
23	253.71	1.30	1.23	0.35	0.53	0.00	0.00
24	286.60	1.40	1.11	0.35	0.55	0.00	0.00
25	321.50	1.23	1.03	0.40	0.58	0.00	0.00
26	358.28	0.92	0.96	0.43	0.60	0.00	0.00
27	396.81	0.92	0.89	0.40	0.63	0.00	0.00
28	436.95	0.92	0.89	0.40	0.65	0.00	0.00
29	478.54	0.95	0.88	0.42	0.66	0.00	0.00
30	521.46	0.96	0.89	0.37	0.65	0.00	0.00
31	565.54	0.98	0.91	0.36	0.60	0.00	0.00
32	610.60	0.95	0.92	0.38	0.55	0.00	0.00
33	656.43	0.95	0.94	0.40	0.50	0.00	0.00
34	702.73	0.95	0.98	0.35	0.45	0.00	0.00
35	749.12	0.94	1.42	0.36	0.41	0.00	0.00
36	795.09	0.95	1.85	0.36	0.36	0.00	0.00
37	839.95	1.08	2.26	0.34	0.32	0.00	0.00
38	882.80	1.75	2.31	0.32	0.28	0.00	*see text
39	922.46	1.78	2.25	0.30	0.25	0.00	*see text
40	957.44	1.80	2.23	0.24	0.21	0.00	*see text
41	985.88	1.80	2.20	0.22	0.18	0.00	*see text
42	1005.43	1.80	2.18	0.20	0.18	0.00	*see text
43	1013.25	1.80	2.15	0.18	0.18	0.00	0.00

Table 3.3. As in Table 3.3, except for surface and cloud parameters. Cloud and emissivity errors are discussed in Chapters IV and V.

Surface and Cloud Parameters	Standard deviation of error $[B_{ii}]^{½}$		Units
	NOGAPS	COAMPS EPAC	
Surface 2 m temperature (T_{2m})	1.80	2.15	K
Surface 2 m specific humidity ($\log_e Q_{2m}$)	0.18	0.18	gkg^{-1}
Surface pressure (P_s)	3.38	3.38	hPa
2 m u-vector wind speed (u_{2m})	0	2	ms^{-1}
2 m v-vector wind speed (v_{2m})	0	2	ms^{-1}
Radiative skin temperature (T_s)	1.57	1.57	K
Cloud top pressure (P_{CT})	*see text	*see text	hPa
Cloud fractional cover (C_{FC})	*see text	*see text	0-1
Surface microwave emissivity (ε_m)	*see text	.02	0-1

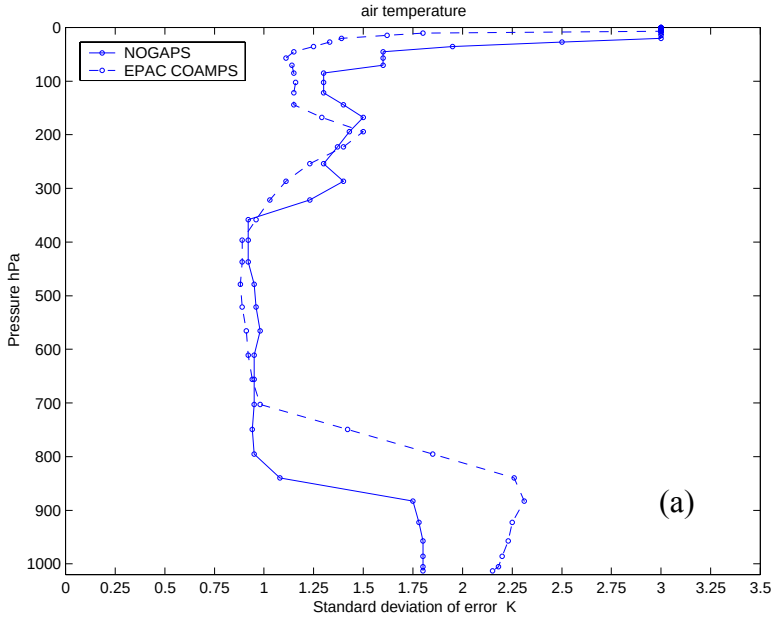

Figure 3.1. NOGAPS and COAMPS background standard deviations of error $(B_{ii})^{½}$ for (a) *T*, and (b) $\log_e Q$. Globally averaged NOGAPS background errors are used operationally at NRL Monterey for satellite data assimilation and are used in this dissertation as the first-order approximation. The COAMPS background errors are based on the EPAC 6-hr forecast statistics for the period 07 July – 30 September 2001.

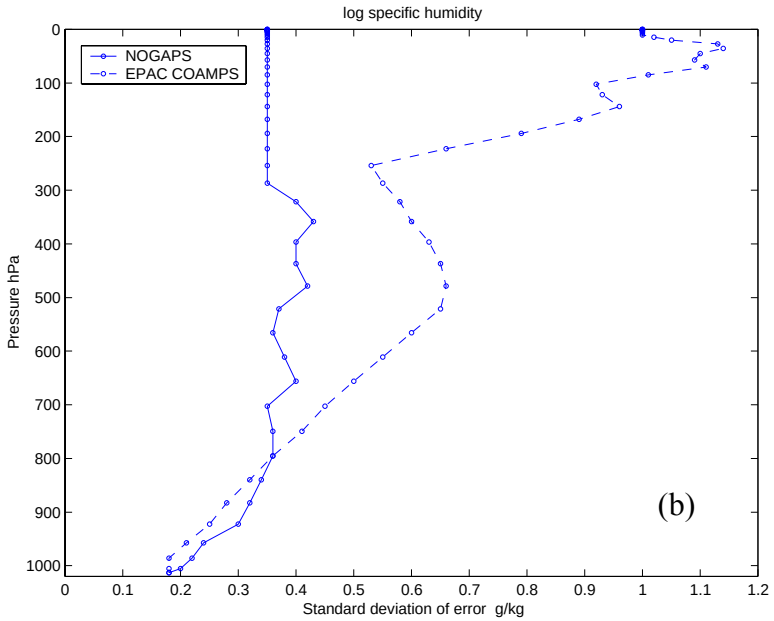

Figure 3.1. Continued.

Vertical *T* error structure is similar for the two models above 700 hPa, but with larger COAMPS EPAC errors below. The larger low-level errors are due, in part, to the uncertainty in the fine-scale MABL temperature, humidity, and cloud structures. The magnitude of COAMPS EPAC $\log_e Q$ errors are similar to NOGAPS below 800 hPa, but then increase with altitude. The ozone (O_3) profile errors are set to zero in this research and in the NRL Monterey 1DVAR scheme, and the default RTTOV-6 O_3 profile is used for all calculations.

This dissertation addresses the complicated problem of cloudy sky infrared and microwave 1DVAR retrievals. Unlike temperature and humidity forecast error, cloud liquid water mixing ratio profile (*CLW*) error is not easily derived from the conventional observing systems. COAMPS model generated *CLW* is typically double the observed value (e.g., 1.0 vice 0.4 g kg^{-1}). This large error is due to at least two reasons. First, and most important is that the COAMPS model does not include a drizzle parameterization and therefore, precipitation occurs only for large values of *CLW*. Second, turbulent mixing within the cloud layer is under-predicted, which results in too little entrainment of

warm dry air into the boundary layer. Both these issues are currently being addressed by NRL Monterey W. Thompson, personal communication). *CLW* errors used in the information content, and the variational retrieval studies are described in Chapters IV and V.

For both $\mathbf{B_N}$ and $\mathbf{B_C}$, the T_{2m} and 2 m $\log_e$ specific humidity ($\log_e Q_{2m}$) errors are set to the respective level-43 value and the same surface pressure (P_s) error is used. Two meter (2 m) vector wind speed (u_{2m}, v_{2m}) errors are set to zero in the NRL Monterey 1DVAR scheme and in $\mathbf{B_N}$. Consistent with the COAMPS EPAC forecast error statistics, non-zero vector wind speed errors are included in $\mathbf{B_C}$. T_s error in $\mathbf{B_N}$ and $\mathbf{B_C}$ has been set to that used in the NRL Monterey 1DVAR scheme. Realistically, this error might be larger for COAMPS model. Cloud-top pressure (P_{CT}) and cloud fractional coverage (C_{FC}) error are set to zero in the NRL Monterey satellite data assimilation scheme (i.e., for clear sky retrievals only). As with *CLW*, this dissertation includes non-zero P_{CT} and C_{FC} errors (see Chapters IV and V).

Surface emissivity (ε) error is set to zero for all channels in the NRL Monterey 1DVAR scheme since all surface sensitive channels are currently rejected. However, the information that is available for $\log_e Q$ at low-levels is highly sensitive to surface microwave emissivity (ε_m) error (English 1999). Microwave surface emissivity (ε_m) error was calculated per Kohn (1995) for AMSU-A channels 1 - 4, 15 and AMSU-B channels 1 - 2 as a function of representative T_s and u_{2m}, v_{2m} error. The ε error for all other channels was set to zero.

B. OBSERVATION ERROR COVARIANCE MATRIX (R)

The diagonal m x m (radiance space) observation error matrix **R** is a combination of the instrument error matrix **O** and the forward model error matrix **F** (e.g., see Uddstrom and McMillin 1994a, 1994b). The diagonal nature of these matrices assumes the errors are uncorrelated between channels. The values of **R** used in this research along with the respective contributions from **O** and **F** are shown in Table 3.4.

Table 3.4. Standard deviations associated with the diagonal elements of the ATOVS instrument error (**O**), RTTOV-6 forward model error (**F**), and combined observation error (**R**) covariance matrices. See text for data sources.

ATOVS Channel	Instrument Channel	$[\mathbf{O}_{ii}]^{1/2}$ (K)	$[\mathbf{F}_{ii}]^{1/2}$ (K)	$[\mathbf{R}_{ii}]^{1/2}$ (K)
	HIRS/3			
1	1	2.77	0.20	2.78
2	2	0.74	0.20	0.77
3	3	0.55	0.20	0.58
4	4	0.31	0.20	0.37
5	5	0.18	0.20	0.27
6	6	0.18	0.20	0.27
7	7	0.14	0.20	0.24
8	8	0.06	0.20	0.21
9	9	0.13	0.20	0.24
10	10	0.17	0.20	0.26
11	11	0.44	0.20	0.48
12	12	0.96	0.20	0.98
13	13	0.10	0.20	0.22
14	14	0.10	0.20	0.22
15	15	0.24	0.20	0.31
	AMSU-A			
16	1	0.21	2.12	2.13
17	2	0.26	2.42	2.43
18	3	0.22	1.23	1.24
19	4	0.14	0.28	0.31
20	5	0.15	0.28	0.32
21	6	0.15	0.28	0.32
22	7	0.13	0.28	0.31
23	8	0.14	0.28	0.31
24	9	0.24	0.28	0.37
25	10	0.25	0.28	0.40
26	11	0.28	0.28	0.40
27	12	0.40	0.28	0.49
28	13	0.54	0.28	0.58
29	14	0.91	0.28	0.95
30	15	0.17	1.92	1.93
	AMSU-B			
31	1	0.40	1.92	1.96
32	2	0.76	1.04	1.29
33	3	1.12	0.28	1.15
34	4	0.73	0.28	0.78
35	5	0.94	0.28	0.98

Elements of **O** corresponding to the 15 HIRS/3 channels used in this study are the radiometer noise equivalent temperature difference (NEΔT) values specified by Kidder and Vonder Haar (1995) and used by Prunet et al. (1998) in their comparison of TOVS and IASI information content. The NEΔT values specified by English (1999; 2000) were used as elements of **O** for the AMSU channels. English (2000) notes that several of the AMSU channels (4-12) have lower NEΔT values than pre-launch measurements specified by Saunders (1993). The diagonal elements of **F** are after Eyre (1990), Prunet et al. (1998) and English (1999). For cloudy scenes, the forward model errors associated with the surface sensitive microwave channels are generally higher due to errors from the dielectric model, scattering, and increased heterogeneity. The AMSU-A window channels 1-3, 15 and AMSU-B window channels 1 - 2 are highly sensitive to cloud liquid water path (English 1999). However, it is not known to what extent the relatively low-level and shallow cloud cover associated with the EPAC MABL will have on forward model errors.

C. BACKGROUND STATE VECTORS

The 215 elements within the RTTOV-6 background state vector ($\mathbf{x}^b$) include profile arrays of atmospheric temperature (T), $\log_e$ specific humidity ($\log_e Q$), ozone (O_3), and cloud liquid water mixing ratio (CLW); surface array of 2 m air temperature (T_{2m}), 2 m $\log_e$ specific humidity ($\log_e Q_{2m}$), surface pressure (P_s), 2 m vector wind speeds (u_{2m}, v_{2m}), and radiative skin temperature (T_s); cloud array of cloud- top pressure (P_{CT}) and cloud fractional coverage (C_{FC}); and surface emissivity (ε) for each channel. Background errors associated with each of these state vector elements were discussed above in Section III.A. The following describes the background state vectors used for the information content analysis of Chapter IV and simulated retrievals of Chapter V.A. Background state vectors based on COAMPS short-term forecasts from the DYCOMS II experiment are discussed in Chapter V.B.

1. Atmospheric Profiles

T and $\log_e Q$ profiles used in the calculation of the Jacobian matrix **H** for the information content analysis (Chapter IV) and simulated retrievals (Chapter V.A) are shown in Fig. 3.2.

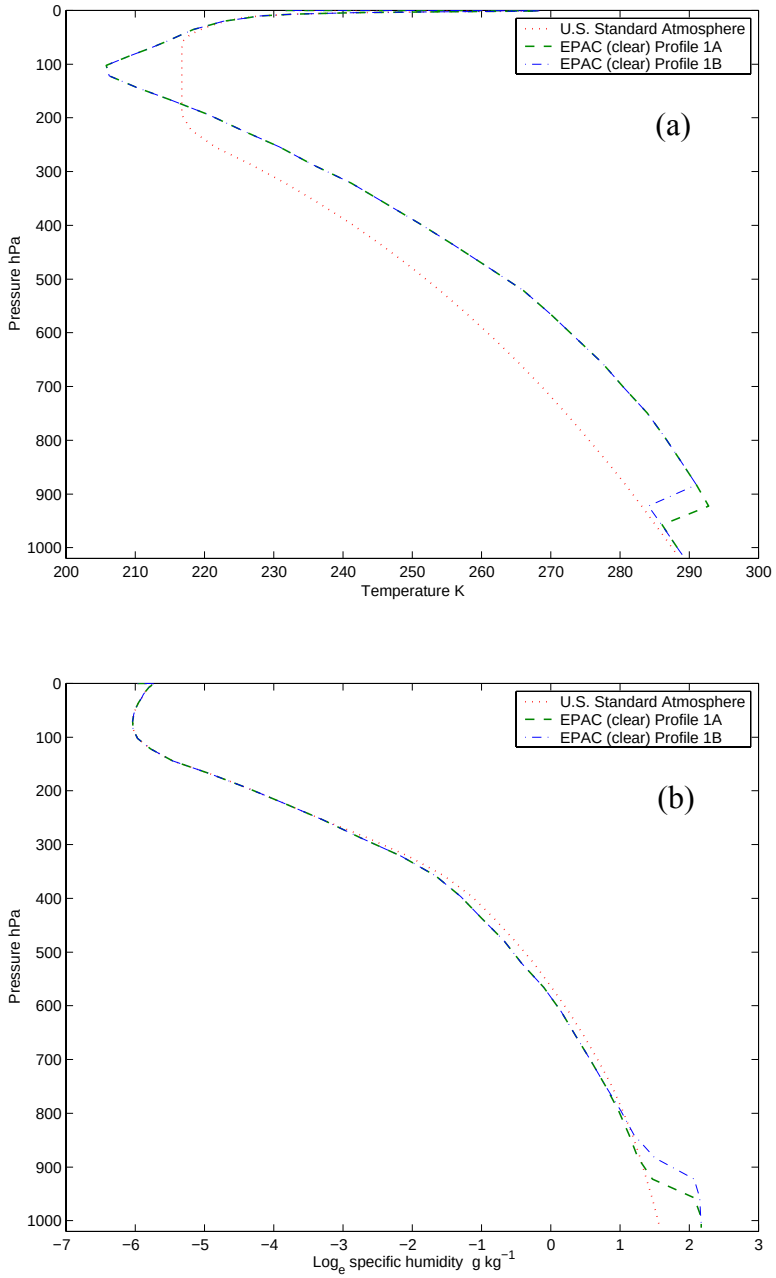

Figure 3.2. Representative profiles of T (upper panel) and $\log_e Q$ (lower panel) for the summertime eastern Pacific (EPAC) oceanic environment. Profiles (a,b) are EPAC Profiles 1A and 1B, the clear sky boundary layer cases, and (c,d) are EPAC Profiles 2A and 2B, the cloudy boundary layer cases. In each example, the first profile (red dotted line) is the U.S. Standard Atmosphere. Cloud liquid water profiles are discussed in the text.

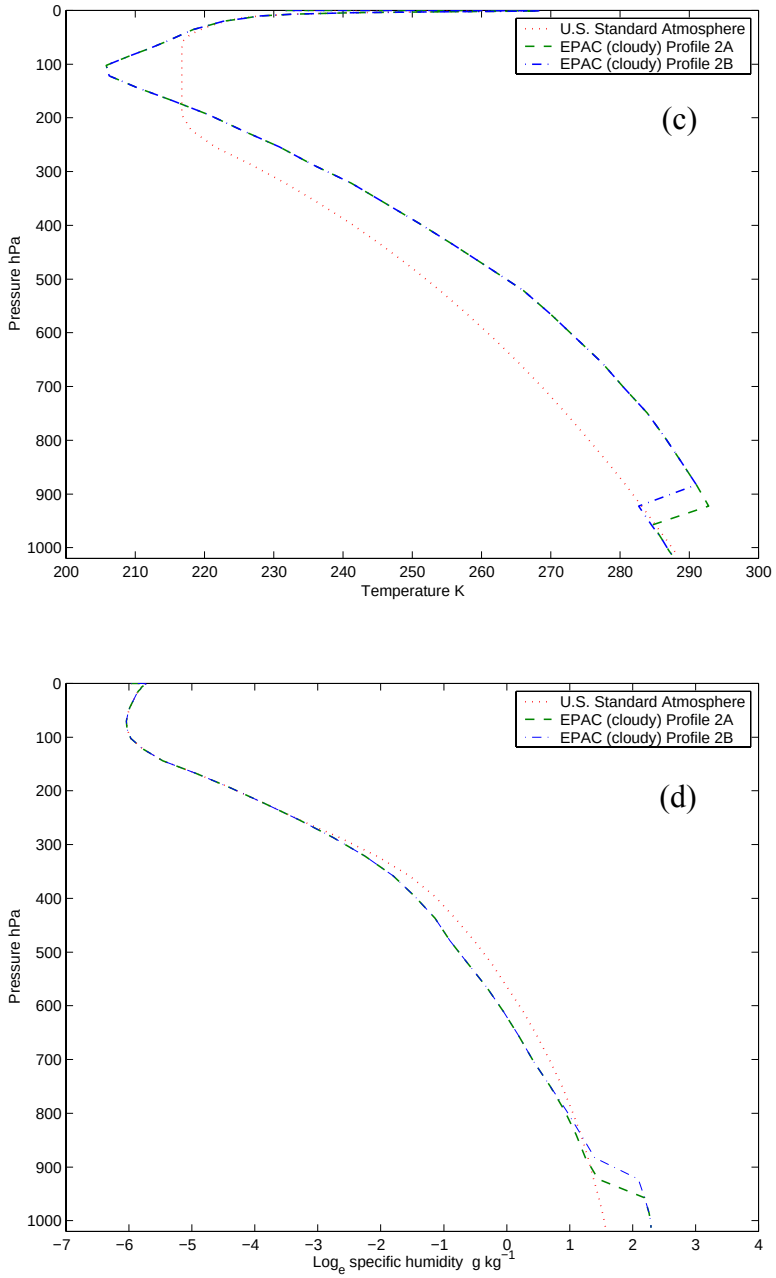

Figure 3.2. Continued.

As previously discussed, humidity soundings are treated non-linearly; however, the Jacobians are less variable and are dimensionless when expressed in terms of $\log_e Q$ vice Q (English 1999). All profiles in this research have been interpolated to the 43 RTTOV-6 fixed pressure levels (see Table 3.2) and the default RTTOV-6 ozone reference profile is used for all calculations.

The profiles in Fig. 3.2 are representations of the summertime EPAC cloud-free, and stratus-topped MABL environment, respectively. These summertime EPAC profiles are based on COAMPS EPAC short-term forecasts for July and August 2001. Model profiles were compared with collocated in-situ observations from the DYCOMS II field study and the research vessel (RV) PT SUR (P. Guest, personal communication). The U.S. Standard Atmosphere (1976) was obtained from the 42 diverse profile set of Garand et al. (2001). This mean mid-latitude profile is the "base-line" reference used to evaluate the effect of *a priori* detail on information content. Comparison with the reference profile shows the summertime EPAC environment has approximately 100% more water vapor near the surface and is drier than the U.S. Standard Atmosphere (later referred to as Profile 3) above the boundary layer.

Two clear sky (Figs. 3.2a-b) and two cloudy sky (Figs. 3.2c-d) idealized EPAC profiles are included in the information content and simulated retrieval study. For this study, the top of the MABL is at level 40 (957.44 hPa) for Profiles 1A and 2A and at level 39 (922.46 hPa) for Profiles 1B and 2B. As discussed by Dorman et al. (2000) the summertime EPAC MABL is fairly shallow near the coast (< 400 m) and gradually deepens off-shore to approximately 800 m. The inversion strength (ΔT) is approximately 7 K for clear sky profiles and 9 K for the cloudy profiles. This inversion strength is also consistent with observations by Dorman et al. (2000). Near surface relative humidity (RH) for clear sky EPAC Profiles 1A and 1B is approximately 80% and is approximately 97% for the cloudy sky EPAC Profiles 2A to 2B. The RH in the cloud is 100%.

Cloudy sky EPAC Profiles 2A and 2B each include two linearly increasing *CLW* profiles (i.e., EPAC Profiles 2A1, 2B1, 2A2, and 2B2); reaching maximum values of 0.25 g kg^{-1} (~0.3 g m^{-3}) and 0.50 g kg^{-1} (~0.6 g m^{-3}) at cloud top, respectively. According to Rodgers and Yau (1989) and Wetzel et al. (2001), *CLW* increases linearly to cloud-top

for maritime stratus. Liquid water path (LWP) is calculated for the four cloudy profiles as LWP = $\sum q_j \, dP_j \, g^{-1}$, where q_j is *CLW*, dP_i (= $-\rho g \, dZ$) is the pressure difference for each cloudy RTTOV-6 layer *j*, and g is acceleration due to gravity. Calculated LWP values for Profiles 2A1 and 2A2 are approximately 90 and 190 g m^{-2}, and 145 and 285 g m^{-2} for Profiles 2B1 and 2B2. These values for LWP and *CLW* are consistent with observed values from COSAT and DYCOMS II (e.g., Wetzel et al. 2001; Stevens et al. 2002). A consequence of interpolating to the fixed RTTOV-6 pressure levels is that some of the MABL detail is unavoidably lost. In this case, the bottom and top of the MABL temperature inversion (as shown in Figs. 3.2a,c) is spread over approximately 35 to 40 hPa. As discussed in Chapter V, this pressure difference is much smaller in reality. The relatively weak gradient of the interpolated profile can make it somewhat difficult to properly assign P_{CT} and *CLW*. Theses cloud profile elements and corresponding *CLW* and LWP values are summarized along with following surface and cloud array elements in Table 3.5.

2. Surface Array

For all simulations using the representative EPAC background state vectors, T_{2m} and $\log_e Q_{2m}$ have been set to the respective atmospheric profile value at level-43. P_s for EPAC Profiles 1A,B and 2A,B is the averaged observed sea level pressure associated with these profiles (1015.50 hPa) and Profile 3, the U.S. Standard Atmosphere, is set to level-43 pressure (1013.25 hPa). The magnitudes of u_{2m} and v_{2m} are set to 2.0 m s^{-1}. T_s is set to the respective T_{2m} minus 0.5 K in order to simulate stable boundary layer conditions.

3. Cloud Array

To model the stratus-topped MABL, cloud fractional coverage (C_{FC}) is set to 1.00. Cloud-top pressure (P_{CT}) is set to 957.44 hPa (level 40) and 922.46 hPa (level 39) for Profiles 2A and 2B at the MABL top, respectively.

4. Surface Emissivity Array

Surface emissivity (ε) is calculated in RTTOV-6 using the Infrared Surface Emissivity Model (ISEM-6) model for infrared and the Fast Generic Millimeter-wave Emissivity Model (FASTEM) model for microwave channels (Saunders 2000). Tangent linear output over ocean for microwave is computed using u_{2m},v_{2m} and T_s.

Table 3.5. Summary of cloud and surface characteristics of the representative clear and cloudy sky EPAC background state vectors (1A, 1B, 2A1, 2A2, 2B1, and 2B2) and the clear sky U.S. Standard Atmosphere (Profile 3).

cloud and surface array characteristics	Profile 3	Profile 1A	Profile 1B	Profile 2A1	Profile 2A2	Profile 2B1	Profile 2B2
sky condition	clear	clear	clear	cloudy	cloudy	cloudy	cloudy
MABL top / P_{CT} (hPa)	----	957.44	922.46	957.44	957.44	922.46	922.46
inversion ΔT (K)	----	7	7	9	9	9	9
C_{FC} (0 – 1)	----	----	----	1.00	1.00	1.00	1.00
CLW max at P_{CT} (g kg^{-1})	----	----	----	0.25	0.50	0.25	0.50
LWP (g m^{-2})	----	----	----	90	190	145	285
P_s (hPa)	1013.25	1015.50	1015.50	1015.50	1015.50	1015.50	1015.50
T_{2m} (K)	288.20	289.0	289.0	287.45	287.45	287.45	287.45
$\log_e Q_{2m}$ (g kg^{-1})	1.57	2.17	2.17	2.29	2.29	2.29	2.29
T_s (K)	287.70	288.50	288.50	286.95	286.95	286.95	286.95
RH_{2m} (%)	46	80	80	97	97	97	97
$\lvert u_{2m} \rvert$ (ms^{-1})	0.0	2.0	2.0	2.0	2.0	2.0	2.0
$\lvert v_{2m} \rvert$ (ms^{-1})	0.0	2.0	2.0	2.0	2.0	2.0	2.0

D. JACOBIAN MATRIX (H)

Calculation of the *35* x *215* (*m x n*) Jacobian matrix (**H**) and its role in information content analysis and non-linear optimal estimation theory was discussed in Chapter II.D. This section describes the Jacobians specific to the representative EPAC background state vectors (Fig. 3.2) and selected surface sensitive ATOVS channels. Jacobians calculated in RTTOV-6 express the change in top of the atmosphere (TOA) brightness temperature (K) for a given change in background state vector element (**x**), i.e., 1 K change in *T* and 100% change in *Q* (see Garand et al. 2001). As previously discussed, the humidity soundings are less variable when calculated with respect to $\log_e Q$ vice *Q*.

The temperature profile (T) and $\log_e$ specific humidity ($\log_e Q$) Jacobians presented in this section are calculated with respect the representative summertime EPAC profiles and the U.S. Standard Atmosphere (Section III.C). These results represent the non-iterated solution, i.e., $H(\mathbf{x}_{i=1})$, and therefore, may be too large. A variational retrieval scheme recalculates, and most likely reduces the magnitude of the Jacobians at each iteration until convergence.

The elements of **H** corresponding to the T and $\log_e Q$ Jacobians for the 15 HIRS/3, 15 AMSU-A and 5 AMSU-B channels used in this research are shown in Figs. 3.3a-c. For this case, the forward model (H) was linearized about the U.S. Standard Atmosphere (Profile 3) and provides a baseline for comparing the magnitude and structure of the Jacobians for each channel.

For both T and $\log_e Q$, the general structure of the Jacobians are similar to the corresponding weighting functions (Fig. 2.3). One interesting difference is the relatively large magnitude of the T Jacobians for HIRS/3 channels 11 – 12 (Fig. 3.3a) and AMSU-B channels 3 –5 (Fig. 3.3c). These channels are associated with the humidity sounding channels, but are shown here to also contribute T information. The large magnitude of the AMSU window channel $\log_e Q$ Jacobians demonstrates the sensitivity of these channels to low-level water vapor gradients. Most notable is AMSU-B channel 2 at 150.0 GHz (Fig. 3.3c) which peaks at approximately 4 K near 900 hPa. Other channels that are very sensitive to the near-surface U.S. Standard Atmosphere water vapor gradient are the 89.0 GHz AMSU-A/B channels 15/1 (Figs. 3.3b-c), and AMSU-A channels 2 and 3 (Fig. 3.3b).

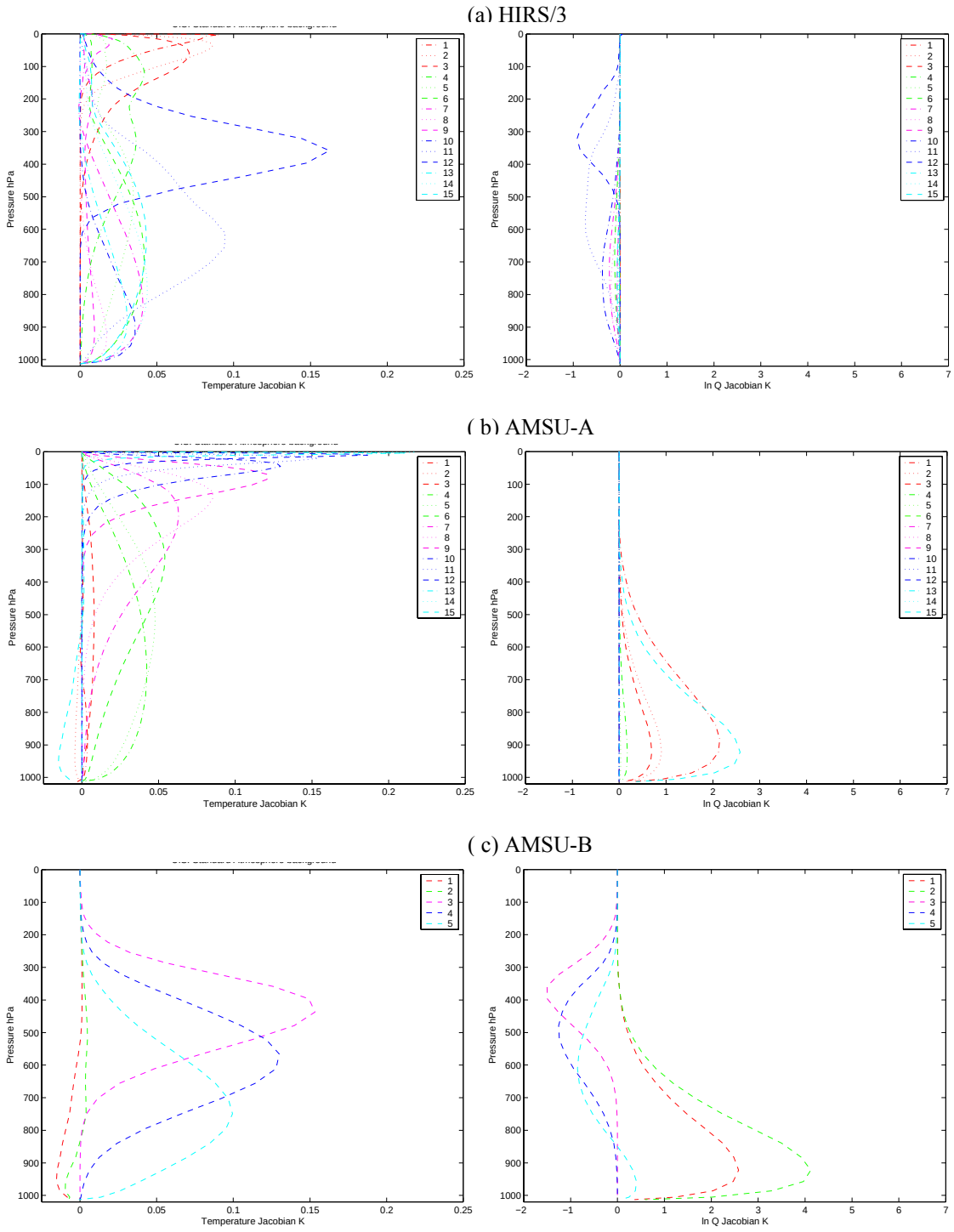

Figure 3.3. T (left panel) and $\log_e Q$ (right panel) Jacobians for the (a) 15 HIRS/3, (b) 15 AMSU-A, and (c) 5 AMSU-B channels used in this study. Elements of **H** are calculated with respect to Profile 3, the U.S. Standard Atmosphere.

The individual *T* Jacobians are presented in Fig. 3.4 for HIRS/3 sounding channels 6, 7, 13, and 14; HIRS/3 surface channel 8; AMSU-A window channels 1, 2, 3, and 15; and AMSU-B window channels 1 and 2. The results are shown as a function of the clear sky EPAC Profiles 1A and 1B, and U.S. Standard Atmosphere (Profile 3). As expected from the general channel characteristics, the *T* Jacobians for the HIRS/3 sounding channels (Figs. 3.4a-b,d-e) are larger in magnitude than the AMSU surface sensitive channels (Figs. 3.4f-j). The most interesting result of the comparison with the U.S. Standard Atmosphere background is the sensitivity of these channels (e.g., Fig. 3.4b) to the low-level EPAC temperature structure (see Figs. 3.2b,d). In addition, the *T* Jacobians are sensitive to the difference in MABL height between EPAC Profiles 1A and 1B. The greatest sensitivity is for HIRS/3 channel 8 (Fig. 3.4c). For the MW channels, AMSU-A/B channels 15/1 (Fig. 3.4i) is the most sensitive to changes in low-level atmospheric temperature.

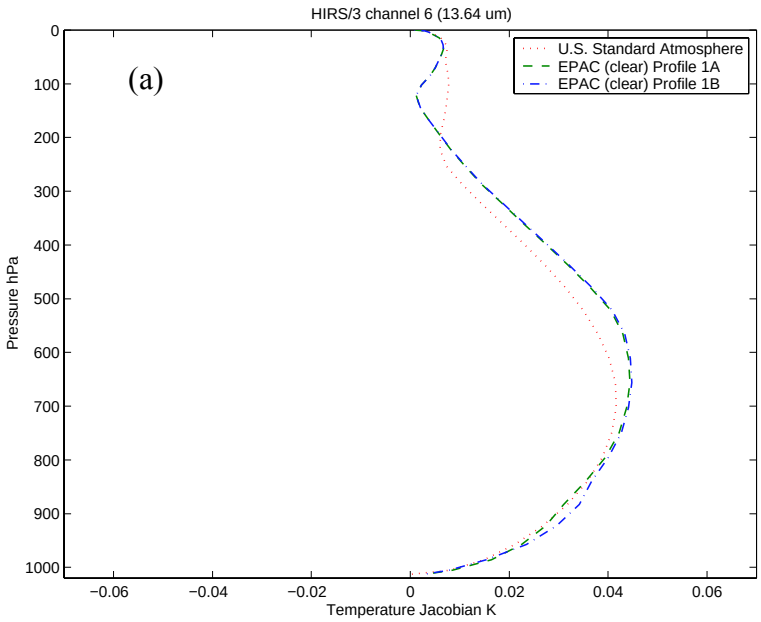

Figure 3.4. Clear sky *T* Jacobians for HIRS/3 channels (a) 6, (b) 7, (c) 8, (d) 13 and (e) 14; AMSU-A channels (f) 1, (g) 2, (h) 3, and (i) 15; and AMSU-B channels (i) 1 and (j) 2. Jacobians are compared for H linearized U.S. Standard Atmosphere (Profile 3) and representative clear sky EPAC Profiles 1A and 1B. MABL inversion heights are at 957.44 hPa for Profile 1A and 922.46 hPa for Profile 1B.

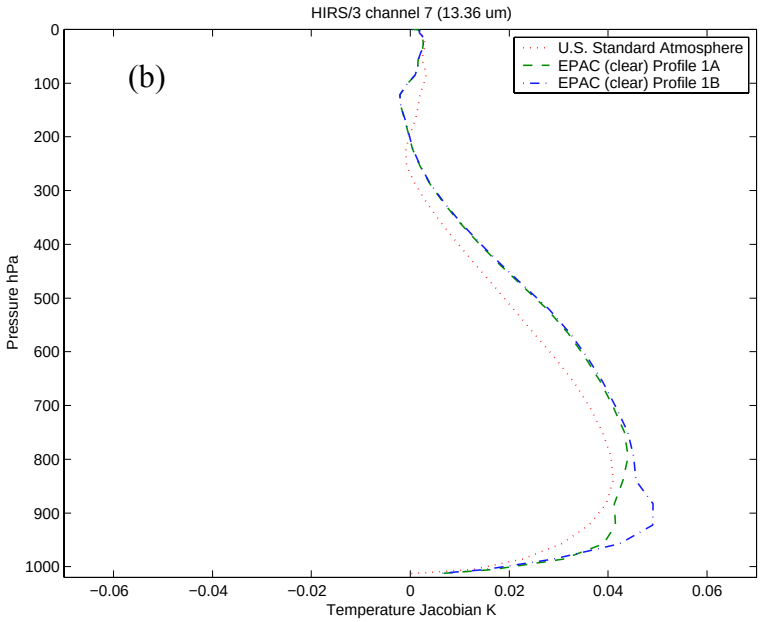

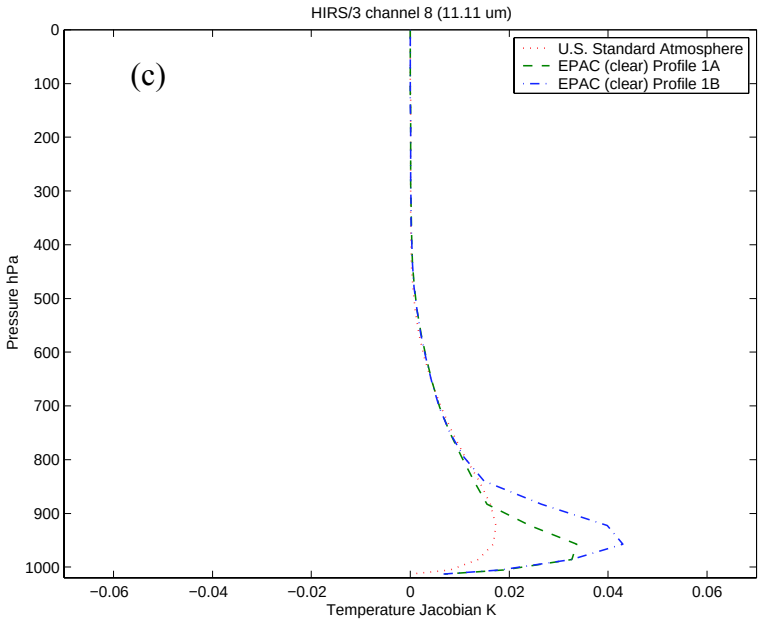

Figure 3.4. Continued.

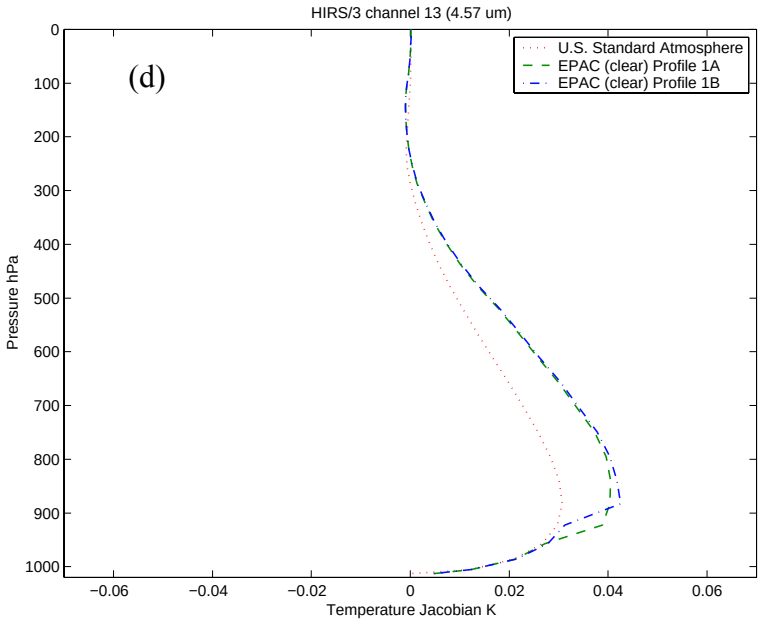

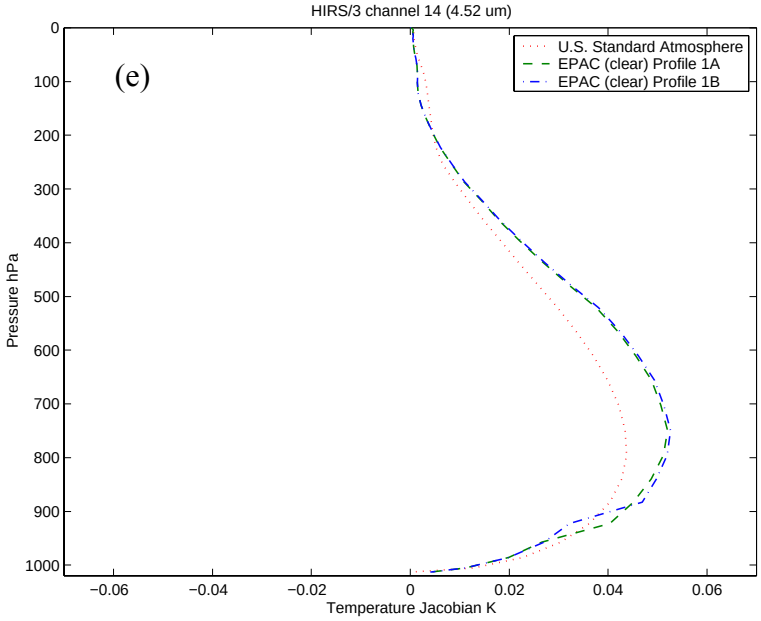

Figure 3.4. Continued.

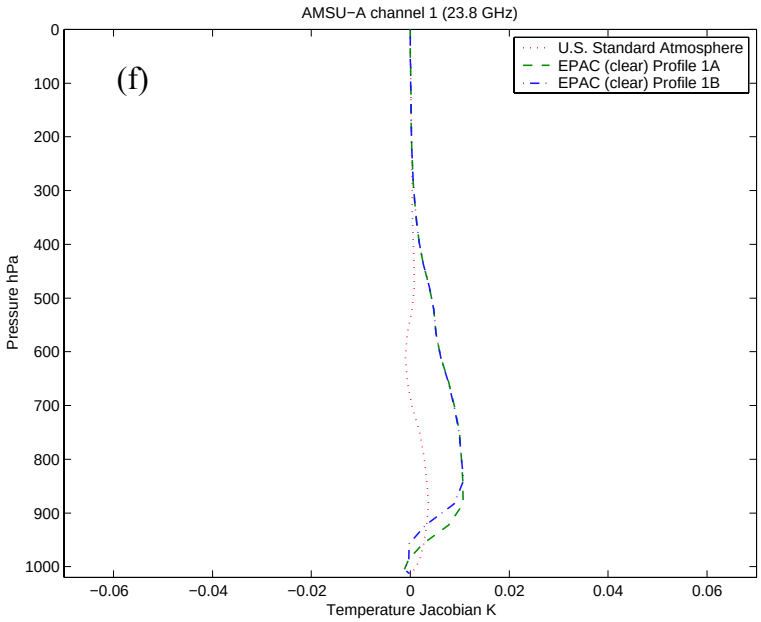

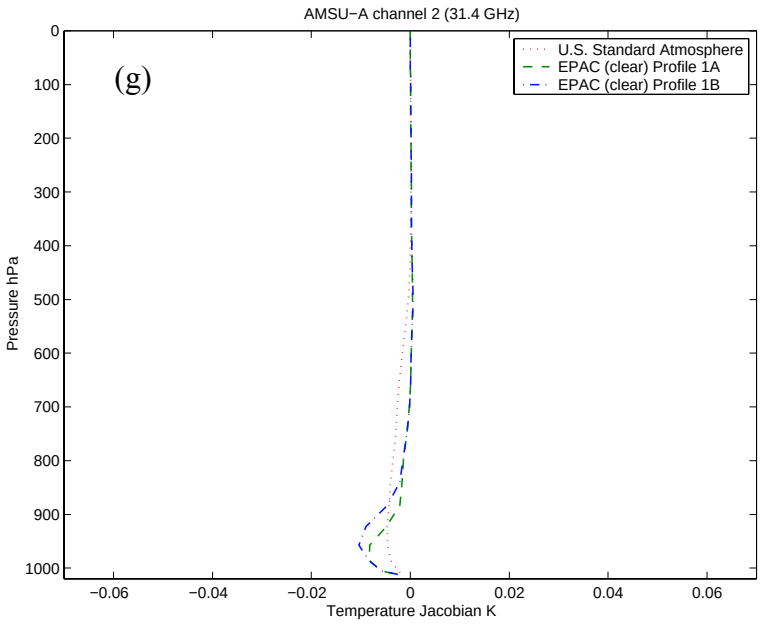

Figure 3.4. Continued.

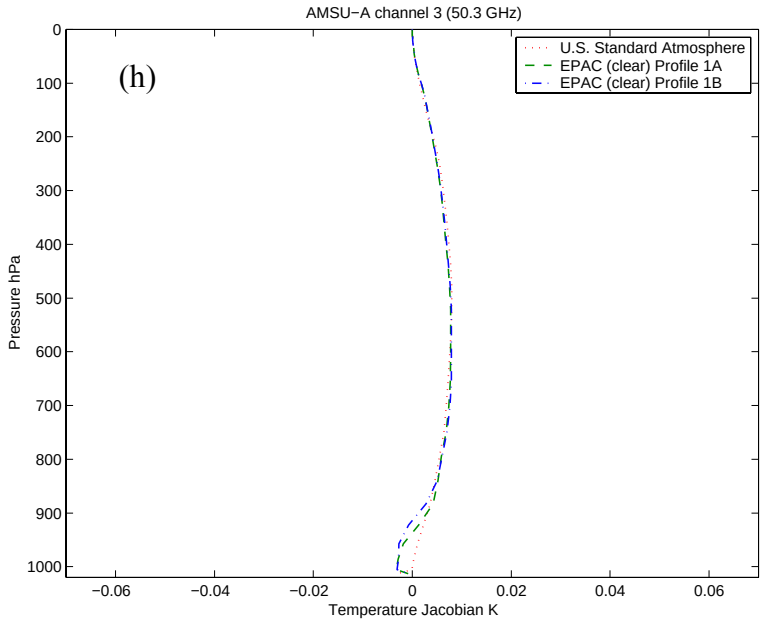

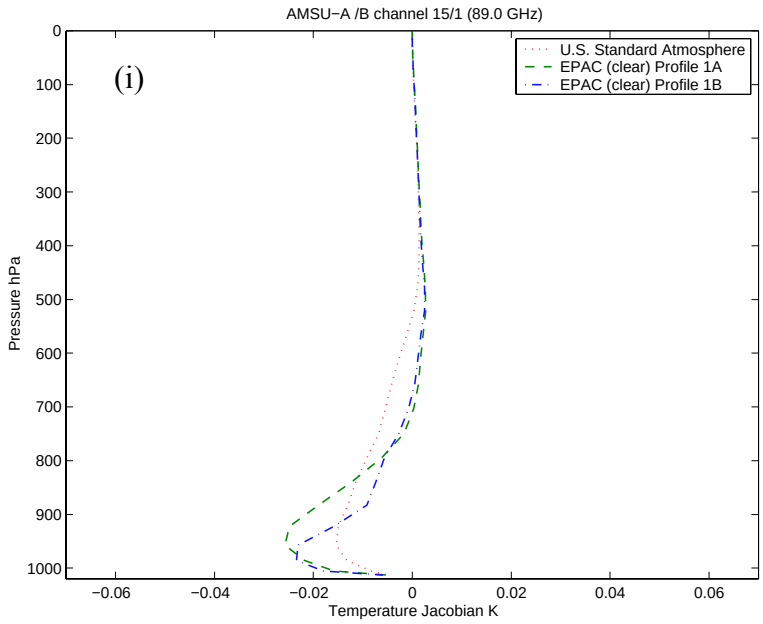

Figure 3.4. Continued.

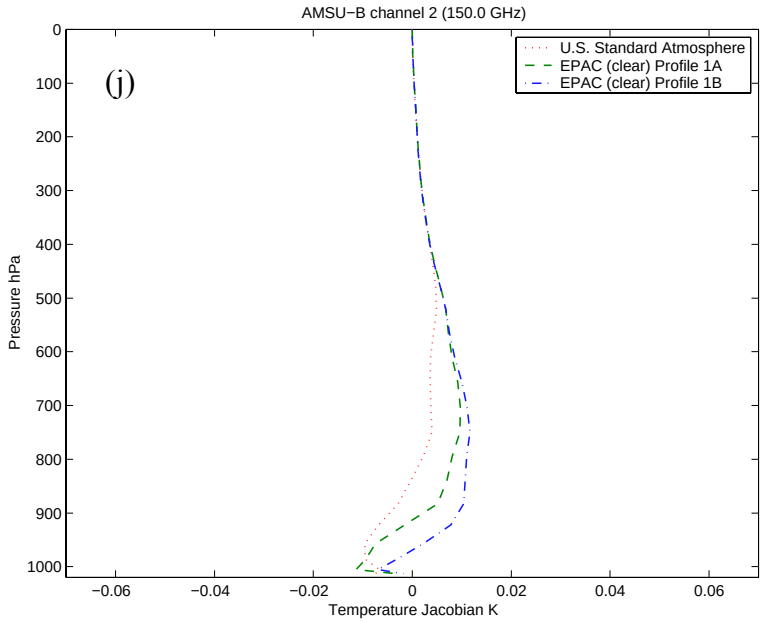

Figure 3.4. Continued.

Temperature profile (T) Jacobians were also calculated with respect to the four representative cloudy sky EPAC profiles (2A1, 2A2, 2B1, and 2B2). As discussed in Section III.C, these cloudy profiles represent two MABL heights of 957.44 hPa (2A) and 922.46 hPa (2B), each with varying amounts of LWP (90, 190, 145, and 285 g m^{-2}, respectively). The corresponding Jacobians for HIRS/3 channel 8; AMSU-A channels 1 –3, 15; and AMSU-B channels 1 - 2 are shown in Fig. 3.5. The result for HIRS/3 channel 8 (Fig. 3.5a) demonstrates the "sharpening" of the sensitivity function at cloud-top for all cloudy profiles. Temperature profile (T) Jacobians for this surface sensitive IR channel approach nearly 1 K change in brightness temperature at the TOA for a 1 K change in cloud-top temperature. When cloud fractional coverage (C_{FC}) is set to 100% within the background state vector this channel is relatively insensitive to changes in LWP (i.e., 90 versus 285 g m^{-2}). HIRS/3 sounding channels 6, 7, 13, and 14 (not shown) were also found not to be sensitive to changes low-level cloud liquid water.

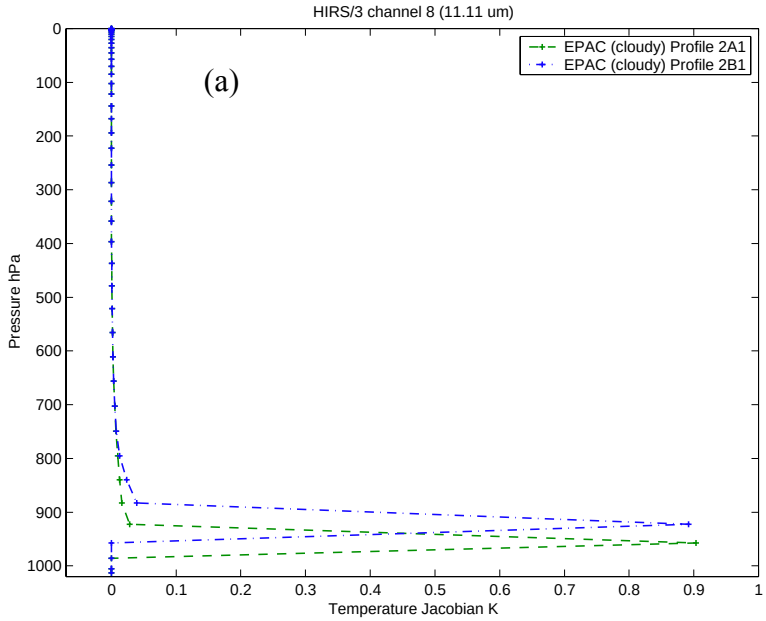

Figure 3.5. Cloudy sky *T* Jacobians for (a) HIRS/3 channel 8; AMSU-A channels (b) 1, (c) 2, (d) 3, and (e) 15; and AMSU-B channels (e) 1 and (f) 2. Jacobians are compared for the elements of **H** calculated with respect to the representative cloudy sky EPAC Profiles. MABL inversion heights are at 957.44 hPa for Profile 2A and 922.46 hPa for Profile 2B. LWP is varied for each profile with 90 and 190 g m^{-2} for Profiles 2A1 and 2A2, and 145 and 285 g m^{-2} for Profiles 2B1 and 2B2.

The magnitudes of the AMSU window channel *T* Jacobians (Figs. 3.5b-f) are much smaller than for the previous IR cloudy case (Fig. 3.5a). However, these MW surface channels are sensitive to LWP and are very sensitive to changes in LWP. There is nearly a two-fold increase in the magnitude of the *T* Jacobians as LWP is increased from 90 to 190 g m^{-2} (Profile 2A) and from 145 to 285 g m^{-2} (Profile 2B). The greatest sensitivity to changes in LWP is calculated for AMSU-B channel 2. Note the *T* Jacobians for this channel are an order of magnitude larger than other AMSU channels.

The change in structure and magnitude of the *T* Jacobians (Figs. 3.5a-f) with the presence of *CLW* in the background state vector is rather dramatic. The effect of this "sharpening" of the IR and MW sensitivity functions on theoretical *T* retrieval performance and retrieval error sensitivity is discussed in Chapter IV.

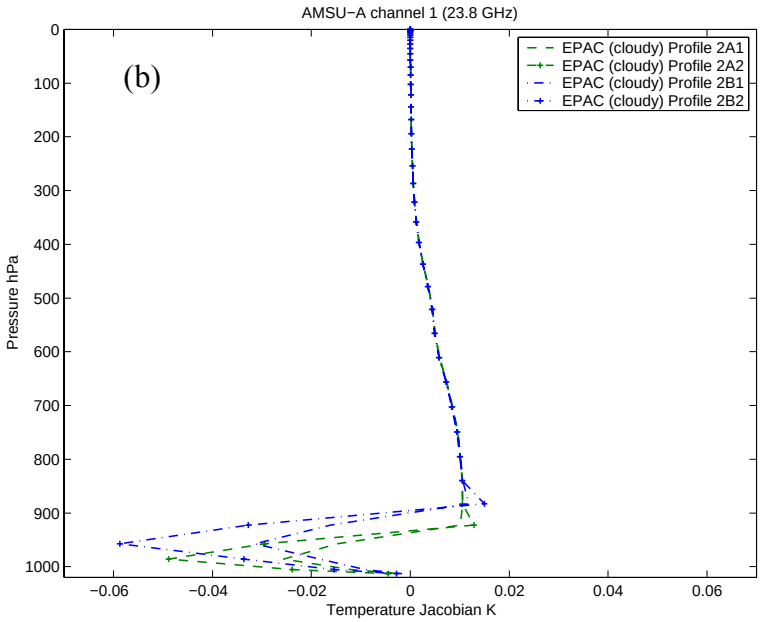

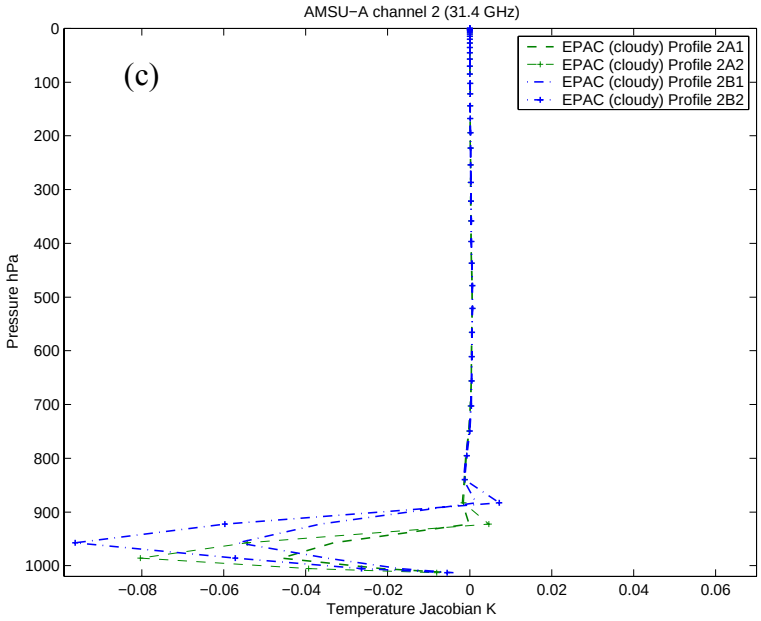

Figure 3.5. Continued.

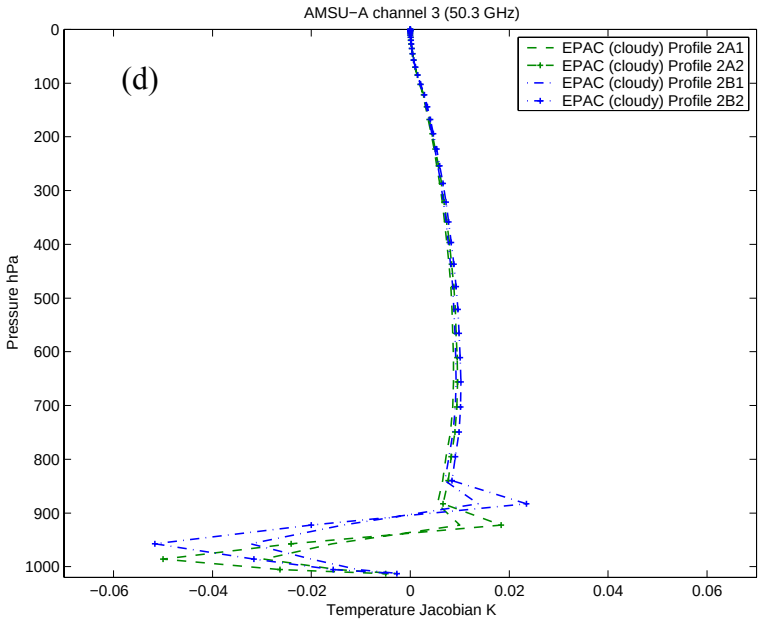

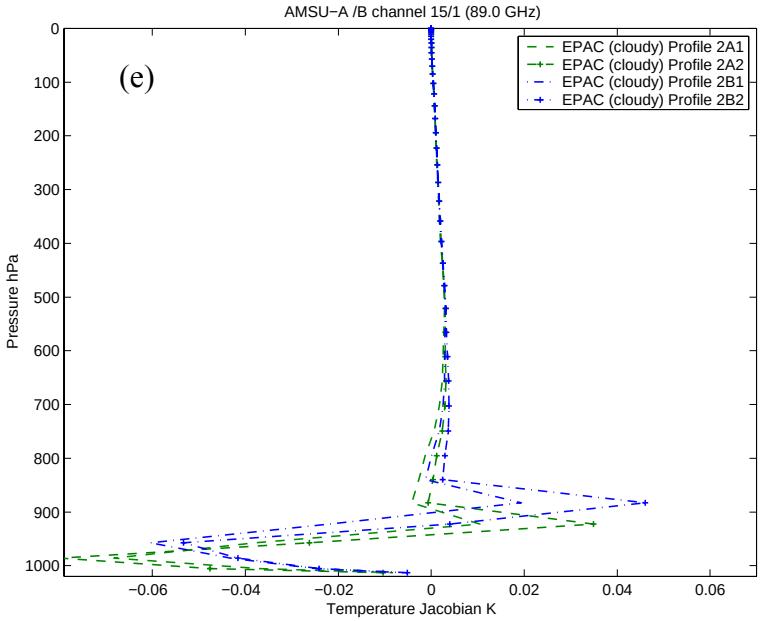

Figure 3.5. Continued.

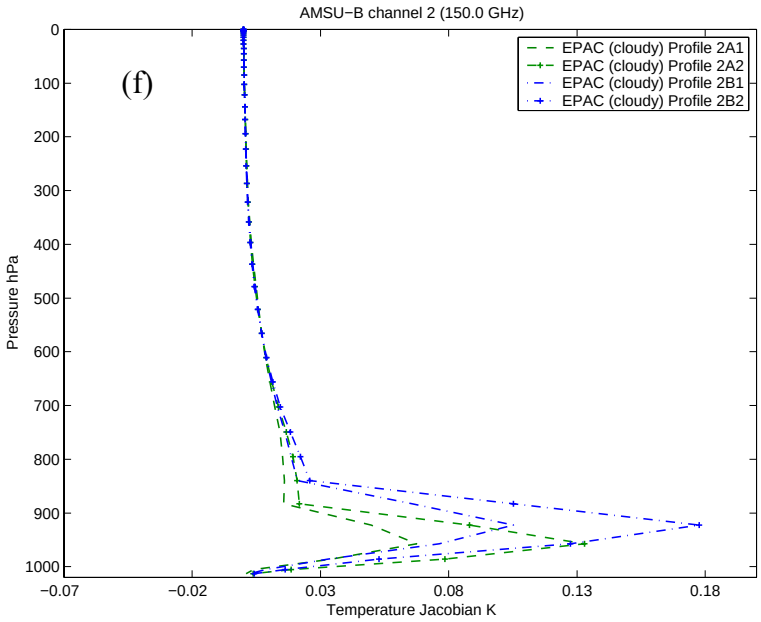

Figure 3.5. Continued.

Log_e Q Jacobians calculated with respect to clear sky EPAC Profiles 1A and 1B, and the U.S. Standard Atmosphere (Profile 3) are shown in Fig. 3.6 for HIRS/3 channel 10, AMSU-A channels 1 - 3, and 15; and AMSU-B channels 1 and 2. This research found the AMSU window channel $\log_e$ Q Jacobians (Figs. 3.6b-f) to be very sensitive to the low-level water vapor gradient of this representative summertime EPAC environment. The two largest $\log_e$ Q Jacobians are for AMSU-B channel 2 (Fig. 3.6f) and AMSU-A/B channel 15/1 (Fig. 3.5e). The magnitude of these $\log_e$ Q Jacobians are approximately 4 K larger near 900 hPa than those calculated with respect to the U.S. Standard Atmosphere. Log_e Q Jacobians for AMSU-A channels 1, 2, and 3 (Figs. 3.6b-d) are also larger at this level. These Jacobians also show the sensitivity the relatively small differences in the representative EPAC MABL water vapor content between Profiles 1A and 1B. In contrast to the MW window channels, the $\log_e$ Q Jacobian corresponding to HIRS/3 channel 10 (Fig. 3.6a) is not very sensitive to the representative EPAC low-level water vapor gradient.

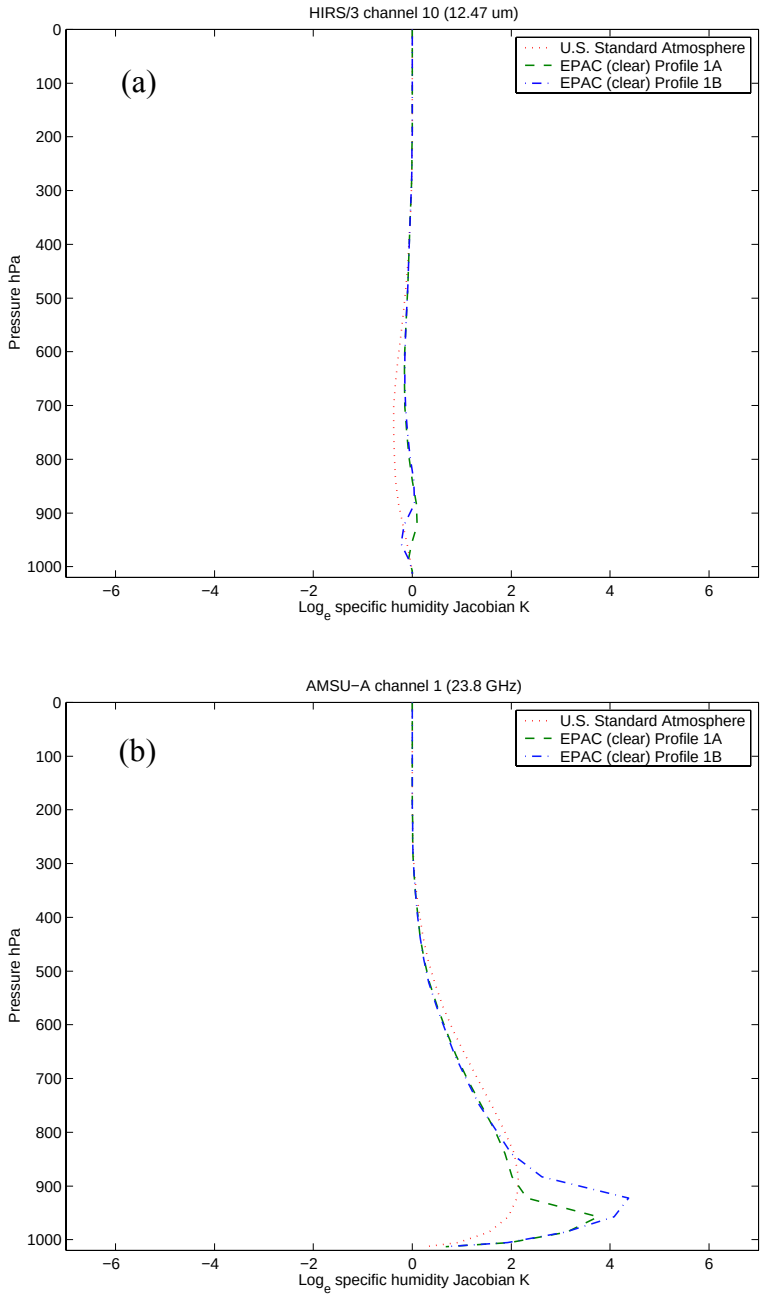

Figure 3.6. Clear sky $\log_e Q$ Jacobians for (a) HIRS/3 channel 10; AMSU-A channels (b) 1, (c) 2 , (d) 3, and (e) 15; and AMSU-B channels (e) 1, and (f) 2. Jacobians are compared for the elements of **H** calculated with respect to the U.S. Standard Atmosphere (Profile 3) and EPAC Profiles 1A and 1B. MABL inversion heights are at 957.44 hPa for Profile 1A and 922.46 hPa for Profile 1B.

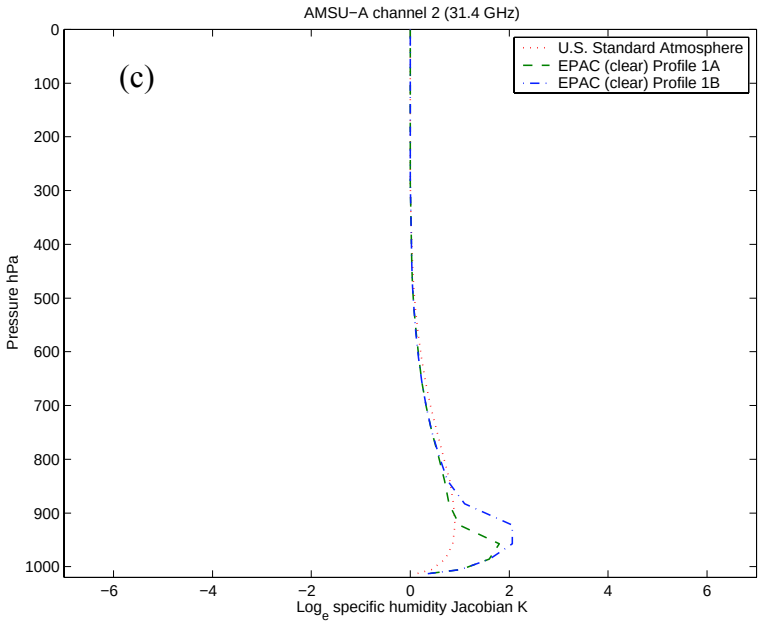

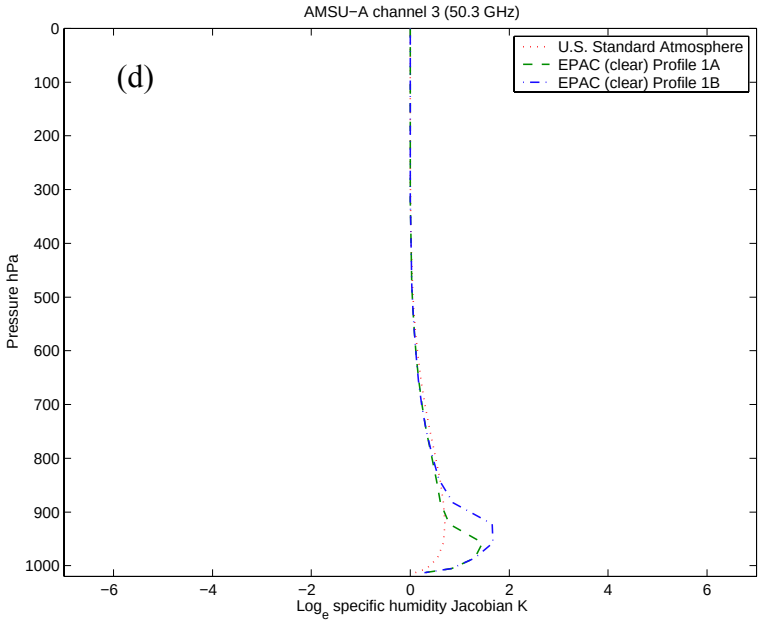

Figure 3.6. Continued.

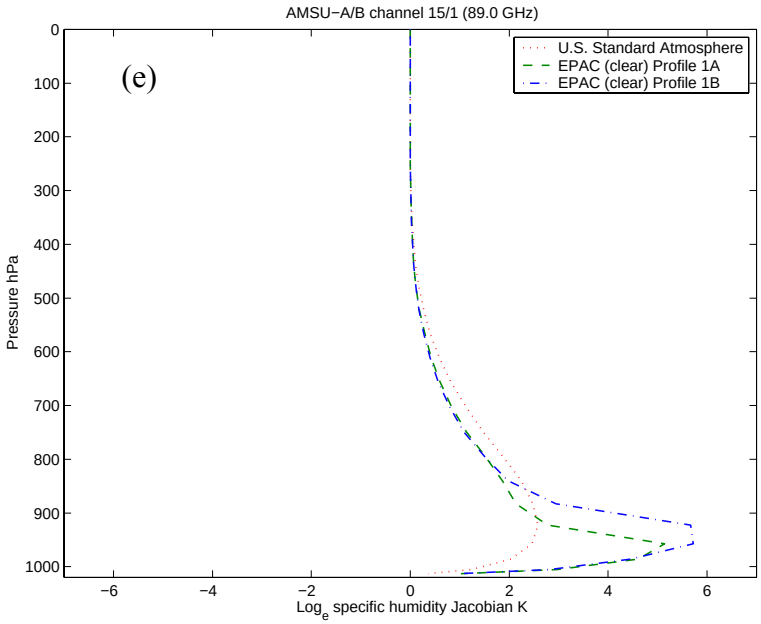

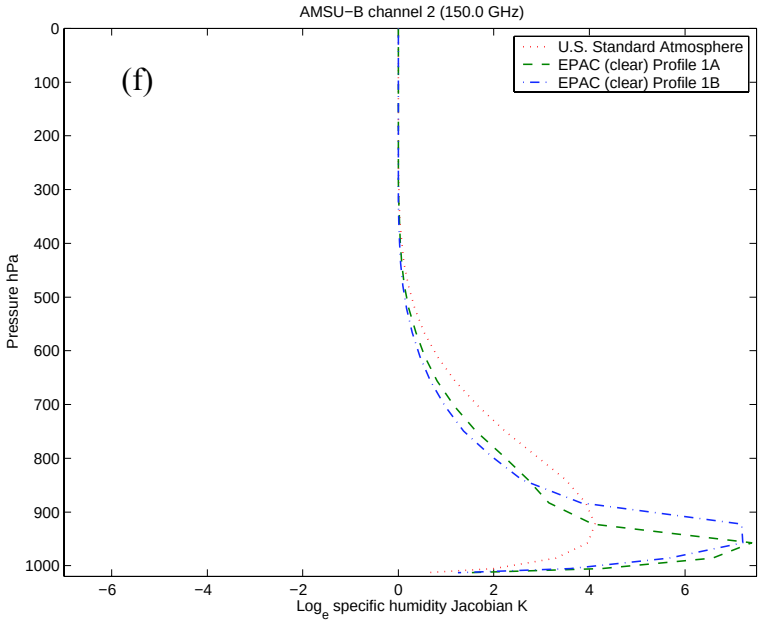

Figure 3.6. Continued.

Log_e Q Jacobians calculated with respect to cloudy sky EPAC Profiles 2A1, 2A2, 2B1, and 2B2 are shown in Fig. 3.7 for HIRS/3 channel 10, AMSU-A channels 1 - 3, and 15; and AMSU-B channels 1 and 2. This comparison shows the effect of low-level clouds on the $\log_e$ Q Jacobians. Overall, the magnitude of the AMSU window channel $\log_e$ Q Jacobians are reduced when CLW is present in the background state vector. However, the sensitivity to changes in LWP depend on channel frequency. Changes in LWP have negligible impact on the magnitude of the $\log_e$ Q Jacobians for AMSU-A channels 1, 2 and 3 (Figs. 3.7b-d). In contrast, the $\log_e$ Q Jacobians for AMSU-A/B channel 15/1 (Fig. 3.7e) and AMSU-B channels 2 (Fig. 3.7f) are sensitive changes in LWP. In these two cases, the magnitude of these Jacobians decrease by approximately 2 K as LWP increases. This reduction in the magnitude suggests that there will be less low-level information available from theses satellite channels as cloud depth increases. Again, note the relatively small magnitude of the HIRS/3 channel 10 Jacobians (Fig. 3.7a).

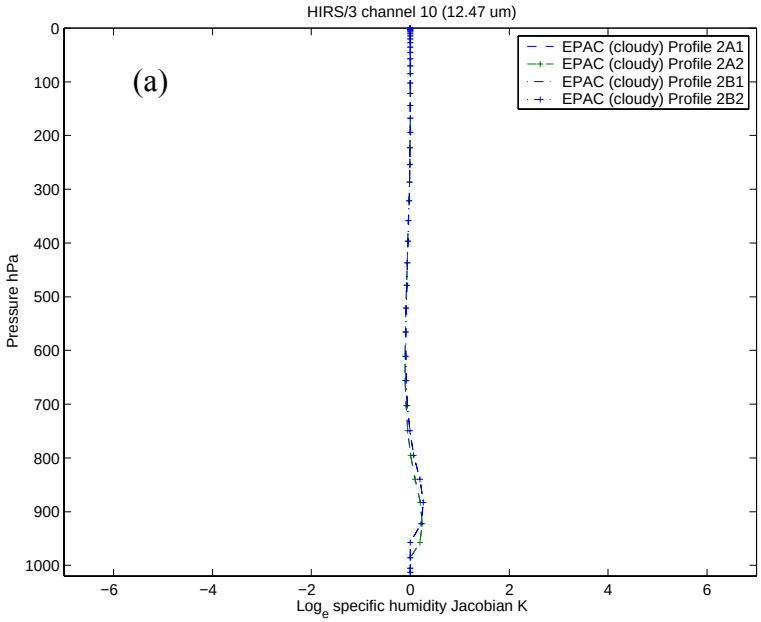

Figure 3.7. As in Fig. 3.6, except elements of **H** calculated with respect to cloudy sky EPAC Profiles 2A1, 2A2, 2B1, and 2B2. MABL inversion heights are at 957.44 hPa for Profile 2A and 922.46 hPa for Profile 2B. LWP is varied for each profile with 90 and 190 g m^{-2} for Profiles 2A1 and 2A2, and 145 and 285 g m^{-2} for Profiles 2B1 and 2B2.

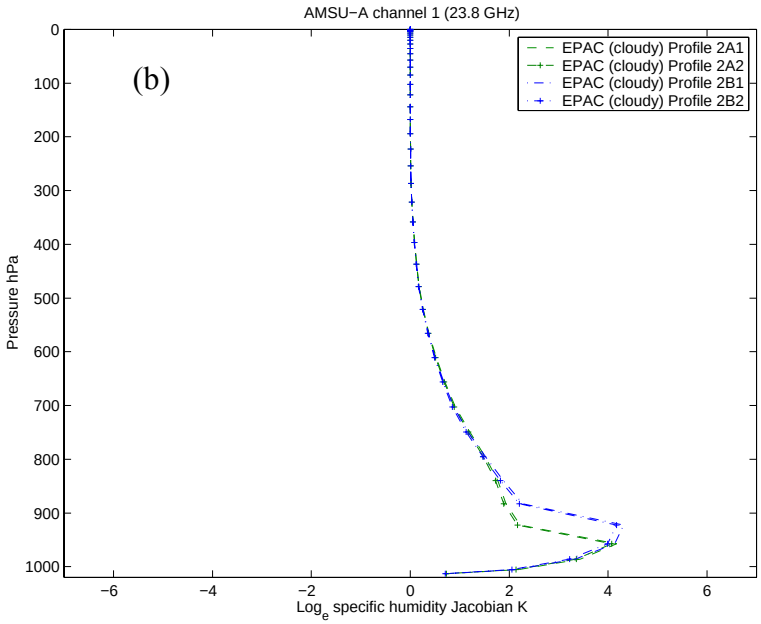

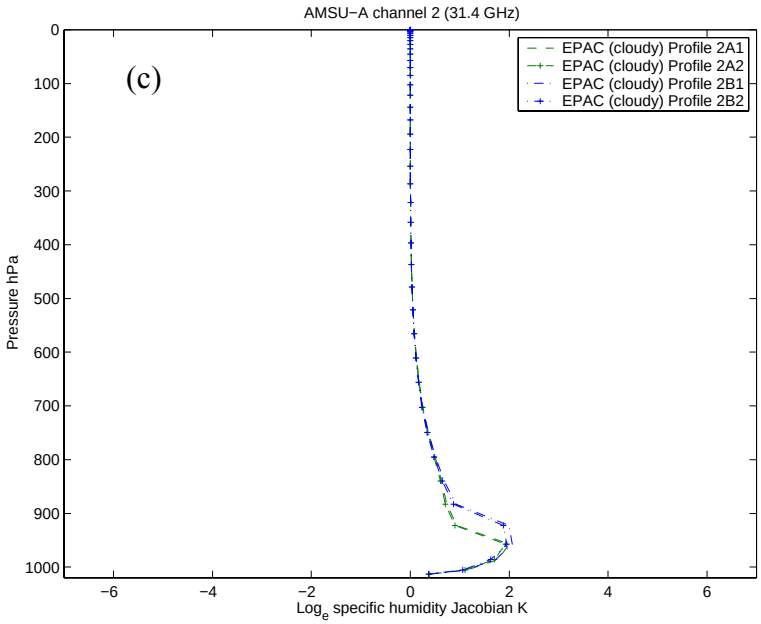

Figure 3.7. Continued.

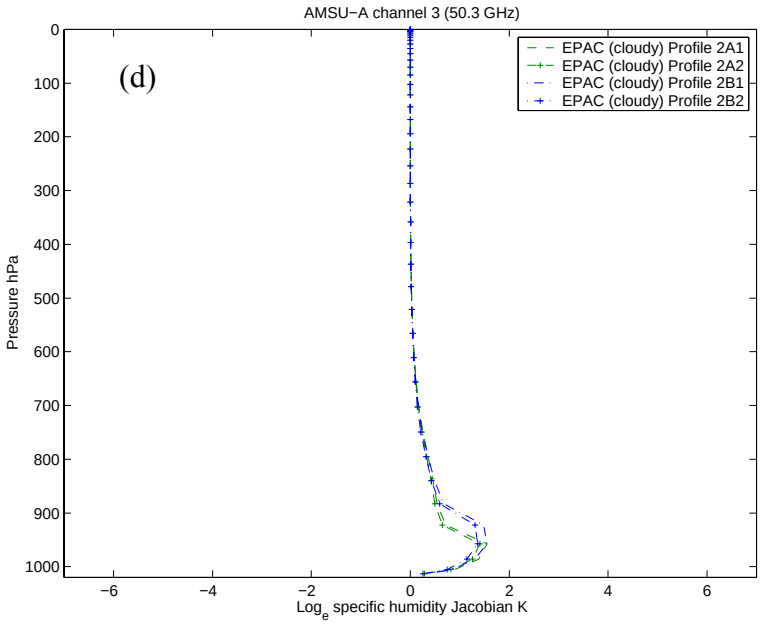

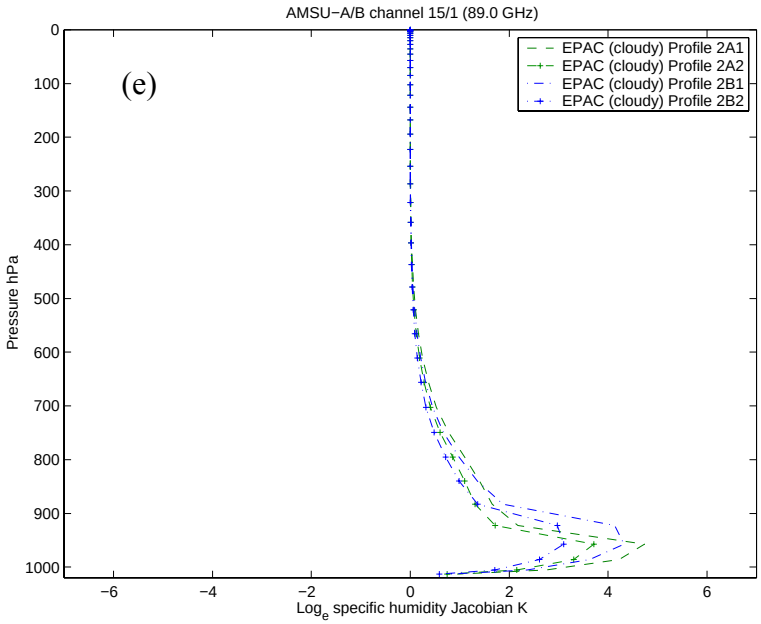

Figure 3.7. Continued.

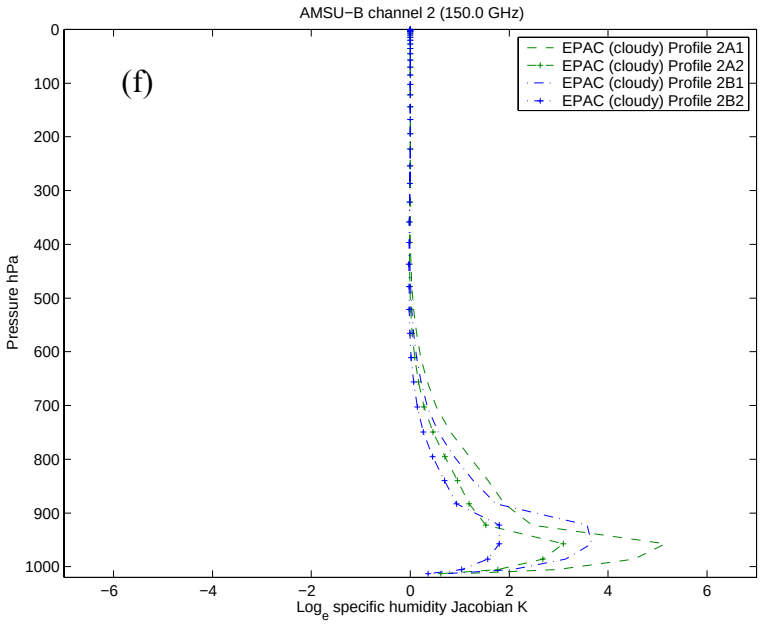

Figure 3.7. Continued.

Elements of **H** corresponding to the Jacobians of radiative skin temperature (T_s), surface pressure (P_s), cloud top pressure (P_{CT}) and cloud fractional coverage (C_{FC}) are shown in Figs. 3.8a-b, Figs. 3.9a-b, Fig. 3.10, and Fig. 3.11, respectively. Other surface parameters are not shown due to their very small magnitudes. As expected, the non-zero T_s Jacobians are associated with the surface sensitive channels. For clear sky conditions (Fig. 3.8a) the observed magnitudes for HIRS/3 channels 8 and 13 are approximately 0.8 K and 0.5 K. This equates to nearly a 0.8 K and 0.5 K change in TOA brightness temperature for a 1 K change in T_s. The clear EPAC profiles have slightly smaller magnitudes due to the increased low-level water vapor. The T_s Jacobians are zero for all HIRS/3 channels for the cloudy boundary layer cases (Fig. 3.8b); however, the AMSU Jacobians remain relatively unchanged except for AMSU-A/B channel 15/1. P_s Jacobians (Figs. 3.9a-b) are non-zero for only the AMSU window channels. Column elements of **H** corresponding to P_{CT} (Fig. 3.10) have negative values associated with HIRS/3 surface sensitive channels. C_{FC} Jacobians (Fig. 3.11) are large for the HIRS/3 surface channels and zero for all AMSU channels.

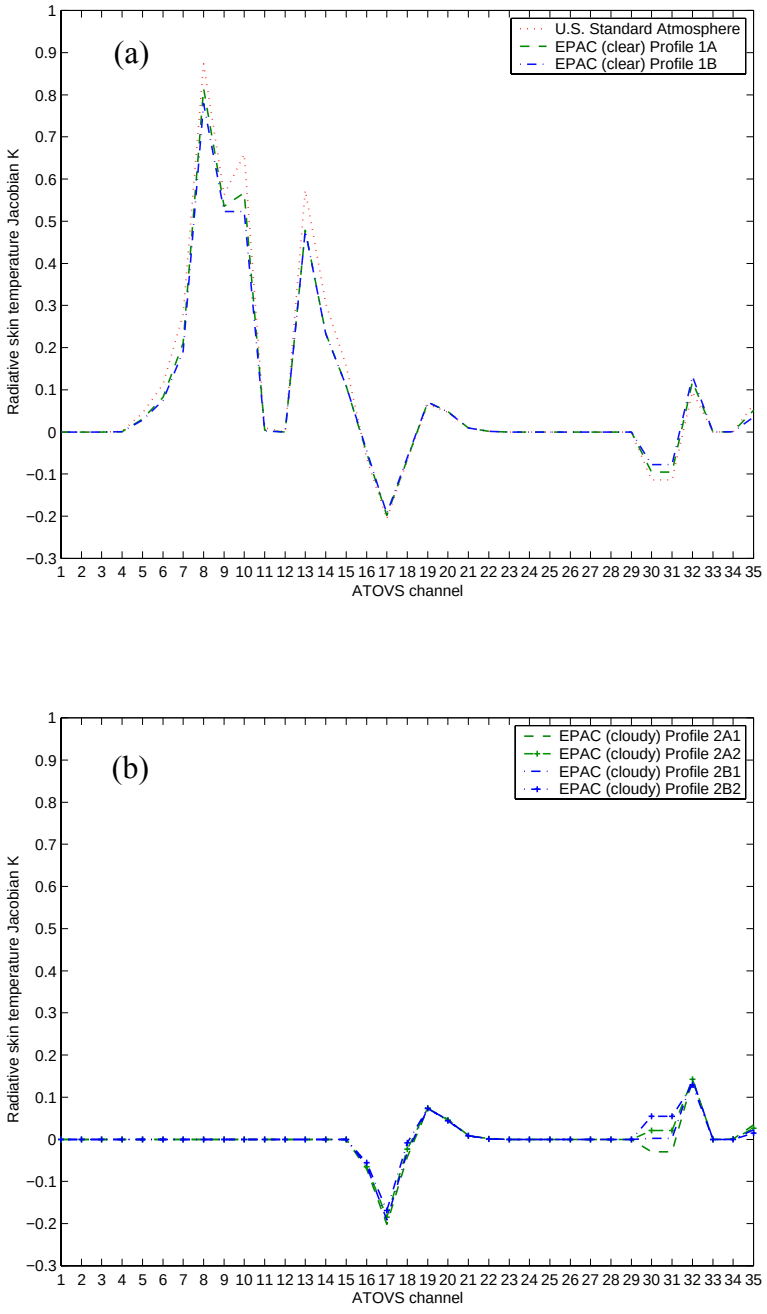

Figure 3.8. Clear and cloudy sky radiative skin temperature (T_s) Jacobians (i.e., $\partial T_B/\partial T_s$) versus ATOVS channel. HIRS/3 channels are 1-15, AMSU-A are 16-30, and AMSU-B are 31-35. Comparisons are made for H linearized about (a) clear sky background profiles, and (b) cloudy sky background profiles.

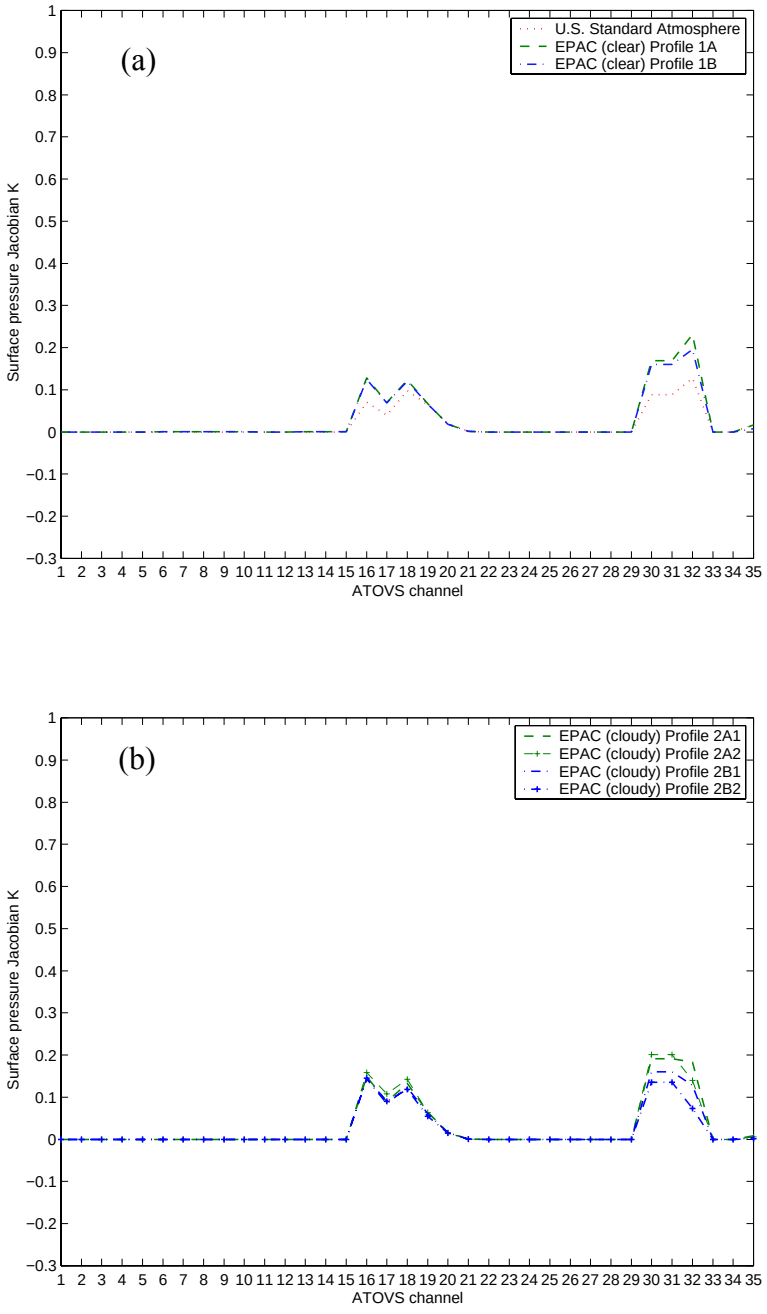

Figure 3.9. As in Fig. 3.8, except for surface pressure (P_s) Jacobians.

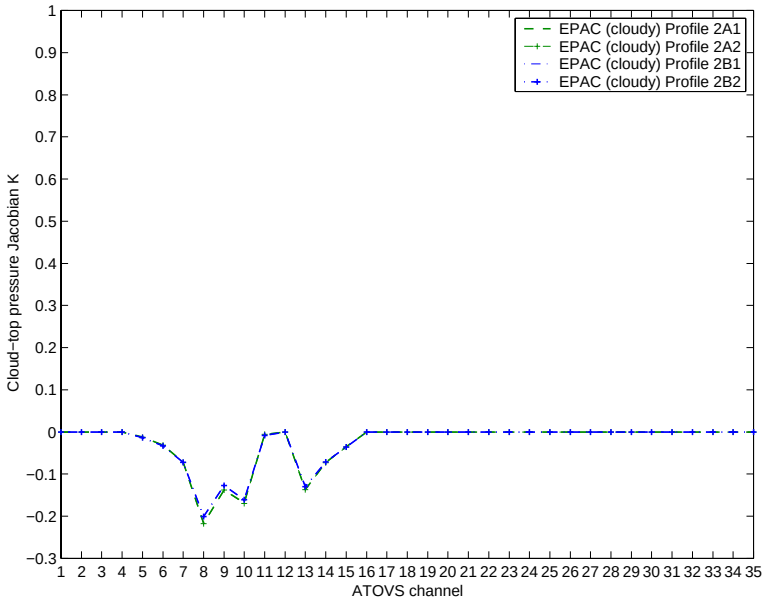

Figure 3.10. As in Fig. 3.8b, except for cloud-top pressure (P_{CT}) Jacobians. Comparisons are made for H linearized about cloudy sky EPAC profiles.

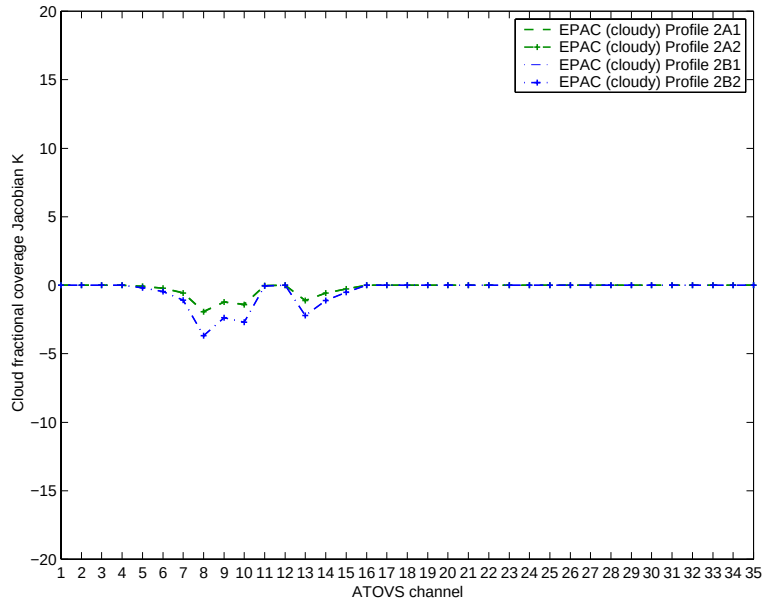

Figure 3.11. As in Fig. 3.8b, except for cloud fractional coverage (C_{FC}) Jacobians.

IV. INFORMATION CONTENT STUDY

Three established approaches are used in this research to examine the information content of ATOVS retrievals with respect to the idealized EPAC background state vectors and associated background errors. The purpose of this study is to quantify the relationship between satellite-derived information and the background. The first method quantifies independent information and vertical resolution based upon related mathematical techniques of principal component analysis and singular value decomposition, and the diagonal elements of the averaging kernel matrix. The second is a radiance space comparison of effective background error and ATOVS observation error. The final method investigates the sensitivity of profile temperature (T) and $\log_e$ specific humidity ($\log_e Q$) retrieval errors to surface and profile *a priori* background errors by comparing the diagonal elements of the retrieval and background error covariance matrices. In addition, retrieval error sensitivity to ATOVS channel selection and observation error, and background profile type is also studied. Information theory and the details of the background germane to this information content study were discussed in Chapters II and III, respectively.

In this research, information content is calculated with respect to the clear sky EPAC Profiles 1A and 1B (Figs. 3.2a-b), cloudy sky EPAC Profiles 2A1 and 2B2 (Figs. 3.2c-d), and for comparison, the mean mid-latitude U.S. Standard Atmosphere (Profile 3). As a reminder, these representative EPAC background state vectors have the top of the MABL at 957.44 (for Profiles 1A and 2A), and 922.46 hPa (for Profiles 1B and 2B). The two cloudy profiles have LWP values of 90, and 285 g m^{-2}, respectively. A full description of the background state vectors is provided in Chapter III.C. The background error covariance matrix $\mathbf{B_N}$ derived from globally averaged NOGAPS background errors is employed as an appropriate first-order approximation of the error structure. Background errors specific to the COAMPS model for the summertime EPAC environment were used to calculate a new background error covariance matrix, namely $\mathbf{B_C}$. This mesoscale specific background error covariance matrix is used to refine the information analyses.

Except for removal of HIRS/3 channels 16-20, no other channel de-selection was performed. This acknowledges that some of the weighting functions do overlap to some extent and will not provide much additional independent information (Prunet et al. 1998). However, this issue becomes more important for retrievals using hyperspectral sounders (see Lerner et al. 2001).

A. INDEPENDENT INFORMATION AND VERTICAL RESOLUTION

1. Principal Component Analysis of S'

Principal component analysis (PCA) of (2.17) was conducted for ATOVS using the non-diagonal background error covariance matrix $\mathbf{B_N}$ and the forward model (H) linearized about the clear sky EPAC Profile 1B and U.S. Standard Atmosphere (Profile 3). Again, $\mathbf{B_N}$ is used here as an appropriate first-order approximation of the background error structure. The significant eigenvectors for profile temperature (T) and $\log_e$ specific humidity ($\log_e Q$) are shown in Fig. 4.1 and the corresponding eigenvalues and percent contributions from each are listed in Table 4.1. As discussed in Chapter II.E, "significant" means at least 10% of the information for each eigenvector is derived from the satellite observations.

In contrast to the 6 (19) significant eigenvectors found by Prunet et al. (1998) for HIRS TOVS (IASI), this summertime EPAC case study shows the ATOVS suite (minus HIRS/3 channels 16-20) has approximately 12 significant eigenvectors. Seven of these eigenvectors (Figs 4.1a-g) have eigenvalues are less than 0.50, i.e., more than 50% of the information is derived from the satellite radiances. Although the total number of significant eigenvectors is the same for both profile types, more low-level T and $\log_e Q$ information is available with the EPAC Profile 1B background.

The first significant $\log_e Q$ eigenvectors (Fig. 4.1a) for both cases have relatively large amplitudes near 900 hPa. The eigenvector for the EPAC Profile 1B has slightly larger amplitude and is "weighed" closer to the surface. This suggests that independent information regarding the low-level humidity structure may be available from the ATOVS retrieval. From Table 4.1, eigenvectors 1 and 2 contain the majority of the humidity information with the associated eigenvalues indicating that approximately 99% (98%) of the information is derived from the radiances for eigenvector 1 and 94% (94%) for eigenvector 2.

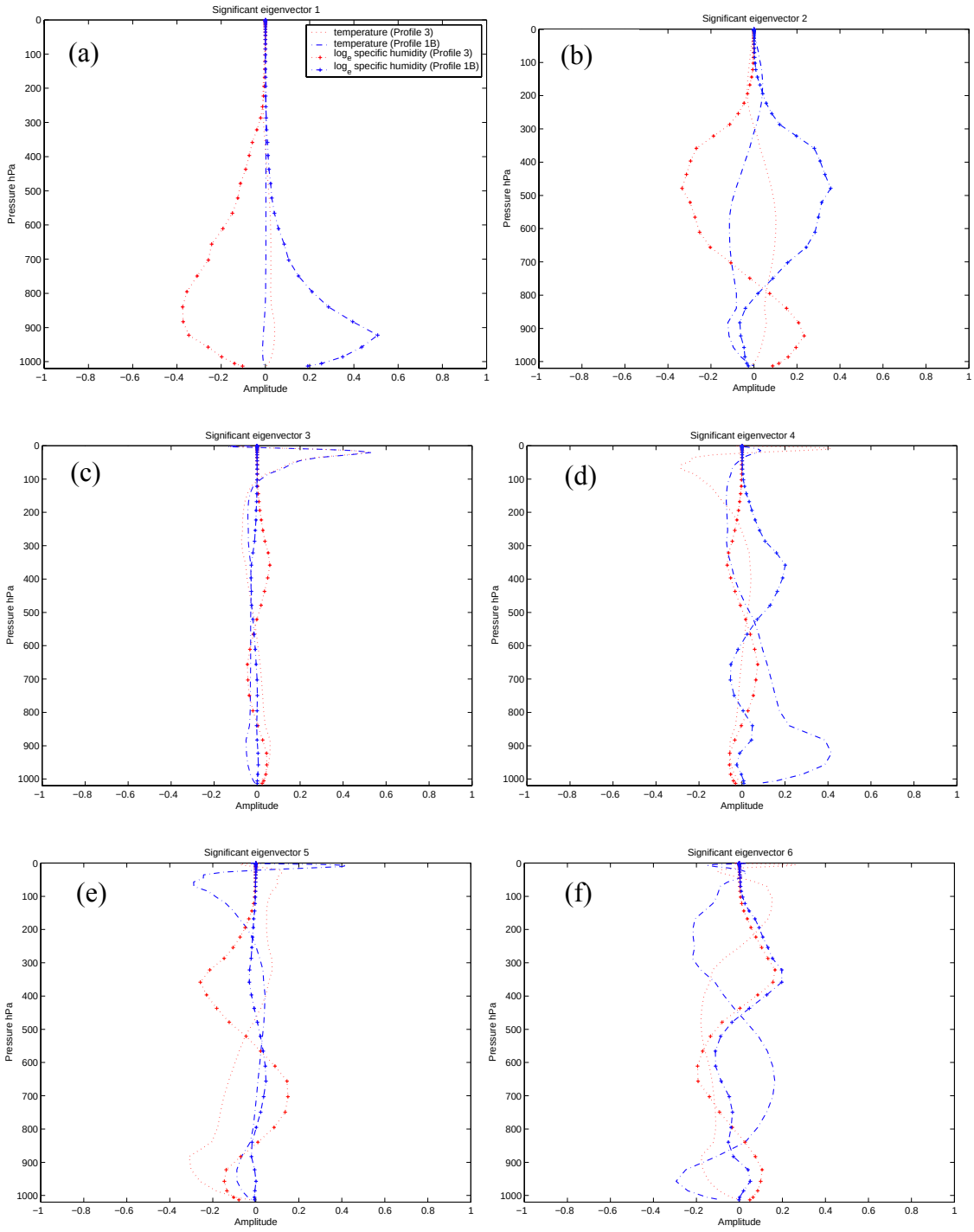

Figure 4.1. The 12 significant T and $\log_e Q$ eigenvectors of (2.17). Significant is defined as at least 10% of the information for each eigenvector is derived from the satellite observation. Comparison for elements of **H** calculated with respect to clear sky EPAC Profile 1B and U.S. Standard Atmosphere (Profile 3) and the results are calculated using $\mathbf{B_N}$.

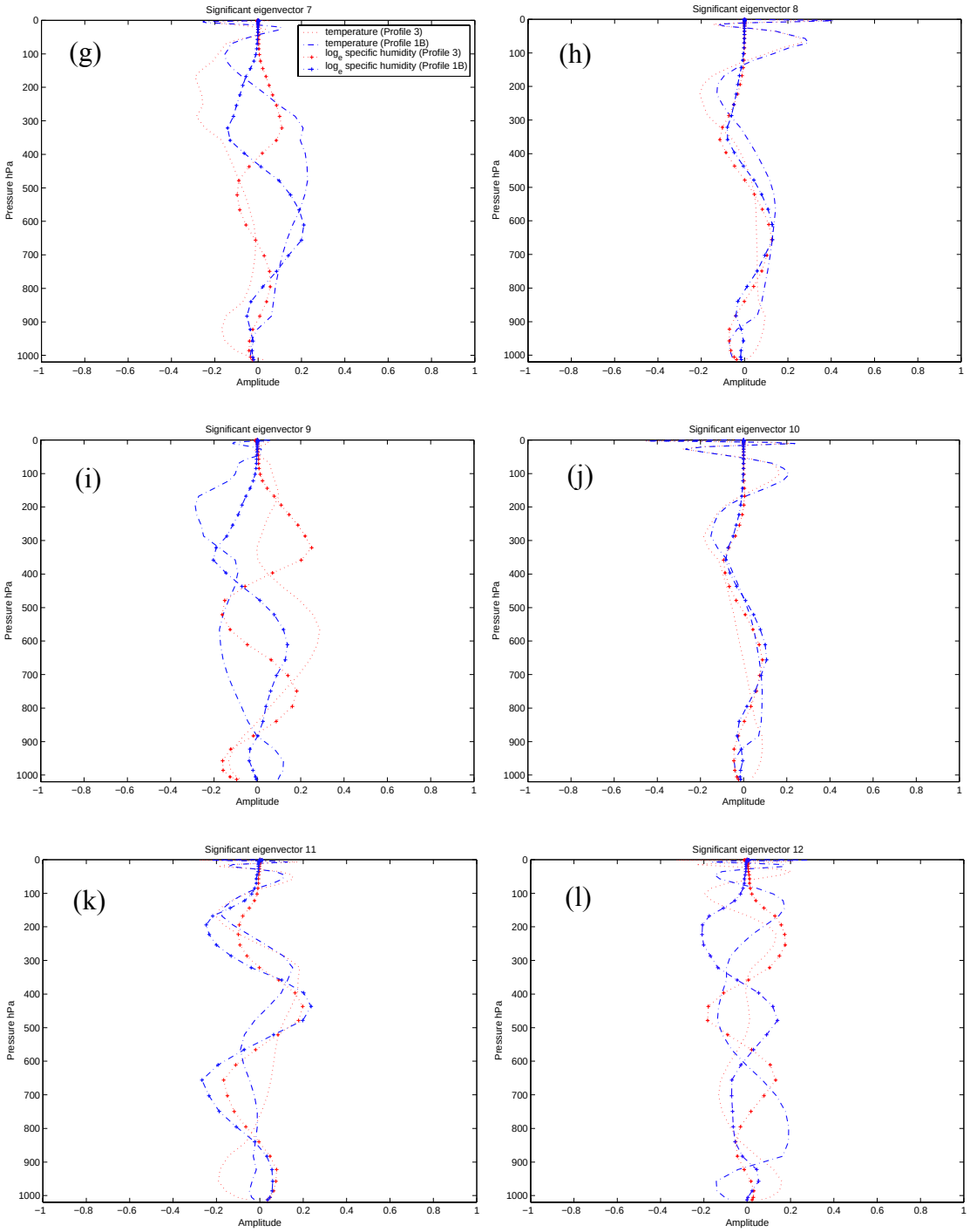

Figure 4.1. Continued.

Table 4.1. Significant eigenvalues from the principal component analysis of (2.17) for the 35 ATOVS channels. H has been linearized about the clear sky EPAC Profile 1B background and U.S. Standard Atmosphere (Profile 3). Profile temperature (T) and $\log_e$ specific humidity ($\log_e Q$) contributions are shown as a percentage of each eigenvector. Results are calculated with respect to $\mathbf{B_N}$.

	Profile 1B			Profile 3		
eigenvector	*eigenvalue*	*T* %	$\text{Log}_e Q$ %	*eigenvalue*	*T* %	$\text{Log}_e Q$ %
1	0.014	1	99	0.021	1	99
2	0.064	16	84	0.061	8	92
3	0.161	77	23	0.180	97	3
4	0.183	99	1	0.195	95	5
5	0.229	98	2	0.226	58	42
6	0.421	78	22	0.381	70	30
7	0.380	73	27	0.448	91	9
8	0.513	90	10	0.503	88	12
9	0.486	77	23	0.572	51	49
10	0.666	94	6	0.681	94	6
11	0.831	37	63	0.822	75	25
12	0.861	70	30	0.889	72	25

In general, T information dominates the remaining eigenvectors (except eigenvector 11 for Profile 1B). For example, eigenvector 3 (Fig. 4.1c) primarily consists of temperature information above 100 hPa for both background state vectors. Eigenvectors 4 – 6 (Figs. 4.1d-f) indicate T information between the surface approximately 900 hPa with larger amplitudes for EPAC Profile 1B.

As shown in Figs. 4.1g-l, the structure of the eigenvectors increases in complexity as the eigenvalues become larger. According to Pruent et al. (1998), the large number of oscillations (or zero crossings) signifies the existence of information on finer scale atmospheric structures. The "semi-period of oscillation" determines the vertical resolution and the eigenvalue is a measure of the resolution quality.

These results suggest that independent, $\log_e Q$ and T information may be available from the ATOVS measured radiances. A goal of this research is to determine whether this satellite-derived information could be used in a variational retrieval scheme to adjust the background toward the true atmospheric state.

2. Singular Value Decomposition of H'

The first 10 of 35 singular values of (2.18) and the contribution of each singular vector to the degrees of freedom of (2.19) and information content from (2.21) are listed in Table 4.2. Calculations are compared for H linearized about clear sky EPAC Profile 1B and the U.S. Standard Atmosphere (Profile 3) for both the full and diagonal $\mathbf{B_N}$ matrices. In contrast to the somewhat arbitrary criterion used in the PCA, the number of independent pieces of information for the retrieval is determined by the number of singular values of (2.18) greater than about unity.

This analysis indicates approximately 9 (8) independent pieces of information are available from ATOVS using Profile 1B (3) background state vector, $\mathbf{R}$, and non-diagonal $\mathbf{B_N}$. The first four to five singular values give close to one degree of freedom and the next three or four about one-half degree of freedom. As expected, the effective rank is reduced for the diagonal $\mathbf{B_N}$ matrix case, indicating that the diagonal case has equal variance at all scales. Summing the total degrees of freedom for the 35 singular vectors (non-diagonal $\mathbf{B_N}$ case) gives approximately 7.4 (7.2) for Profile 1B (3). This indicates that about seven to seven and a half quantities can be independently measured. Daley and Barker (2000), in their discussion of temperature retrievals with TOVS, quote the number of degrees of freedom as 5.2 for a climatological background with errors of 10 K, and 3.0 for a forecast background of with errors of 2.5 K.

Total information content is approximately 8.1 (7.7) bits (i.e., binary units of information) for Profile 1B (3). Information content analysis using entropy reduction (2.22) also confirms a decrease in information for the diagonal $\mathbf{B_N}$ and slight increase in information for Profile 1B background. From Chapter II.E, a decrease in entropy of the PDF is related to an increase in information.

Table 4.2. First 10 singular values (λ_i) of (2.18) and associated degrees of freedom (ds_i) and information content (H) for clear sky EPAC Profile 1B and U.S. Standard Atmosphere (Profile 3). Totals are for all 35 singular values. Results for full and diagonal covariance $\mathbf{B_N}$ are shown.

EPAC (clear) Profile 1B						
	Full **B**			Diagonal **B**		
i	λ_i	ds_i	H_i(bits)	λ_i	ds_i	H_i(bits)
1	9.3464	0.9887	2.2407	4.8924	0.9599	1.6082
2	3.8674	0.9373	1.3849	3.7701	0.9343	1.3611
3	2.3952	0.8516	0.9538	2.8155	0.8880	1.0945
4	2.1153	0.8173	0.8500	2.1866	0.8270	0.8773
5	1.8392	0.7718	0.7388	1.8409	0.7722	0.7395
6	1.3018	0.6289	0.4957	1.5731	0.7122	0.6227
7	1.1935	0.5875	0.4428	1.1119	0.5528	0.4024
8	1.0360	0.5177	0.3649	0.8463	0.4174	0.2701
9	0.9887	0.4943	0.3409	0.7600	0.3661	0.2280
10	0.7126	0.3368	0.2053	0.5932	0.2603	0.1508
Total		7.4065	8.1127		6.9370	7.3438

U.S. Standard Atmosphere Profile						
	Full **B**			Diagonal **B**		
i	λ_i	ds_i	H_i(bits)	λ	ds_i	H_i(bits)
1	6.8239	0.9790	1.9311	3.8779	0.9376	1.3875
2	3.9118	0.9387	1.3957	3.7279	0.9329	1.3506
3	2.1337	0.8199	0.8571	2.6102	0.8720	1.0279
4	2.0343	0.8054	0.81834	2.2082	0.8298	0.8855
5	1.8505	0.7740	0.7436	1.6802	0.7384	0.6705
6	1.2724	0.6182	0.4814	1.4527	0.6785	0.5673
7	1.1088	0.5515	0.4009	1.1054	0.5499	0.3992
8	0.9933	0.4967	0.3432	0.8594	0.4248	0.2766
9	0.8646	0.4278	0.2791	0.6180	0.2764	0.1617
10	0.6838	0.3186	0.1918	0.5627	0.2405	0.1376
Total		7.1717	7.6779		6.7366	6.9971

3. Averaging Kernel Matrix

As discussed in Chapter II, the trace of the averaging kernel matrix **A** from (2.20) is another way to calculate the total degrees of freedom for signal (ds_i). The diagonal of **A** is a measure of the number of degrees of freedom for signal per level and its reciprocal, the number of levels per degree of freedom, is a measure of vertical resolution. In contrast to the single number provided by total ds_i, the diagonal of **A** provides an estimate of which level of the atmosphere the satellite information is the greatest. The vertical resolution for this theoretical T and $\log_e Q$ retrieval is shown in Figs. 4.2a-d. Comparison is shown for H linearized about the clear sky EPAC Profiles 1A and 1B, cloudy sky Profiles 2A1 and 2B2, and the U.S. Standard Atmosphere (Profile 3). These results are calculated for (2.20) using covariance matrices $\mathbf{B_N}$ (Figs. 4.2a,c) and $\mathbf{B_C}$ (Figs. 4.2b,d).

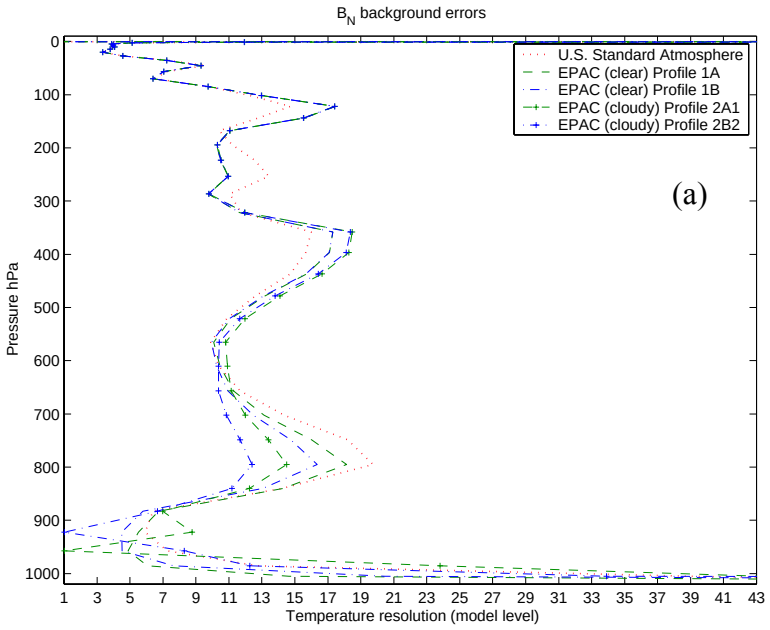

Figure 4.2. Vertical resolution of theoretical (a,b) T, and (c,d) $\log_e Q$ retrievals calculated as the reciprocal of the diagonal elements of **A**. H linearized about U.S. Standard Atmosphere, EPAC (clear) Profiles 1A, 1B and EPAC (cloudy) Profiles 2A1, 2B2. Results shown for **A** calculated with respect to (a,c) $\mathbf{B_N}$ and (b,d) $\mathbf{B_C}$.

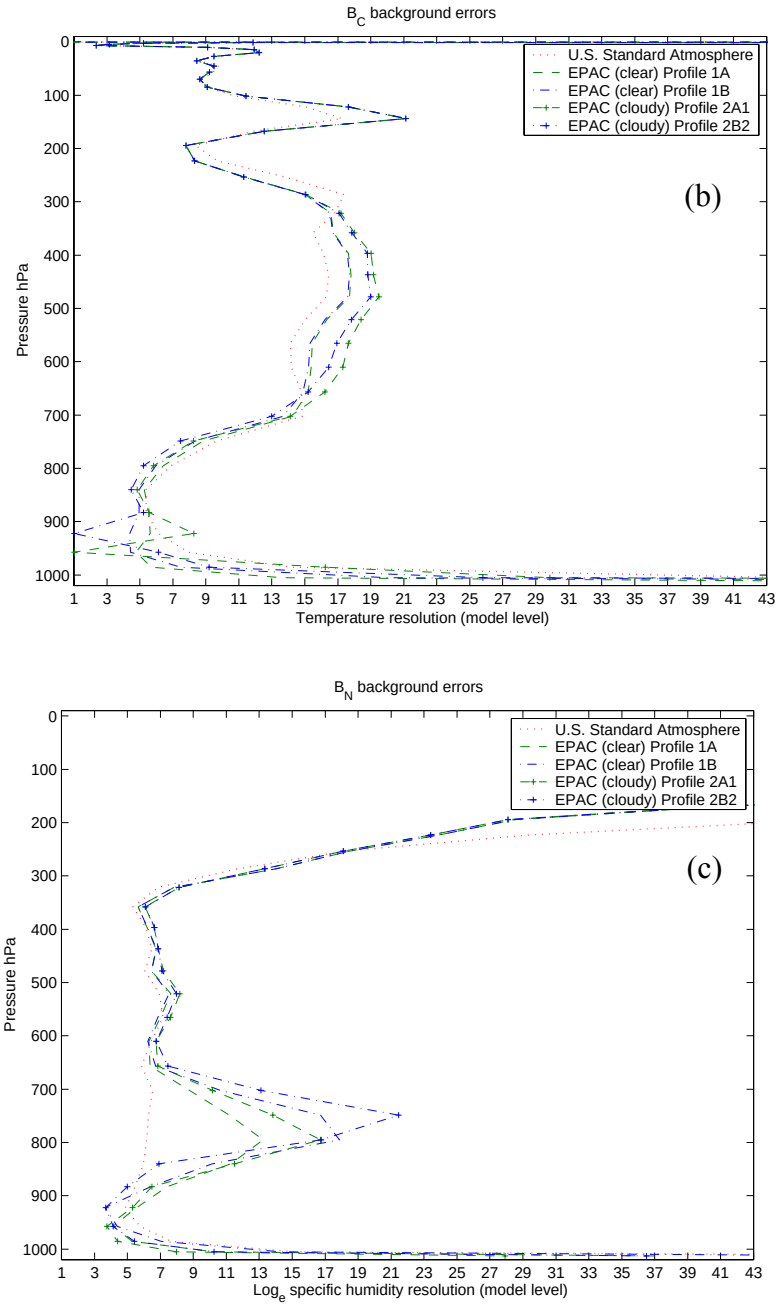

Figure 4.2. Continued.

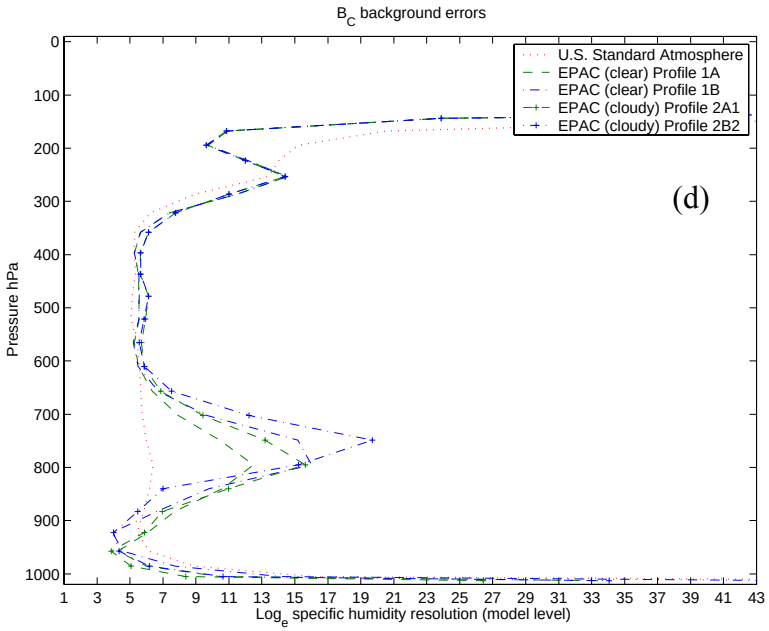

Figure 4.2. Continued.

Vertical resolution of approximately one model level per degree of freedom (or conversely one degree of freedom per level) is indicated for T at the cloud-tops (just below 900 hPa) for the cloudy profiles in Figs. 4.2a-b. Without cloud, the low-level T vertical resolution is approximately four to six levels (~ 100 hPa) per ds_i. For $\log_e Q$ (Figs. 4.2c-d), low-level vertical resolution of approximately 4 levels per ds_i and is slightly greater for the EPAC profiles than the U.S. Standard Atmosphere profile (Profile 3). However, above the EPAC boundary layer, vertical resolution decreases rapidly in contrast to Profile 3. With respect to the two background error covariance matrices, the largest difference in ds_i (resolution) occurs for T between 700 and 900 hPa (Figs. 4.2a-b).

These results are consistent with the PCA / SVD analysis in that the vertical distribution of the diagonal elements of **A** indicates there is independent low-level temperature and humidity information. The vertical resolution of 4 to 5 model levels per ds_i for the EPAC clear sky cases is inadequate to independently resolve the MABL temperature inversion. However, as previously hypothesized, ATOVS may provide enough information to adjust the background profile toward the true atmospheric state.

B. EFFECTIVE BACKGROUND ERROR

As discussed by Garand (2000) and English et al. (2000), effective background error, defined as $\mathbf{H\ B\ H}^T$, is the projection of the background error covariance matrix **B** into *m* x *m* radiance space. Via the Jacobian matrix **H**, effective background error is also a function of the background state vector profile and is therefore related to the synoptic situation. This projection into radiance space allows for a direct comparison with the ATOVS observation error matrix (**R**) and provides a channel-by-channel estimation of information.

These two matrices are components of the Kalman gain (or weight) matrix, $\mathbf{K} = \mathbf{BH}^T\ [\mathbf{H\ B\ H}^T + \mathbf{R}]^{-1}$. Through the inverse, as $[\ \mathbf{H\ B\ H}^T + \mathbf{R}]$ becomes smaller, **K** becomes larger and the retrieval error covariance **S** in (2.16) becomes smaller. In terms of the general analysis problem (e.g., Daley 1991) and the NRL Monterey 1DVAR algorithm (2.14), **K** is weight-matrix for the innovation vector $[\mathbf{y}^o - \mathrm{H}(\mathbf{x})]$. If **K** increases, the innovation is given more weight in the analysis. As can be seen from this relationship, the size of **K** depends on the relative magnitude of $\mathbf{HBH}^T$ and **R**. According to Garand (2000), "one should be satisfied when [the observation error standard deviation] becomes significantly (up to an order of magnitude) lower than [the effective background error standard deviation]." However, he also states that larger reductions in observation error provide no significant improvement if the retrieval becomes unconstrained. In this case, convergence to the correct solution may be difficult to achieve.

Figs. 4.3 shows the effective background error calculated with respect to the background error covariance matrices $\mathbf{B_N}$ (Fig. 4.3a) and $\mathbf{B_C}$ (Fig. 4.3b) compared to the ATOVS observation standard deviations of error $(R_{ii})^{½}$. The forward model (H) was linearized about clear and cloudy sky idealized EPAC profile (see Fig. 3.2) and the U.S. Standard Atmosphere (Profile 3).

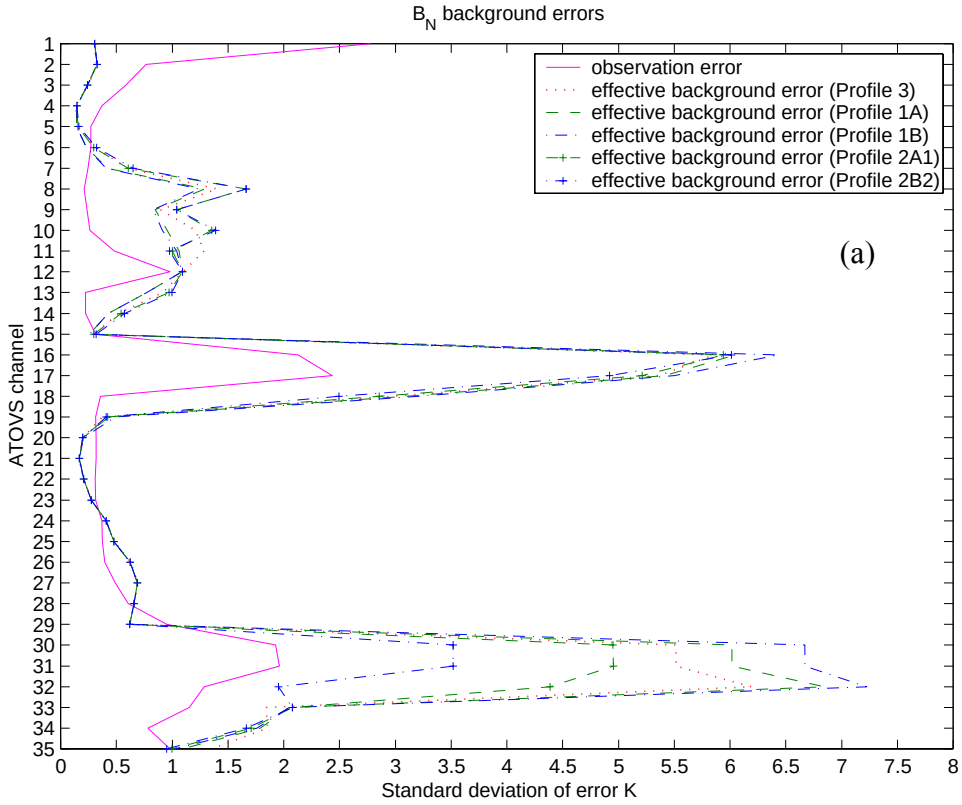

Figure 4.3. Square root of the diagonal elements of effective background error ($\mathbf{H}\,\mathbf{B}\,\mathbf{H}^{T}$) and observation error (**R**). Results are calculated with respect to background error covariance (a) $\mathbf{B_N}$, and (b) $\mathbf{B_C}$. HIRS/3 channels are 1-15, AMSU-A channels 1 - 15 are shown as ATOVS channels 16-30, and AMSU-B channels 1 –5 are shown as ATOVS channels 31-35. Comparisons are made for H linearized about profiles described in legend.

According to Healy and Eyre (2000), channels with large corresponding effective background error, the retrievals are nearly insensitive to the "background-error level" and the solution is determined primarily by the satellite observations. The relative magnitude of the effective background error to observation error for the AMSU window channels (AMSU-A channels 1, 2, 3 and 15 and AMSU-B channels 1 and 2) suggests there is a large amount of humidity information available from these channels. For the cloudy sky cases the effective background error becomes smaller for AMSU-A channel 15 and AMSU-B channels 1 and 2 as LWP increases, which indicates that less information will be available from these channels. In contrast, the effective background error (and

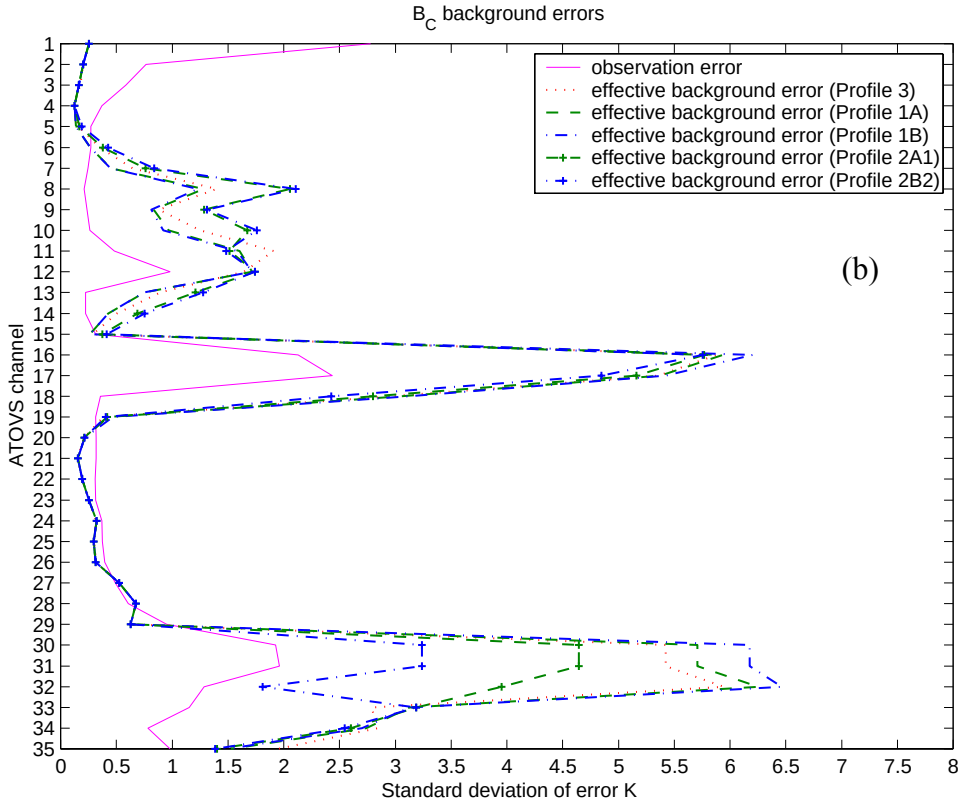

Figure. 4.3. Continued.

expected information) associated with HIRS/3 channel 8 (Figs. 4.3a-b) is larger for the cloudy sky EPAC profiles. The effective background errors are slightly smaller for the AMSU-B surface channels, and larger for the cloudy sky HIRS/3 surface channels when calculated with respect to $\mathbf{B}_C$ (Fig. 4.3b).

C. RETRIEVAL ERROR SENSITIVITY

In this section, (2.23) is used to quantify the effect of surface, cloud, and profile background errors on profile temperature (T) and $\log_e$ specific humidity ($\log_e Q$) theoretical retrieval performance. As discussed in Chapter II.E, theoretical retrieval performance is expressed as percent improvement with respect to a given background state vector and its associated errors. The background state vectors used in this retrieval error sensitivity study are the representative summertime EPAC clear sky profiles and the U.S. Standard Atmosphere (see Chapter III.C). Unless otherwise indicated, cloud free profiles are known to be cloud free. Results are presented in terms of both $\mathbf{B}_N$ and $\mathbf{B}_C$

where appropriate. Again, $\mathbf{B_N}$ is calculated using the globally averaged short-term forecast errors for NOGAPS from the NRL 1DVAR scheme, and $\mathbf{B_C}$ represents the structure of the short-term forecast errors for COAMPS EPAC (see Chapter III.A).

Implications of ATOVS channel selection, observation error and inter-level error correlations on theoretical retrieval performance are also discussed. These are important considerations since there is a complex relationship between actual information content, individual channel sensitivity (English 1999) and vertical correlations of error. In addition to the effects on profile variables, this research calculates the theoretical retrieval performance for T_s and P_s.

The results of (2.23) are estimates of what improvements can theoretically be made with the 1DVAR retrieval scheme. Again, in the linear case, **S** is equal to the retrieval error and for the weakly non-linear case it is a good approximation if it varies slowly with the atmospheric state **x**. Linear behavior is assumed for atmospheric temperature retrieval errors; however, it does not hold true for water vapor. The linear estimates provided by (2.15) and (2.16) are optimistic and more realistic error estimates are obtained through nonlinear Newtonian iteration of (2.14). As previously mentioned, **S** was calculated in (2.16) using the full *215* x *215* **B** covariance matrix and *215* x *35* **H** matrix. Also as previously discussed, (2.23) only compares the diagonal elements (variances) of **S** and **B** and the covariance information is not directly included in this comparison.

1. Background, Background Error, and Inter-Level Correlations of Error

T and $\log_e$ *Q* retrieval performance is measured with respect to a particular background state vector and assigned background errors. In addition, retrieval performance (*P*) is sensitive to the strength of the inter-level correlations of error included within the background error covariance matrix. The percent improvement in *T* and $\log_e$ *Q* retrieval performance is calculated with respect to background state vector and choice of background error covariance matrix (i.e., $\mathbf{B_N}$ versus $\mathbf{B_C}$) is shown in Figs. 4.4 and 4.5. These results are calculated for H linearized about three clear sky (EPAC Profiles 1A and 1B and the U.S. Standard Atmosphere (Profile 3)), and two cloudy sky

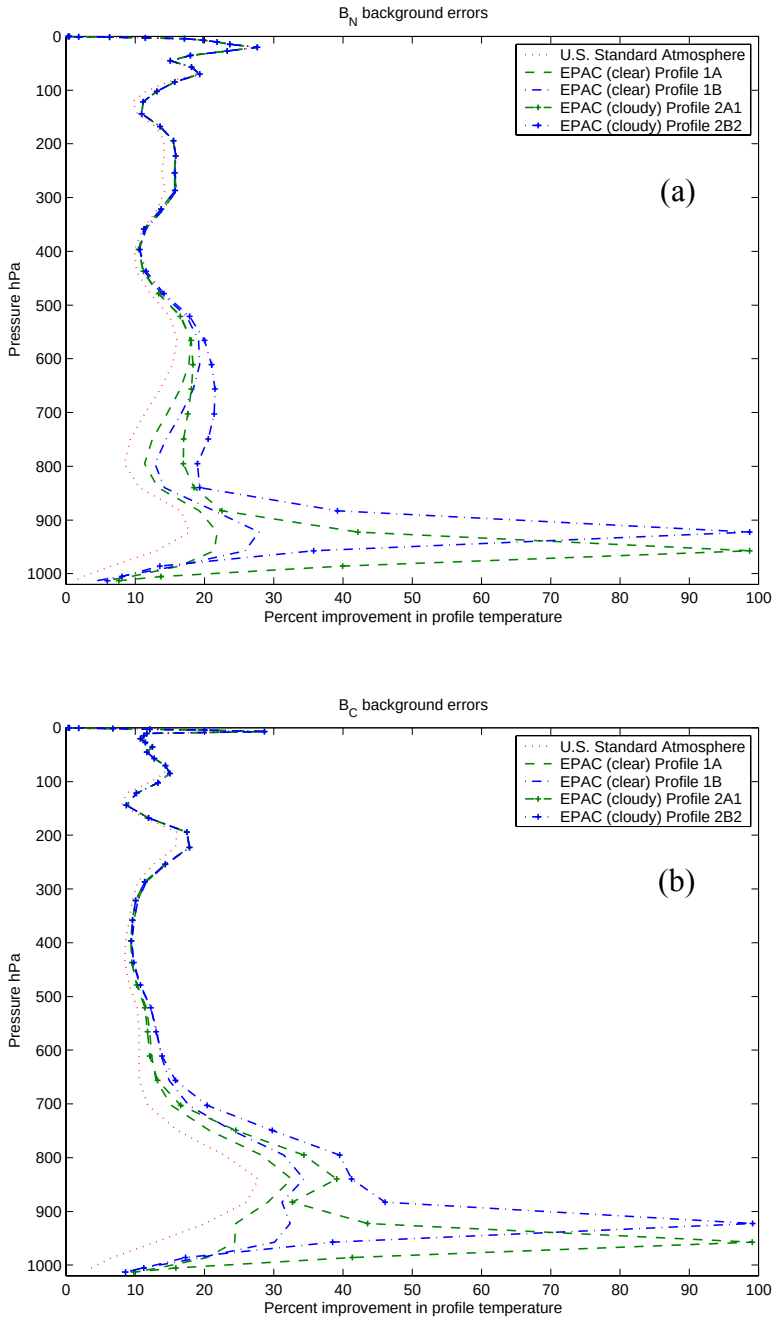

Figure 4.4. Theoretical *T* retrieval performance ($P = 100[1-(S_{ii}/B_{ii})]$) as function of background state vector (see legend) and background error covariance matrix (a) $\mathbf{B_N}$, and (b) $\mathbf{B_C}$.

(EPAC Profiles 2A1 and 2B2) background state vectors. The 35 ATOVS channels and associated instrument and forward model errors listed in Table 3.4 were used to calculate retrieval performance.

The theoretical *T* retrieval performance calculated with respect to U.S. Standard Atmosphere and $\mathbf{B_N}$ (Fig. 4.4a) shows that ATOVS-derived information reduces the profile retrieval error variance (i.e., increases *P*) by less than 20%. More satellite-derived information is available from the warmer EPAC temperature profiles below approximately 500 hPa. The largest increases in *P* of approximately 5 to 10% are below 900 hPa, the RTTOV-6 pressure levels corresponding to the top of the respective EPAC profile MABL. In contrast to these relatively small increases in theoretical retrieval performance, the ATOVS derived information is very large ($P \rightarrow 100\%$) at the specified cloud-top for EPAC Profiles 2A1 and 2B2. These large reductions in retrieval error variance are consistent with the values calculated from the diagonal elements of **A** (Section IV.A), which showed approximately one ds_i at the specified cloud-top pressure (P_{CT}). According to Eyre (1989a), cloudy IR radiances, when treated optimally, should theoretically improve the *T* retrieval at and above cloud-top. This effect is observed for the two cloudy profiles where retrieval performance is larger above cloud-top than for the corresponding clear sky EPAC profiles. This indicates that ATOVS-derived information may be able to improve the *T* retrieval above the cloudy EPAC MABL.

Results presented in Fig. 4.4b include a comparison of theoretical *T* retrieval performance calculated with respect to the COAMPS EPAC specific background error covariance matrix, $\mathbf{B_C}$. Overall, the low-level retrieval error variance is reduced more with respect to the larger COAMPS EPAC background errors (see Fig. 3.1). Clear sky *T* retrieval performance is improved approximately 25 – 30% over the background and the two cloud sky profiles show additional increases in retrieval performance above cloud-top.

$\text{Log}_e\ Q$ theoretical retrieval performance calculated with respect to the five background state vectors and two background error covariance matrices is shown in Fig. 4.5. Results using $\mathbf{B_N}$ (Fig. 4.5a) indicate relatively large reductions in retrieval error variances near 900 hPa for all profile types. Low-level retrieval performance is

approximately 20% larger with the EPAC background state vectors than for the U.S. Standard Atmosphere. This difference in low-level $\log_e Q$ retrieval P is consistent with the larger humidity values and associated steeper gradient of the representative EPAC environment. Above the EPAC MABL, retrieval performance rapidly decreases to a minimum near 750 hPa. However, at this level, more humidity information is expected to be available from the U.S. Standard Atmosphere profile. These differences are again consistent with the vertical humidity structure of these background profiles (see Fig. 3.2). The results (Fig. 4.5a) also show that, unlike profile temperature, low-level $\log_e Q$ retrieval performance is not greatly affected by cloud liquid water when the cloud elements are perfectly known.

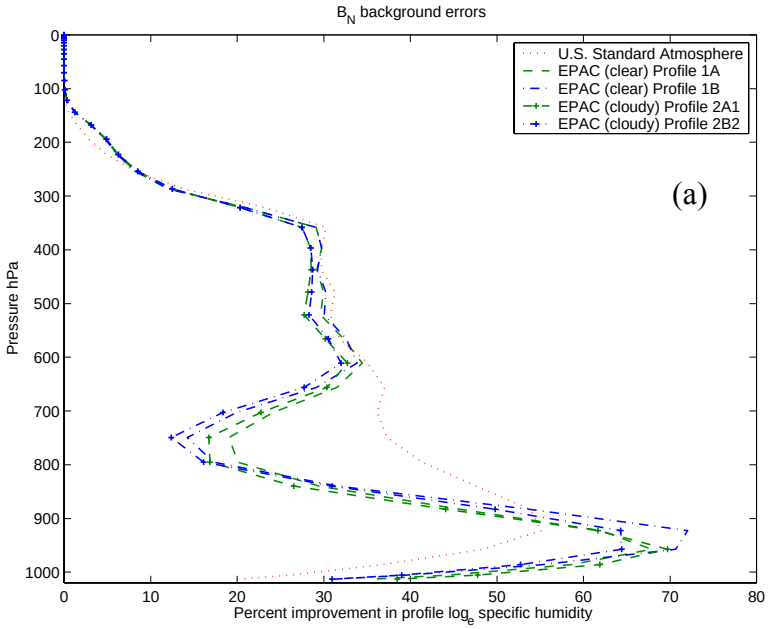

Figure 4.5. As in Fig. 4.4, except for $\log_e Q$ retrieval performance (P).

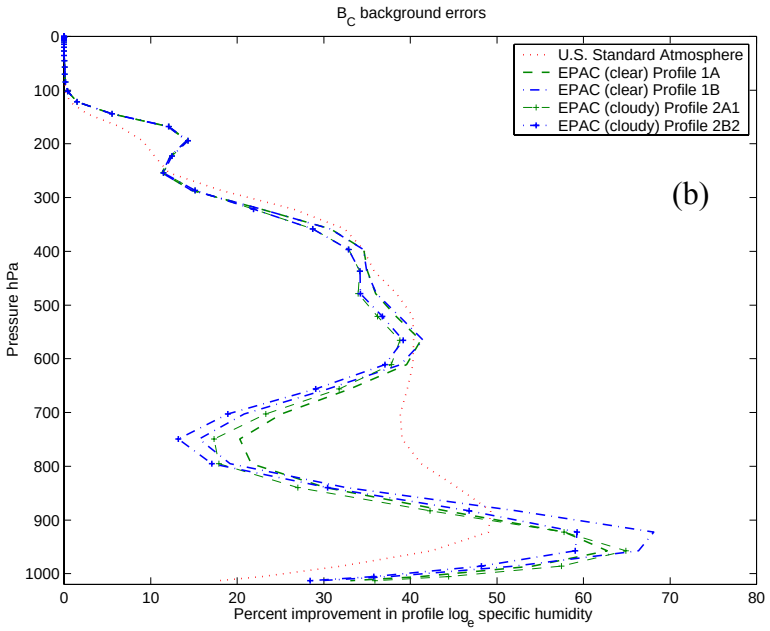

Figure 4.5. Continued.

Low-level $\log_e Q$ errors are similar for the two background error covariance matrices and therefore, the relative low-level retrieval performance is roughly unchanged. At upper-levels the $\log_e Q$ retrieval performance (Fig. 4.5b) increases between 350 and 650 hPa using larger errors associated with the larger errors in $\mathbf{B_C}$.

These results demonstrate that at least theoretically, low-level T and $\log_e Q$ information can be obtained from ATOVS within the clear and cloudy sky summertime EPAC environment. The smaller errors associated with $\mathbf{B_N}$ may over-constrain the low-level T, and upper-level $\log_e Q$ retrieval problem. However, caution should be exercised when making direct comparisons using different **B** matrices since, these covariance matrices are calculated for different geographic regions, synoptic situations, and record lengths.

Theoretical retrieval error $(S_{ii})^{1/2}$ and corresponding retrieval performance for P_s and T_s as a function of background state vector (Profiles 1B, 2B2 and 3) and background error ($\mathbf{B_N}$) were calculated and the results are listed in Table 4.3. These values assume perfect knowledge of all cloud parameters. T_s and P_s background errors are set to 1.57 K

and 3.38 hPa, respectively. Under clear sky conditions there are very large gains for T_s and relatively large gains for P_s. The satellite-derived information for these surface parameters is much less using the cloudy sky EPAC Profile 1B.

Table 4.3. Background $(B_{ii})^{½}$ and theoretical retrieval $(S_{ii})^{½}$ errors and percent improvement (P) for surface pressure (P_s) and radiative skin temperature (T_s) as a function of selected background statevectors. Background profiles are shown in Fig. 3.2 and described in the text. Results were calculated with cloud errors set to zero in $\mathbf{B_N}$.

Surface parameter	Background error $(B_{ii})^{½}$	Theoretical retrieval error $(S_{ii})^{½}$			Percent improvement $P = 100[1 - (S_{ii} / B_{ii})]$		
		Profile 1B	Profile 2B2	Profile 3	Profile 1B	Profile 2B2	Profile 3
P_s	3.38 hPa	2.95 hPa	3.11 hPa	2.88 hPa	24 %	15 %	27 %
T_s	1.57 K	0.31 K	1.48 K	0.23 K	96 %	11 %	98 %

As described in Chapter III.A, the inter-level correlations of error between surface array elements and profile elements are zero for the NRL Monterey 1DVAR scheme, which in effect decouples T_s, T_{2m}, and T errors. Using COAMPS EPAC background errors, the effect of coupling surface and atmospheric profile errors on T and $\log_e Q$ retrieval performance is shown for selected cases in Fig. 4.6. The uncoupled case assumes no inter-level correlation of error between $<T_s\ T_{2m}>$, $<T_s\ T>$, and $<T_{2m}\ T>$. In contrast, the "strongly coupled" case assumes a near perfect (i.e., 1:1) inter-level correlation of error between $<T_s\ T_{2m}>$ and inter-level correlations of error of 91% for $<T_s\ T_{43}>$ and 94% for $<T_{2m}\ T_{43}>$. This research uses the inter-level correlations of error listed in Table 3.1 and is shown as the "weakly coupled" in Fig. 4.6.

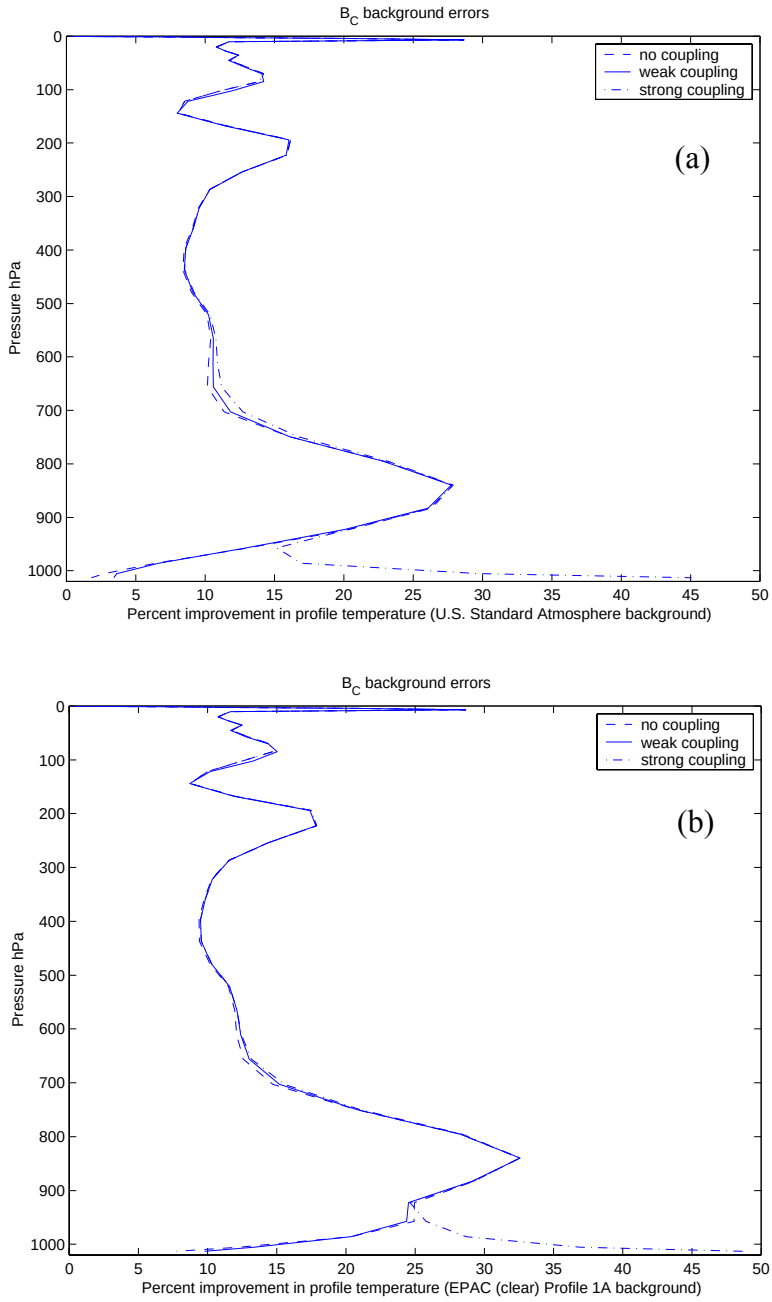

Figure 4.6. Theoretical *T* retrieval performance (*P*) as a function of surface and atmosphere inter-level correlations of error calculated with respect to $\mathbf{B_C}$ and background state vector (a) U.S. Standard Atmosphere, (b) clear sky EPAC Profile 1A, and (c) cloudy sky EPAC Profile 2B2. The "no coupling" case assumes inter-level correlations of error are zero between $<T_s\ T_{2m}>$, $<T_s\ T>$, and $<T_{2m}\ T>$. The "weakly coupled" case includes the inter-level correlations of error shown in Table 3.1. The "strongly coupled" case assumes a near 1:1 $<T_s\ T_{2m}>$ inter-level correlation of error and large $<T_s\ T>$, $<T_{2m}\ T>$ error correlations.

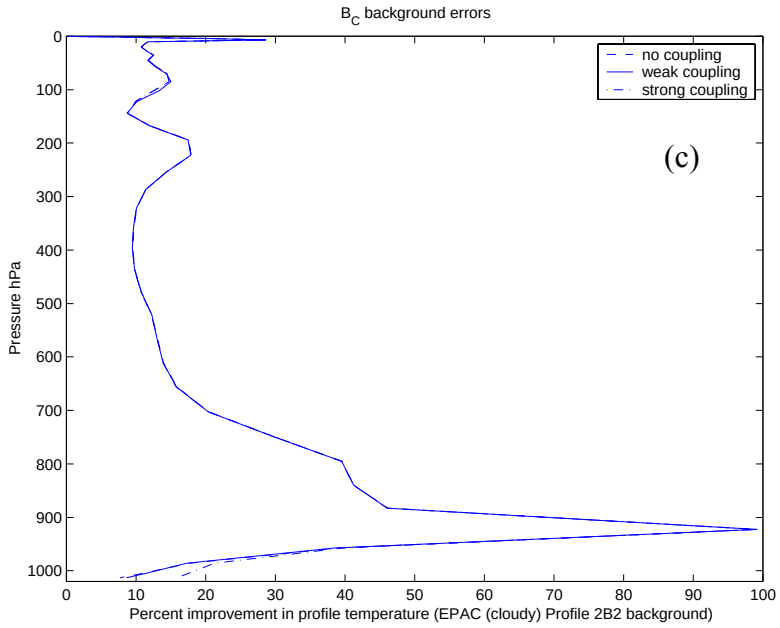

Figure 4.6. Continued.

These findings reveal the relationship between information and the inter-level correlations of error prescribed within the background error covariance matrix, $\mathbf{B}_C$. Strong coupling of the surface and atmosphere errors results in relatively large gains in near-surface T theoretical retrieval performance (Figs. 4.6a-b) for the clear sky profiles. In these cases, the satellite-derived surface information (T_s) is able to reduce the low-level profile retrieval errors. Conversely, less satellite-derived information (Fig. 4.6c) is available for the cloudy sky case resulting in only minor increases in near-surface retrieval performance.

2. ATOVS Instrument and AMSU Window Channel Selection

Theoretical T and $\log_e Q$ retrieval performance as a function of ATOVS instrument (i.e., HIRS/3, AMSU-A, and AMSU-B) is compared in Figs. 4.7 and 4.8. The forward model (H) was linearized about the clear sky EPAC Profile 1A, cloudy sky EPAC Profile 2B2, and the U.S. Standard Atmosphere (Profile 3). All results are calculated with respect to $\mathbf{B}_N$ with cloud background errors set to zero.

The largest overall improvement in theoretical *T* retrieval performance (or correspondingly, the largest decrease in theoretical retrieval error) is observed when all three ATOVS instruments are selected. For both EPAC clear (Figs. 4.7a-b) and cloudy sky (Fig. 4.7c) profiles, HIRS/3 contributes the most total *T* information below 300 hPa with AMSU-A providing most of the temperature information above 300 hPa. These results should not be surprising considering the distribution of the ATOVS weighting functions (Fig. 2.3). An interesting finding of this research is the critical role of HIRS/3 channels in providing the majority of clear sky *T* information (Figs. 4.7a-b) between approximately 800 hPa and the surface. The AMSU channels contribute significantly less information at these levels.

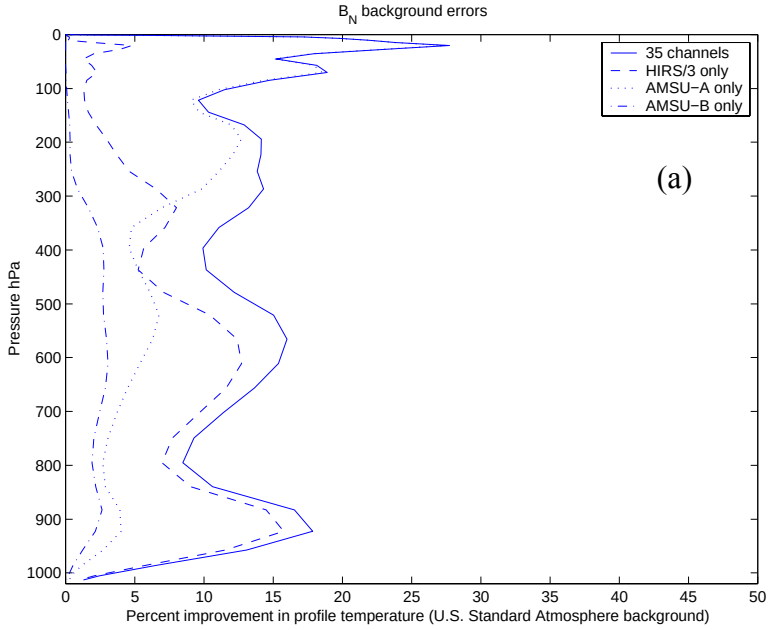

Figure 4.7. Theoretical *T* retrieval performance (*P*) as a function of ATOVS instrument (channels) calculated with respect to $\mathbf{B_N}$ and background state vector (a) U.S. Standard Atmosphere, (b) clear sky EPAC Profile 1A, and (c) cloudy sky EPAC Profile 2B2. The 35-channel curve (solid line) includes the 15 HIRS/3 (dashed), 15 AMSU-A (dotted), and 5 AMSU-B (dash-dot) channels used in this study.

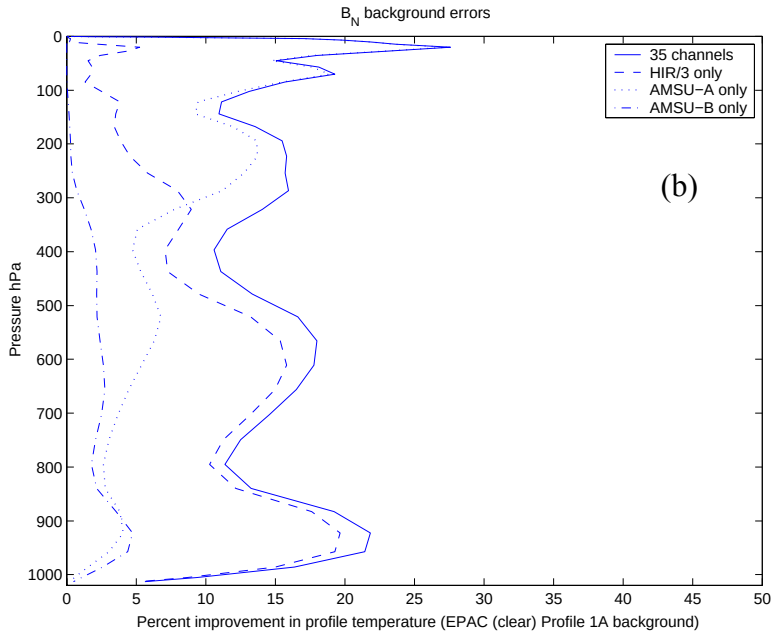

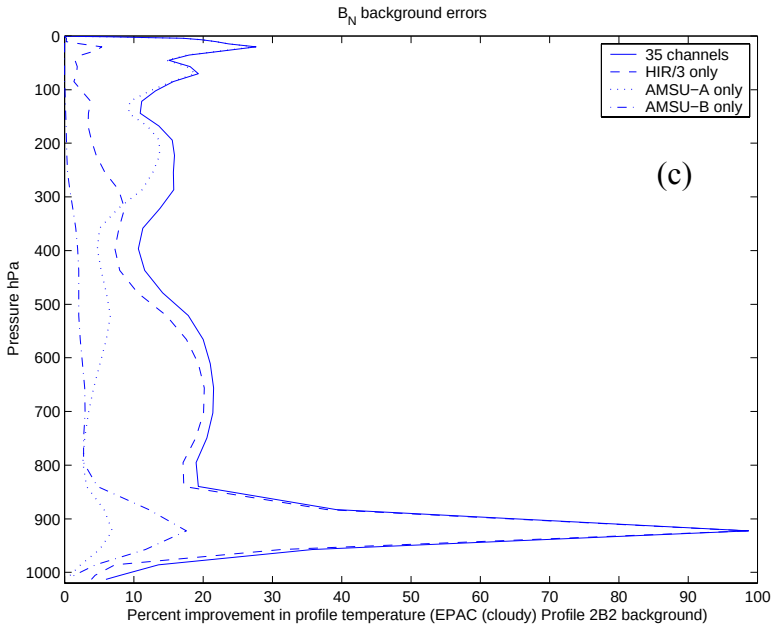

Figure 4.7. Continued.

The large increase in T retrieval performance ($P \rightarrow 100\%$) at the specified P_{CT} is consistent with the corresponding diagonal element of **A** (i.e., $ds_i \approx$ unity at cloud-top), and this information is derived almost exclusively from HIRS/3 surface channels. Temperature profile (T) information from the humidity sounder AMSU-B is expected to be small; however, as suggested by the structure of the Jacobians (Fig. 3.4b), more T information is available from this instrument with increasing LWP.

Humidity information from the lower atmosphere is derived primarily from the AMSU surface sensitive channels 1-4 and 15-17. The large increase in theoretical retrieval performance (Figs. 4.8a-c) observed increase near 900 hPa corresponds to the large water vapor gradient associated with the representative EPAC background state vectors (see Figs. 3.2b,d). HIRS/3 channels 10 –12 and AMSU-B sounding channels 3 – 5 provide humidity information in the mid-, to upper atmosphere.

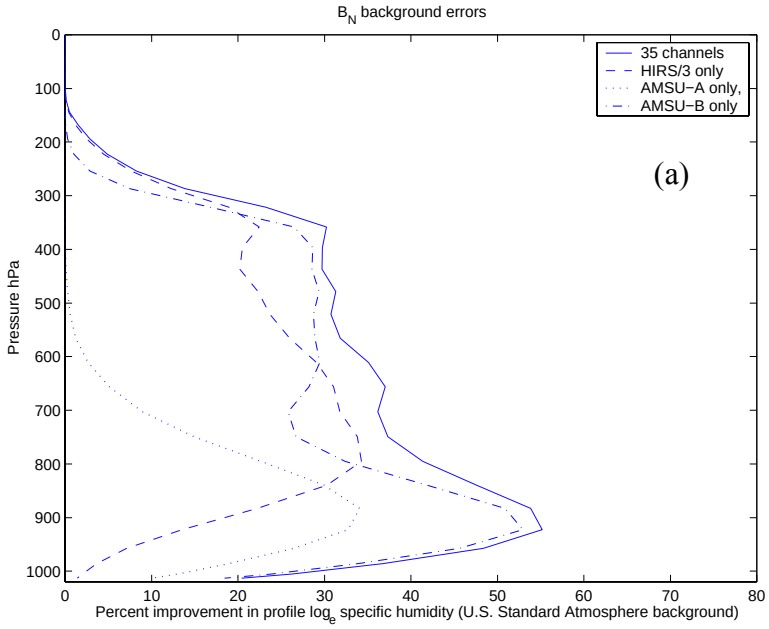

Figure 4.8. As in Fig. 4.7, except for theoretical $\log_e Q$ retrieval performance.

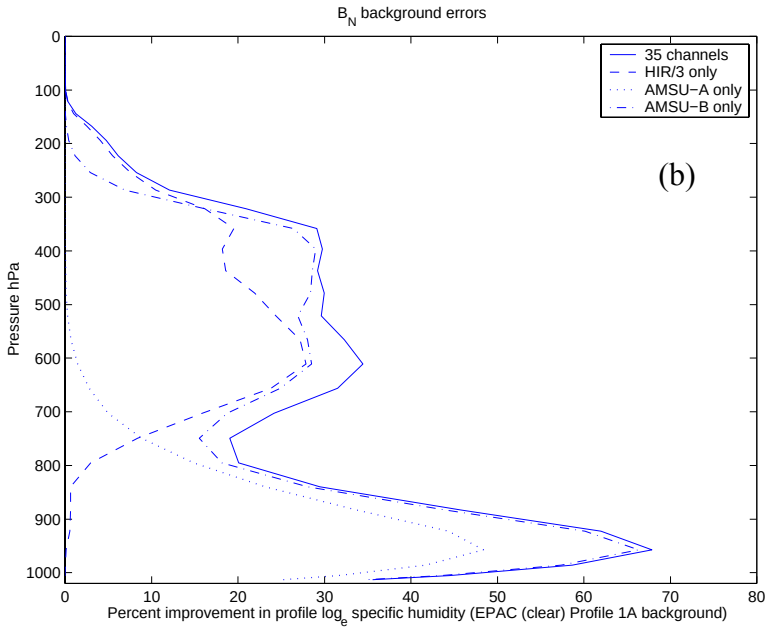

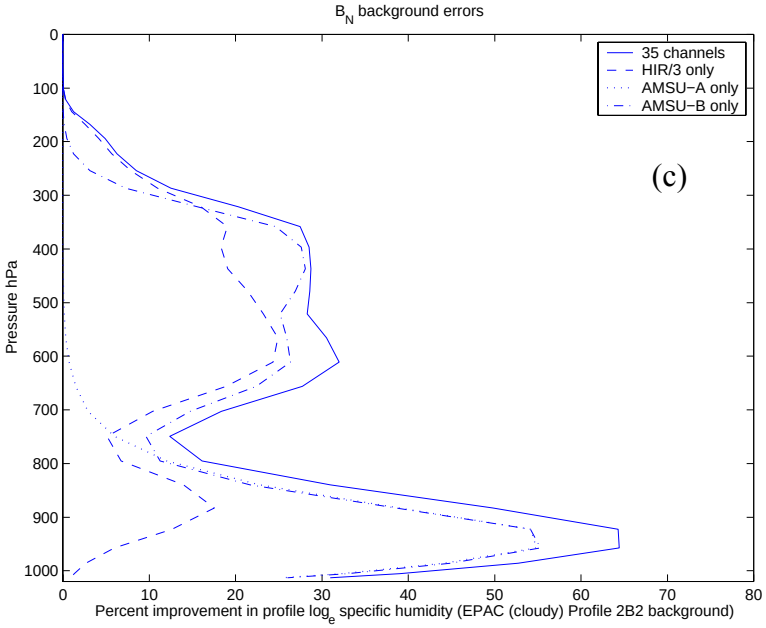

Figure 4.8. Continued.

For the clear sky profiles, the HIRS/3 channels provide little to no $\log_e Q$ information (Figs. 4.8a-b) below 800 hPa. However, for cloudy sky EPAC Profile 2B2, $\log_e Q$ retrieval performance (Fig. 4.8c) for HIRS/3 channels is increased by approximately 20% above the specified P_{CT}. Similar to the results discussed for T, this increase in performance suggests that cloudy IR radiances, when treated optimally, may also improve the humidity retrieval above the cloud top.

The contribution of individual AMSU window channels to clear sky $\log_e Q$ retrieval performance is shown in Fig. 4.9. These channels are AMSU-A channels 1 – 4, 15 and AMSU-B channels 1 and 2. As a reminder, these two AMSU-B channels are also referred to as AMSU channels 16 and 17. Clear sky EPAC Profiles 1A and 1B, and U.S. Standard Atmosphere are included here for comparison. Near-surface $\log_e Q$ retrieval performance (Figs. 4.9a-c) increases for all profile types when all AMSU window channels are selected. These results show the majority of the low-level, boundary layer

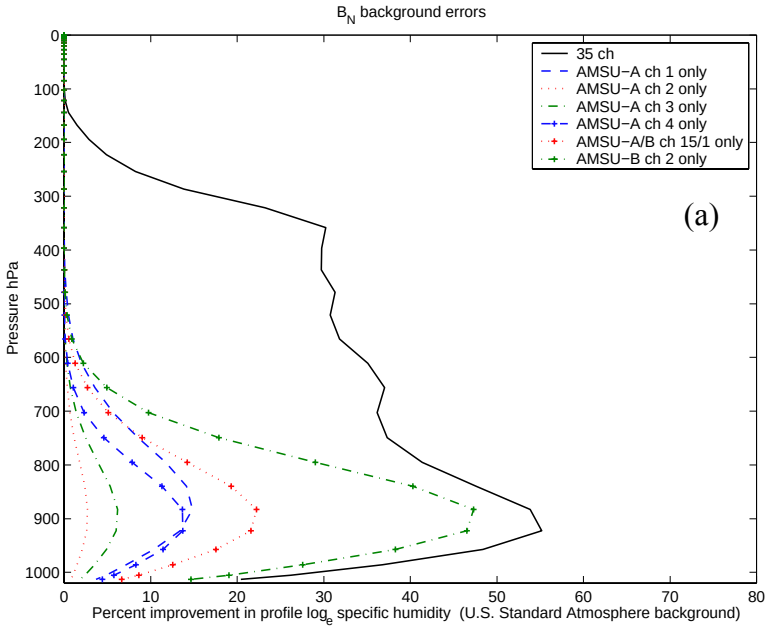

Figure 4.9. Theoretical $\log_e Q$ retrieval performance (P) as a function of AMSU-A channels 1-4, 15 and AMSU-B channels 1 and 2. Calculated with respect to $\mathbf{B_N}$ and background state vector (a) U.S. Standard Atmosphere, (b) clear sky EPAC Profile 1A, and (c) clear sky EPAC Profile 1B.

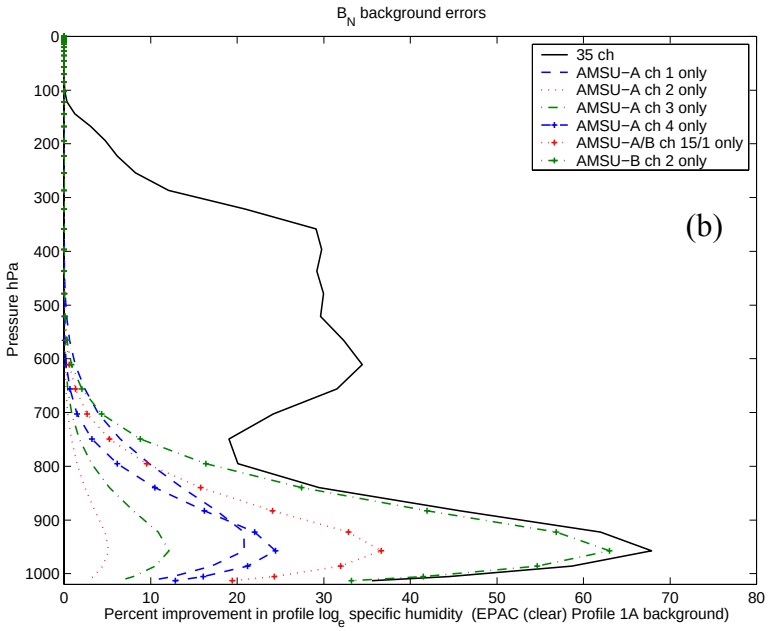

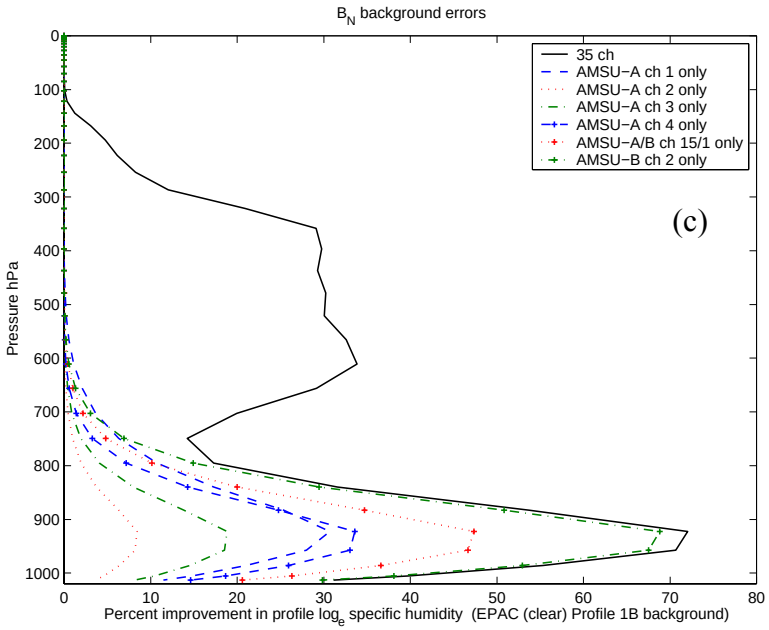

Figure 4.9. Continued.

humidity information is derived from AMSU-B channel 2 (150.0 GHz). AMSU-A/B channels 15/1 also provide a good quantity of information (Figs. 4.9b-c) for the representative EPAC environment. AMSU-A channels 2 or 3 alone increase retrieval performance by less than 20%. However, larger contributions to total information are provided by AMSU-A channels 1 and 4. Above approximately 700 hPa, the humidity information is derived from AMSU-B sounding channels 3 –5 and HIRS/3 channels 10 – 12 (not shown).

As discussed in Chapter II.E, the retrieval is basically independent of the background as the ratio $S_{ii} / B_{ii} \rightarrow$ zero. As the water vapor sensitive channels are added, more information is expected to be available from the profiles that contain more water vapor (e.g., EPAC Profile 1B), since the Jacobians of **H** are calculated with respect to $\log_e Q$ and are proportional to Q (i.e., $\partial R / \log_e Q = Q \partial R / \partial Q$, where R is discrete form of the radiative transfer equation).

The results of this theoretical retrieval performance analysis are consistent with the structure of the ATOVS T and $\log_e Q$ Jacobians (Figs. 3.4 and 3.5) and the previous two information methods (Sections A and B). HIRS/3 surface channels provide a large amount of information on cloud-top temperature and the AMSU window channels "bring a lot to the table" in terms of low-level humidity information. The majority of the low-level, boundary layer humidity information is derived from AMSU-B channel 2 with AMSU-A/B channel 15/1 as close second.

3. Observation Error

The results shown in Figs. 4.10 and 4.11 are included in this dissertation in order to demonstrate the relationship between ATOVS observation error (**R**) and T and $\log_e Q$ theoretical retrieval error. As discussed in Chapter III.B, **R** is combination of ATOVS instrument error and forward model error. In this experiment $(R_{ii})^{½}$ corresponding to each of the 35 channels was uniformly increased by three orders of magnitude from 0.01 to 10.0 K. The forward model (H) was linearized about clear sky EPAC Profile 1A, cloudy sky EPAC Profile 2B2, and the U.S. Standard Atmosphere (Profile 3). $\mathbf{B_N}$ was used for this analysis with perfect knowledge of all cloud parameters.

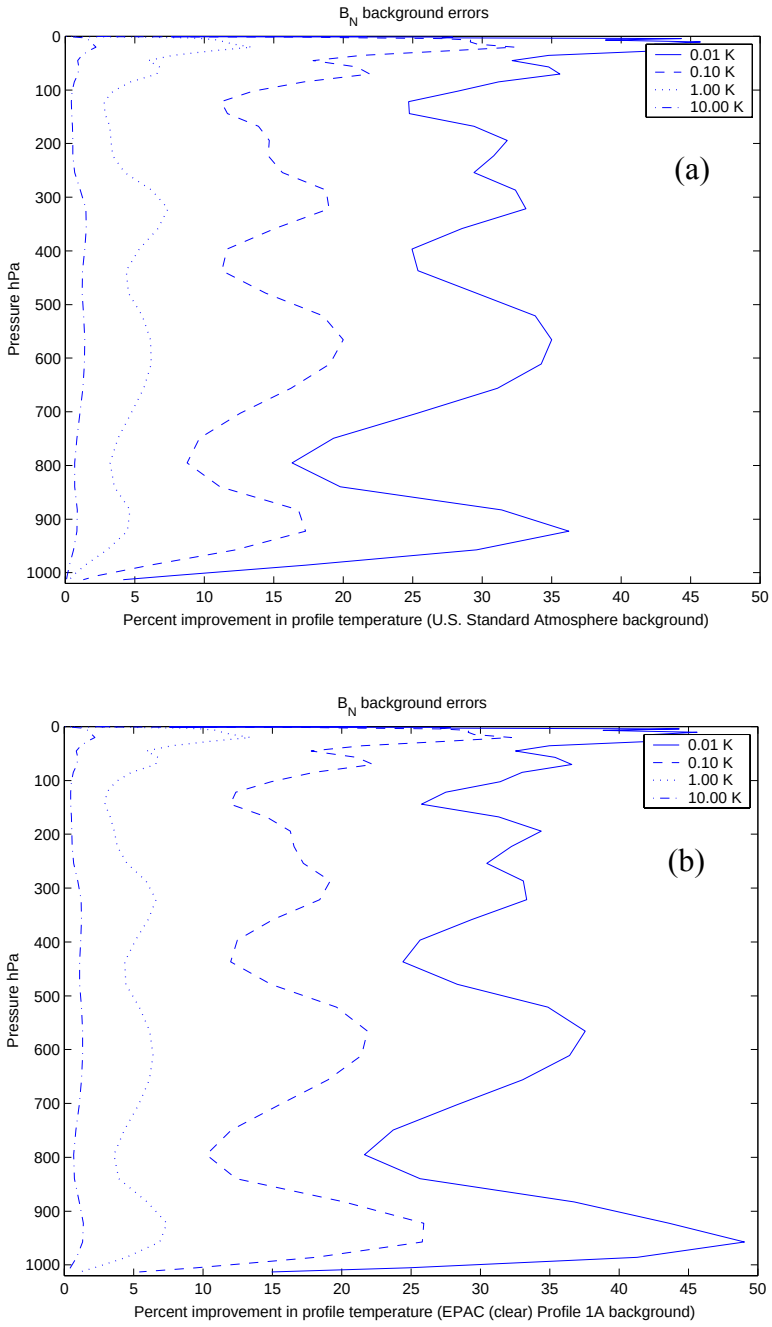

Figure 4.10. Theoretical *T* retrieval performance (*P*) as a function of 0.01, 0.10, 1.00, and 10.0 K observation error $(R_{ii})^{1/2}$. Results are calculated with respect to $\mathbf{B_N}$ and background state vector (a) U.S. Standard Atmosphere, (b) clear sky EPAC Profile 1A, and (c) cloudy sky EPAC Profile 2B2.

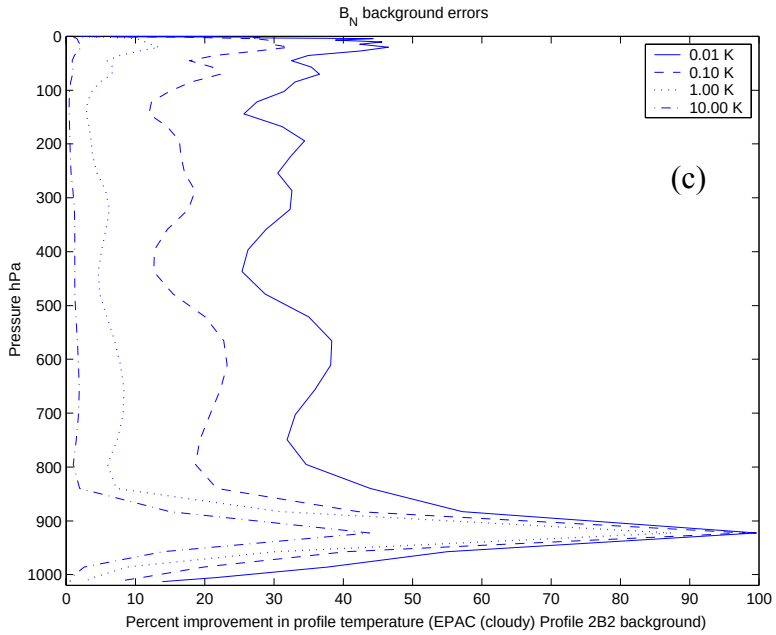

Figure 4.10. Continued.

As $(R_{ii})^{½}$ is increased from 0.01 to 10 K, theoretical *T* retrieval performance (Fig. 4.10a-b) approaches zero for all clear sky background profiles. For these cases the ratio $S_{ii} / B_{ii} \rightarrow$ unity and the ATOVS observations do not provide information to the retrieval. Theoretical *T* retrieval performance (Fig. 4.10c) with H linearized about the cloudy sky profiles still shows approximately 40% improvement with respect to background near cloud-top. This relatively large retrieval performance value at cloud-top is most likely associated with the larger effective background error of HIRS/3 channels 8 (see Fig 4.3).

Results for $\log_e Q$ show retrieval performance (Figs. 4.11a-c) above 700 hPa associated with the HIRS/3 and AMSU-B humidity sounding channels steadily decreases as observation error increases. However, below 900 hPa there is still greater than 50% improvement in $\log_e Q$ retrieval performance for all EPAC profiles.

A probable explanation is that the effective background error covariance matrix ($\mathbf{HBH}^T$) discussed in Section IV.B was found to be relatively large for the AMSU window channels (see Fig 4.3a). This would suggest that even with large observation errors there is still humidity information available from the AMSU window channels.

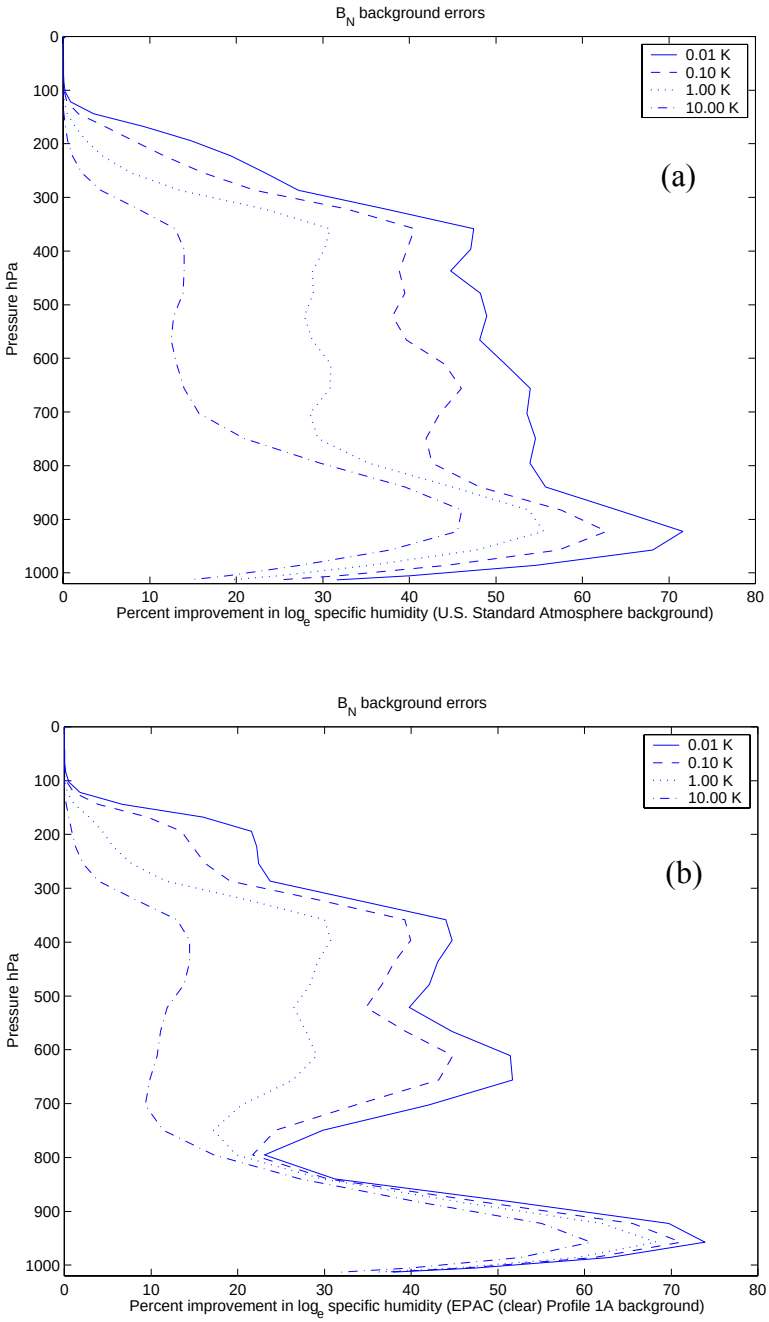

Figure 4.11. As in Fig 4.10, except for theoretical $\log_e Q$ retrieval performance.

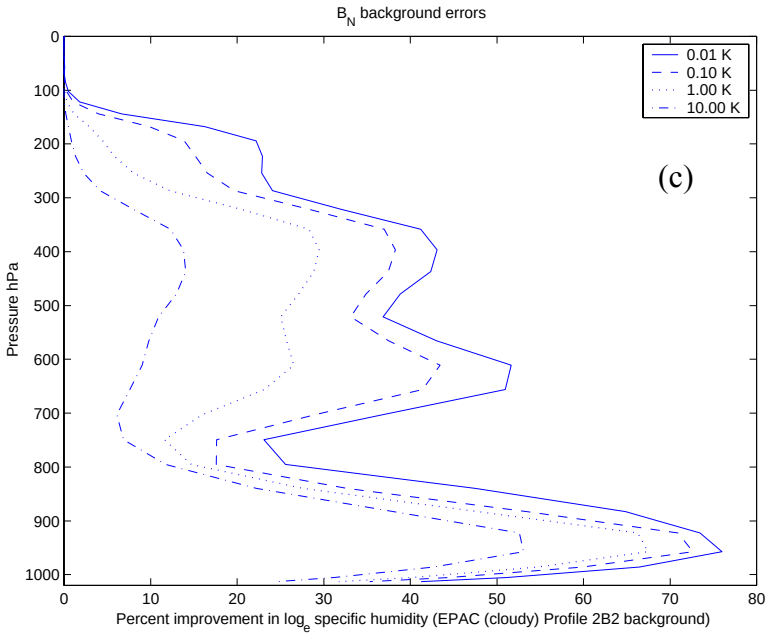

Figure 4.11. Continued.

Within the context of this summertime EPAC case study, the results presented in the previous sub-sections quantified the effects of background state vector, background error, inter-level correlations of error, channels selection, and observation error on T and $\log_e Q$ theoretical retrieval performance. These performance analyses provide a baseline for interpreting the effects of individual background errors. The following sensitivity analyses were conducted in order to determine the effect of individual surface, cloud, and profile errors on T and $\log_e Q$ theoretical retrieval performance.

4. Surface Array Errors

a. Radiative Skin Temperature Error

The T and $\log_e Q$ theoretical retrieval performance are compared for three different T_s errors of 0.0, 1.57, and 3.14 K. These background errors were chosen by: 1) assuming perfect knowledge of T_s, 2) using values listed in Tables 3.2 and 3.3, and 3) doubling these values. The forward model (H) was linearized about clear sky EPAC Profiles 1A and 1B, cloudy sky EPAC Profiles 2A1 and 2B2, and the U.S. Standard

Atmosphere (Profile 3). Results are presented in Figs. 4.12 and 4.13 for theoretical T and $\log_e Q$ retrieval performance calculated with respect to $\mathbf{B}_C$. As previously discussed, this background error covariance matrix is based on the summertime COAMPS EPAC error statistics. For comparison, theoretical T retrieval performance results using $\mathbf{B}_N$ are shown for selected cases in Fig. 4.14. The effect of strong surface and atmosphere inter-level correlations of error on theoretical T retrieval performance is shown in Fig. 4.15.

As discussed in Chapter II.E, the low-level T retrieval performance is expected to be sensitive at the microwave frequencies to prior knowledge of T_s. When surface and atmosphere errors are uncorrelated or weakly correlated, the largest gain in low-level clear sky T performance (Figs. 4.12a-c) occurs when T_s is precisely known, or in this case, if it is less than 1.57 K. Doubling the error to 3.14 K was observed to have little additional negative impact on T retrieval performance.

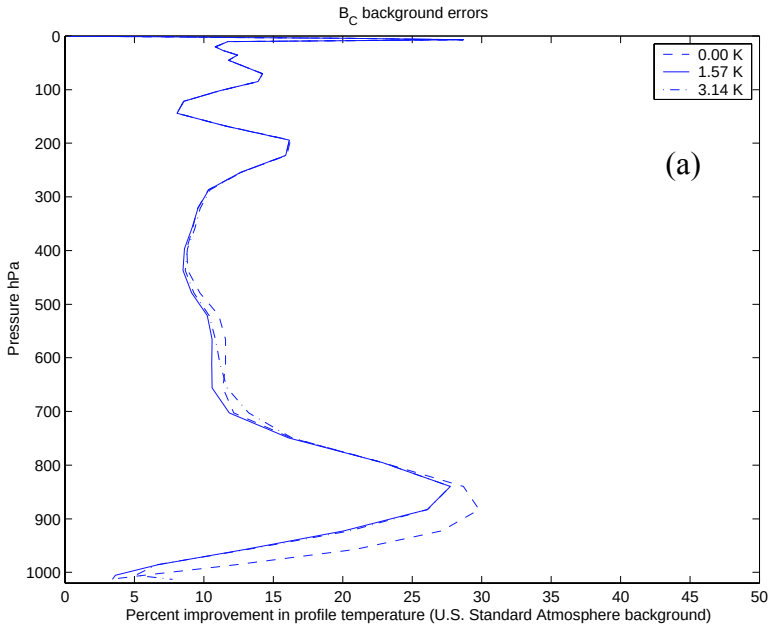

Figure 4.12. Theoretical T and $\log_e Q$ retrieval performance a function of 0.00, 1.57, and 3.14 K radiative skin temperature (T_s) error. Performance is calculated with respect to $\mathbf{B}_C$ (weak surface-atmosphere correlations of error) and background state vector (a) U.S. Standard Atmosphere, (b) clear sky EPAC Profile 1A, (c) clear sky EPAC Profile 1B, (d) cloudy sky EPAC Profile 2A1, and (e) cloudy sky EPAC Profile 2B2.

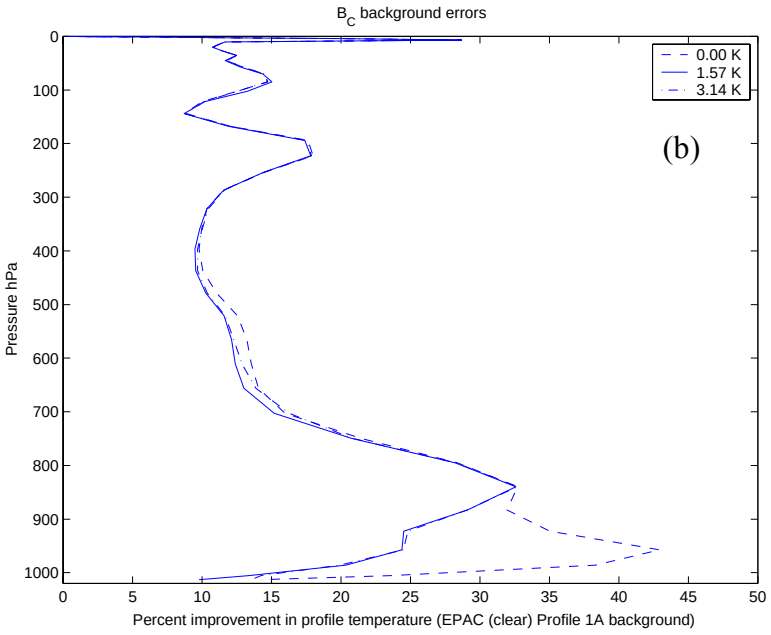

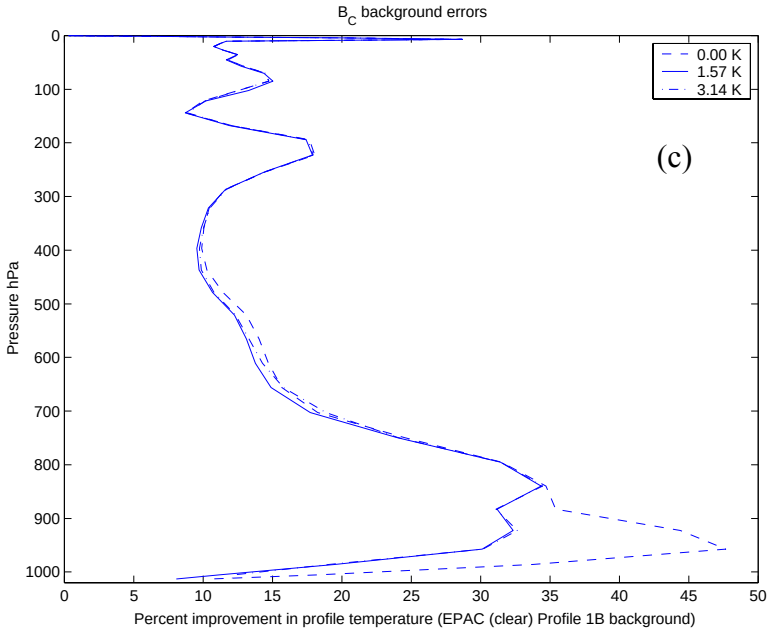

Figure 4.12. Continued.

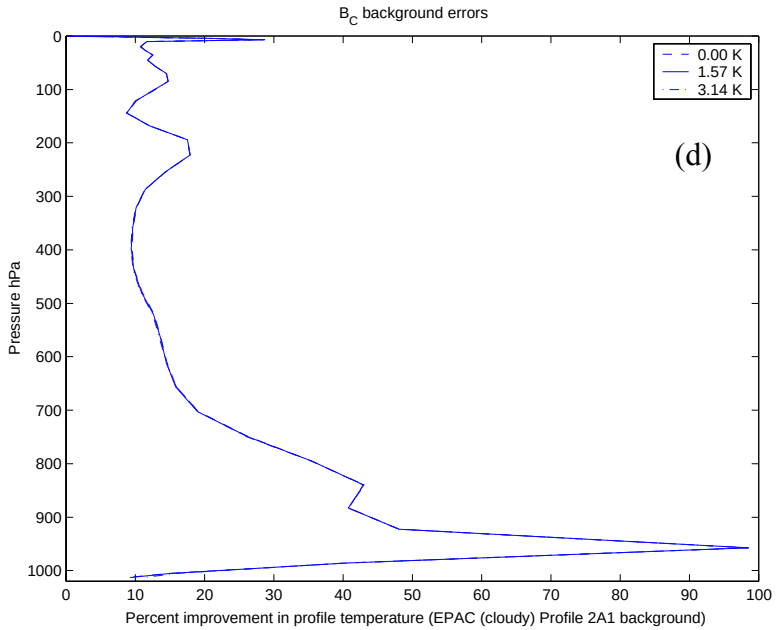

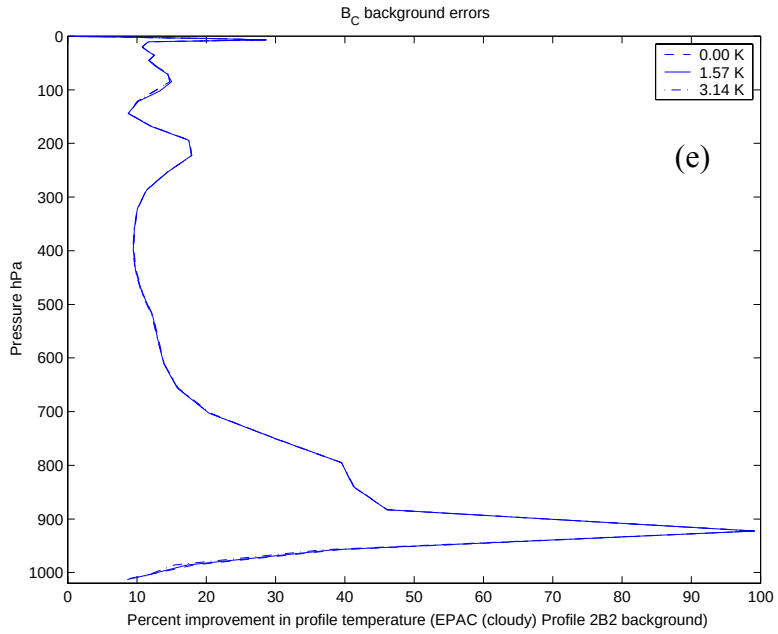

Figure 4.12. Continued.

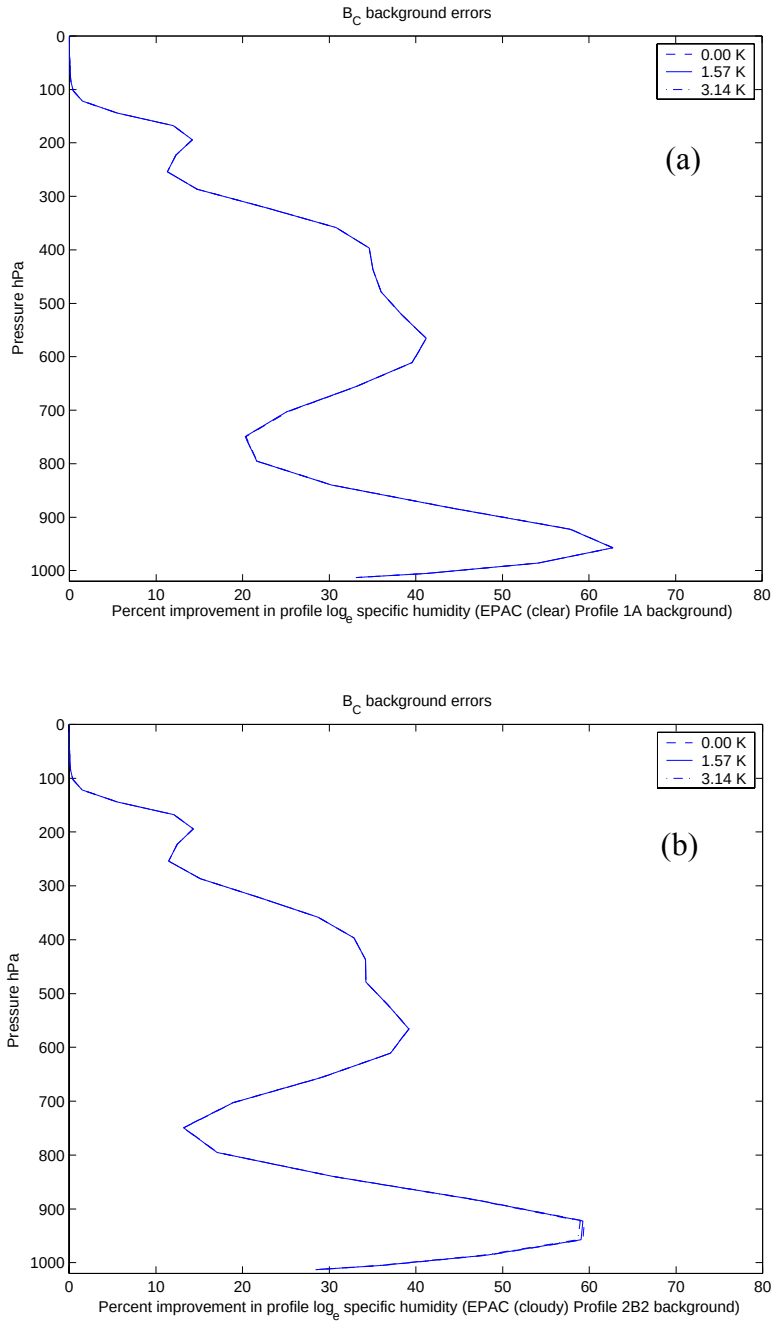

Figure 4.13. As in Fig. 4.12, except for $\log_e Q$ theoretical retrieval performance (P) calculated with respect to (a) clear sky EPAC Profile 1A, and (b) cloudy sky EPAC Profile 2B2.

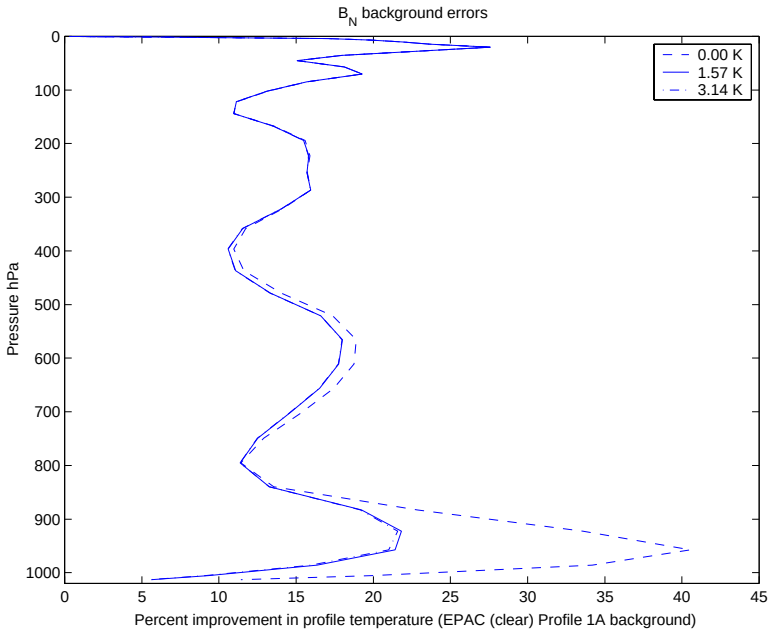

Figure 4.14. As in Fig. 4.12b, except theoretical *T* retrieval performance calculated with respect to $\mathbf{B_N}$.

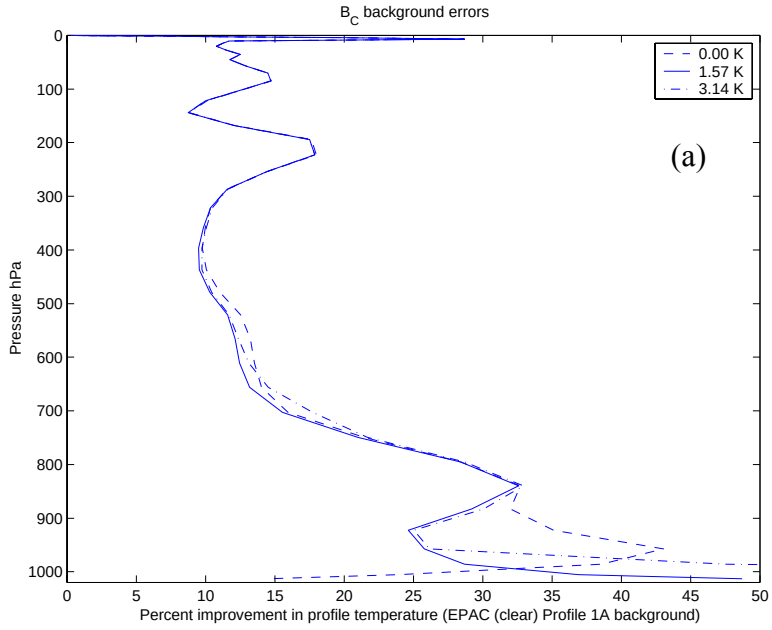

Figure 4.15. As in Fig. 4.12, except for *T* theoretical retrieval performance with "strong" surface and atmosphere inter-level correlations of error calculated for (a) clear sky EPAC Profile 1A, and (b) cloudy sky EPAC Profile 2B2.

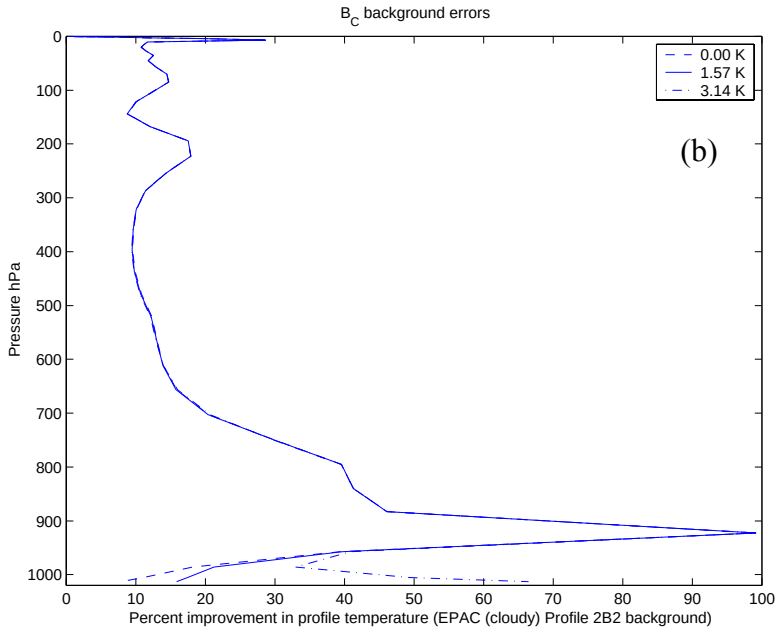

Figure 4.15. Continued.

For cloudy sky cases, T_s error did not affect the *T* theoretical retrieval performance (Figs. 4.12d-e). Consistent with English (1999) for ocean surfaces, there is little to no sensitivity of $\log_e Q$ retrieval error to changes in T_s error (Figs. 4.13a-b).

As shown in Fig. 4.14, there is a relatively large increase low-level *T* retrieval performance when calculated with respect to $\mathbf{B_N}$ and clear sky EPAC Profile 1A. Similar results were observed (not shown) when calculated for the other clear sky profiles. If clear sky theoretical *T* performance (Fig. 4.15a) is calculated with respect to $\mathbf{B_C}$ with strong surface and atmosphere inter-level correlations, then non-zero T_s errors were observed to improve near-surface *T* retrieval performance. This result was also observed for the cloudy sky case (Fig. 4.15b). However, perfect knowledge of T_s did result in greater clear sky *T* retrieval performance near 900 hPa. The use of these strong surface and atmosphere error correlations may not be appropriate, because in practice, these errors may not be coupled in a short-term NWP forecast. However, the results are interesting and provide an insight into the relationship between information and vertical correlation functions.

These results confirm that low-level clear *T* retrieval performance can theoretically be improved by accurately specifying T_s using a high-resolution SST product. However, for cloudy sky retrievals, it might be useful to increase T_s background error to increase *P* between cloud-top and the surface.

b. Microwave Surface Emissivity Error

Microwave surface emissivity (ε_m) error of 0, 1, 2 and 5% was applied to AMSU-A channels 1 – 4, 15, and AMSU-B channels 1 and 2. Emissivity (ε) error for all other channels was set to zero. Results are shown in Figs. 4.16 and 4.17 for *T* and $\log_e Q$ retrieval performance calculated with respect to $\mathbf{B_C}$. The forward model (H) was linearized about clear sky EPAC Profiles 1A and 1B, cloudy sky EPAC Profiles 2A1 and 2B2, and the U.S. Standard Atmosphere (Profile 3). Profile cloud liquid water mixing ratio (*CLW*) errors were set to zero for both cloud profiles.

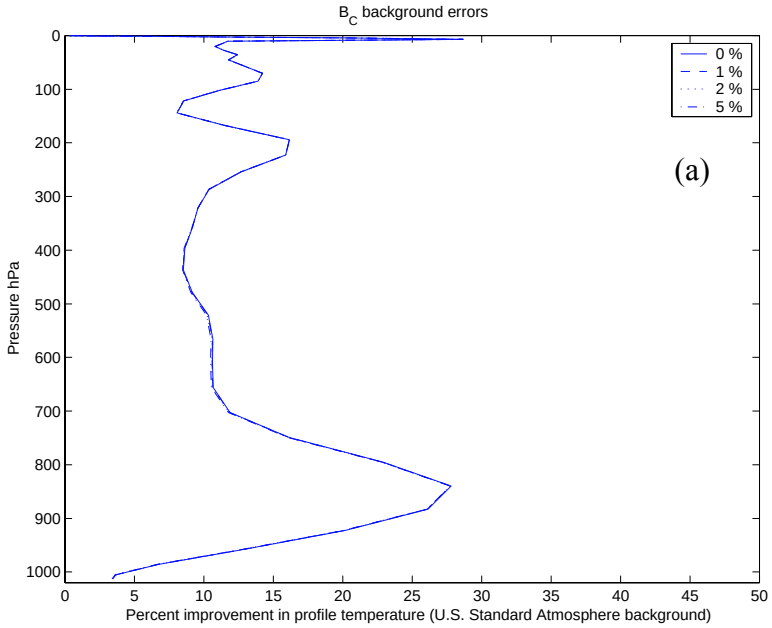

Figure 4.16. Theoretical *T* retrieval performance a function of 0, 1, 2, and 5% microwave surface emissivity error (ε_m) applied to AMSU window channels. Performance is calculated with respect to $\mathbf{B_C}$ background state vector (a) U.S. Standard Atmosphere, (b) clear sky EPAC Profile 1A, (c) clear sky EPAC Profile 1B, (d) cloudy sky EPAC Profile 2A1, and (e) cloudy sky EPAC Profile 2B2.

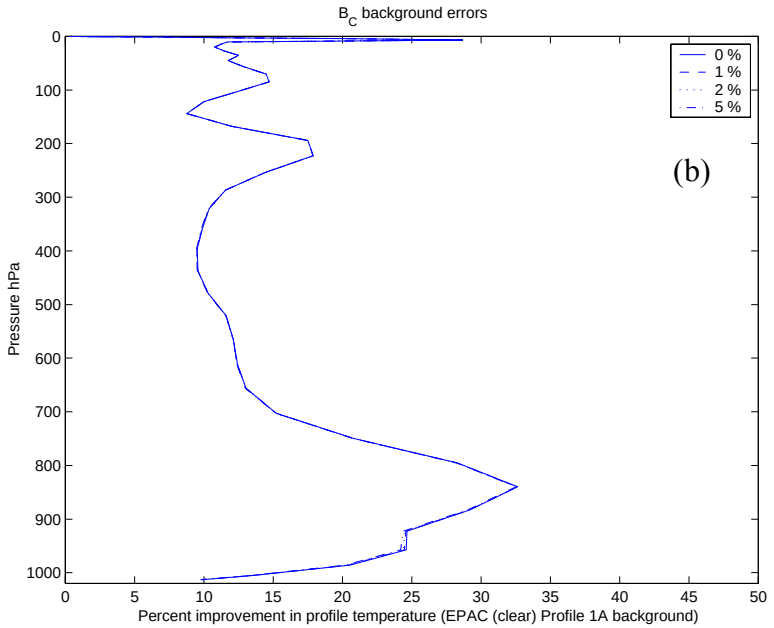

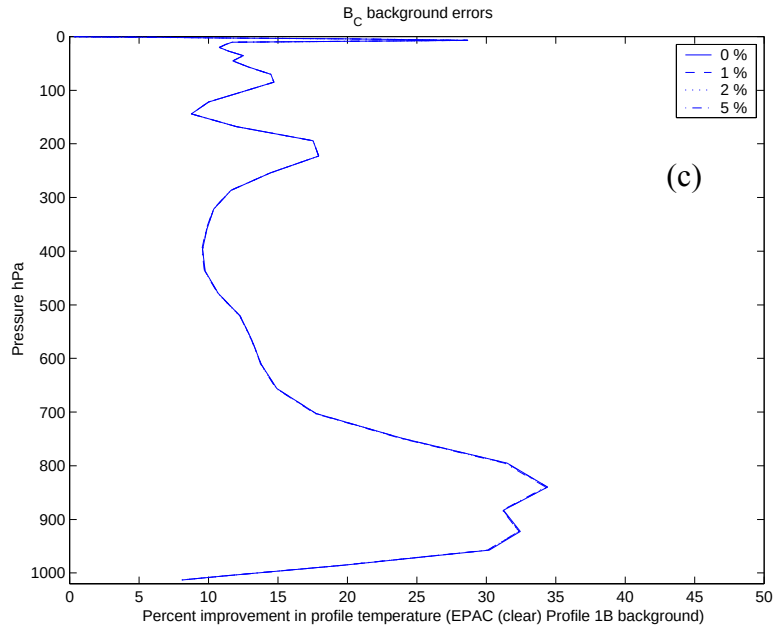

Figure 4.16. Continued.

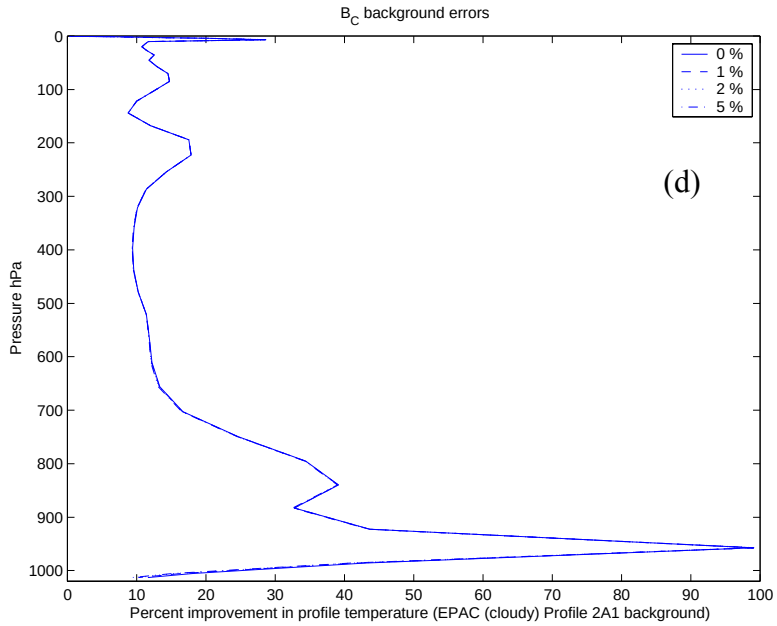

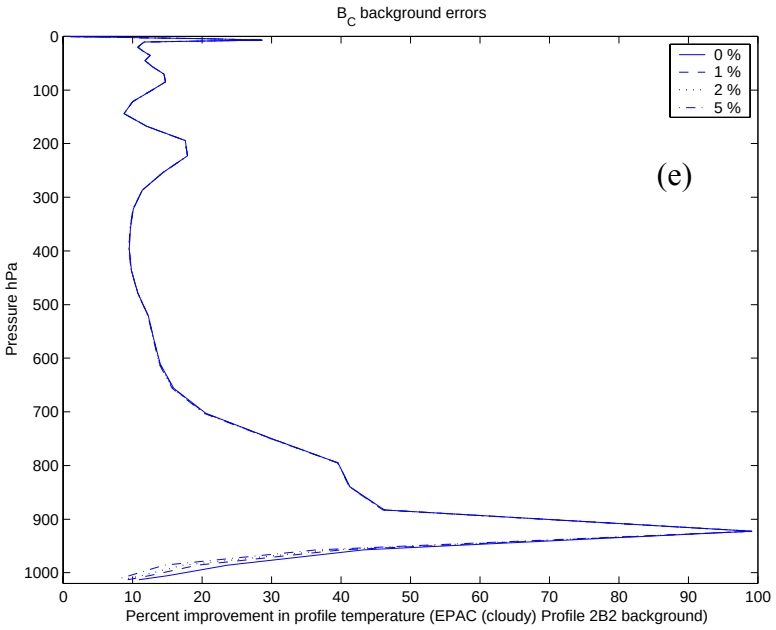

Figure 4.16. Continued.

Consistent with English (1999), *T* retrieval performance for all clear sky background state vectors is virtually insensitive to ε_m error of these magnitudes shown in Figs. 4.16a-c, since the IR channels provide most of the surface temperature information. The *T* retrieval performance (Figs. 4.16d-e) calculated using the cloudy sky profiles is only slightly sensitive to ε_m error below the cloud top. As discussed in Chapter II.E, even thin clouds are expected to increase the sensitivity to ε_m and ε_m error if there is no prior knowledge of *CLW*.

In contrast to the relative insensitivity for theoretical *T* retrieval performance to ε_m error, the low-level $\log_e Q$ retrieval performance (Figs. 4.17a-e) is sensitive to changes in ε_m error. Additionally, as ε_m increases, the retrieval error becomes more sensitive to ε_m error (English 1999).

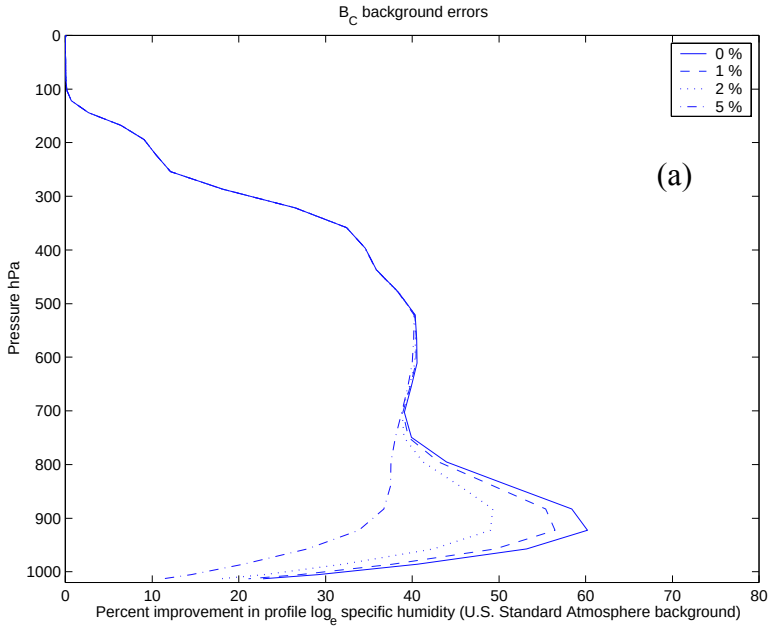

Figure 4.17. As in Fig. 4.16, except for $\log_e Q$ theoretical retrieval performance (*P*).

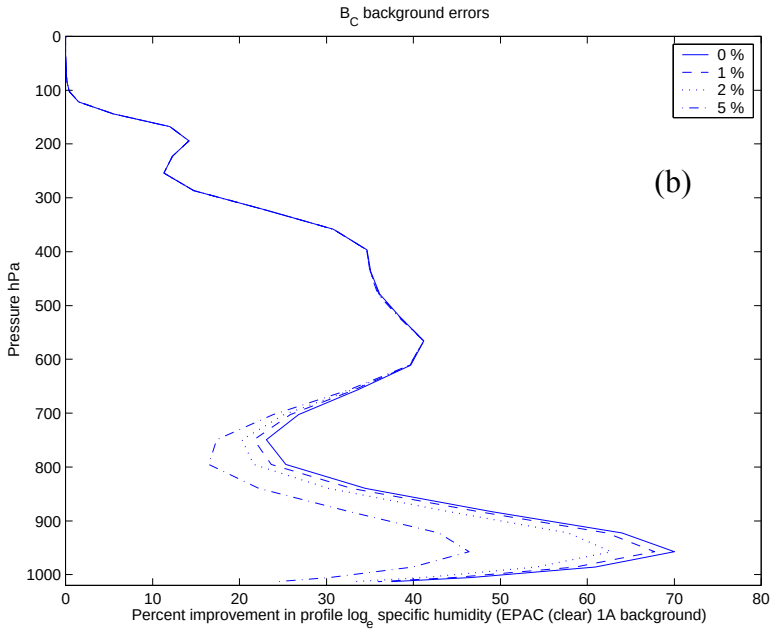

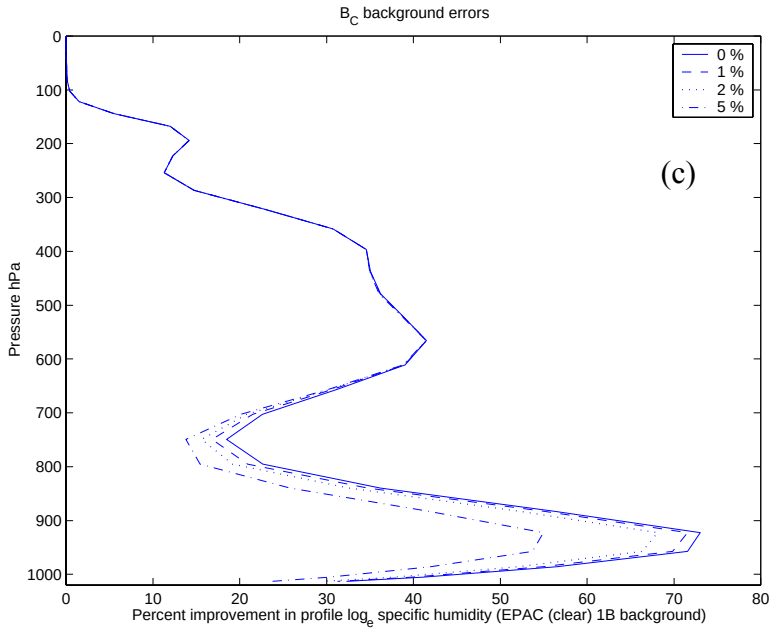

Figure 4.17. Continued.

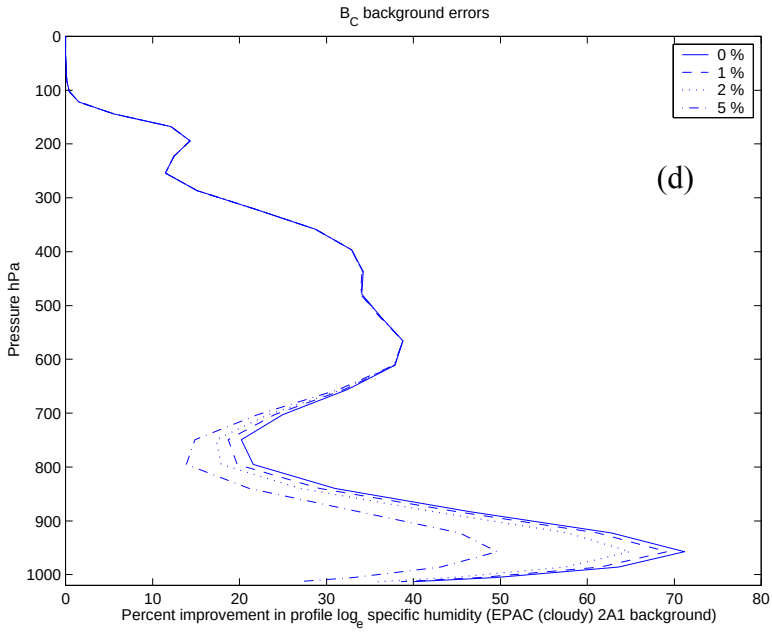

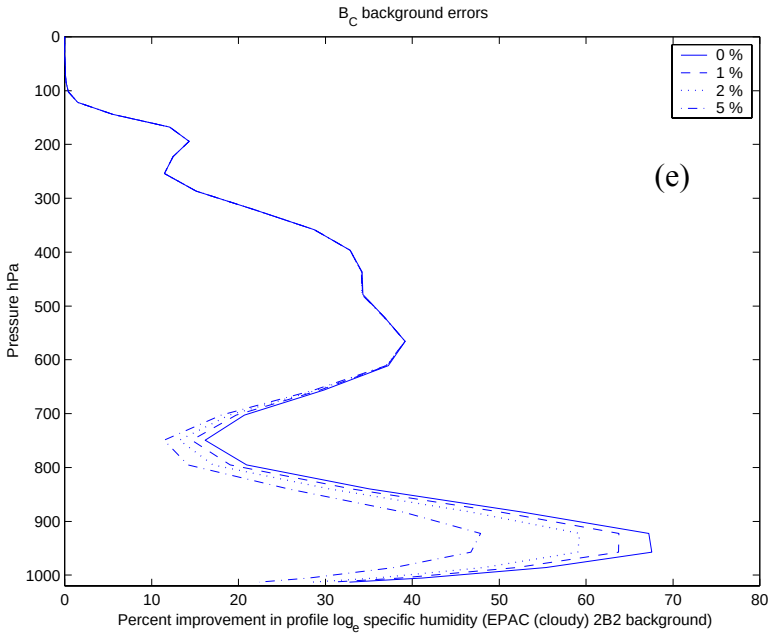

Figure 4.17. Continued.

The low-level $\log_e Q$ retrieval performance decreases as ε_m error is increased from 0 to 5% for all five background state vectors tested. Small ε_m errors of 1 – 2% were found to not greatly affect $\log_e Q$ retrieval performance for the clear sky EPAC profiles. However, the U.S. Standard Atmosphere (Profile 3) background and the cloudy EPAC profiles were found to be more sensitive to these ε_m errors. Results were similar for both T and $\log_e Q$ retrieval performance (not shown) when calculated with respect to $\mathbf{B_N}$.

This research found a greater sensitivity of $\log_e Q$ performance to ε_m error with the U.S. Standard Atmosphere background vice the idealized clear EPAC backgrounds. Profile 3 has less water vapor near the surface, but overall is more humid at mid-levels than the EPAC profiles. Following English (1999), more channels "see" the surface with a drier profile and performance is more sensitive to changes in ε_m as opposed to ε_m error. For the U.S. Standard Atmosphere, AMSU should be able to retrieve ε_m and T_s even without accurate background information, because fewer window channels are expected to "see" the surface using the more humid profile and therefore, performance is more sensitive to ε_m error.

c. Surface Pressure and 2m Wind Speed Errors

Theoretical T retrieval performance was found to be virtually insensitive to background surface pressure (P_s) errors of 0.00, 3.38, and 6.76 hPa (not shown) and 2 m wind speed errors of 0.0, 2.0, or 4.0 m s^{-1} (not shown). Results for T were similar for all profile type tested. Low-level $\log_e Q$ retrieval error and performance was found to be only slightly sensitive to P_s and 2 m wind speed errors for the U.S. Standard Atmosphere background (Profile 3).

From (2.16) and (2.23), this research shows P_s and 2m wind speed errors specified within the **B** matrix do not to greatly change corresponding elements of the retrieval error covariance matrix **S**. However, from Chapter III.A, 2 m wind speed errors do influence ε_m error, which as discussed above does impact retrieval performance.

5. Cloud Array Errors

a. Cloud-top Pressure Error

Retrieval performance for T and $\log_e Q$ is evaluated for cloud top pressure (P_{CT}) errors of 0, 5, 10, 20, and 50 hPa. For comparison, the forward model (H) has been linearized about cloudy EPAC Profiles 2A1 and 2B2 where P_{CT} is at 957.44 and 922.46 hPa, respectively. Results are calculated with respect to $\mathbf{B_C}$ (Figs. 4.18a-b) and $\mathbf{B_N}$ (Fig. 4.19). Cloud fractional coverage (C_{FC}) within the background state vectors is 1.00.

The results of this sensitivity analysis show that T retrieval performance rapidly decreases as the prior uncertainty in P_{CT} increases. $\text{Log}_e Q$ retrieval performance was found to be insensitive to these P_{CT} errors. Even with a relatively small P_{CT} error of 10 hPa, T performance at cloud-top for both EPAC profiles is reduced by nearly one-half. For errors of 20 to 50 hPa, the retrieval behaves as if there is no prior knowledge of P_{CT}.

The ATOVS instrument selection and observation error sensitivity analyses show that HIRS/3 surface channels provide the vast majority of temperature information at cloud-top. These results suggest that prior knowledge of P_{CT} is necessary for the successful retrieval of profile temperature at cloud-top.

As discussed in Chapter II.C, previous research has demonstrated success in retrieving cloud free, and stratocumulus-topped boundary layer height from infrared and visible satellite imagers (e.g., AVHRR). These observation types and derived products could be used to either assign confidence to COAMPS background cloud field or as additional observations or constraints to a 3DVAR retrieval scheme. Additionally, retrieval methods to determine the height of both clear, and stratocumulus-topped MABL's have been studied by numerous researchers (e.g., Kren 1987; Minnis et al. 1992; Betts et al. 1992; McBride 2000). The techniques developed by Kren (1987) and McBride (2000) are independent of a background NWP model, but all these methods combine a thermodynamic boundary layer model with satellite retrievals of MABL parameters such as cloud-top temperature and sea surface temperature. The McBride (2000) technique has a stated error of 60 – 70 m for boundary layer depth.

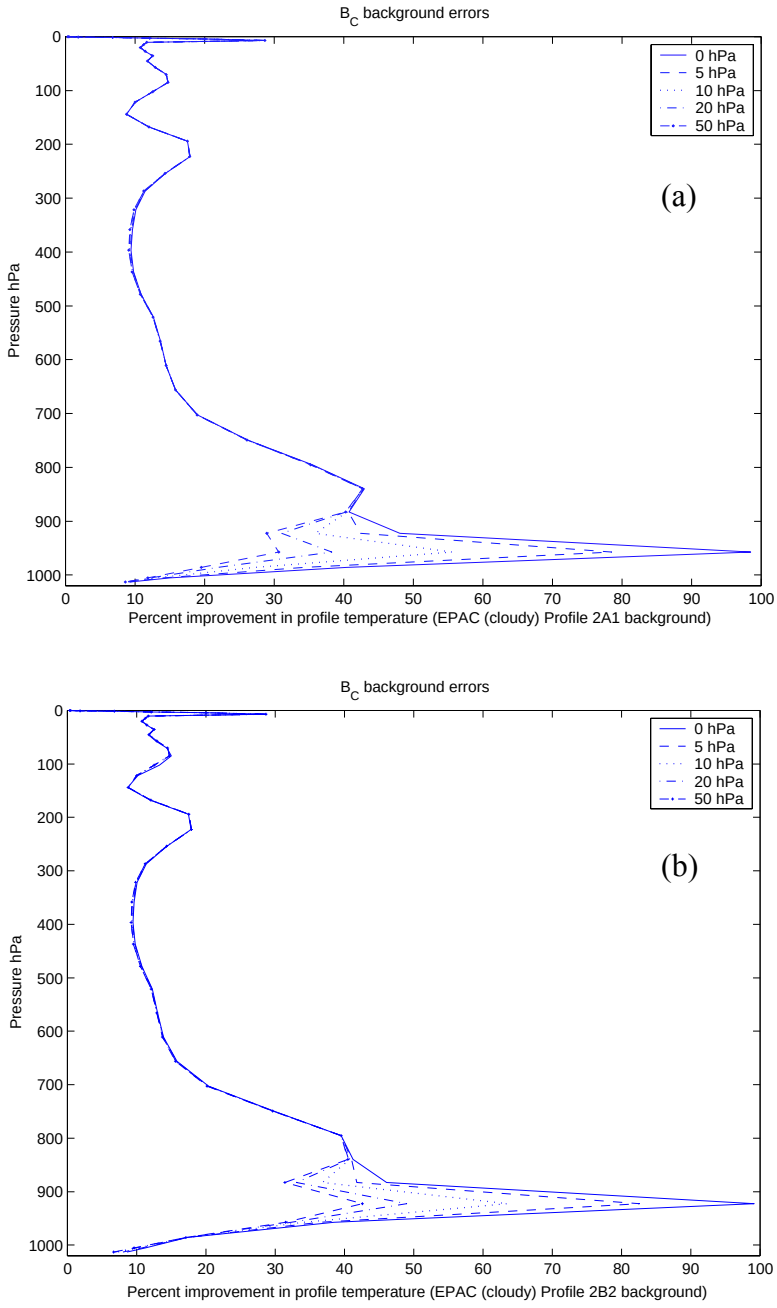

Figure 4.18. Theoretical *T* retrieval performance (*P*) as a function of 0, 5, 10, 20 and 50 hPa cloud-top pressure (P_{CT}) error calculated with respect to $\mathbf{B_C}$ and (a) cloudy sky EPAC Profile 2A1, and (b) cloudy sky EPAC Profile 2B2.

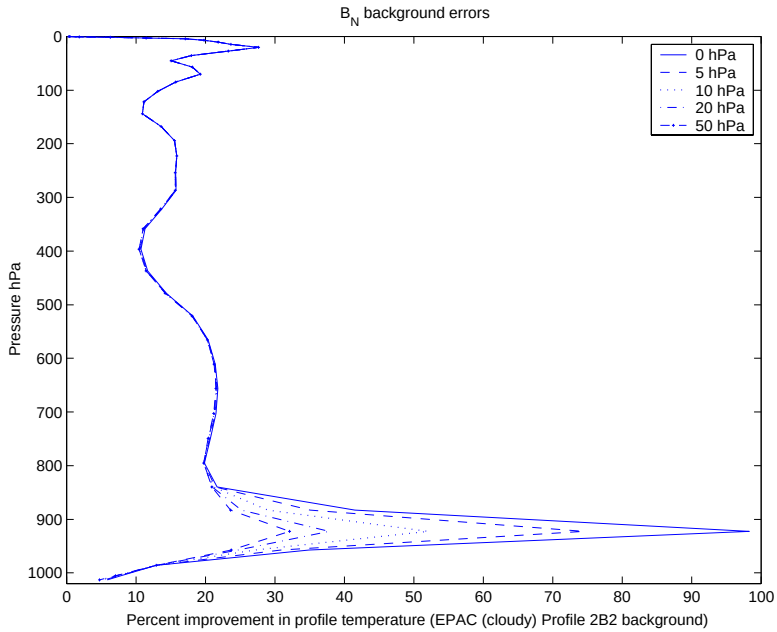

Figure 4.19. As in Fig. 4.18b, except for calculated with respect to $\mathbf{B_N}$.

b. Cloud Fractional Coverage Error

The effect of cloud fractional coverage (C_{FC}) error on theoretical *T* retrieval performance is shown in Figs. 4.20 and 4.21. Background errors of 0, 10, 50 and 100% were used to examine the range of retrieval sensitivity from perfect to no prior knowledge. The forward model (H) has been linearized about Profiles 2A1 and 2B2 and results were calculated with respect to $\mathbf{B_C}$ (Figs. 4.20a-b) and $\mathbf{B_N}$ (Fig. 4.21). Cloud fractional coverage was set to 1.00 in the background state vector for these cases. The effect of non-zero C_{FC} error on theoretical clear sky T retrieval performance is shown in Fig. 4.22.

Similar to the effect of P_{CT} error, this research found that increases in C_{FC} error (with 100% cloud cover in the background state vectors) resulted in reduced *T* retrieval performance with no change in $\log_e Q$ retrieval performance (not shown). There is a greater reduction in *T* retrieval performance (Fig. 4.20b and Fig. 4.21) for Profile 2B2 as C_{FC} is increased from 0 to 50%. In this case the retrieval performance is reduced by

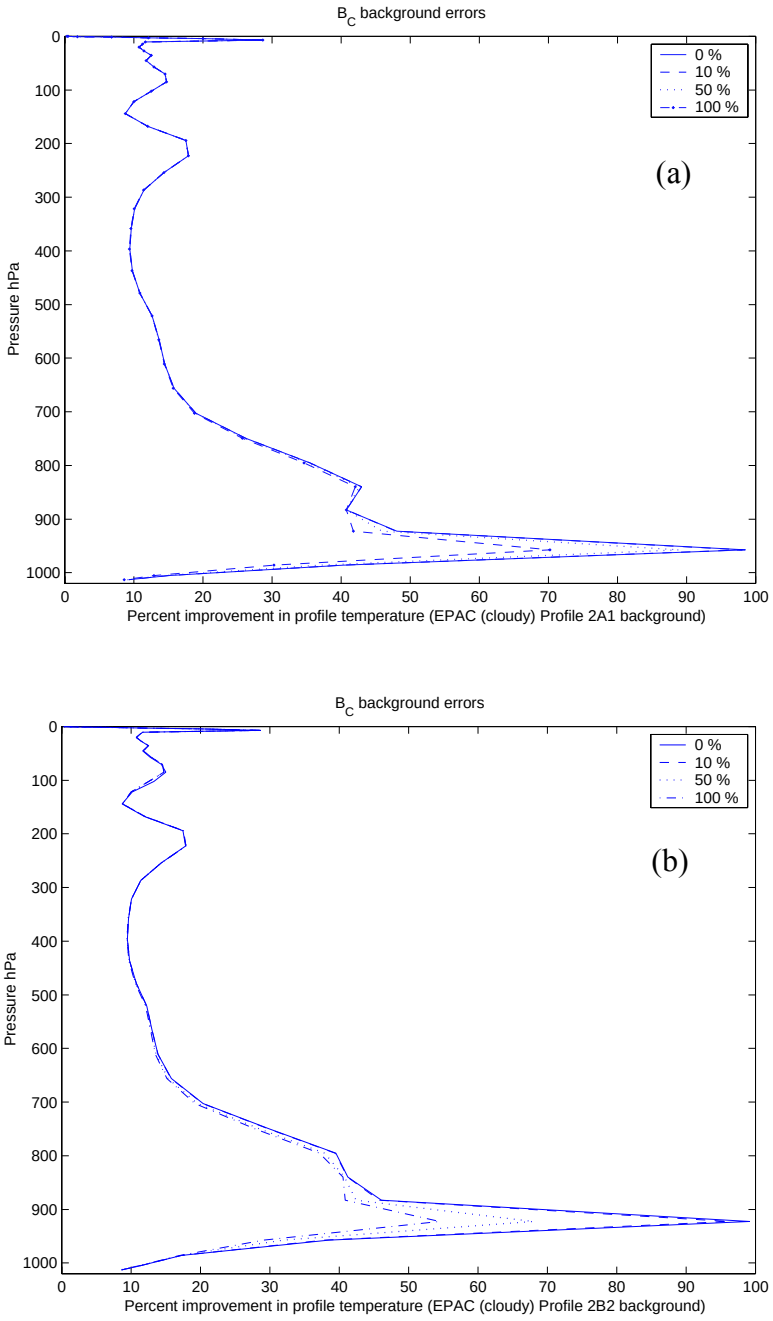

Figure 4.20. Theoretical *T* retrieval performance (*P*) as a function of 0, 10, 50 and 100% cloud fractional coverage (C_{FC}) error calculated with respect to $\mathbf{B_C}$ and (a) cloudy sky EPAC Profile 2A1, and (b) cloudy sky EPAC Profile 2B2..

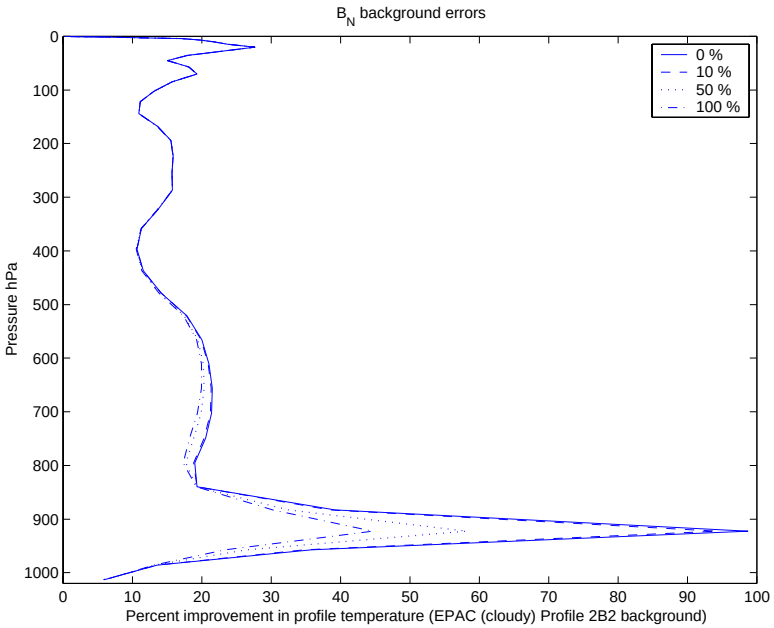

Figure 4.21. As in Fig. 4.20b, except calculated with respect to $\mathbf{B_N}$.

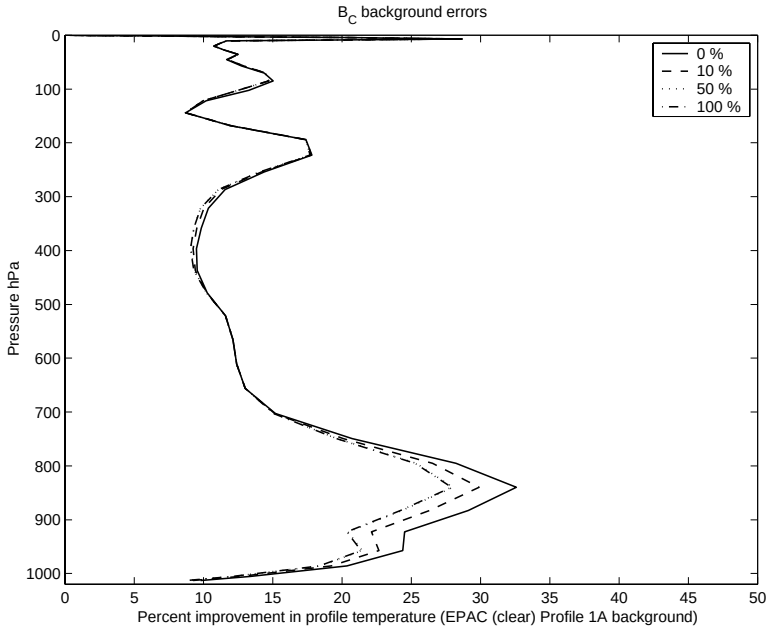

Figure 4.22. Theoretical *T* retrieval performance (*P*) as a function of 0, 10, 50 and 100% cloud fractional coverage (C_{FC}) error calculated with respect to $\mathbf{B_C}$ and clear sky EPAC Profile 1A.

approximately 50% as C_{FC} error is increased from 0 to 50%. However, even with no prior knowledge of C_{FC}, the sensor is able to add some *T* information. This sensitivity study has shown that C_{FC} error has a large effect on theoretical *T* retrieval performance when the background state vector is cloudy. If the background state vector is clear, then non-zero C_{FC} error in the background error covariance matrix will degrade *T* retrieval performance (Fig. 4.22). The use collocated satellite imagery to independently verify cloud cover could reduce prior uncertainty in C_{FC}.

6. Profile Array Errors

a. Temperature and Log$_e$ Specific Humidity Profile Errors

The effect of *T* and $\log_e Q$ background errors applied uniformly to all 43 levels on *T* and $\log_e Q$ retrieval performance is shown in Fig. 4.23. For this sensitivity analysis, H was linearized about U.S. Standard Atmosphere (Profile 3) and results were calculated with respect to $\mathbf{B_N}$. Three sets of *T* and $\log_e Q$ profile errors were tested. The first assumes perfect knowledge by setting the *T* and $\log_e Q$ standard deviations of error to zero. In contrast to (2.15), the information matrix form of (2.16) does not require inversion of **B** and zero elements are acceptable. The second uses the standard deviations of error specified in Table 3.2 for $\mathbf{B_N}$ and the third set doubles these specified errors.

Errors for *T* ($\log_e Q$) of 0.0 K (0.0 g kg^{-1}) assume a perfect background profile and as expected, the percent improvement or information available from the satellite radiances is zero. Of course, if we had perfect background profiles there would be no need for the satellite retrieval. Since we must work with some degree of uncertainty in the first-guess profile it is important to determine the sensitivity of the retrieval to increases in profile errors. In general, both *T* and $\log_e Q$ theoretical retrieval performance (Figs. 4.23a-b) increase as the background error increase. The largest reduction in retrieval errors occurs for low-level *T*. Smaller reductions in analysis error are generally observed for $\log_e Q$. In a related sensitivity analysis (Fig. 4.24), the *T* and $\log_e Q$ background errors were uniformly increased from zero to double the specified values for $\mathbf{B_N}$ (Table 3.2) between RTTOV-6 levels 34 - 43 (702.73 – 1013.25 hPa). Profile errors at all other levels remained fixed. The purpose of this simulation is to determine the effect of low-level profile errors, specifically within the MABL, on *T* and $\log_e Q$ theoretical retrieval performance (Figs. 4.24a-b).

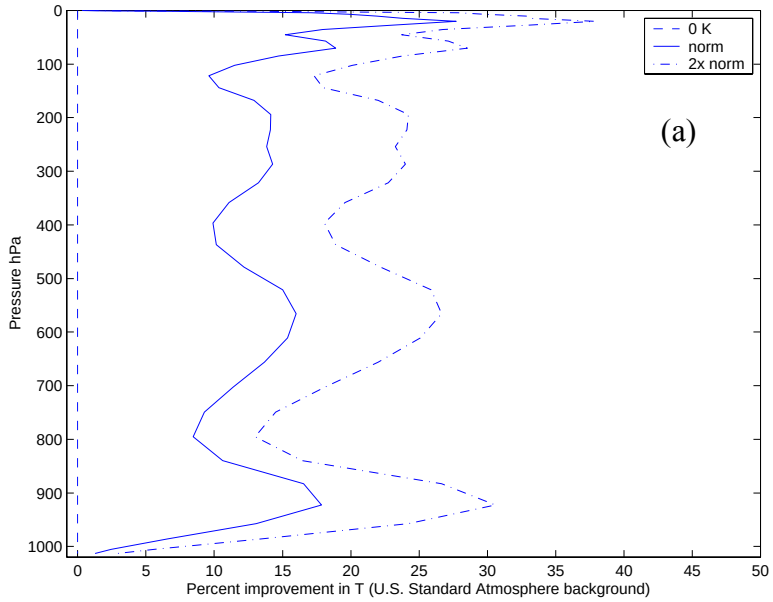

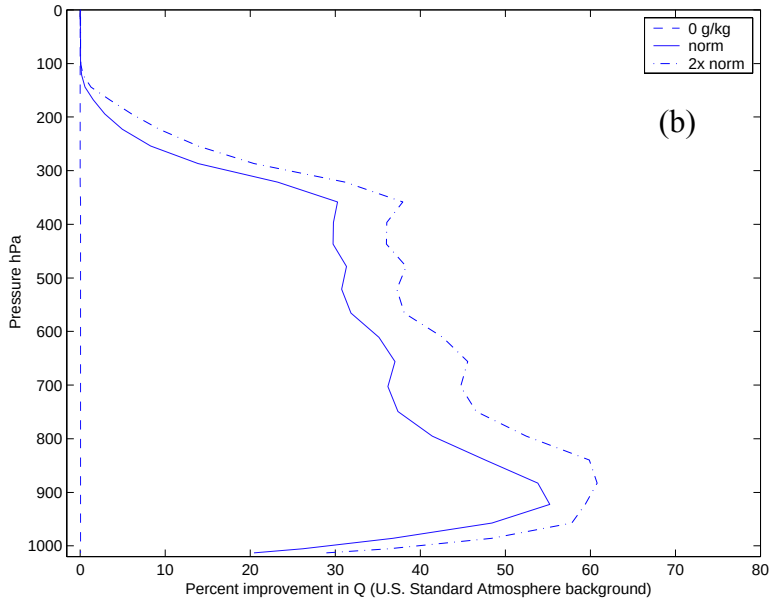

Figure 4.23. Theoretical (a) T, and (b) $\log_e Q$ retrieval performance as a function of uniform profile T and $\log_e Q$ errors applied to all 43 RTTOV-6 levels. Results were calculated with respect to $\mathbf{B}_N$.

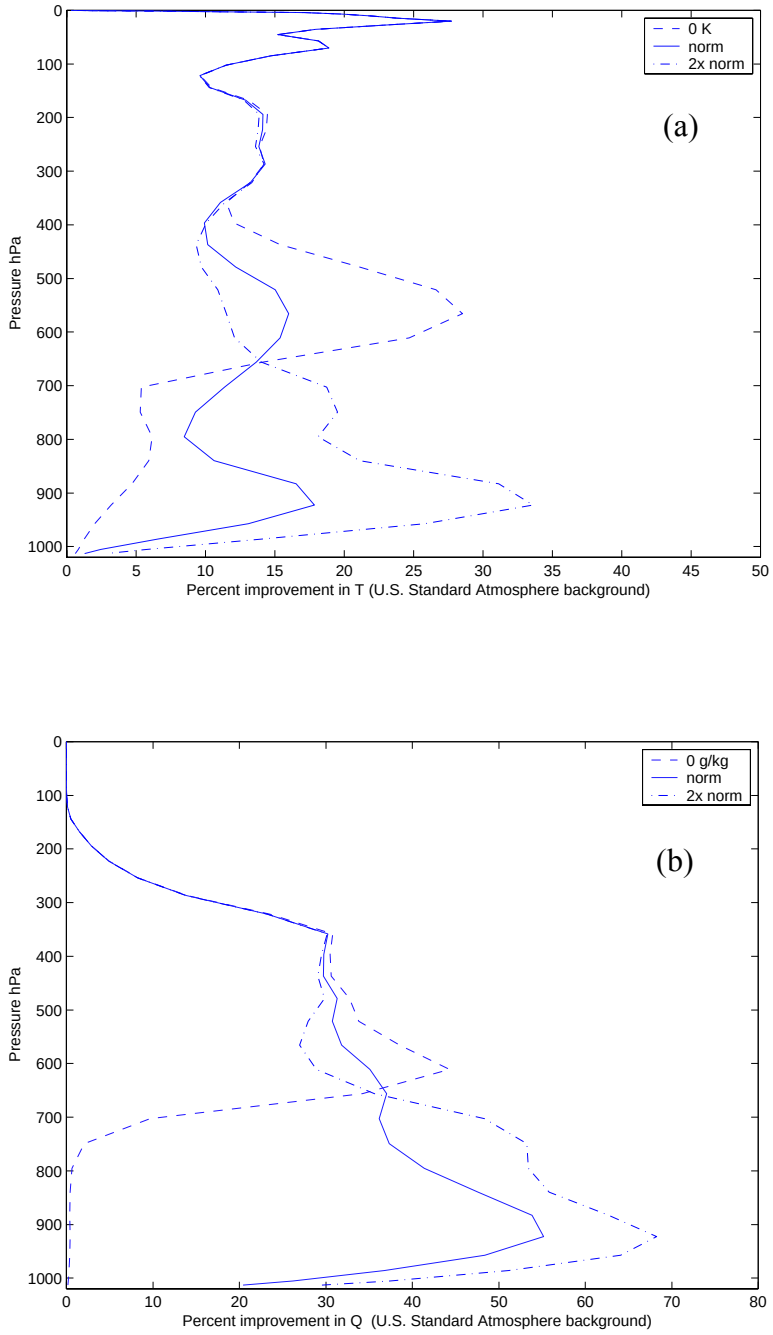

Figure 4.24. As in Fig. 4.23, except as a function of uniform low-level (a) T and (b) $\log_e Q$ errors applied to RTTOV-6 levels 34 – 43.

The results for levels 34 – 43 are similar to those in shown Figs. 4.23. Less information is derived from the radiances as the background profile errors approach zero and more information is derived as the background errors increase. Above level 34 (702.73 hPa) the opposite effect is observed. Analysis errors between 300 – 700 hPa are decreased (increased) as low-level background profile errors are decreased (increased). This demonstrates how information is distributed through the vertical error correlations. As previously discussed, profile retrieval performance is very sensitive to the strength of the inter-level correlations of error.

b. Cloud Liquid Water Profile Array Errors

Cloud liquid water mixing ratio profile (*CLW*) errors were allowed to vary in the following simulations in order to determine the affect on T and $\log_e Q$ theoretical retrieval performance. Thin liquid water cloud has negligible impact on the AMSU sounding channels, but the window channels are sensitive to LWP. If *CLW* increases, $\log_e Q$ information is rapidly lost (English 1999). Information content analyses conducted previously in this dissertation assumed perfect knowledge of *CLW* elements. This simulation is conducted primarily for the EPAC cloudy sky profiles (Profiles 2A1 and 2B2). Profile 2A1 (2B2) has a maximum *CLW* amount of 0.25 (0.50) g kg^{-1} at cloud-top with LWP value of 90 (285) g m^{-2} (see Chapter III.C).

Theoretical T and $\log_e Q$ retrieval performance as a function of *CLW* error of 0.00, 0.05, 0.25, and 0.50 g kg^{-1} is shown in Figs. 4.25 and 4.26. These errors were uniformly applied to all 43 RTTOV-6 levels. Low-level $\log_e Q$ retrieval performance was found to be slightly improved if these errors were applied only to those levels with cloud (not shown). All other background errors remained fixed to the standard deviations of error associated with $\mathbf{B}_C$. Perfect knowledge was assumed for P_{CT} and C_{FC} with C_{FC} set to 1.00 in the background state vectors.

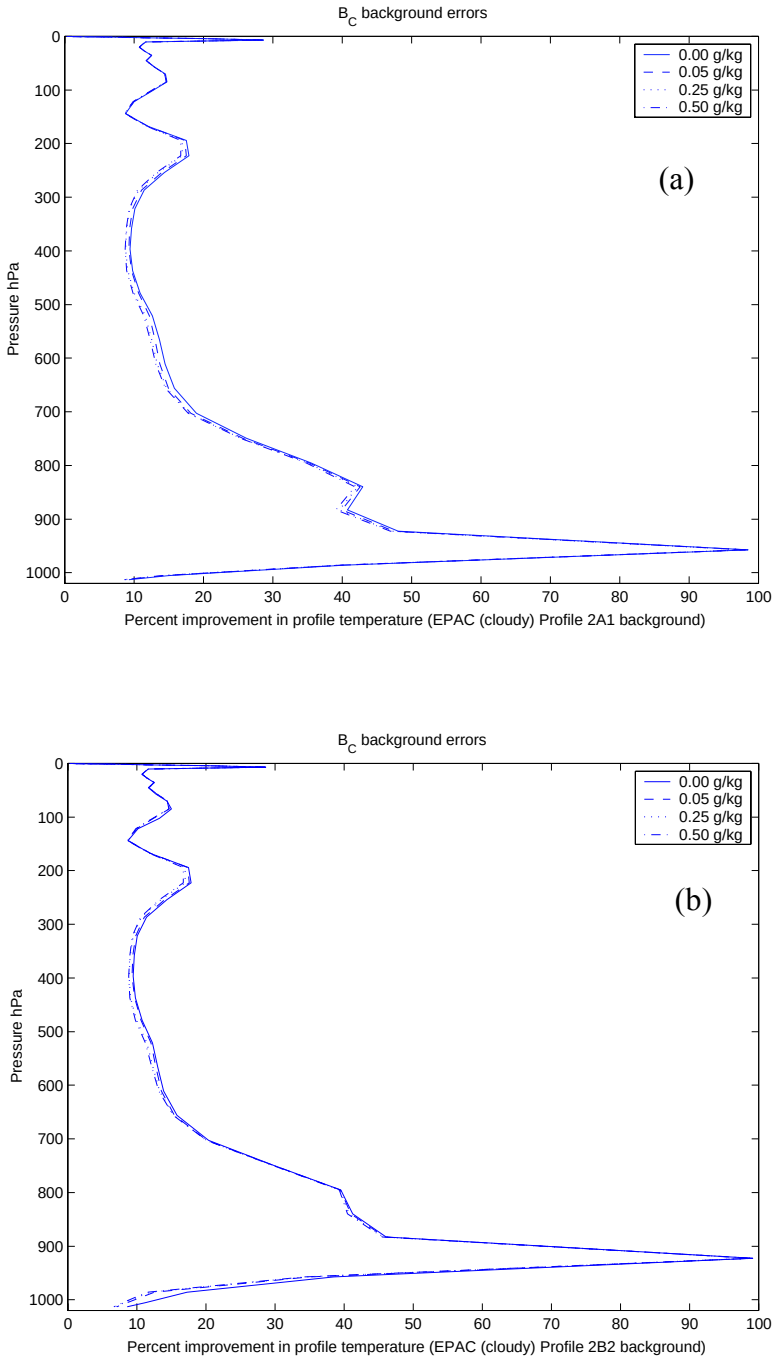

Figure 4.25. Theoretical *T* retrieval performance (*P*) as a function of 0.00, 0.05, 0.25, and 0.50 g kg^{-1} cloud liquid water mixing ratio (*CLW*) error and EPAC cloudy sky background state vectors (a) EPAC Profile 2A1, and EPAC Profile 2B2. *P* is calculated using covariance $\mathbf{B}_C$.

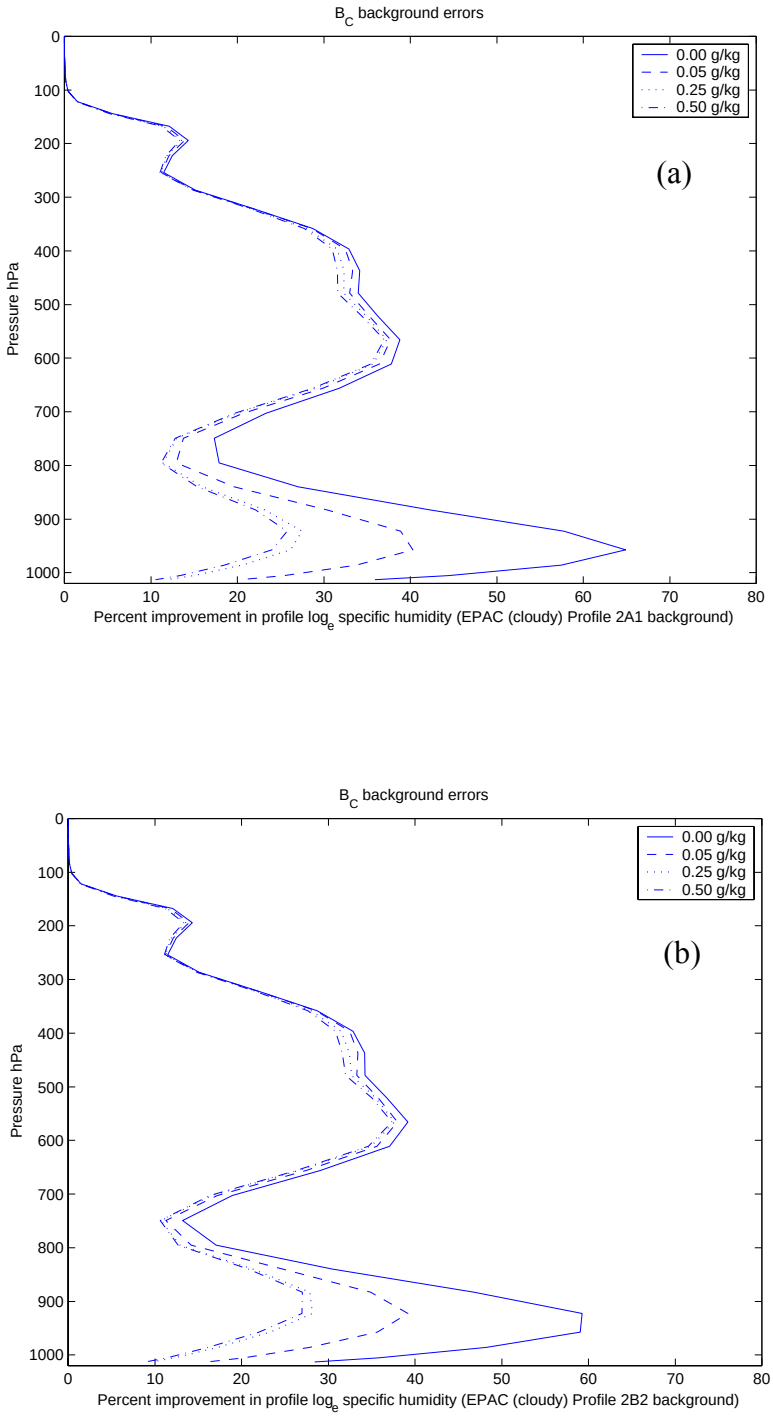

Figure 4.26. As in Fig. 4.25, except for $\log_e Q$ theoretical retrieval performance (P).

Overall, *T* retrieval performance was found to remain relatively unaffected by changes in *CLW* error. For Profile 2B2, there is a slight change in *T* retrieval performance (Fig. 4.25b) below cloud-top. Log_e *Q* theoretical retrieval performance (Figs. 4.26a-b) for all cases decreases as *CLW* error increases. For all profile types and both background error covariance matrices, the largest decrease in retrieval performance occurs between perfect knowledge and *CLW* error of 0.25 g kg^{-1}. Smaller decreases in retrieval performance occur between 0.25 and 0.50 g kg^{-1}. Sensitivity to *CLW* error was found to be similar when calculated with respect to $\mathbf{B_N}$ (not shown).

EPAC Profile 1A is included in this study to demonstrate the effect of *CLW* error on clear sky *T* and $\log_e$ *Q* retrievals. This situation would arise if *CLW* elements within the background error covariance matrix are non-zero and the matrix is then used for clear sky retrievals. As compared with the results for clear sky retrieval performance (see Fig. 4.4b), degraded $\log_e$ *Q* retrieval performance (Fig. 4.27) was observed for the clear sky background state vector (EPAC Profile 1A) when these *CLW* errors were included in background error covariance matrix.

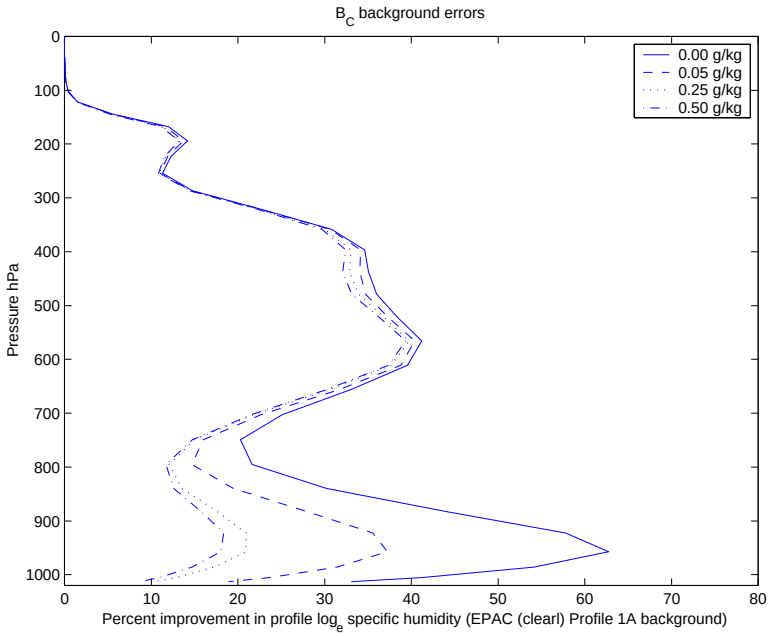

Figure 4.27. As in Fig. 4.26, except with theoretical $\log_e$ *Q* retrieval *P* calculated using clear sky background state vector, EPAC Profile 1A.

These theoretical results indicate that we can improve both the cloud-free and cloudy EPAC boundary layer water vapor retrievals if *CLW* is accurately specified within the background. This might be accomplished by use of collocated satellite retrieval techniques and/or through improved cloud modeling in the COAMPS model. The effect of *CLW* error will be examined again using simulated retrievals (Chapter V).

D. SUMMARY OF CHAPTER RESULTS

Three approaches were used to examine the information content of ATOVS retrievals with respect to the idealized summertime EPAC background state vectors and associated background errors. The first method quantified independent information and vertical resolution based upon related mathematical techniques of principal component analysis (PCA) and singular value decomposition (SVD) and the diagonal elements of the averaging kernel matrix. The second compared the background errors in radiance space to the ATOVS observation errors. The final method investigated the sensitivity of profile temperature and $\log_e$ specific humidity retrieval errors to surface and profile *a priori* errors.

Results of the PCA based information content study found 12 significant eigenvectors, with seven having eigenvalues less than 0.50. This indicates that for these seven eigenvectors, more than 50% of the information is derived from the satellite observations. The first two significant eigenvectors contain the majority of the humidity information and in general, temperature information generally dominates the remaining eigenvectors. For the clear sky EPAC profiles, the total degrees of freedom for signal (non-diagonal $\mathbf{B_N}$ case) is approximately 7.5. This indicates that about seven to seven and a half quantities can be independently measured. Total quantity of information available from ATOVS is basically independent of background profile, which is consistent with other studies (e.g., Prunet et al 1998). However, this research suggests that low-level humidity information can be obtained from the summertime EPAC MABL.

Vertical resolution of the cloudy sky theoretical *T* retrievals is approximately one model level per degree of freedom at cloud-top when *a priori* cloud errors are perfectly known. Low-level (i.e., ~ 900 hPa) *T* resolution for the clear sky EPAC profiles is approximately four levels per degree of freedom. For $\log_e Q$, the low-level vertical resolution for the EPAC profiles is approximately 3 levels per degree of freedom.

The relative magnitude of the clear sky effective background error to observation error for the AMSU window channels suggests there is a large amount of humidity information available from these channels. For the cloudy sky cases the effective background error becomes smaller for AMSU-A channel 15 and AMSU-B channels 1 and 2 as LWP increases. This indicates that less information will be available from these channels. In contrast, the effective background error (and expected information) associated with HIRS/3 channel 8 is larger for the cloudy sky EPAC profiles.

Results of the retrieval error sensitivity and performance analysis show that HIRS/3 surface channels provide information on cloud-top temperature. The majority of the low-level, boundary layer humidity information is derived from AMSU-B channel 2 followed by AMSU-A/B channel 15/1.

Consistent with other studies (e.g., English 1999), the results confirm that low-level clear sky *T* retrieval performance can theoretically be improved by prior knowledge of T_s. In addition, *T* retrieval performance for all clear sky background state vectors is virtually insensitive to ε_m error. Cloudy sky profiles with large amounts of *CLW* are slightly sensitive below cloud-top to ε_m error. However, even thin clouds are expected to increase the sensitivity to ε_m and its error if there is no prior knowledge of *CLW*. Low-level $\log_e Q$ retrieval performance is sensitive to ε_m error. However, small ε_m errors of 1 – 2% were found to not greatly affect $\log_e Q$ retrieval performance for the clear sky EPAC profiles. The U.S. Standard Atmosphere (Profile 3) background and the cloudy EPAC profiles were found to be more sensitive to ε_m error.

Temperature profile (*T*) retrieval performance rapidly decreases as the uncertainty in P_{CT} and/or C_{FC} increases. Log_e *Q* retrieval performance was found to be insensitive to these cloud errors. Even with a relatively small P_{CT} error of 10 hPa, *T* performance at cloud-top for both EPAC profiles is reduced by nearly one-half. Prior knowledge of P_{CT} and C_{FC} was found to be a necessary for the successful retrieval of profile temperature.

Overall, *T* retrieval errors were found to remain relatively unaffected by changes in *CLW* error. Log_e *Q* theoretical retrieval performance, however, decreases as *CLW* error increases. The largest decrease in retrieval performance occurs between perfect knowledge and *CLW* error of 0.25 g kg^{-1} with smaller decreases between 0.25 - 0.50 g kg^{-1}. Clear sky log_e *Q* retrieval performance was also degraded when these *CLW* errors were included in background error covariance matrix. Again, this situation would arise if *CLW* elements within the background error covariance matrix are non-zero and the matrix is then used for clear sky retrievals.

As discussed in Chapter II, Eyre (1989a) showed the effects of cloud on IR radiances, when treated optimally, can improve some aspects of retrieval performance. Specifically, this improvement is at the levels just above cloud-top. This research finds reductions in *T* and log_e *Q* retrieval error above the idealized cloudy boundary layer when compared with the clear sky. Though there are slight differences in *T* and log_e *Q* between these profiles, this observed increase in retrieval performance above the cloudy boundary layer was confirmed by including a *CLW* profile with a clear sky profile.

V. 1DVAR RETRIEVAL STUDY

Results presented in Chapter IV demonstrated that, when treated optimally, significant humidity and temperature information could theoretically be derived from ATOVS radiances within the summertime EPAC environment. A study of theoretical retrieval error sensitivity to representative EPAC background state vector elements and associated errors was also conducted to establish the *a priori* elements needed for successful 1DVAR retrievals. Research presented in this chapter builds upon these findings and uses a modified version of the NRL 1DVAR retrieval scheme to continue this investigation of the complex relationship between satellite-derived information and *a priori* constraint. 1DVAR temperature and humidity profile retrievals were generated using both simulated and actual ATOVS observations constrained by a synoptically relevant background error covariance matrix ($\mathbf{B_C}$) and simulated background or short-term model forecast fields.

The first half of this chapter presents comparisons of theoretical retrieval errors and the error statistics calculated from 1DVAR simulated retrievals. The purpose of this comparison is to test the reliability of the NRL 1DVAR retrieval scheme within the framework of this mesoscale application. The second half of Chapter V presents the results of 1DVAR profile temperature (T) and humidity ($\log_e Q$) retrievals calculated using simulated and actual ATOVS observations and COAMPS short-term forecasts. The time period of this study coincides with the Dynamics and Chemistry of Marine Stratocumulus (DYCOMS) Phase II field study. The goal here is to determine if ATOVS observations can provide information that, when used in concert with a reasonable first-guess field (i.e., COAMPS), reduces the analysis error and adjusts the retrieval within the shallow MABL toward the designated "true" profile.

The simulated observations and background profiles are used in (2.14) to find the most probable solution of the atmospheric state ($\mathbf{x}$) - the retrieval. The NRL Monterey 1DVAR 1DVAR scheme iterates equation (2.14) up to a maximum of four times and convergence occurs if $|\mathbf{x}_i - \mathbf{x}_{i+1}|$ is less than or equal to $0.4(B_{ii})^{1/2}$. This study

uses the same convergence criterion, but increases the maximum number of iterations per profile to 10, since computational cost was not an issue. This increase allows for a thorough investigation of the non-linear humidity and cloud liquid water retrieval problem.

In the nonlinear Newtonian iterative procedure of (2.14), the Jacobian matrix $\mathbf{H}(\mathbf{x}_i)$ is recalculated at each iteration. During iteration, the largest change in magnitude occurs for $\log_e Q$ Jacobians since, as previously discussed, the forward problem is not a linear function of humidity. As an example, the $\log_e Q$ Jacobians for AMSU-A channel 1 at the first and final (in this case 7th) successful iteration of a selected retrieval is shown in Fig. 5.1 At the first iteration, H is linearized about a selected background profile ($\mathbf{x}^b$) from (2.24) and is then recalculated at each iteration about the updated estimate of the state vector until convergence. The number of iterations and this AMSU-A channel were chosen for illustrative purposes only. At convergence, the $\log_e Q$ Jacobian is smoothed and reduced in magnitude by approximately 2 K.

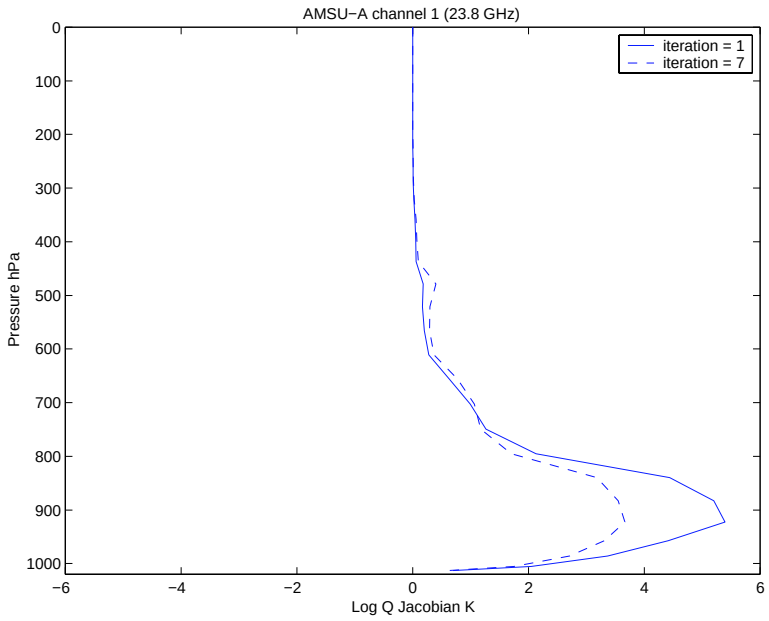

Figure 5.1. Example of $\log_e Q$ Jacobian modification during 1DVAR iteration. Results of the 1st and 7th (final) iteration of $\mathbf{H}_i(\mathbf{x}_i)$ for AMSU-A channel 1. The background state vector ($\mathbf{x}_i$) is taken from the set of 1000 simulated profiles and the "true" profile ($\mathbf{x}^t$) is cloudy sky EPAC Profile 2B2.

A. 1DVAR RETRIEVALS WITH SIMULATED BACKGROUND STATE VECTORS AND SIMULATED ATOVS OBSERVATIONS

This research calculated 1DVAR retrievals using a statistically significant number of simulated observations and simulated background state vectors. In this section, the retrieval error statistics calculated from the clear and cloudy sky 1DVAR retrievals are compared with the corresponding theoretical values. The purpose of the comparison is to test the reliability of the NRL 1DVAR retrieval scheme within the framework of this mesoscale application. Examples of individual 1DVAR retrievals are presented at the end of this section.

1. Simulated Observation Vectors

Simulated observation vectors ($\mathbf{y}_s^o$), of length *m*, were calculated using (2.25) by projecting random combinations of the eigenvectors of the *35* x *35* (*m* x *m*) ATOVS observation error covariance matrix (**R**) onto output from the RTTOV-6 forward radiative transfer model ($H(\mathbf{x}^t)$), where $\mathbf{x}^t$ is the designated "true" profile. This technique ensures the perturbations are consistent with the errors in **R**.

For the first set of simulated 1DVAR retrievals, $\mathbf{x}^t$ is designated as one of the representative EPAC background state vectors (see Chapter III.C) and 1000 different $\mathbf{y}_s^o$ were then calculated. A collocated global forecast profile derived from the DYCOMS II data set was selected as $\mathbf{x}^t$ for the COAMPS case study (see Section B). An advantage of using simulated observations is that the instrument and air mass retrieval biases discussed in Chapter II.A need not be applied.

2. Simulated Background State Vectors

Equation (2.24) was used for this research in order to construct a statistically significant number (1000) of simulated background state vectors ($\mathbf{x}^b$), each of length *n*. This was accomplished by superimposing random combinations of the eigenvectors of the *215* x *215* (*n* x *n*) background error covariance matrix ($\mathbf{B_C}$ or $\mathbf{B_N}$) onto the designated $\mathbf{x}^t$. The simulated temperature (*T*) and $\log_e$ specific humidity ($\log_e Q$) profiles were calculated independently and therefore, individual *T* and $\log_e Q$ pairs may not be physically consistent. This is an acknowledged limitation of this technique and may reduce the overall convergence rates.

As described in Chapter III.A, $\mathbf{B_C}$ is specific to the summertime COAMPS EPAC short-term forecast errors and $\mathbf{B_N}$ was calculated using globally averaged NOGAPS short-term forecast errors. All elements of $\mathbf{x}^b$ except for the cloud parameters and surface emissivity were simulated in this manner. Surface emissivity was allowed to vary randomly from "truth" by 0.005 and cloud errors are discussed in the following paragraphs.

As shown Figs. 5.2a-e, the overall structure of the T and $\log_e Q$ background profiles is consistent with the magnitudes of the projected background error. Simulated T and $\log_e Q$ profiles calculated using $\mathbf{B_C}$ and the U.S. Standard Atmosphere, clear sky EPAC Profile 1A, or EPAC cloudy sky Profile 2A1 as $\mathbf{x}^t$ are shown in Figs. 5.2a-c. Simulated profiles were also calculated for clear sky EPAC Profile 1B and EPAC cloudy sky Profile 2B2 (not shown). The low-level temperature inversion is well defined for the simulated EPAC profiles even when calculated with the relatively larger COAMPS background errors. Upper-level $\log_e Q$ errors are substantially larger for $\mathbf{B_C}$ than $\mathbf{B_N}$, which results in a greater spread between simulated $\log_e Q$ profiles. However, humidity is generally quite low at upper-levels.

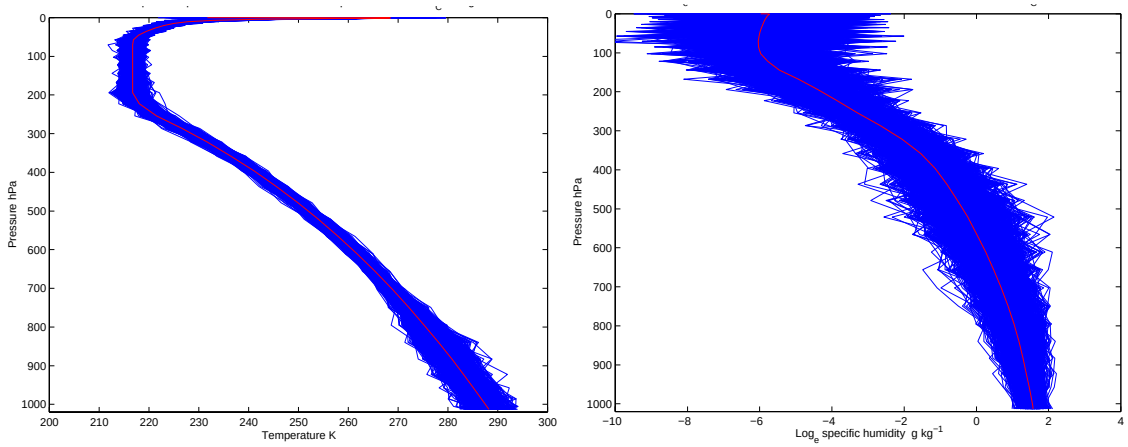

Figure 5.2a. 1000 simulated profile temperature (left panel) and $\log_e$ specific humidity (right panel) background profiles ($\mathbf{x}^b$) calculated by (2.16) with random error perturbations based on $\mathbf{B_C}$. "True" profiles ($\mathbf{x}^t$) shown here is the U.S. Standard Atmosphere.

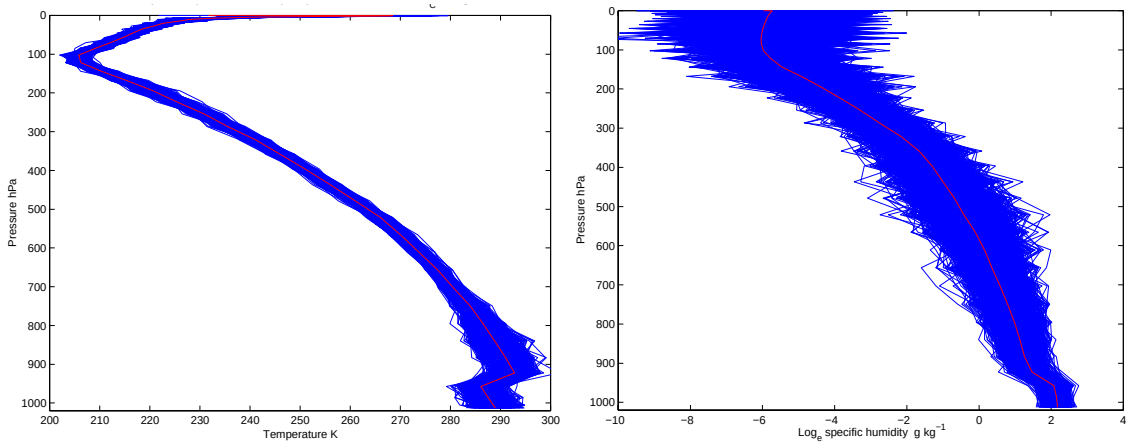

Figure 5.2b. As in Fig. 5.2a, except $\mathbf{x}^t$ is clear sky EPAC Profile 1A.

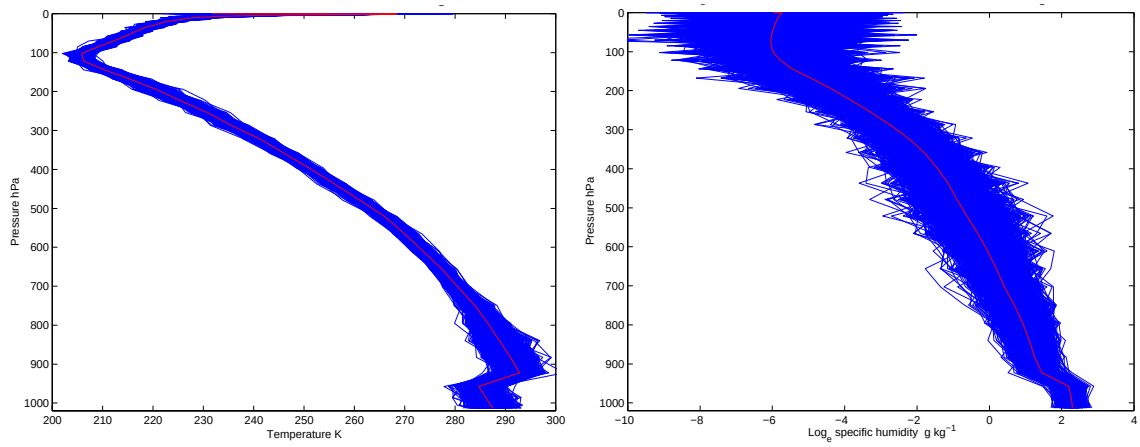

Figure 5.2c. As in Fig. 5.2a, except $\mathbf{x}^t$ is cloudy sky EPAC Profile 2A.

The simulated T and $\log_e Q$ background profiles calculated using $\mathbf{B_N}$ and the U.S. Standard Atmosphere as $\mathbf{x}^t$ are shown for comparison in Fig. 5.2d. Simulated T and $\log_e Q$ are again consistent with the background errors. The smaller upper-level errors in $\log_e Q$ result in a smaller range of simulated $\mathbf{x}^b$.

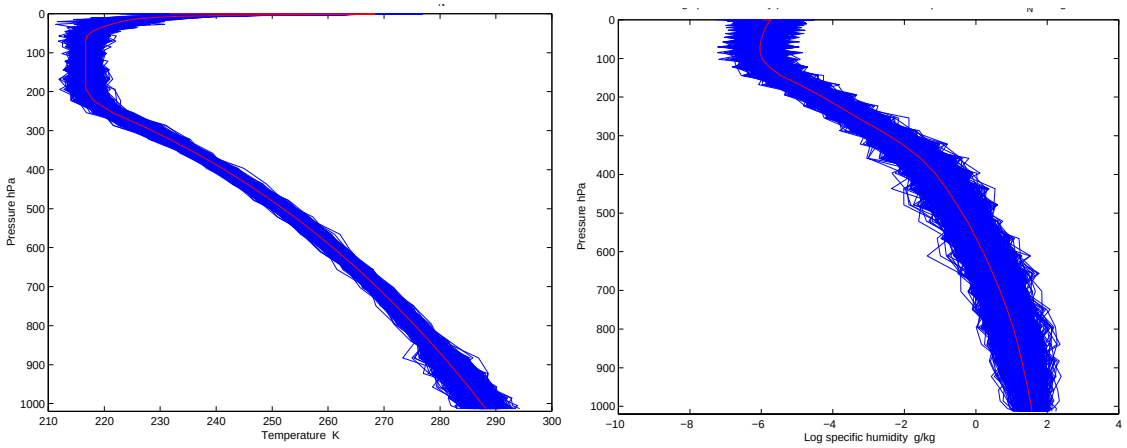

Figure 5.2d. As in Fig. 5.2a, except random error perturbations calculated using $\mathbf{B}_N$. The "true" profile is the U.S. Standard Atmosphere (Profile 3).

Temperature profile (T) errors larger than those listed in Table 3.2 might be necessary to properly represent the model error in boundary layer cloud-top temperatures. COAMPS cloud-top temperature errors for the summertime EPAC environment are estimated at approximately 4 - 6 K (A. Zhao, personal communication).

To test the effect of this uncertainty, the standard deviations of error (Table 3.2) for T at RTTOV-6 levels 37 – 43 (839.95 – 1013.25 hPa) were increased to 5.00 K. $\mathbf{B}_C$ was then recalculated using these new T errors. The resulting 1000 simulated T profiles with EPAC Profile 2A1 as "truth" are shown in Fig. 5.2e. These increases in T background error effectively eliminate any structure of the low-level temperature inversion within the set of simulated $\mathbf{x}^b$.

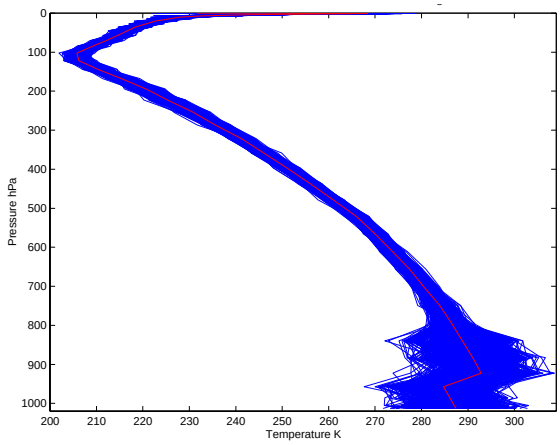

Figure 5.2e. As in Fig. 5.2a, except *T* error set to 5.00 K at RTTOV-6 levels 37 - 43 (839.35 – 1013.25 hPa). The "true" background state vector is EPAC Profile 2A1.

Fig. 5.3 shows the normalized error perturbations for the simulated profiles calculated by (2.24). All values are near unity and the small deviations from unity are due to the finite sample size (Healy and Eyre 2000).

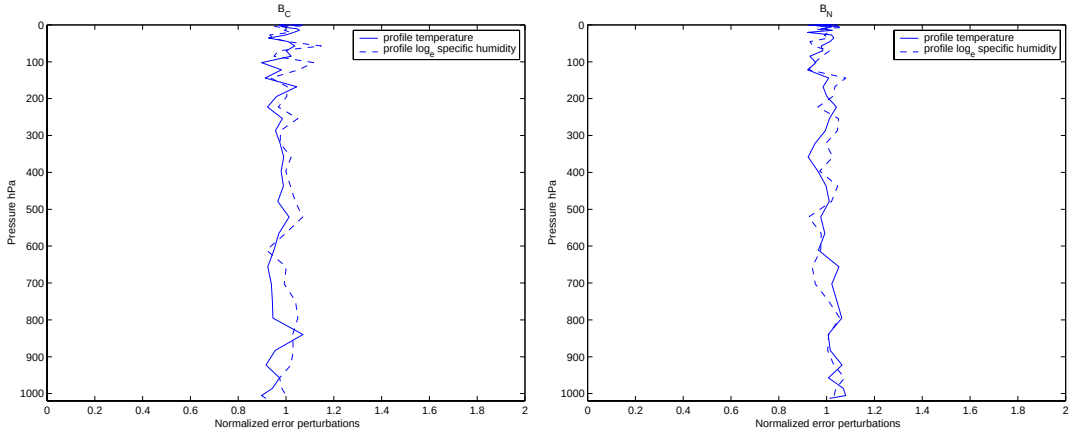

Figure 5.3. *T* and $\log_e Q$ random error perturbations sum$(\Sigma_i \gamma_i (\lambda_i)^{1/2} \mathbf{C}_i)^2$ normalized by the respective background error for $\mathbf{B_C}$ (left panel) and $\mathbf{B_N}$ (right panel).

Clear sky background profiles were assumed to be clear for the 1DVAR simulated retrievals so cloud errors were set to zero for the $\mathbf{B_N}$ and $\mathbf{B_C}$ calculations. For cloudy sky cases, the relatively strong low-level *T* inversion present in the simulated profiles limited the range at which P_{CT} was allowed to vary. A large distribution of random P_{CT} values

was found to be unsatisfactory for the case of a low-level temperature inversion, since T and $\log_e Q$ random errors calculated by (2.24) do not sufficiently alter the inversion height to match large random variations in P_{CT}. Other research based upon (2.24) considered only mid-level clouds with very large standard deviation of error (~ 425 hPa) for P_{CT}, or they only simulated only clear sky conditions (Eyre 1989a; Healy and Eyre 2000). In order to construct a set of background profiles physically consistent with the simulated MABL inversions, this dissertation allowed P_{CT} to randomly and uniformly vary within ± 20 hPa of "truth". The random error perturbations are calculated with these errors.

3. 1DVAR Retrieval Error and Performance for T and $\text{Log}_e Q$

Clear and cloudy sky 1DVAR retrievals were generated using the simulated background state vectors and simulated ATOVS observations described in the previous sections. The mean from equation (2.26) and standard deviation from equation (2.27) were calculated from the statistically significant number of simulated background state vectors and observation vectors. Only those retrievals that successfully converged were included in the error statistics. Reliability of the 1DVAR retrieval scheme, as applied to this mesoscale case study, was evaluated by comparing the simulated and theoretical retrieval errors. Agreement between the two indicates consistency of the retrieval method. Simulated retrieval error (σ_r) is compared with the square root of the principal diagonal of (2.28), where $\mathbf{S}_i$ is calculated at the final iteration and then averaged over the total number of successful retrievals. $\mathbf{S}_i$ is also used in this study to calculate the theoretical retrieval performance in (2.23). To calculate simulated retrieval performance, S_{ii} is replaced in (2.23) by the simulated retrieval error variance $(\sigma_r)^2$. Temperature profile (T) and $\log_e Q$ retrieval biases, defined as the retrieval mean normalized by the respective background error $(B_{ii})^{1/2}$, were calculated for each simulated retrieval.

a. Clear Sky T and $\log_e Q$ Retrievals

1DVAR simulated retrievals based upon a clear sky background state vector as "truth" are assumed clear and all cloud background errors were set to zero. When calculations were made with $\mathbf{B}_N$, approximately 99% of the 1DVAR retrievals converged in 10 iterations or less for clear sky EPAC Profile 1A and the U.S. Standard

Atmosphere background (Profile 3). Convergence rates at 10 iterations using $\mathbf{B_C}$ were reduced slightly to approximately 97%. In contrast, the convergence rate was approximately 86% for both of these profiles using the criterion of four iterations or less.

The absolute T and $\log_e Q$ background, theoretical, and simulated retrieval errors calculated with respect to $\mathbf{B_C}$ and $\mathbf{B_N}$ and the clear sky U.S. Standard Atmosphere profile are shown in Figs. 5.4a and 5.5a, respectively. Corresponding theoretical and simulated retrieval performance for this clear sky case is shown in Figs. 5.4b and 5.5b, and the normalized retrieval biases are shown in Figs. 5.4c and 5.5c. Similar comparisons are shown in Figs. 5.6a-c and 5.8a-c for clear sky EPAC Profiles 1A and 1B.

Radiative skin temperature (T_s) error and microwave emissivity (ε_m) error were set to zero to simulate perfect knowledge of these surface elements. Fig. 5.7a shows the effect of zero T_s error on T retrieval error and performance. The effect of zero ε_m error on $\log_e Q$ retrieval error and performance is shown in Fig 5.7b. For these simulations, H was linearized about clear sky EPAC Profile 1A.

Overall, there is good agreement between the simulated and theoretically derived T and $\log_e Q$ retrieval errors (Figs. 5.4a, 5.5a, 5.6a, and 5.8a) when calculated for the two different background error covariance matrices and various clear background state vectors. The results also substantiate the findings presented in Chapter IV that low-level humidity and temperature information should be able to be derived from ATOVS radiances. Small differences in $\log_e Q$ theoretical and simulated retrieval errors are most likely due to the linear versus non-linear assumptions.

Clear sky T and $\log_e Q$ retrieval biases (Figs. 5.4c, 5.5c, 5.6c, and 5.8c) are generally small, indicating a systematic agreement between the simulated retrievals and "truth". Temperature profile (T) biases are less than ~ |0.05| near the surface. $\mathrm{Log}_e Q$ retrieval biases are somewhat larger, but near the surface are ~|0.15| when calculated with respect to the COAMPS errors. Humidity biases are expected to be larger than for profile temperature since $H(\mathbf{x}^t)$ is not a linear function of $\log_e Q$ (Healy and Eyre 2000).

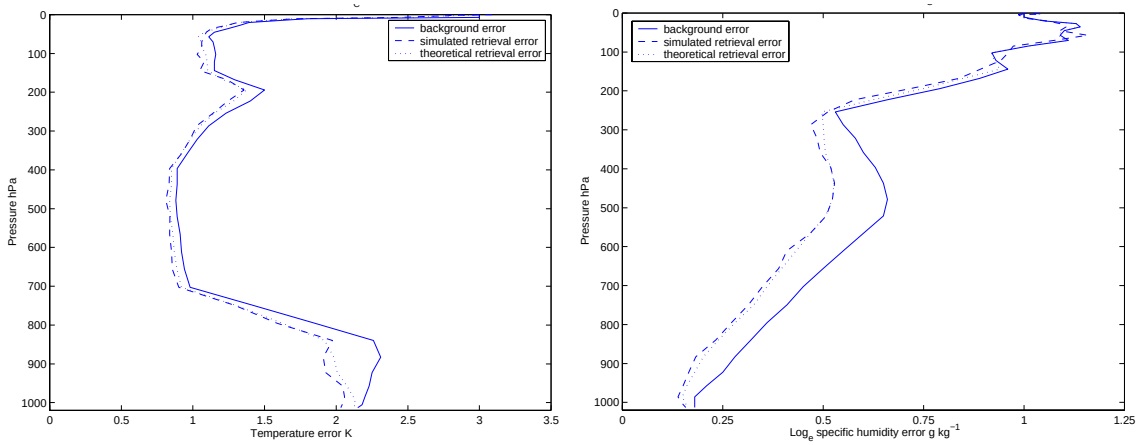

Figure 5.4a. Absolute T (left panel) and $\log_e Q$ (right panel) background errors $(B_{ii})^{1/2}$, theoretical retrieval errors $(S_{ii})^{1/2}$, and simulated retrieval errors (σ_r) calculated with respect to $\mathbf{B}_C$ and the clear sky U.S. Standard Atmosphere as "truth".

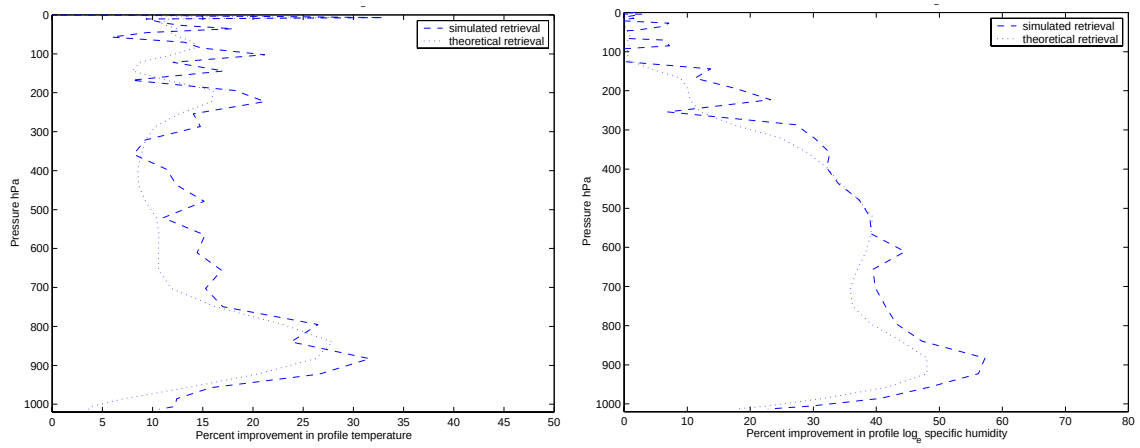

Figure 5.4b. As in Fig. 5.4a, except for simulated and theoretical retrieval performance.

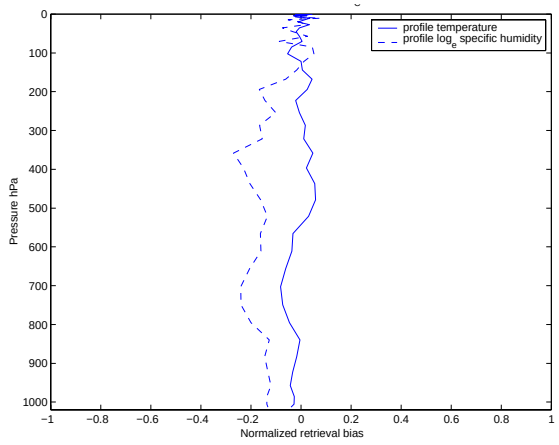

Figure 5.4c. Normalized retrieval bias for T and $\log_e Q$.

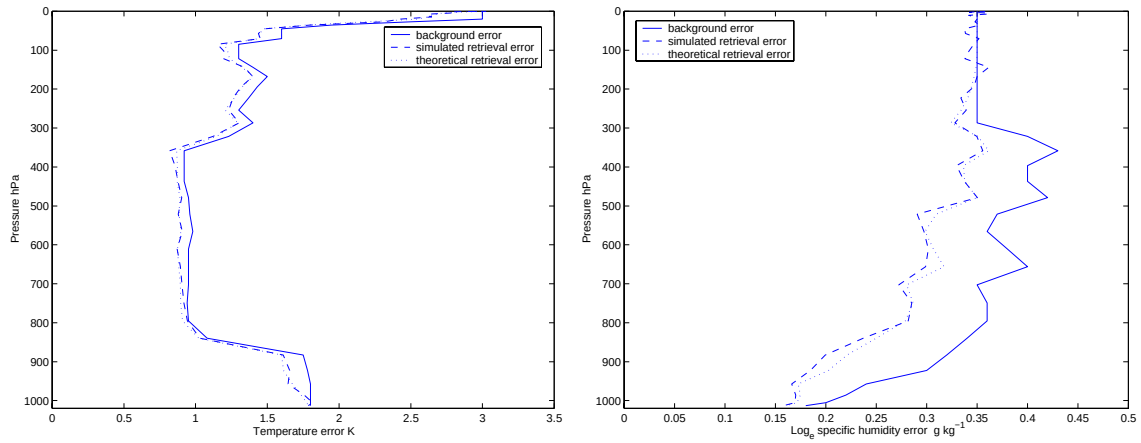

Figure 5.5a. As in Fig. 5.4a, except errors calculated with respect to $\mathbf{B_N}$.

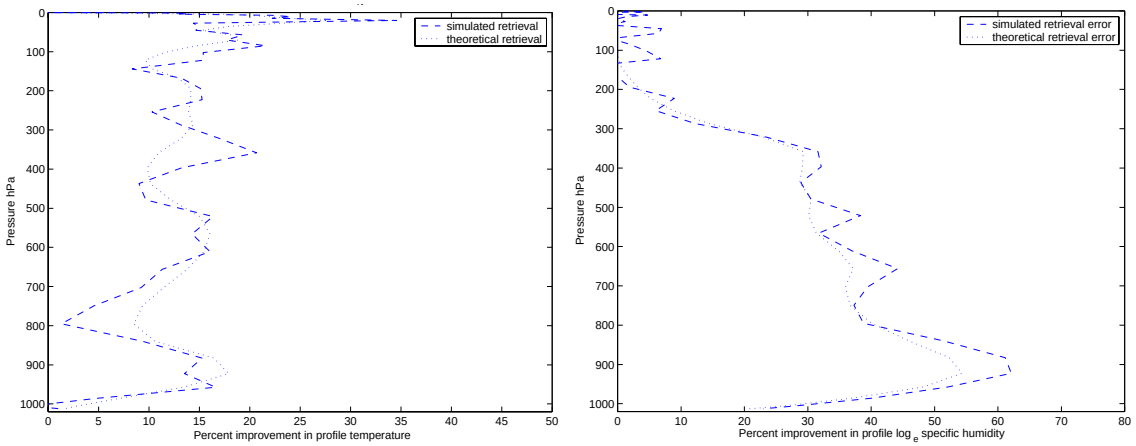

Figure 5.5b. As in Fig. 5.4b, except calculated with respect to $\mathbf{B_N}$.

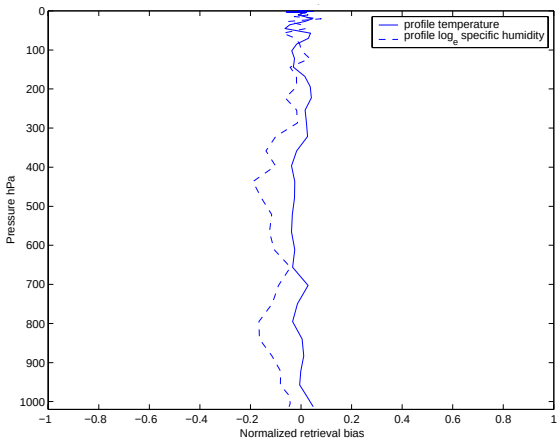

Figure 5.5c. As in Fig. 5.4c, except calculated with respect to $\mathbf{B_N}$.

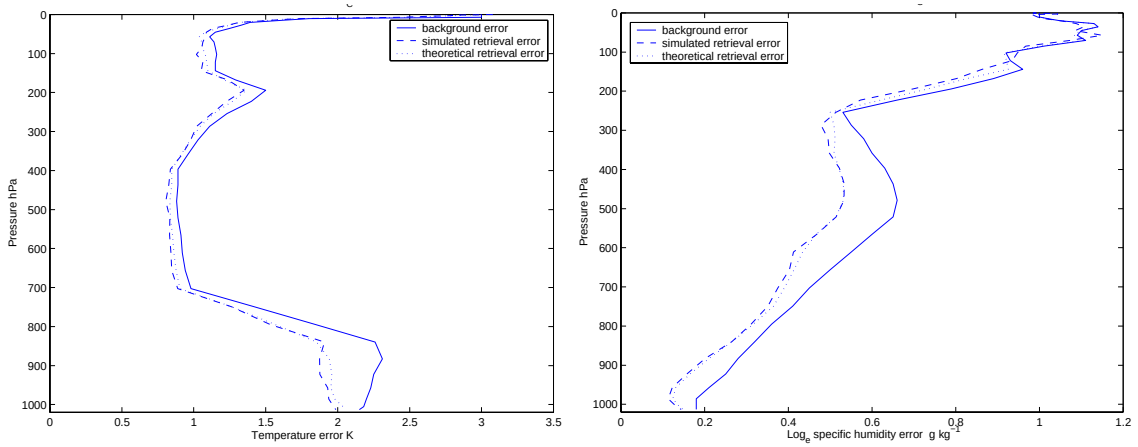

Figure 5.6a. As in Fig. 5.4a, except calculated with respect clear sky EPAC Profile 1A.

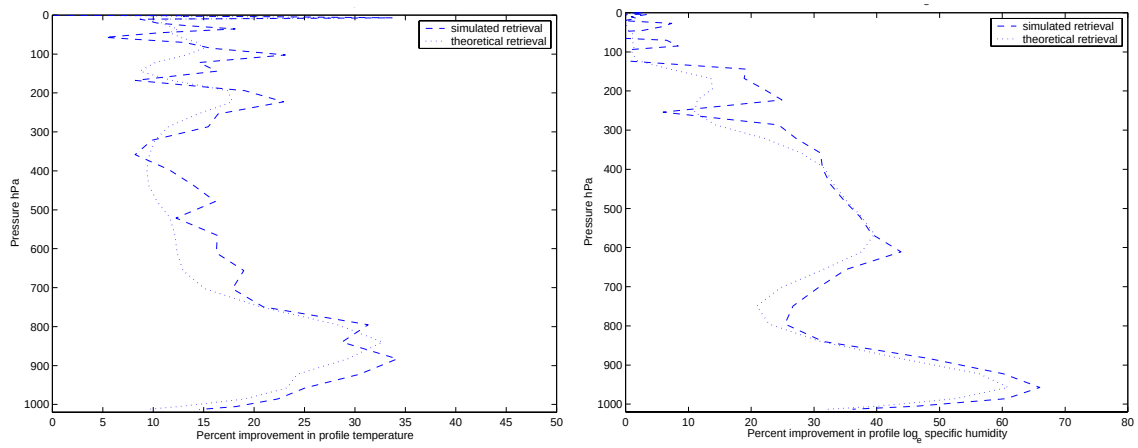

Figure 5.6b. As in Fig. 5.4b, except calculated with respect clear sky EPAC Profile 1A.

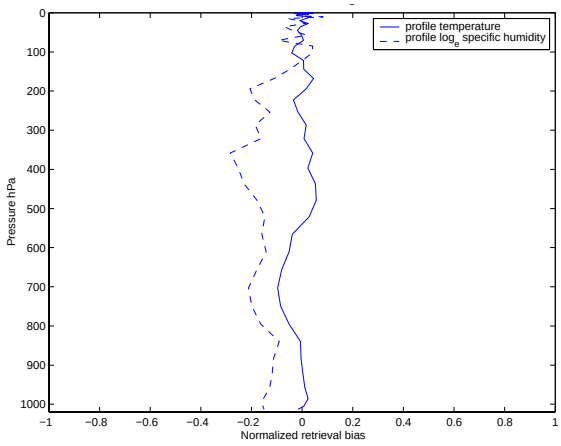

Figure 5.6c. As in Fig. 5.4c, except calculated with respect clear sky EPAC Profile 1A.

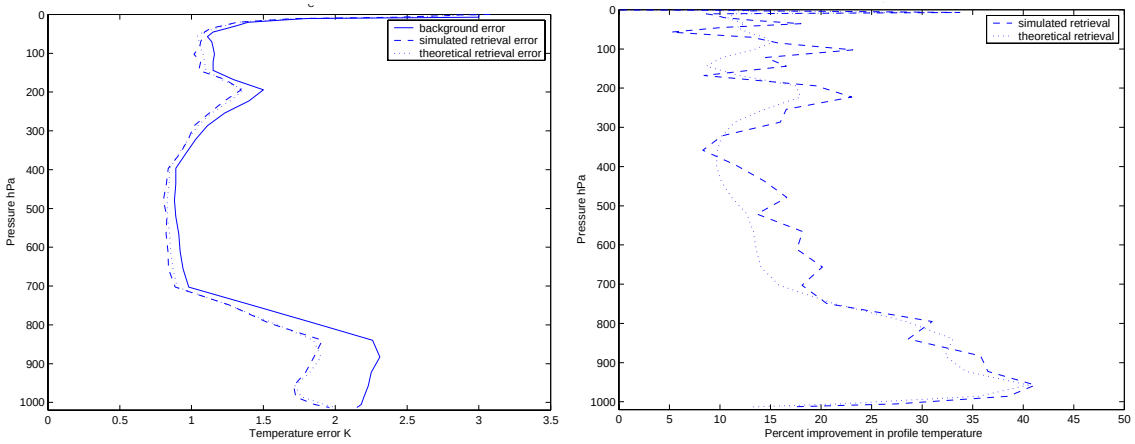

Figure 5.7a. As in Figs 5.6a and 5.6b, except for only *T* retrieval errors and performance calculated with T_s background error of 0.00 K.

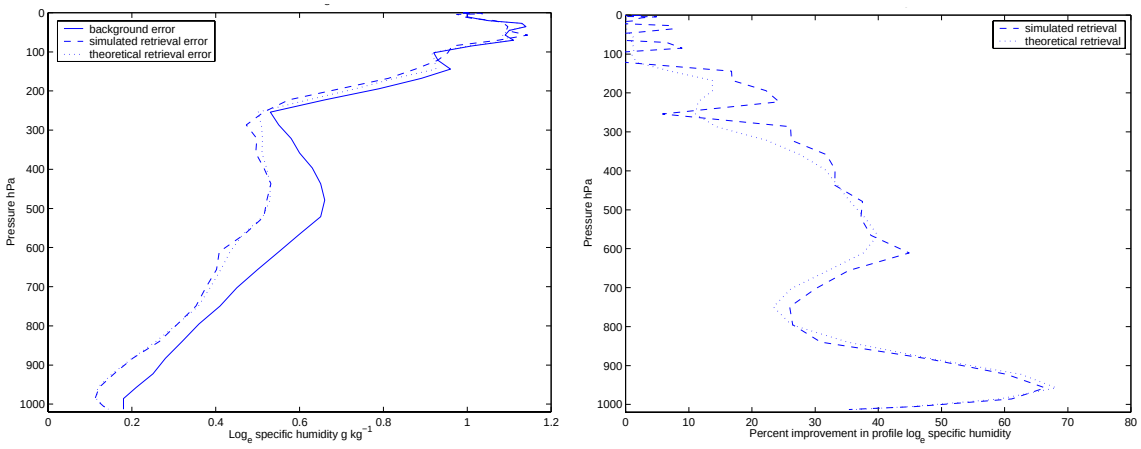

Figure 5.7b. As in Figs 5.6a and 5.6b, except for only $\log_e Q$ retrieval errors and performance calculated with ε_m background error of 0%.

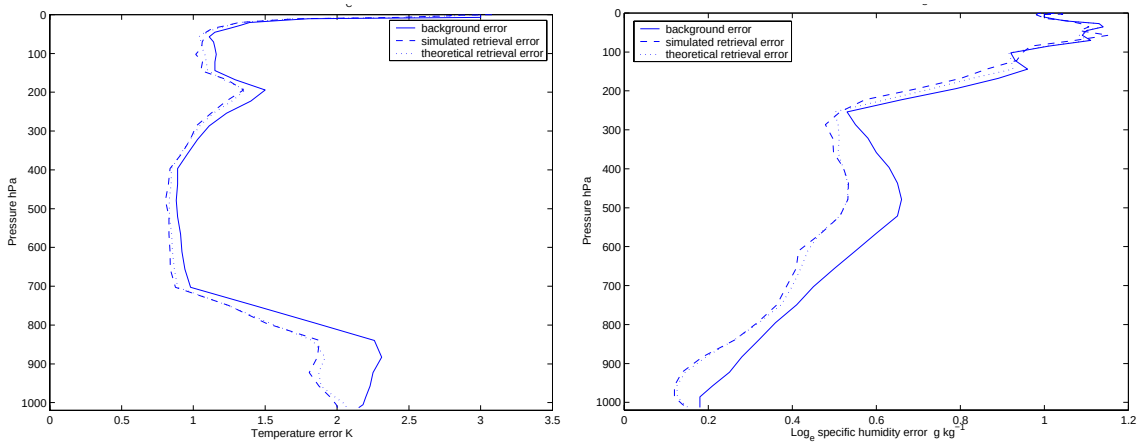

Figure 5.8a. As in Fig. 5.4a, except calculated with respect clear sky EPAC Profile 1B.

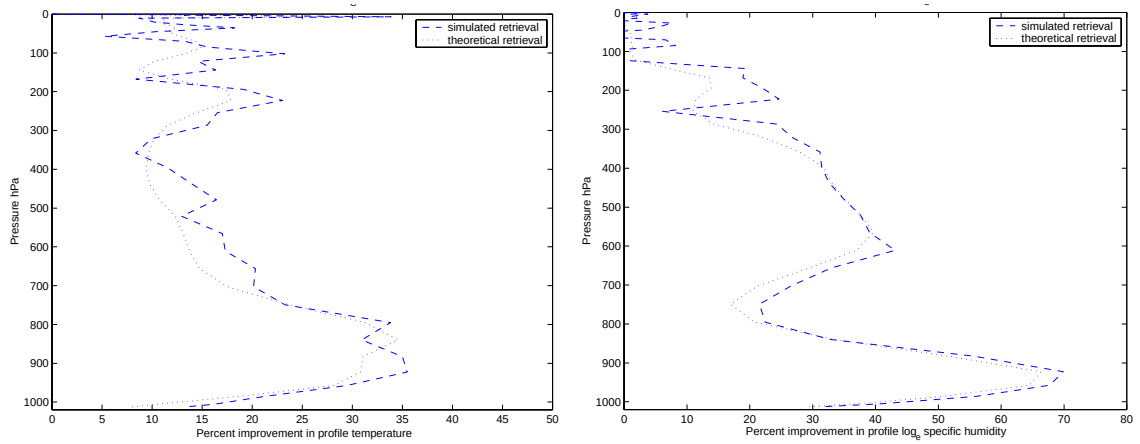

Figure 5.8b. As in Fig. 5.4b, except calculated with respect clear sky EPAC Profile 1B.

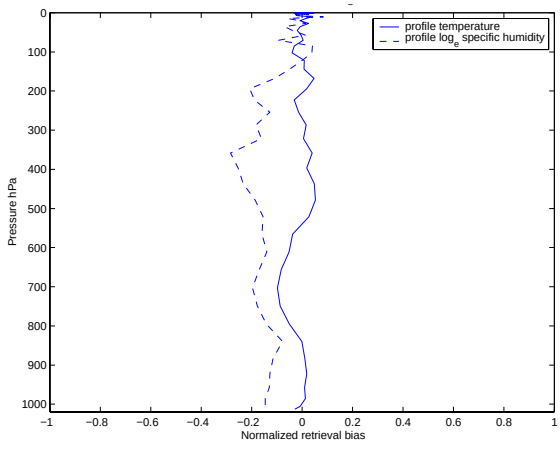

Figure 5.8c. As in Fig. 5.4c, except calculated with respect clear sky EPAC Profile 1B.

b. Cloudy Sky T and Log$_e$ Q Retrievals

Four sets of cloud background errors are used for the cloudy sky 1DVAR simulated retrievals. All cloudy sky simulations are performed using EPAC Profiles 2A1 and/or 2B2 as $\mathbf{x}^t$. For the first simulation (Figs 5.9a-c and 5.10a-c), P_{CT} is allows to randomly vary by 20 hPa in $\mathbf{x}^b$, C_{FC} is set to 0.50 (i.e., 50% fractional cloud cover) in $\mathbf{x}^t$ and is allowed to randomly vary in between 0.00 and 1.00. Cloud liquid water mixing ratio (*CLW*) was allowed to randomly vary in $\mathbf{x}^b$ between 0.00 and 0.50 g kg^{-1}. The background errors for P_{CT}, C_{FC} and *CLW* were set to 20 hPa, 0.50, and 0.25 g kg^{-1}. All other errors are the same as those used to calculate $\mathbf{B_C}$. The second case (Figs. 5.11a-c and 5.12a-c) simulates a fully cloud covered stratus-topped MABL in which background C_{FC} is perfectly known. For this case C_{FC} in both $\mathbf{x}^t$ and $\mathbf{x}^b$ was set to 1.00. All other errors are the same as in the first cloud case. The third case (Figs. 5.13 a-c) calculates simulated cloudy sky retrievals with respect to the cloud errors of case two, but uses larger low-level *T* errors of 5.00 K (see Fig. 5.2c). As previously discussed, these larger *T* errors might be necessary in order to properly represent the uncertainty in COAMPS cloud-top temperature. The fourth case (Fig. 5.14) sets the *CLW* error within the background to zero. In this case, it is assumed that *CLW* is perfectly known.

For cloudy sky cases, convergence rates were slightly less than those for the clear sky simulated retrievals. The convergence rates decreased to near 80% at 10 iterations for both cloudy sky EPAC profiles when no prior knowledge of cloud parameters was assumed. However, with perfect knowledge of cloud elements, approximately 96% converged in 10 iterations or less.

Overall, the theoretical and simulated retrieval errors for *T* (Figs. 5.9a, 5.10a, 5.11a, and 5.12a) are nearly equal with a consistent reduction in retrieval error at the cloud-top level. As expected from the information content study (Chapter IV), there is a larger reduction in retrieval error at this level when C_{FC} is perfectly known in the background state vector (as in Figs. 5.11a and 5.12a). The corresponding *T* retrieval performance is shown in Figs. 5.9b, 5.10b, 5.11b, and 5.12b.

Log$_e$ *Q* retrieval errors (performance) calculated from the simulated 1DVAR retrievals are generally smaller (larger) than the theoretical values with the greatest difference near 900 hPa (see Figs. 5.9b. 5.10b, 5.11b, and 5.12b). Non-linear

Newtonian iteration (2.14) is expected to produce better results with respect to non-linear $\log_e Q$ retrievals. Results of the corresponding simulated retrieval performance calculations are consistent with the cloud error sensitivity study (Chapter III.C), which showed reduced low-level T retrieval performance due to *a priori* errors in P_{CT} and C_{FC} and reduced $\log_e Q$ retrieval performance due to CLW error.

As with the clear sky cases, there is generally good agreement between the simulated and theoretically calculated T and $\log_e Q$ errors, except where there is relatively large normalized retrieval bias. Retrieval biases for the cloudy sky cases depend on prior knowledge of cloud parameters and magnitude of low-level temperature errors. Temperature profile (T) biases are still relatively small when C_{FC} is set to 0.50 in the "truth" and cloud elements for P_{CT}, C_{FC}, and *CLW* are allowed to randomly vary by 20 hPa, 0.50, and 0.25 g kg^{-1} (Fig. 5.10c). For the case when C_{FC} is set to 1.00 in "truth" and *a priori* error to zero (i.e., cloudy known to be cloudy) and all other errors are unchanged, T biases of ~|0.35| are observed at the level corresponding to the "true" cloud top (e.g., Fig. 5.12b). As shown in Fig. 5.13c, these cloud-top temperature biases were reduced by increasing low-level temperature errors to 5.00 K. The larger low-level T errors may allow the 1DVAR retrieval to better match cloud-top temperature with P_{CT}, but might also degrade the T retrieval below cloud-top. This negative impact on the T retrieval is suggested by the larger absolute T retrieval errors shown in Fig. 5.13a.

Fig. 5.14 shows the smaller retrieval errors and corresponding improved $\log_e Q$ retrieval performance when *CLW* is perfectly known within the background state vector. There is also a much closer match between the simulated retrieval errors and theory.

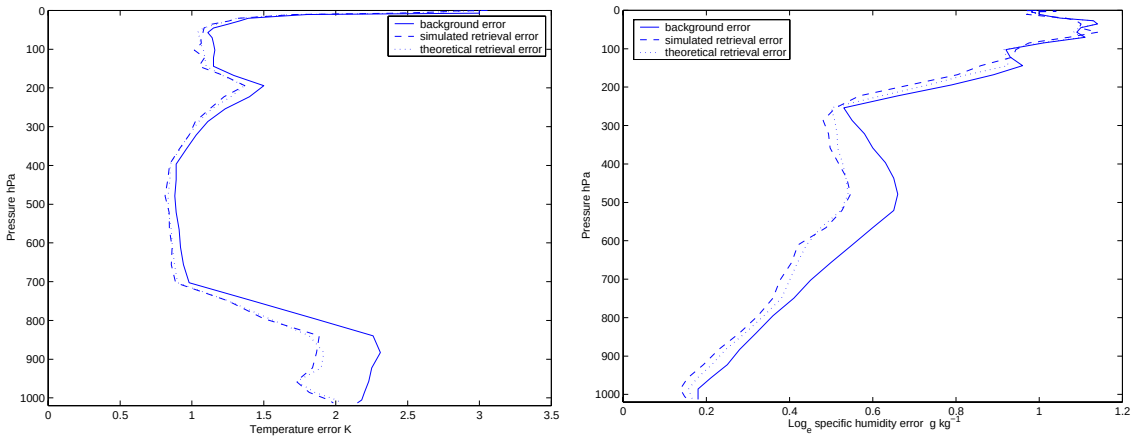

Figure 5.9a. Absolute T (left panel) and $\log_e Q$ (right panel) background errors $(B_{ii})^{1/2}$, theoretical retrieval errors $(S_{ii})^{1/2}$, and simulated retrieval errors (σ_r) calculated with respect to $\mathbf{B}_C$ and cloudy sky EPAC Profile 2A1 as "truth". C_{FC} set to 0.50 in "truth" and the cloud errors for P_{CT}, C_{FC} and CLW are 20 hPa, 0.50, and 0.25 g kg^{-1}, respectively.

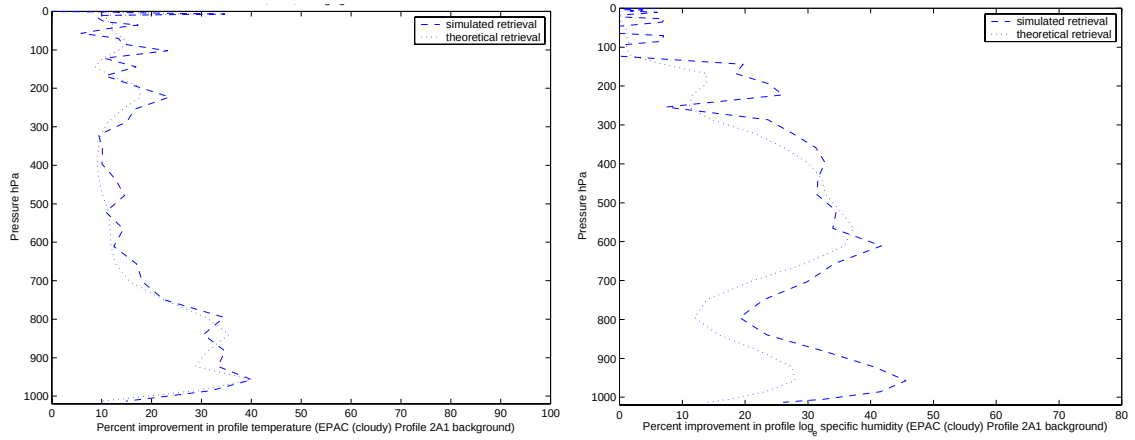

Figure 5.9b. As in Fig. 5.9a, except for simulated and theoretical retrieval performance.

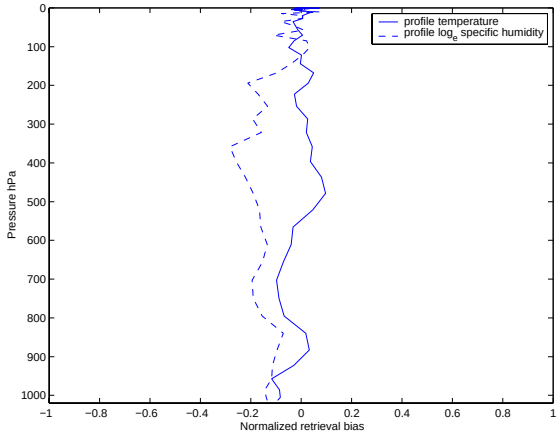

Figure 5.9c. As in Fig. 5.9a, except for normalized retrieval bias for T and $\log_e Q$.

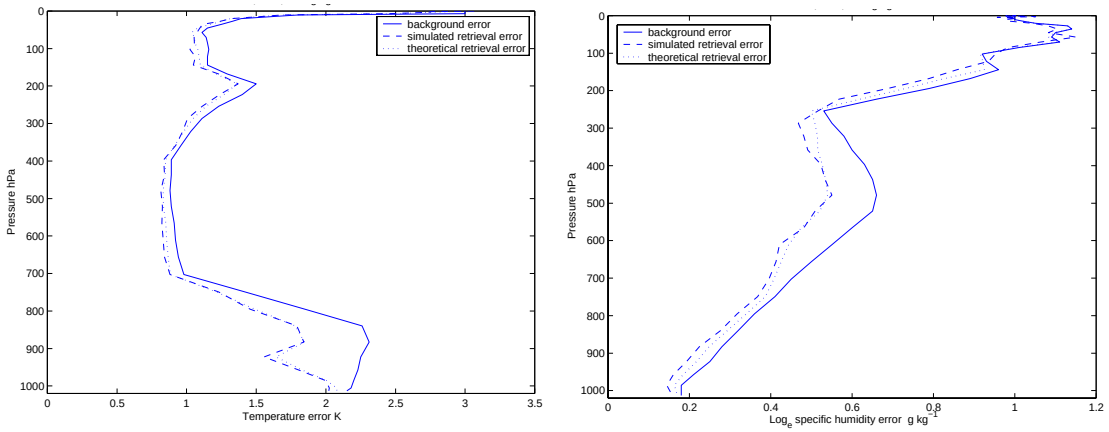

Figure 5.10a. As in Fig. 5.9a, except calculated with respect to cloudy sky EPAC Profile 2B2.

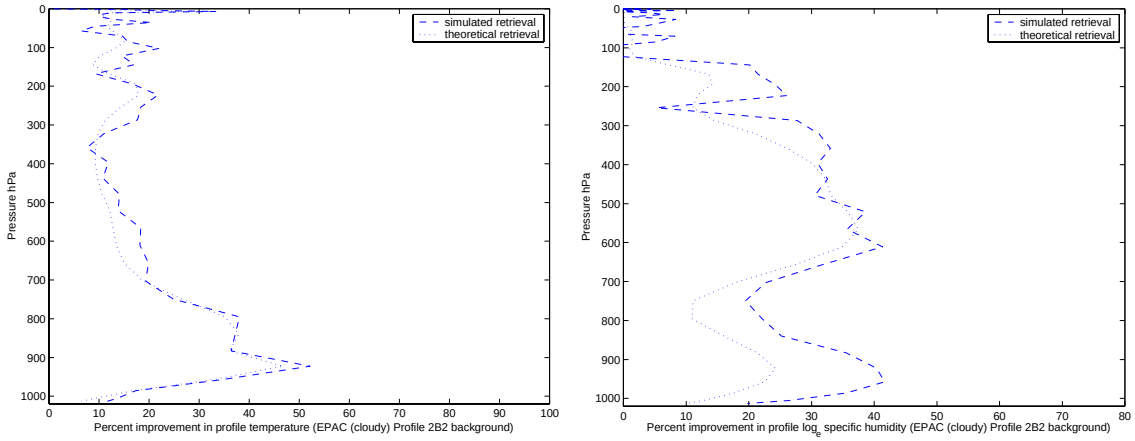

Figure 5.10b. As in Fig. 5.9b, except calculated with respect to cloudy sky EPAC profile 2B2.

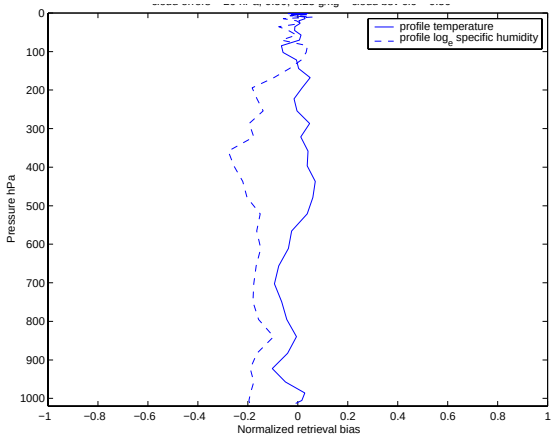

Figure 5.10c. As in Fig. 5.9c, except calculated with respect to cloudy sky EPAC Profile 2B2.

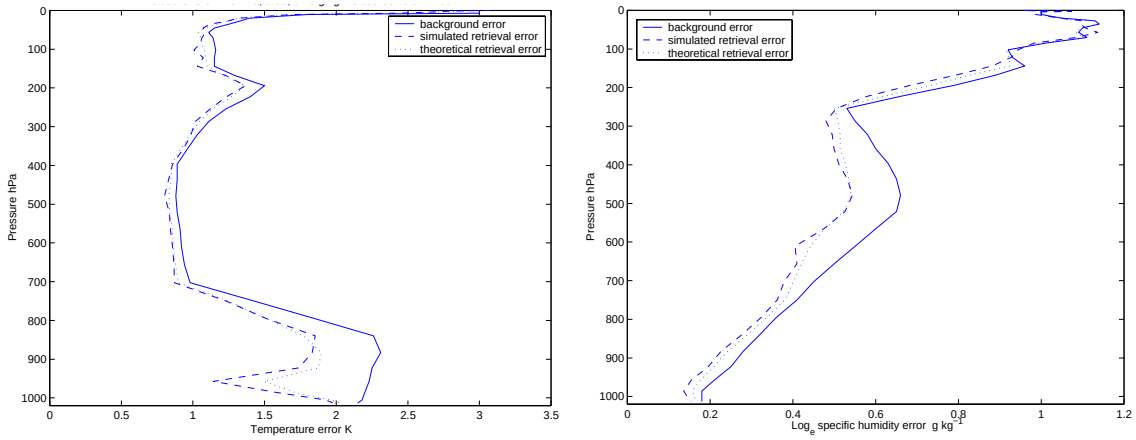

Figure 5.11a. Absolute T (left panel) and $\log_e Q$ (right panel) background errors $(B_{ii})^{1/2}$, theoretical retrieval errors $(S_{ii})^{1/2}$, and simulated retrieval errors (σ_r) calculated with respect to $\mathbf{B}_C$ and cloudy sky EPAC Profile 2A1 as "truth". C_{FC} set to 1.00 in "truth" and cloud errors for P_{CT}, C_{FC} and CLW are 20 hPa, 0.00, and 0.25 g kg^{-1}, respectively.

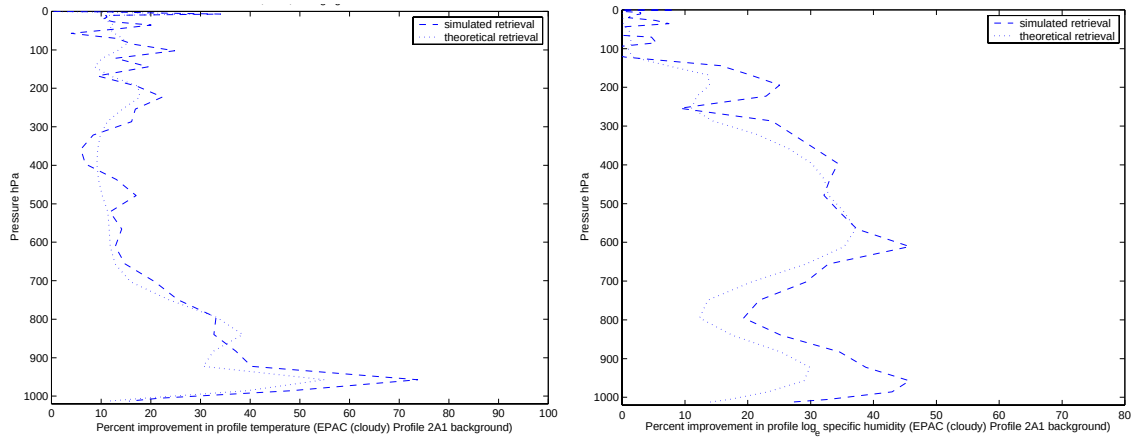

Figure 5.11b. As in Fig. 5.11a, except for simulated theoretical retrieval performance.

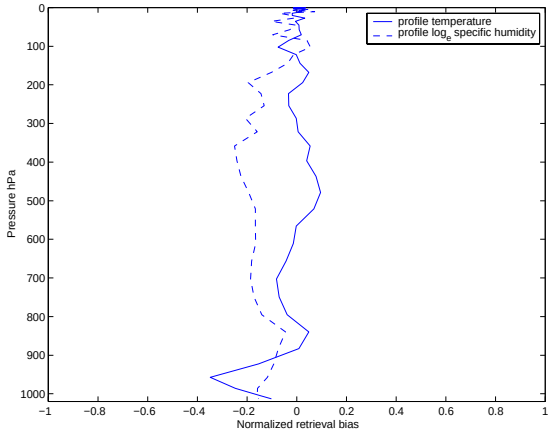

Figure 5.11c. As in Fig. 5.11a, except for normalized retrieval bias.

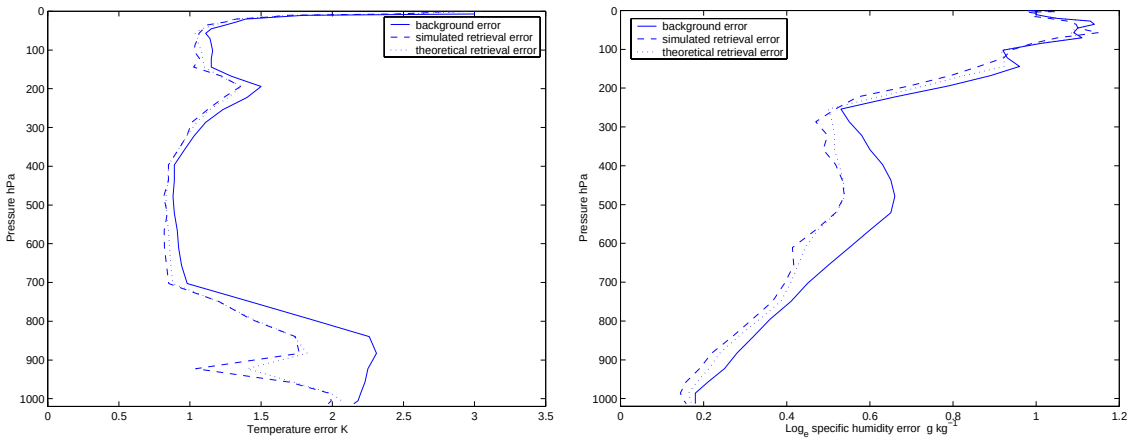

Figure 5.12a. As in Fig. 5.11a, except calculated with respect to cloudy sky EPAC Profile 2B2.

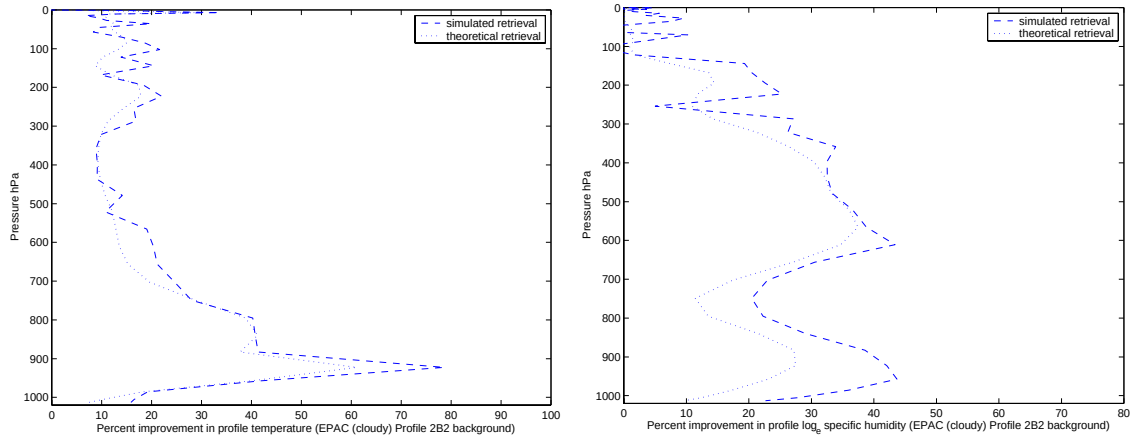

Figure 5.12b. As in Fig. 5.11b, except calculated with respect to cloudy sky EPAC Profile 2B2.

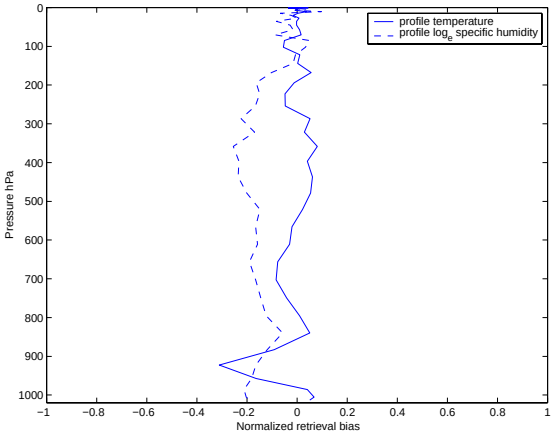

Figure 5.12b. As in Fig. 5.11c, except calculated with respect to cloudy sky EPAC Profile 2B2.

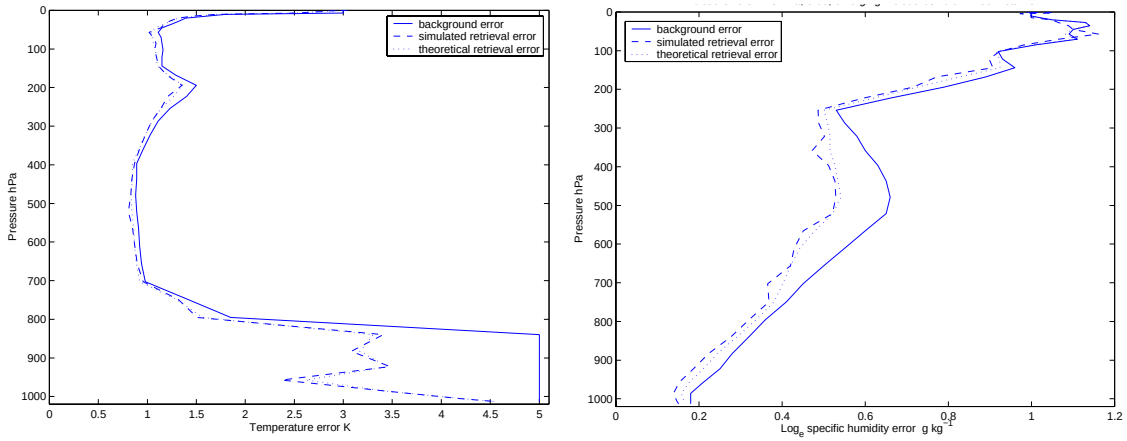

Figure 5.13a. As in Fig. 5.11a, except background *T* errors set to 5.00 K at levels 37-43 (839.95 – 1013.25 hPa).

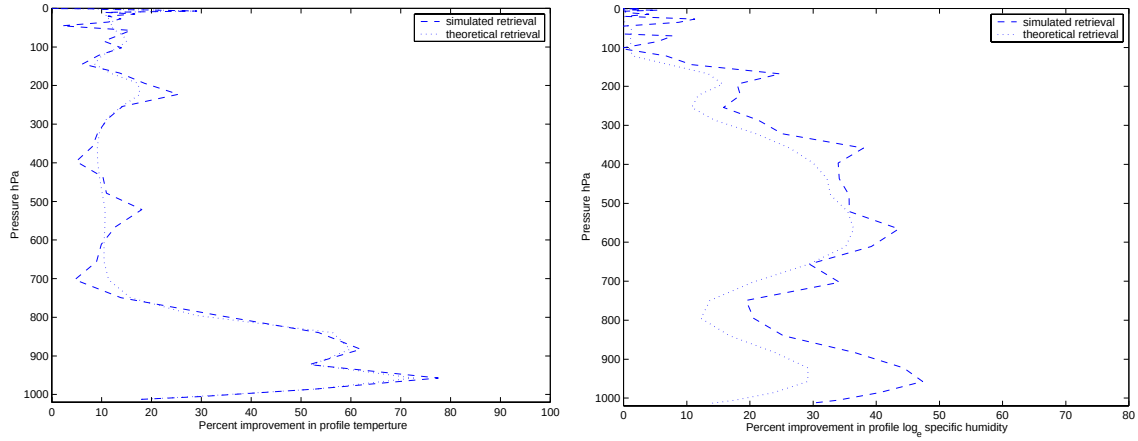

Figure 5.13b. As in Fig. 5.11b, except background *T* errors set to 5.00 K at levels 37-43.

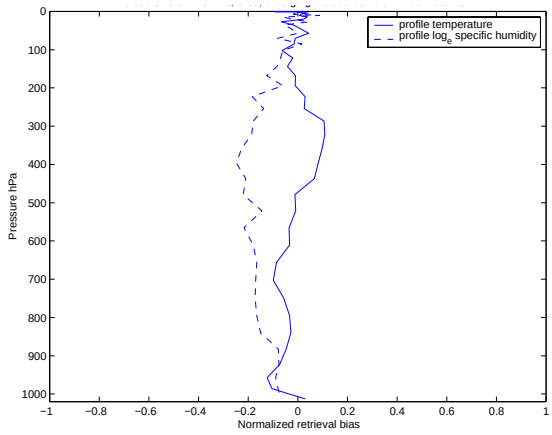

Figure 5.13c. As in Fig. 5.11c, except background *T* errors set to 5.00 K at levels 37-43.

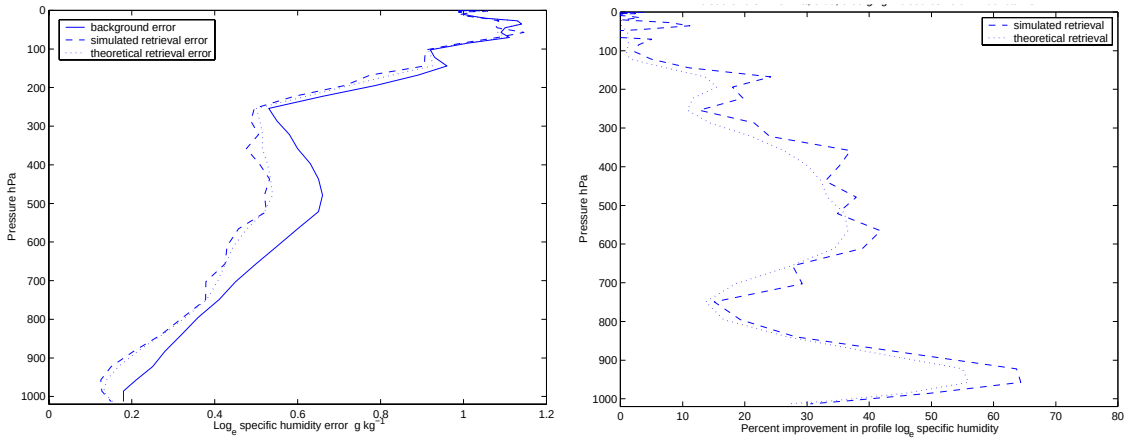

Figure 5.14. As in Figs. 5.11a-b, except for $\log_e Q$ retrieval errors (left panel) and performance (right panel) were the *CLW* background errors were set to 0.00 g kg^{-1}.

4. Surface and Cloud Parameter Retrieval Errors

Simulated retrieval errors and biases for P_s, T_s, P_{CT}, and *CLW* calculated with respect to $\mathbf{B}_C$ and the cloud errors described below are listed in Table 5.1. The corresponding theoretical retrieval errors are shown for comparison. Clear sky EPAC Profiles 1A and 1B and the U.S. Standard Atmosphere (Profile 3) are known to be clear. Cloudy sky retrieval errors are calculated with errors of 20 hPa, 0.50, and 0.25 g kg^{-1} for P_{CT}, C_{FC}, and *CLW*. C_{FC} in the cloudy sky EPAC Profiles 2A1 and 2B2 "true" profiles is set to 0.50. Clear sky retrieval errors are small for T_s (e.g., 0.27 K for EPAC Profile 1A) with a corresponding retrieval performance of approximately 97%. Cloudy sky retrieval errors are much larger (e.g., 1.44 K for EPAC Profile 2A1) with a corresponding retrieval performance of approximately 16%. Retrieval errors for P_s are also smaller for the clear sky cases, but the corresponding retrieval performance is approximately 27% for EPAC Profile 1A. Retrieval errors for P_{CT} and *CLW* are both reduced with respect to background.

Table 5.1. Background errors $(B_{ii})^{1/2}$, simulated retrieval errors (σ_r) and biases for surface pressure (P_s), radiative skin temperature (T_s), cloud-top pressure (P_{CT}), and cloud liquid water mixing ratio (*CLW*). Cloud errors are 25 hPa for P_{CT}, 0.50 for C_{FC}, and 0.25 g kg^{-1} for *CLW*. Results are calculated with respect to $\mathbf{B}_C$ and for cloudy sky EPAC Profiles 2A1 and 2B2. Theoretical retrieval errors are shown for comparison.

	$(B_{ii})^{1/2}$	Simulated retrieval error (σ_r) and bias				
Surface parameter		Profile 1A	Profile 1B	Profile 2A1	Profile 2B2	Profile 3
P_s retrieval error (hPa)	3.38	2.88	2.91	3.01	3.13	2.83
P_s retrieval bias		-0.08	-0.09	-0.04	-0.02	-0.09
T_s retrieval error (K)	1.57	0.27	0.29	1.44	1.53	0.23
T_s retrieval bias		0.00	0.00	-0.06	0.02	0.00
P_{CT} retrieval error (hPa)	20			11	11	
P_{CT} retrieval bias				< 1	< 1	
CLW retrieval error (g kg^{-1})	0.25			0.21	0.23	
CLW retrieval bias				0.02	0.02	

	$(B_{ii})^{1/2}$	Theoretical retrieval error $(S_{ii})^{1/2}$				
Surface parameter		Profile 1A	Profile 1B	Profile 2A1	Profile 2B2	Profile 3
P_s retrieval error (hPa)	3.38	2.93	2.95	3.14	3.21	2.88
T_s retrieval error (K)	1.57	0.28	0.30	1.34	1.38	0.24
P_{CT} retrieval error hPa)	20			5	8	
CLW retrieval error (g kg^{-1})	0.25			0.23	0.24	

5. 1DVAR Simulated *T* and Log$_e$ *Q* Retrievals

The discussion thus far has quantified the 1DVAR retrieval in terms of theoretical or simulated retrieval error. This measure has been used to determine the retrieval performance with respect to the background, which has allowed for a thorough assessment of information content and reliability of 1DVAR retrievals for mesoscale applications. The reduction in retrieval (analysis) error is also important with respect to NWP data assimilation efforts.

The simulated retrievals ($\mathbf{x}$) derived from the 1DVAR minimization process (2.14) are used along with $\mathbf{x}^t$ to calculate the retrieval error standard deviation (2.27). In this context when the solution is dependent upon a significant number of simulated background state vectors ($\mathbf{x}^b$), the individual retrievals $\mathbf{x}$ are not very meaningful by themselves. It is only when averaged over the large number of realizations that the error statistics are significant. However, individual $\mathbf{x}$ can demonstrate the 1DVAR minimization process with respect to how the solution is adjusted toward "truth".

An example of a T and $\log_e Q$ simulated retrieval that converged in 10 iterations of less (hereby defined as a "successful retrieval") is shown in Fig. 5.15. This successful retrieval was calculated with respect to the clear sky EPAC Profile 1A as $\mathbf{x}^t$ For this case the solution converged in 2 iterations and overall, the retrieved T and $\log_e Q$ profiles were adjusted closer to $\mathbf{x}^t$. The exception is for T below the temperature inversion. Here $\mathbf{x}$ moved further from $\mathbf{x}^t$ as the solution is moved closer to "truth" directly above the inversion. This result may indicate a limitation of the 1DVAR scheme. A cloudy sky T and $\log_e Q$ retrieval is shown in Fig. 5.16. Again, the complete $\log_e Q$ retrieved profile is moved closer to "truth" by the simulated observation. The T retrieval does well above the temperature inversion, but adjusts only slightly toward "truth".

One of the retrievals that failed to converge in 10 iterations or less is shown for a cloudy sky case in Fig. 5.17. The reason that this profile did not converge is most likely due to the inherent non-linear nature of the cloudy sky retrieval problem, or is due to the inability of the 1DVAR scheme to simultaneously retrieve one or more of the randomly generated cloud elements. By design the simulated T, $\log_e Q$, and surface array elements are generated to be consistent with the errors in $\mathbf{B_C}$. However, the random cloud elements are calculated differently and may not always be consistent with the T and $\log_e Q$ profile.

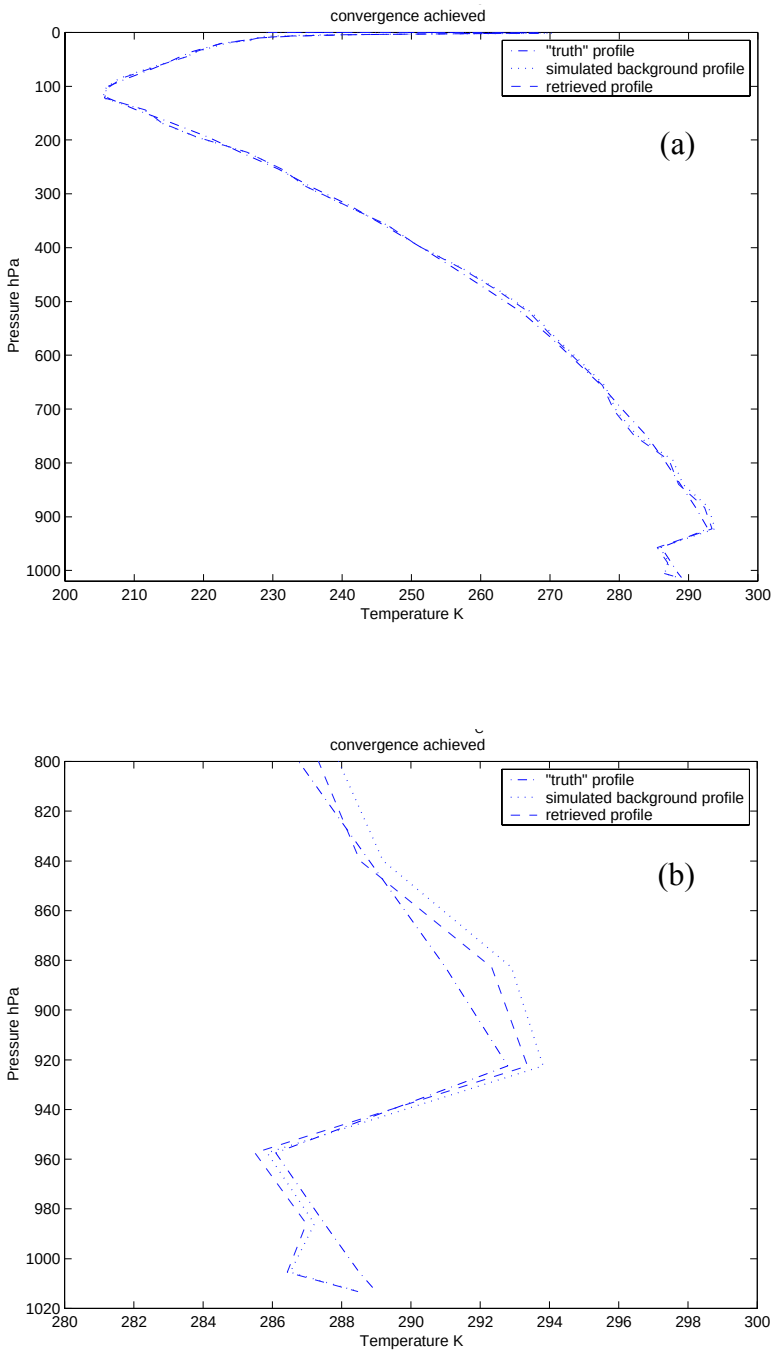

Figure 5.15. Example of a "successful" (a) T and (c) $\log_e Q$ simulated retrieval with clear sky EPAC Profile 1A. Convergence was achieved in 2 iterations. An expanded view of the lower atmosphere for (a) and (c) is provided in (b) and (d), respectively.

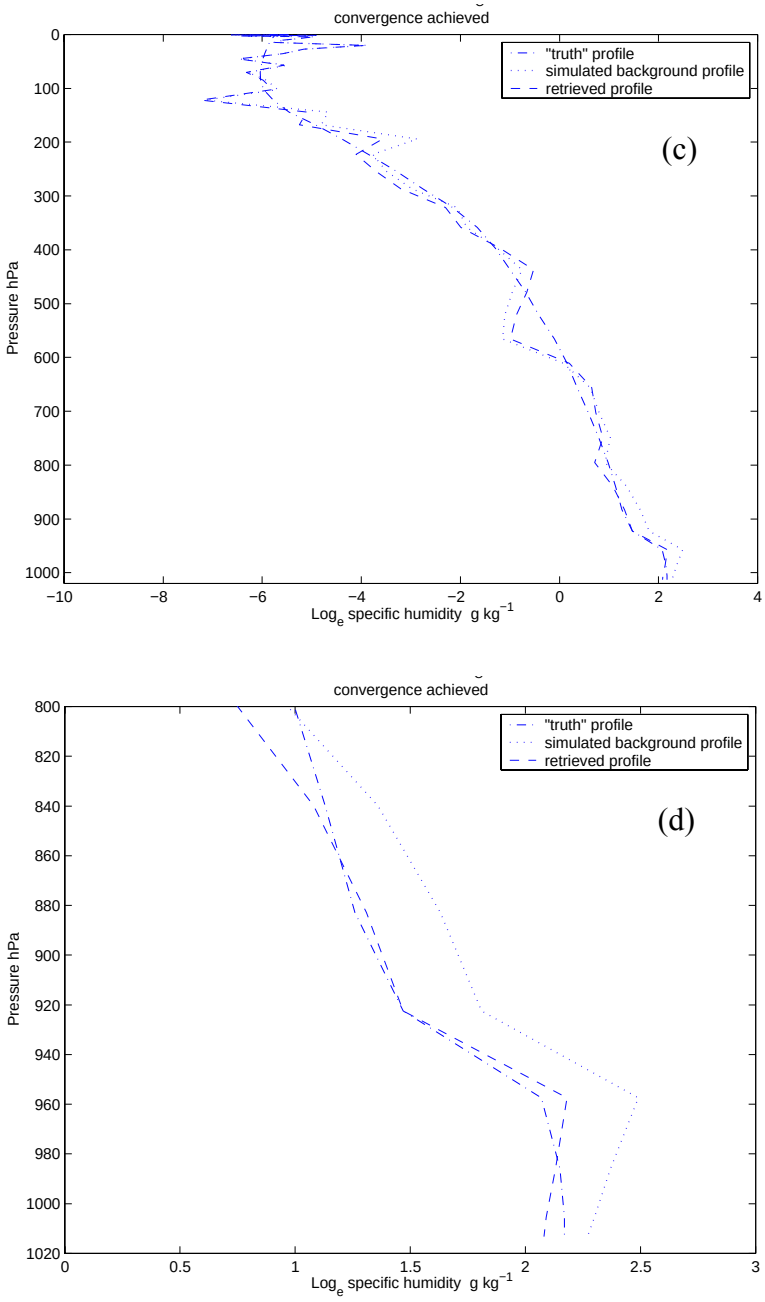

Figure 5.15. Continued.

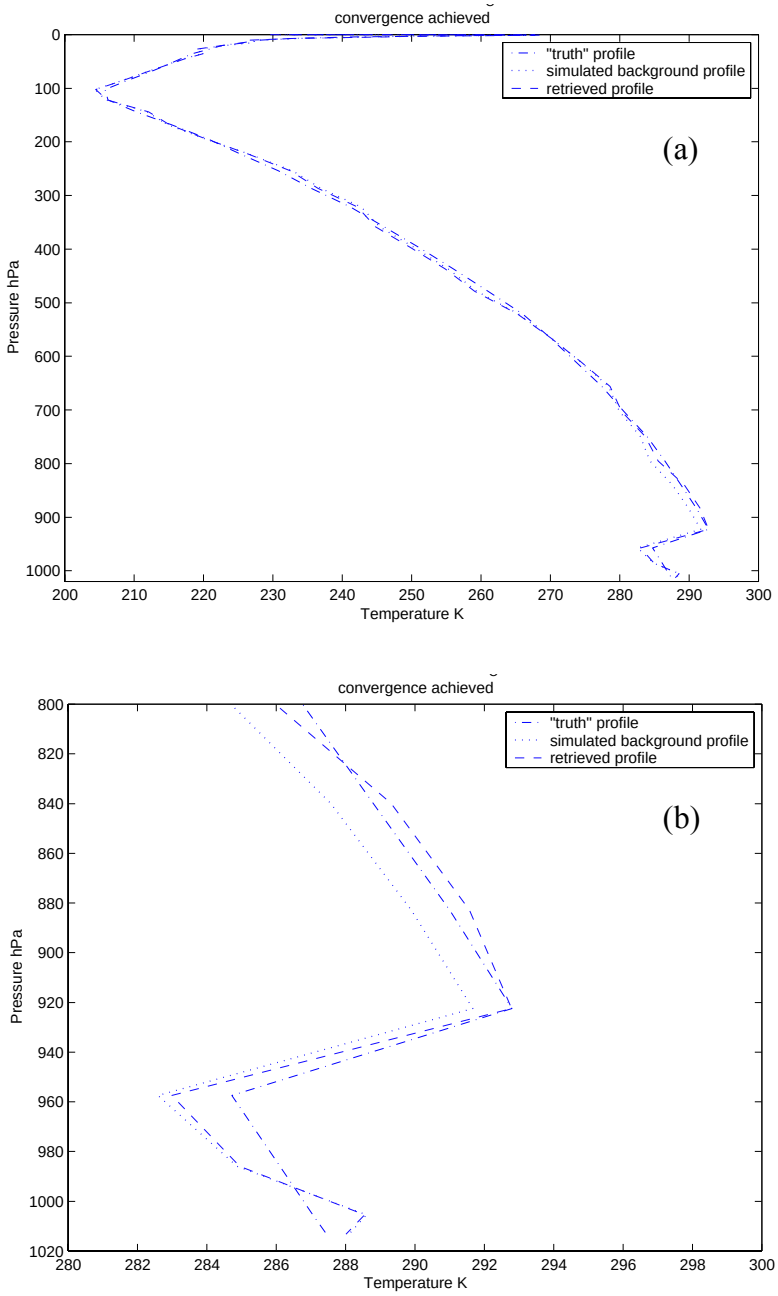

Figure 5.16. As in Fig. 5.15, except for cloudy sky EPAC Profile 2A1.

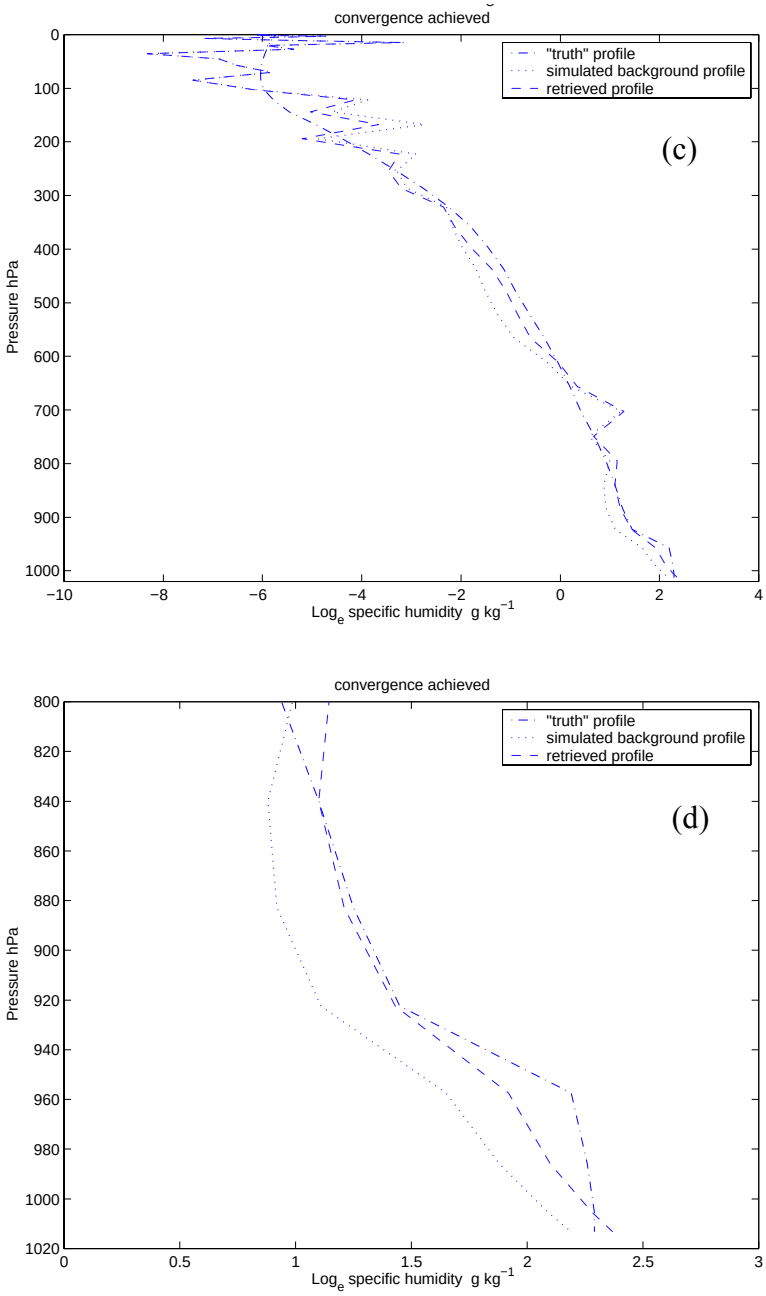

Figure 5.16. Continued.

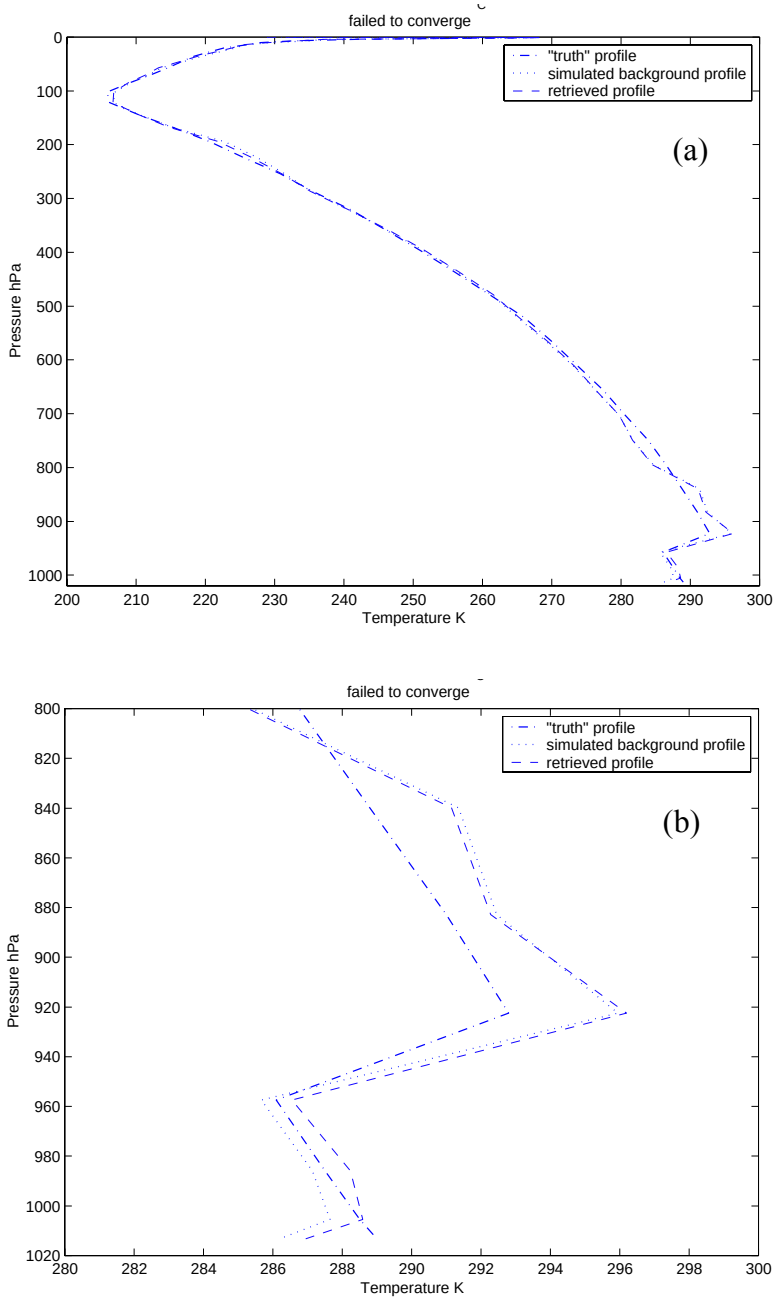

Figure 5.17. As in Fig. 5.16, except is an example of retrieval that failed to converge in 10 iterations or less.

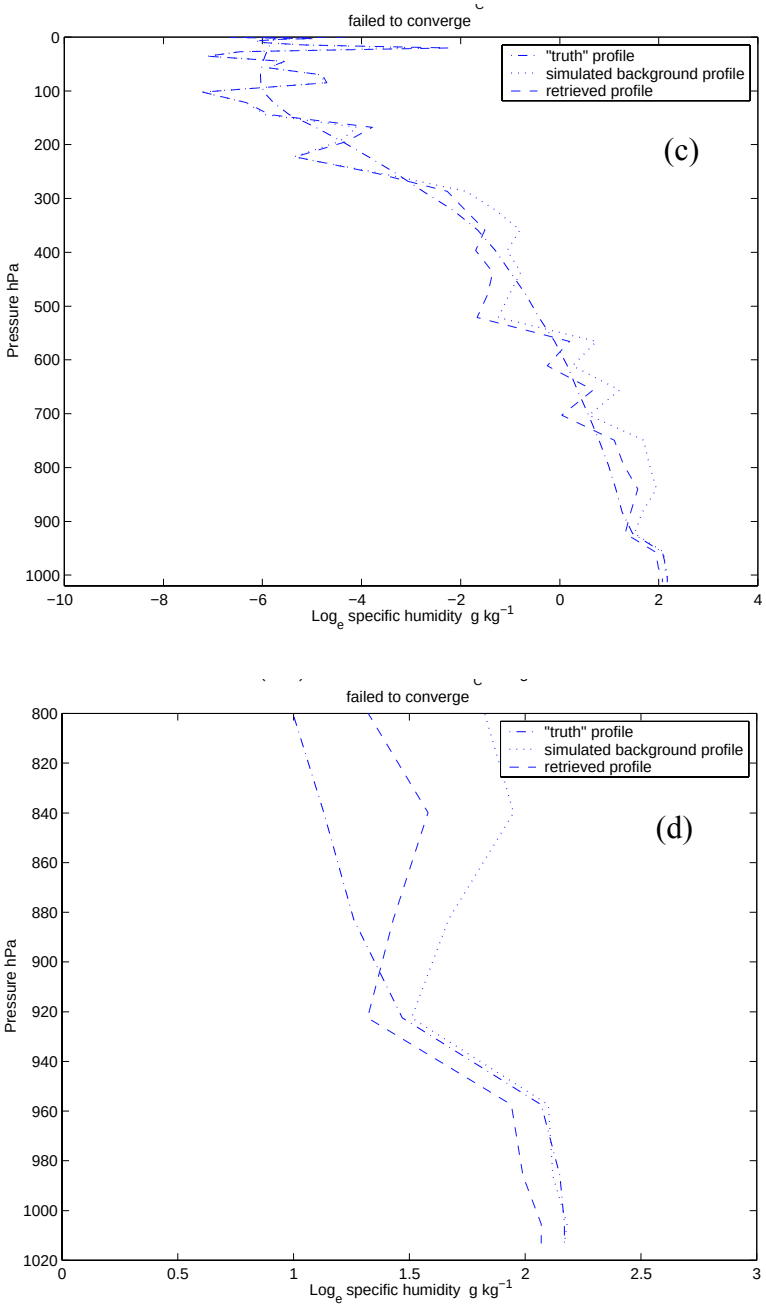

Figure 5.17. Continued.

6. Section Summary

The purpose of this study was to determine if the NRL 1DVAR scheme could, for a number of representative clear and cloud sky cases, produce retrievals errors consistent with theory. 1DVAR retrievals were generated using a statistically significant number of simulated background profiles and simulated ATOVS observations. Simulations were conducted using the representative EPAC background state vectors as "truth" and the retrievals were calculated with respect to the COAMPS model specific background error covariance matrix $\mathbf{B_C}$. Results were also compared with those calculated using the U.S. Standard Atmosphere and the globally averaged NOGAPS error covariance matrix $\mathbf{B_N}$.

This study found generally good agreement between the retrieval errors calculated using non-linear iteration and the corresponding theoretical values. Clear sky retrieval cases compared better to theory than the cloudy sky retrievals, but overall, the differences were relatively small. This result demonstrates the consistency and reliability of the NRL 1DVAR retrieval scheme for this mesoscale application.

B. 1DVAR SIMULATED RETRIEVALS WITH COAMPS BACKGROUND STATE VECTORS AND SIMULATED ATOVS OBSERVATIONS

The 1DVAR retrievals that were discussed in the previous section were calculated using a statistically significant number of simulated background state vectors and simulated observation vectors. Retrieval error statistics were then calculated from the 1DVAR retrievals and compared with the theoretically derived retrieval errors. This comparison confirmed that through the 1DVAR retrieval method, significant humidity and temperature information could be obtained for the summertime EPAC environment.

This section presents the results of 1DVAR retrievals generated using simulated ATOVS observations and COAMPS background state vectors derived from the Dynamics and Chemistry of Marine Stratocumulus (DYCOMS) Phase II data set. The DYCOMS II field experiment was conducted off–shore of southern California, near 31 N, 122 W, between 7 – 28 July 2001 (see Stevens et al. 2002). The COAMPS forecast fields were obtained for this research from the University Corporation for Atmospheric Research / Joint Office for Science Support (UCAR / JOSS) and were used "as is" with

no additional quality control. The purpose of this research, thus far, is to simply demonstrate the 1DVAR retrieval technique using COAMPS short-term forecasts as the background state vectors. Chapter II.B provides an overview of the COAMPS model.

The simulated ATOVS observations are calculated in the same manner as previously discussed, except in this case the forward model $H(\mathbf{x}^t)$ was linearized about a collocated European Centre for Medium Range Weather Forecasting (ECMWF) forecast profile. The 60 vertical level "true" profile ($\mathbf{x}^t$) was also obtained from the UCAR/JOSS DYCOMS II data set and represents the averaged values for the area 30.0 – 32.5 N, 120.0 – 124.5 W.

The appropriate 30 sigma level and surface forecast fields from COAMPS 3rd nested grid (horizontal grid distance of 6 km) are used as background state vectors ($\mathbf{x}^b$). Above the COAMPS model top at 10 hPa, the collocated ECMWF profile data were used. The COAMPS inner nest was used since all required forecast fields were available at this grid space resolution. Grid point (1,1) for the 3rd nested grid is at approximately 30.15 N and 123.12 W with 61 grid points in the E-W direction and 49 in the N-S direction. The set of $\mathbf{x}^b$ used in this research excludes the outer 5 grid points and includes only every third grid point for a total of 663, which reduces the effective horizontal grid spacing to 18 km. The associated outer grids are at horizontal grid spacing of 18 and 54 km. COAMPS 6-, or 9-hr T, $\log_e Q$, and CLW forecasts at 30 sigma levels were interpolated to the 43 RTTOV-6 pressure levels. Overall, the vertical interpolation resulted in little loss of model profile structure, even in the MABL. However, the potential does exist for loss of important profile features, such as the inversion base and CLW amount. For example, CLW within a relatively shallow MABL may only be represented in a forecast model at one or two vertical levels and may be lost, or diminished in magnitude after interpolation to the fixed RTTOV-6 pressure levels (see Table 3.2). Model surface fields were used directly and as before, SST is used as proxy for T_s.

Two cloudy sky case studies using the DYCOMS II data set are presented in this section. The first is based on the 9-hr COAMPS forecasts valid at 0900Z 11 July 2001 and the second cloud case uses 6-hr COAMPS forecasts valid at 1800Z 15 July 2001.

1DVAR simulated T and $\log_e Q$ retrievals are calculated for various sets of cloud and low-level T background errors. Theoretical retrieval errors and performance calculated from the diagonal of $\mathbf{S}_i$ (2.28) are shown for selected cases.

1. Case Study: 0900Z 11 July 2001

This 1DVAR retrieval case study was conducted using COAMPS 9-hr forecasts as the set of $\mathbf{x}^b$ and the collocated averaged ECMWF 21-hr forecast as $\mathbf{x}^t$. Both forecast models are valid at 0900Z on 11 July 2001. The corresponding GOES-10 channel 2 satellite image and the approximate geographic location of the region of interest is shown in Fig. 5.18. As confirmed by observations (e.g., Stevens et al. 2002) the area is mostly cloud covered at the forecast valid time. The true profile ($\mathbf{x}^t$) and five of the 663 COAMPS background profiles for T, $\log_e Q$ and CLW are presented in Fig. 5.19. These COAMPS profiles were selected in order to demonstrate the horizontal variations within the area of interest at the scale of the COAMPS 3rd nested grid.

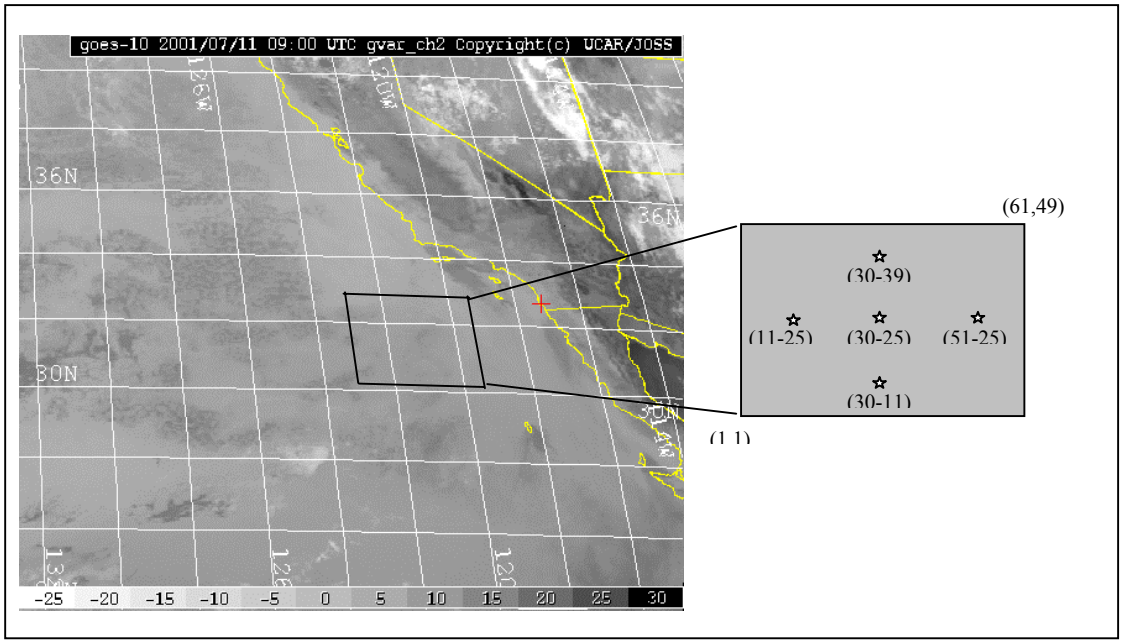

Figure 5.18. GOES-10 channel 2 image 20010711 0900Z of DYCOMS II area. [After http://www.joss.ucar.edu.] The box indicates the approximate geographic extent of the 360 x 288 km COAMPS 3rd nested grid and locations of the COAMPS reference profiles (Fig. 5.18). Reference grid point (1,1) is at 30.15 N, 123.19 W.

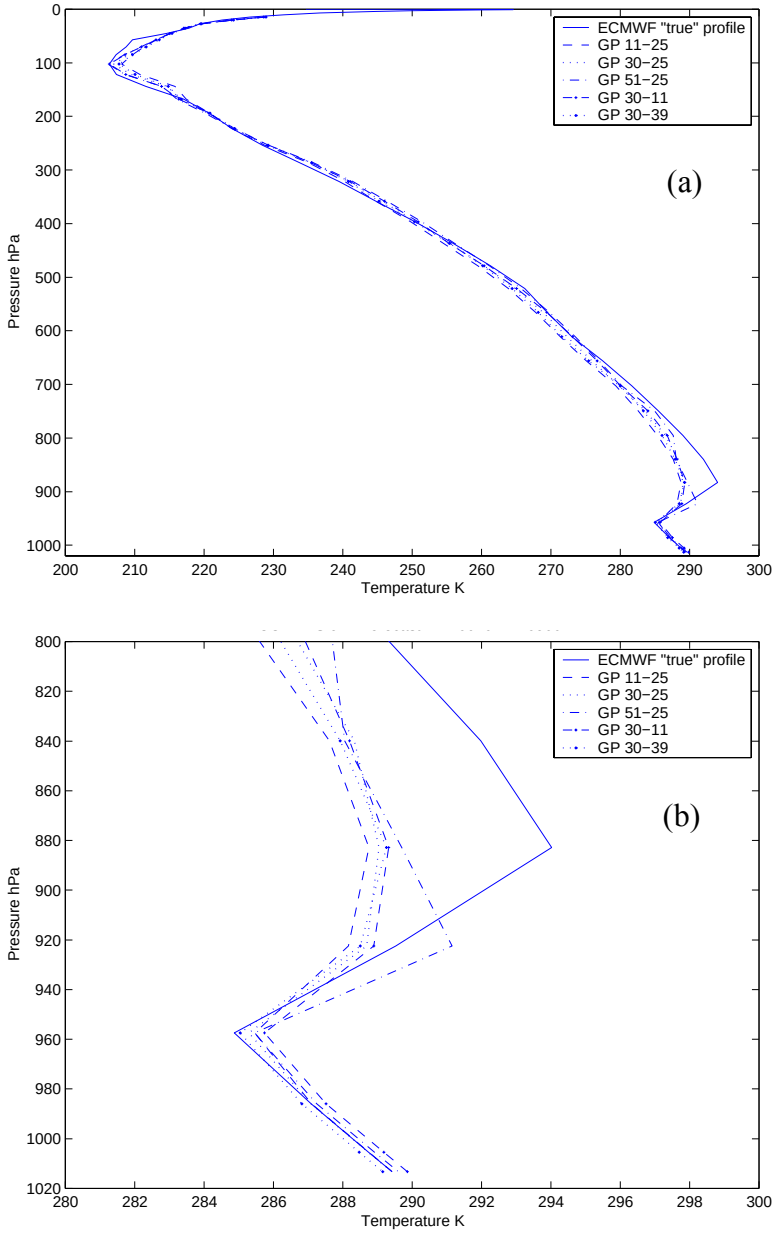

Figure 5.19. ECMWF "true" profile representing the averaged values for the area 30.0 – 32.5 N, 120.0 – 124.5 W, and selected COAMPS 9-hr forecast (a) T, (c) $\log_e Q$, and (e) CLW profiles from the 3rd nest (6 km horizontal grid spacing) interpolated to the 43 RTTOV-6 pressure levels. Expanded view of (a), (c), and (e) is provided in (b), (d), and (f), respectively.

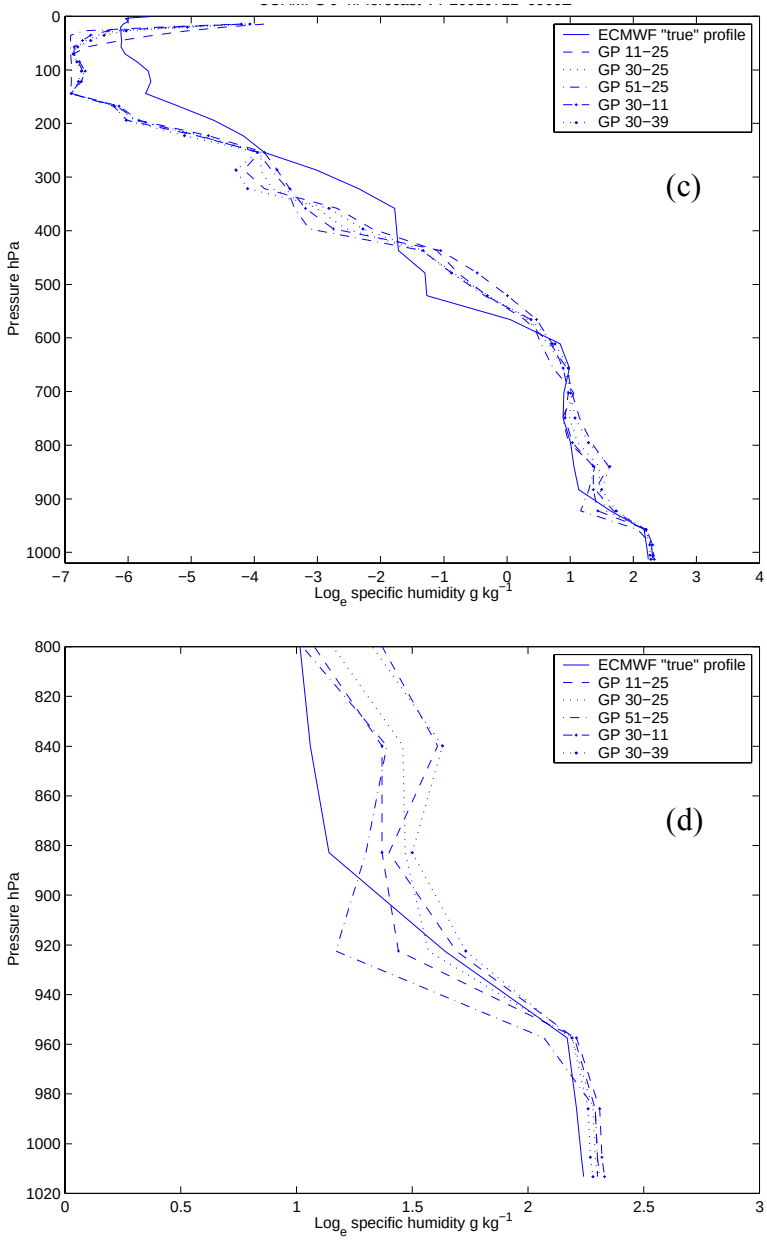

Figure 5.19. Continued.

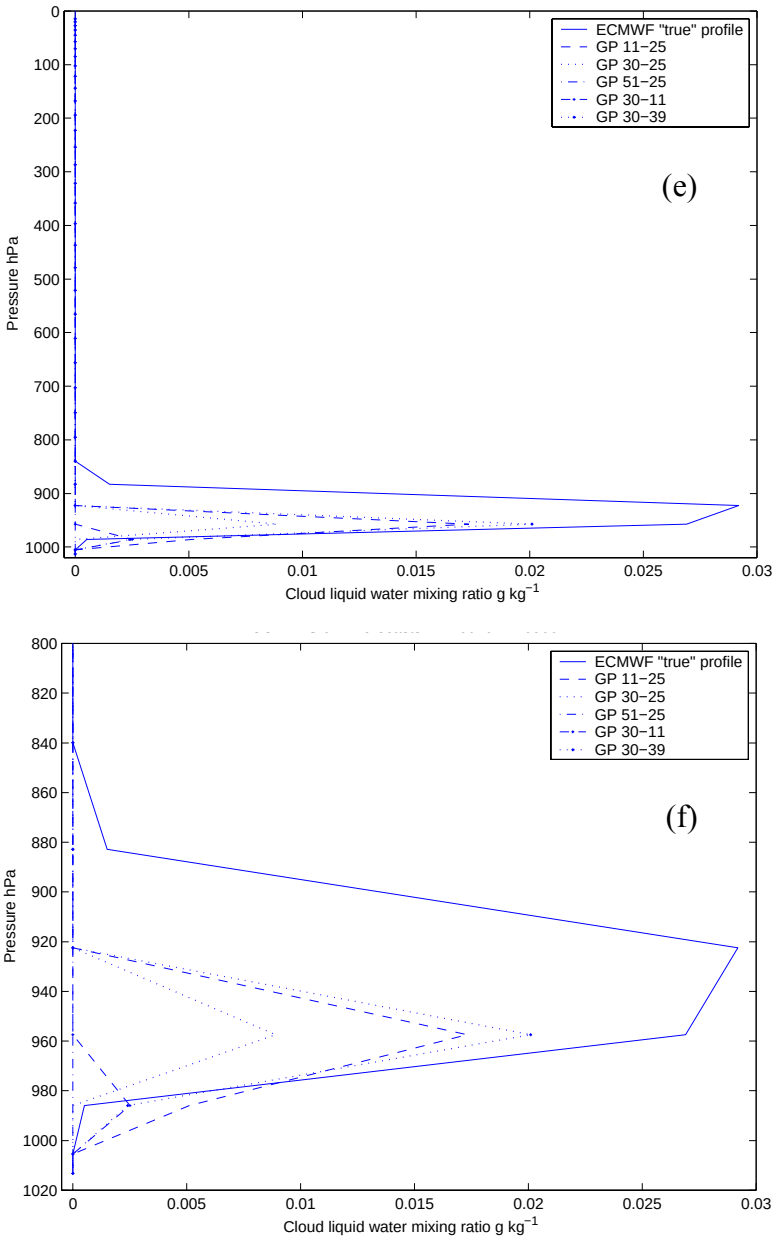

Figure 5.19. Continued.

Surface background state vector elements for $\mathbf{x}^t$ and averaged $\mathbf{x}^b$ compared very closely and are listed in Table 5.3. Overall, the two forecast models compare fairly well at mid-, and upper-levels of the atmosphere. At lower levels $\mathbf{x}^t$ is generally drier than the representative COAMPS background profiles and has a larger low-level temperature inversion of near 10 vice 5 K between 960 and 880 hPa. *CLW* is similar in magnitude between background and "truth". The corresponding COAMPS 500 m cross-section shown in Fig. 5.20 indicates small *CLW* amounts (~0.02 g kg^{-1}) at this altitude throughout most of the model domain.

Table 5.3. Surface parameters for ECMWF "true" profile ($\mathbf{x}^t$) and averaged COAMPS background state vectors ($\mathbf{x}^b$). Forecast valid time of 0900Z 11 July 2001.

	$\mathbf{x}^t$	$\overline{\mathbf{x}^b}$
T_{2m} (K)	290.44	289.70
Q_{2m} (g kg^{-1})	2.31	2.39
U_{10m} (m s^{-1})	4.06	4.03
V_{10m} (m s^{-1})	-7.58	-4.75
P_s (hPa)	1017.40	1016.14

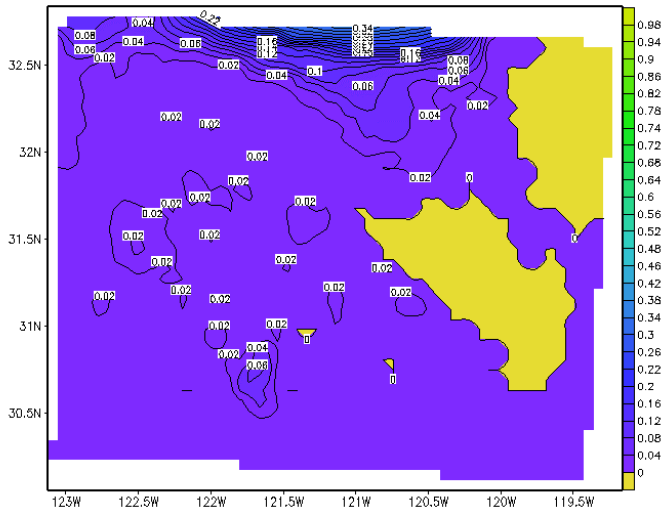

Figure 5.20. Horizontal cross-section at 500 m of cloud mixing ratio (g kg^{-1}) for DYCOMS II COAMPS 6 km grid. The 9-hr forecast valid time is 0900Z 11 July 2001. [From http://www.joss.ucar.edu.] The maximum observed values for 11 July were near 0.6 g kg^{-1} (Stevens et al. 2002).

The corresponding T, $\log_e Q$, and relative humidity from the 0815 Z (32.135 N 121.673 W) dropsonde observation along with the uninterpolated ECMWF and COAMPS model profiles are shown in Fig. 5.21. The designated "true" profile fairly accurately represents the temperature above the inversion, both $\mathbf{x}^t$ and $\mathbf{x}^b$ are too warm and moist within the MABL. In this case, a limitation in the vertical resolution of the models is demonstrated at the base of the MABL inversion. The base of the inversion in the in-situ observation near 930 hPa has been "missed" by both models, which show the inversion base near 960 hPa. As previously mentioned, when interpolated to the RTTOV-6 pressure levels there is some additional loss of vertical detail (see Fig 5.19). The COAMPS T and $\log_e Q$ background errors (Tables 3.2 and 3.3) are used for these simulations unless otherwise stated.

As previously stated, the observed *CLW* values during the DYCOMS II experiment were much larger than model forecasts. Maximum observed values on 11 July were near 0.6 g kg^{-1} (Stevens et al. 2002). In order to conduct a more rigorous test of the 1DVAR retrieval scheme, the 11 July case study was conducted for three *CLW* situations. The first simulated clear sky conditions by setting *CLW* to zero in both $\mathbf{x}^b$ and $\mathbf{x}^t$. The second directly used the under-predicted *CLW* forecasts. For the third case the maximum *CLW* in $\mathbf{x}^t$ was increased to 0.25 g kg^{-1} and the COAMPS *CLW* were increased by an order of magnitude. This modified cloud case set cloud-top in $\mathbf{x}^t$ at the base of the inversion.

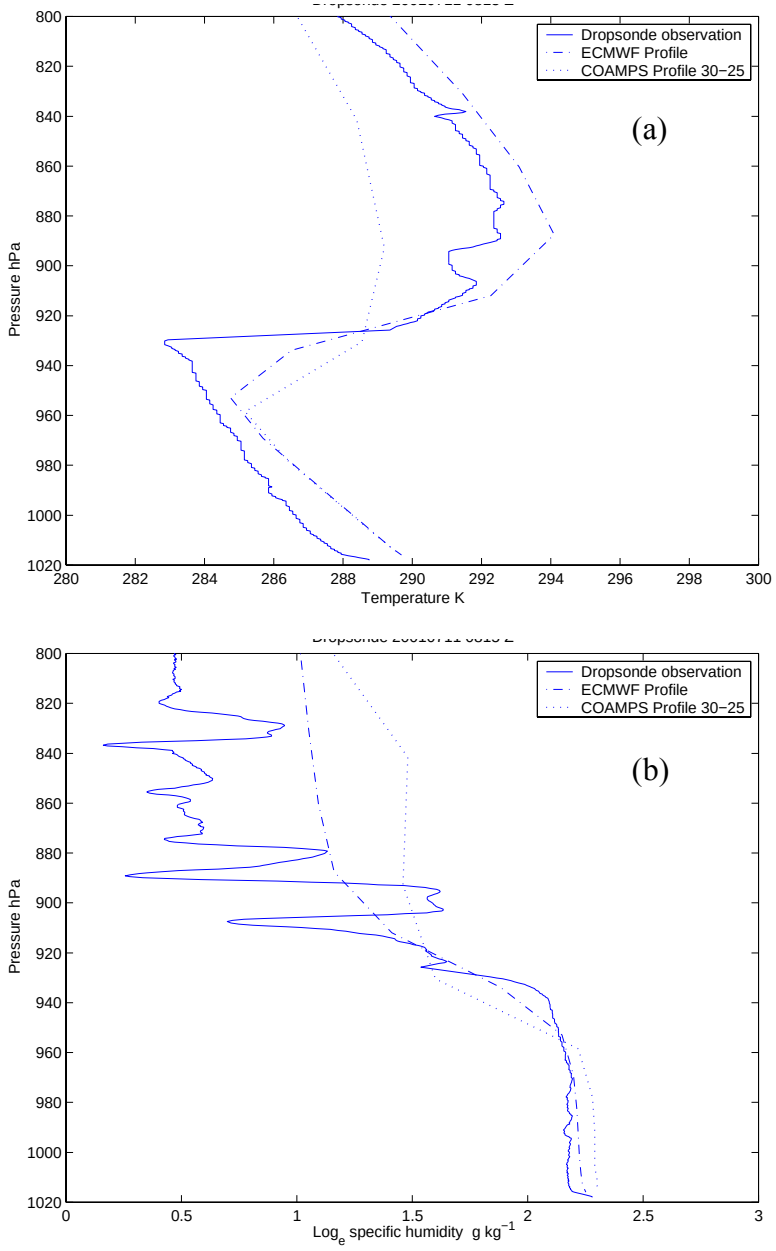

Figure 5.21. High-resolution dropsonde observation of (a) T, (b) $\log_e Q$, and (c) RH for 11 July 2001. Drop time was 0815Z at 32.135 N 121.673 W. [After http://www.joss.ucar.edu.] The collocated, vertically uninterpolated ECWMF and COAMPS (grid point 30-25) forecast profiles are also shown.

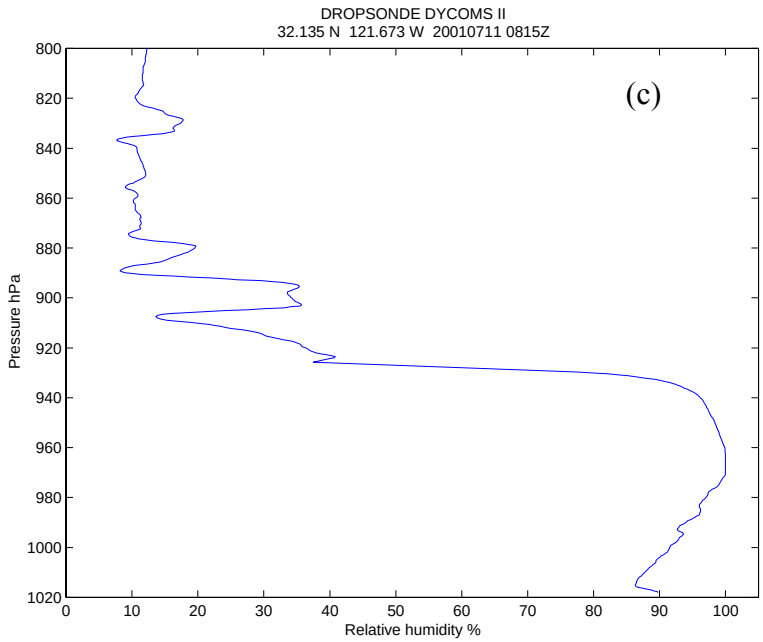

Figure 5.21. Continued.

a. 1DVAR Retrievals with Clear Sky Profiles

For this set of 1DVAR retrievals, *CLW* in $\mathbf{x}^b$ and $\mathbf{x}^t$ were set to zero in order to test the retrieval scheme under simulated clear sky conditions. Background errors are those listed for $\mathbf{B}_C$ (Tables 3.2 and 3.3).

Theoretical retrieval error $(S_{ii})^{½}$ and corresponding retrieval performance (P) are shown in Figs. 5.22a-b. The observed reduction (increase) in theoretical analysis error (performance) is consistent with the results presented earlier, i.e., under these conditions and background errors, there is a gain in near-surface T and $\log_e Q$ information. Theoretical T retrieval performance below 900 hPa increases to near 45% when T_s error is set to zero (not shown). When surface micowave emissivity (ε_m) error is set to zero, low-level $\log_e Q$ performance increases by 5% to approximately 65% (not shown). These changes are consistent with results from the information sensitivity study presented in Chapter IV.

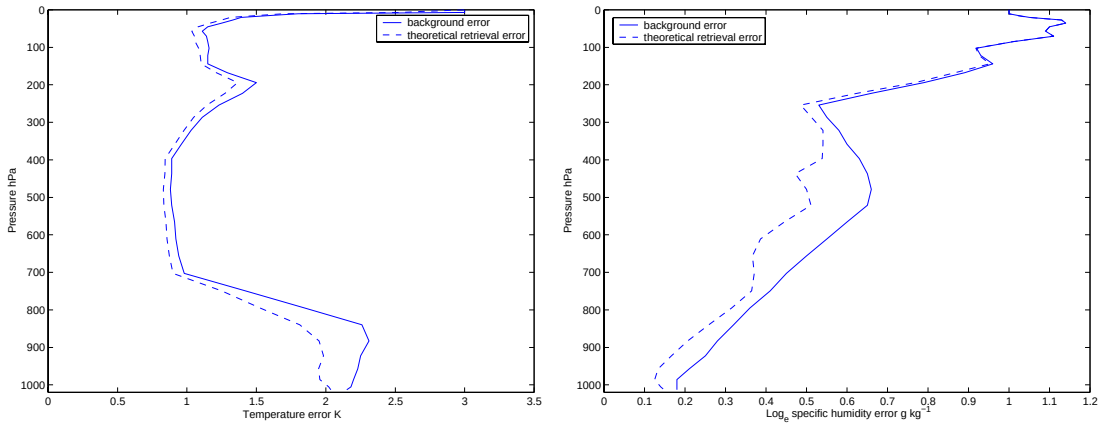

Figure 5.22a. Background, and theoretical retrieval T (left panel) and $\log_e Q$ (right panel) errors. *CLW* set to zero to simulate clear sky conditions. Background state vectors are DYCOMS II COAMPS 9-hr forecasts VT 20010711 0900Z.

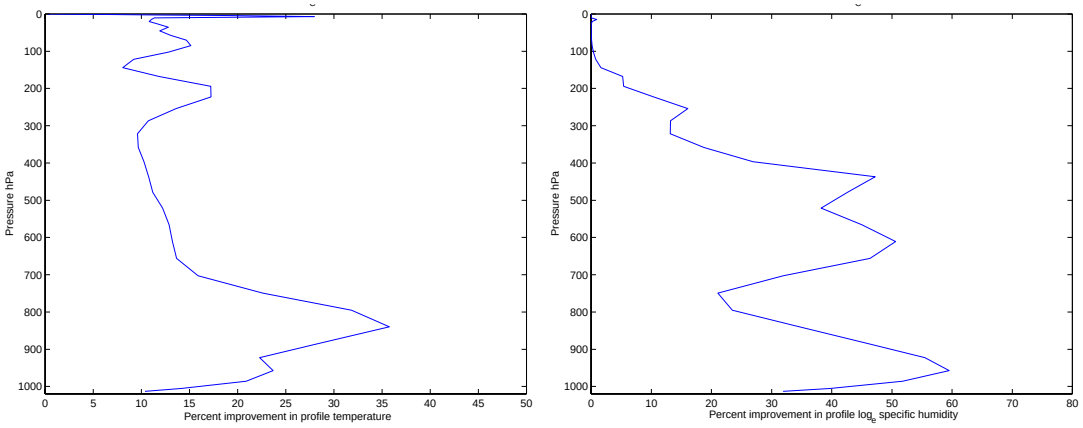

Figure 5.22b. As in Fig. 5.22a, except for theoretical T and $\log_e Q$ retrieval performance ($P = 100[1- (S_{ii}/B_{ii})]$).

The 1DVAR T and $\log_e Q$ simulated clear sky averaged retrievals are shown in Fig. 5.23. The bottom two panels are expanded views of the lower atmosphere from the surface to 800 hPa. At 10 iterations the convergence rate was very high (99%) for these retrievals. Overall, the 1DVAR retrieval scheme did a good job for both T and $\log_e Q$ in its ability to adjust toward $\mathbf{x}^t$. The averaged T retrieval strengthened the low-level temperature inversion to within approximately 2 K of $\mathbf{x}^t$. Below 800 hPa, the averaged $\log_e Q$ retrieval was adjusted toward $\mathbf{x}^t$ near the surface and at the top of the inversion. However, this adjustment, the averaged retrieval within the inversion is slightly warmer and dryer than $\mathbf{x}^t$ or averaged $\mathbf{x}^b$. The largest reduction (increase) in low-level analysis error (performance) is coincident with improvement in the inversion temperature structure and near surface humidity.

When T_s error is set to zero, the averaged T retrieval (Fig. 5.24) is slightly improved at the inversion base, and as expected there was no change in the $\log_e Q$ retrieval. Negligible improvement was observed for the low-level $\log_e Q$ retrieval when ε_m error was set to zero (not shown). However, as was discussed in Chapter IV, the difference in theoretical retrieval performance is very small for changes in ε_m error of 2%.

This simulated clear sky case suggests the 1DVAR retrieval scheme can produce a better first-guess T and $\log_e Q$ profile within the summertime EPAC environment. These 1DVAR profiles could then be used to initialize the COAMPS model or to generate a subsequent analysis field. The results are consistent with the information content study presented in Chapter IV and simulated retrievals based upon simulated background state vectors.

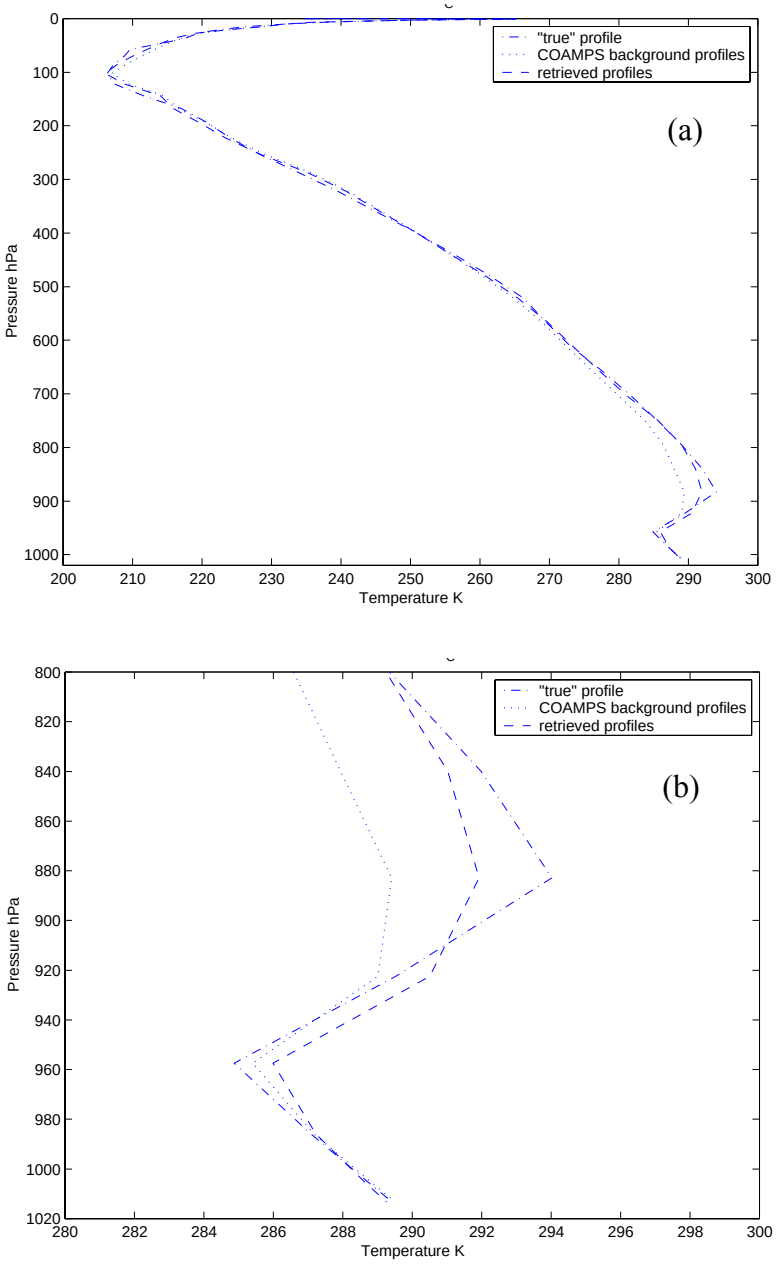

Figure 5.23. 1DVAR (a) T, and (c) $\log_e Q$ simulated clear sky retrievals with *CLW* profiles set to zero in $\mathbf{x}^b$ and $\mathbf{x}^t$. DYCOMS II COAMPS 9-hr forecasts VT 20010711 0900Z from the set of background state vectors ($\mathbf{x}^b$) and the simulated observations are calculated from the collocated ECMWF "true" forecast profile ($\mathbf{x}^t$). Background and retrieved profiles represent the averaged values over all successful retrievals. Lower panels are expanded views of the lower atmosphere from surface to 800 hPa. Expanded view of (a) and (c) are provided in (b) and (d), respectively.

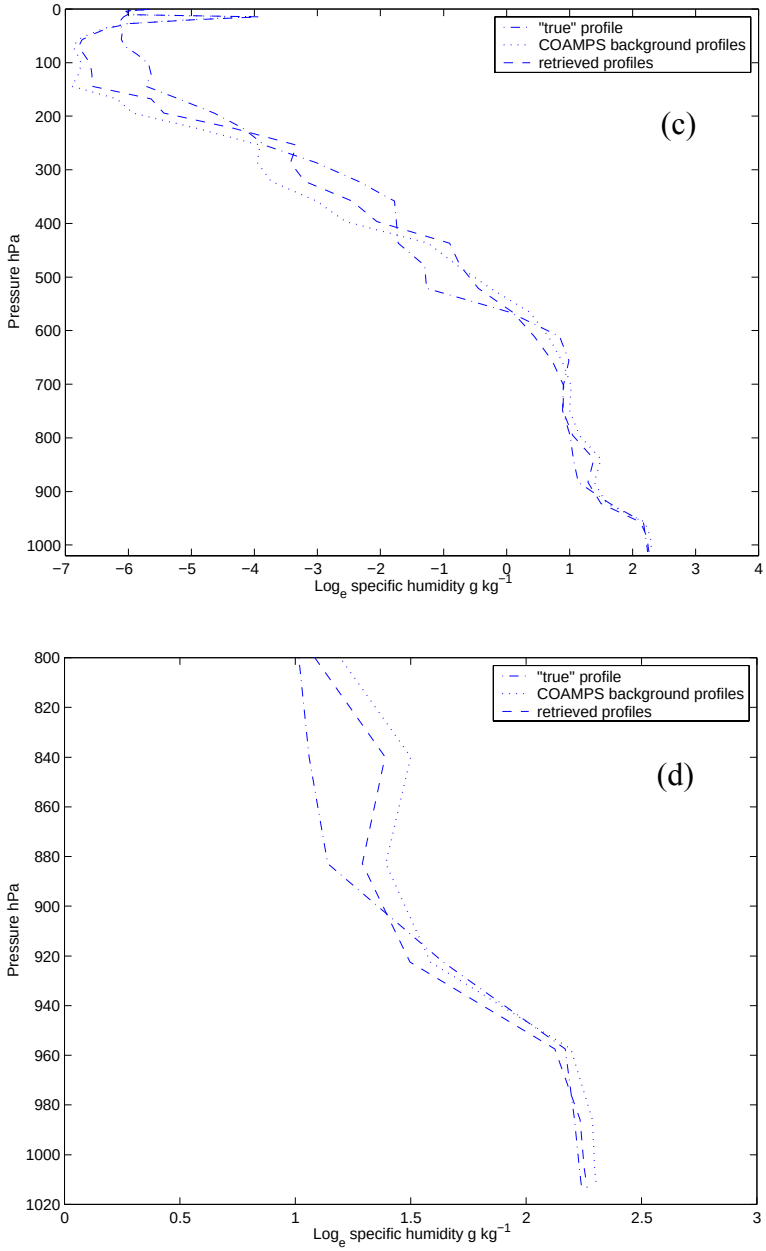

Figure 5.23. Continued.

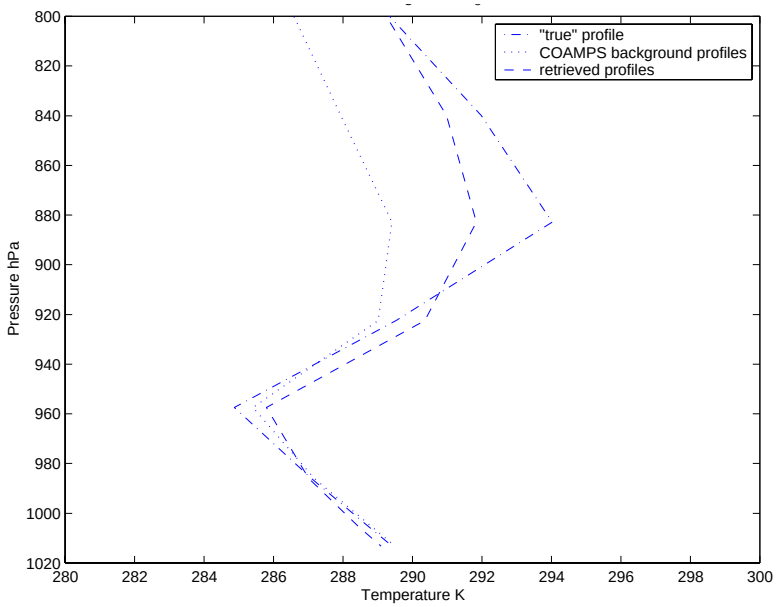

Figure 5.24. As in Fig. 5.23b, except T_s error set to zero.

b. 1DVAR Retrievals with Model CLW Profiles

The following 1DVAR retrieval simulations use *CLW* as specified by the model forecasts (see Fig. 5.19). As previously discussed, *CLW* is under-predicted in both $\mathbf{x}^t$ and $\mathbf{x}^b$ and cloud-top pressure is not very well defined.

Theoretical retrieval errors and theoretical retrieval performance were calculated with P_{CT}, C_{FC} and *CLW* errors of 20 hPa, 0.50, and 0.10 g kg^{-1}, respectively (Figs. 5.25a-b). C_{FC} in $\mathbf{x}^t$ was set to 0.50 for these simulations. As expected from the results presented in Chapter IV, the theoretical low-level $\log_e Q$ performance decreases when *CLW* is not perfectly known. If *CLW* error is set to zero (not shown), then as expected, the low-level theoretical $\log_e Q$ retrieval performance increases to values similar to those from the simulated clear sky cases (Fig. 5.22b). Temperature profile (*T*) theoretical retrieval performance is very similar to the simulated clear sky case.

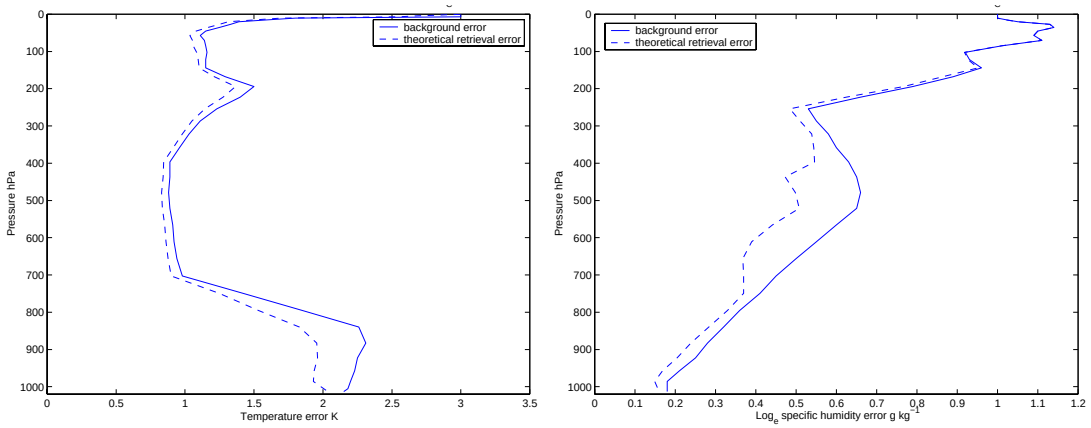

Figure 5.25a. Background, and theoretical retrieval T (left panel) and $\log_e Q$ (right panel) errors for cloudy sky 1DVAR simulated retrievals calculated using model CLW profiles. Cloud background errors are 20 hPa, 0.50, and 0.10 g kg^{-1} for P_{CT}, C_{FC} and CLW, respectively.

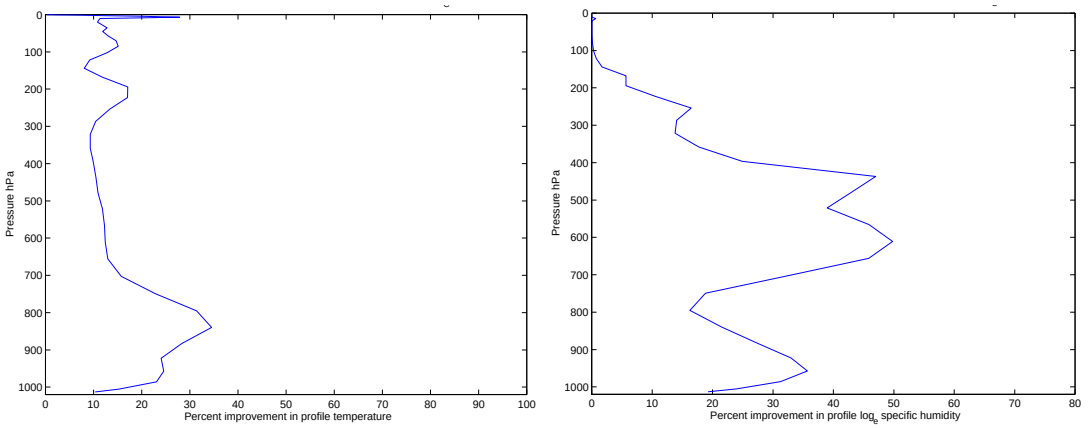

Figure 5.25b. As in Fig. 5.25a, except for theoretical T and $\log_e Q$ retrieval performance.

Temperature profile (T) and $\log_e Q$ simulated retrievals calculated with the cloud background errors described above and averaged over the total number of successful retrievals are shown in Fig. 5.26. The results for T are similar to the clear sky case (Fig. 5.23), but with a closer agreement between the averaged T retrieval and $\mathbf{x}^t$ near the top of the inversion. The warmer T retrieval within the inversion is most likely due to the systematic difference in P_{CT} between $\mathbf{x}^t$ and $\mathbf{x}^b$. The averaged $\log_e Q$ retrieval calculated with the 0.10 g kg^{-1} CLW background error differs slightly from the clear sky case with less adjustment toward $\mathbf{x}^t$ near the surface and at the top of the inversion.

As shown in Fig. 5.27, by increasing T error to 5.00 K for the lowest seven RTTOV-6 pressure levels (839.95 – 1013.25 hPa) and setting P_{CT} error to 60 hPa, the averaged T retrieval is able to better match the temperature at the top of the MABL inversion. The larger background errors allow the IR derived information to determine cloud-top temperature. However, the retrieved temperatures below cloud-top also become warmer and move further from $\mathbf{x}^t$. This behavior is most likely due to the influence of the vertical error correlations and the resulting distribution of information between levels. The background T errors used to calculate $\mathbf{B}_C$ may over-constrain the retrieval with respect to the relatively strong temperature inversion in $\mathbf{x}^t$.

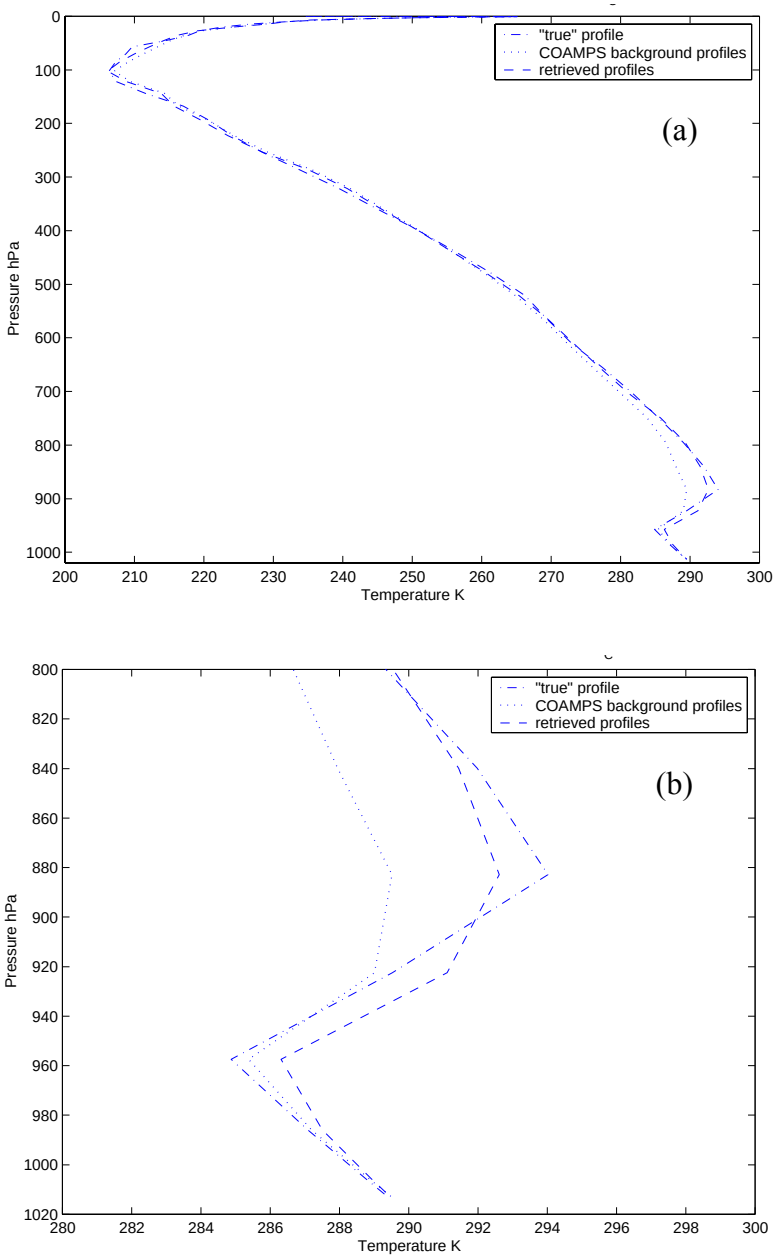

Figure 5.26. As in Fig. 5.23, except for cloudy sky simulated retrievals with P_{CT}, C_{FC} and *CLW* errors of 20 hPa, 0.50, and 0.10 g kg^{-1}, respectively. The model *CLW* values were used for these simulations.

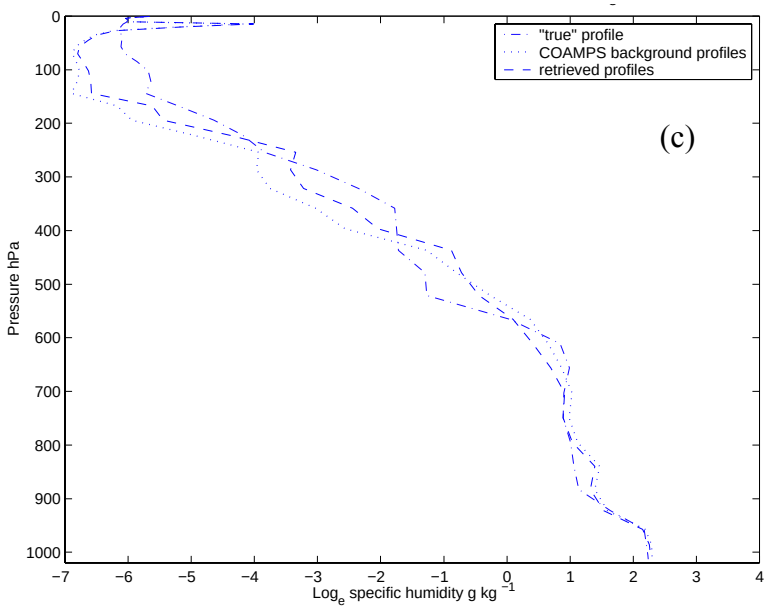

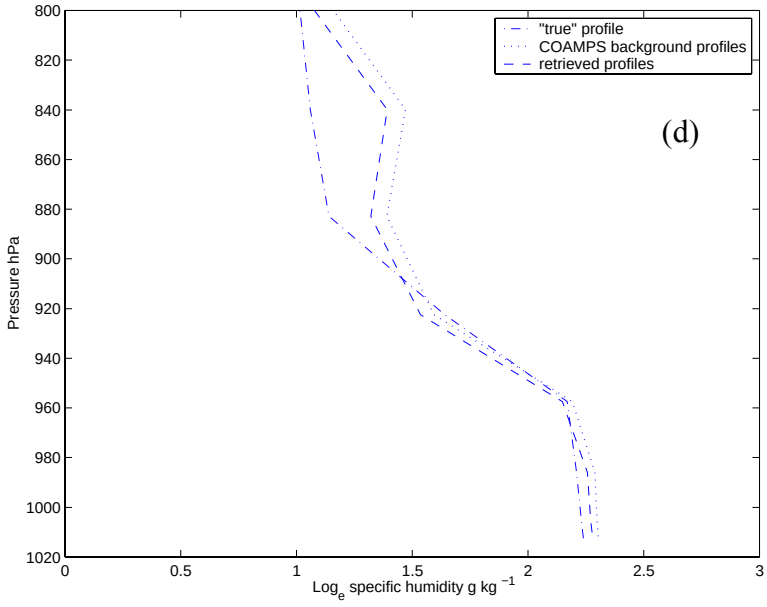

Figure 5.26. Continued.

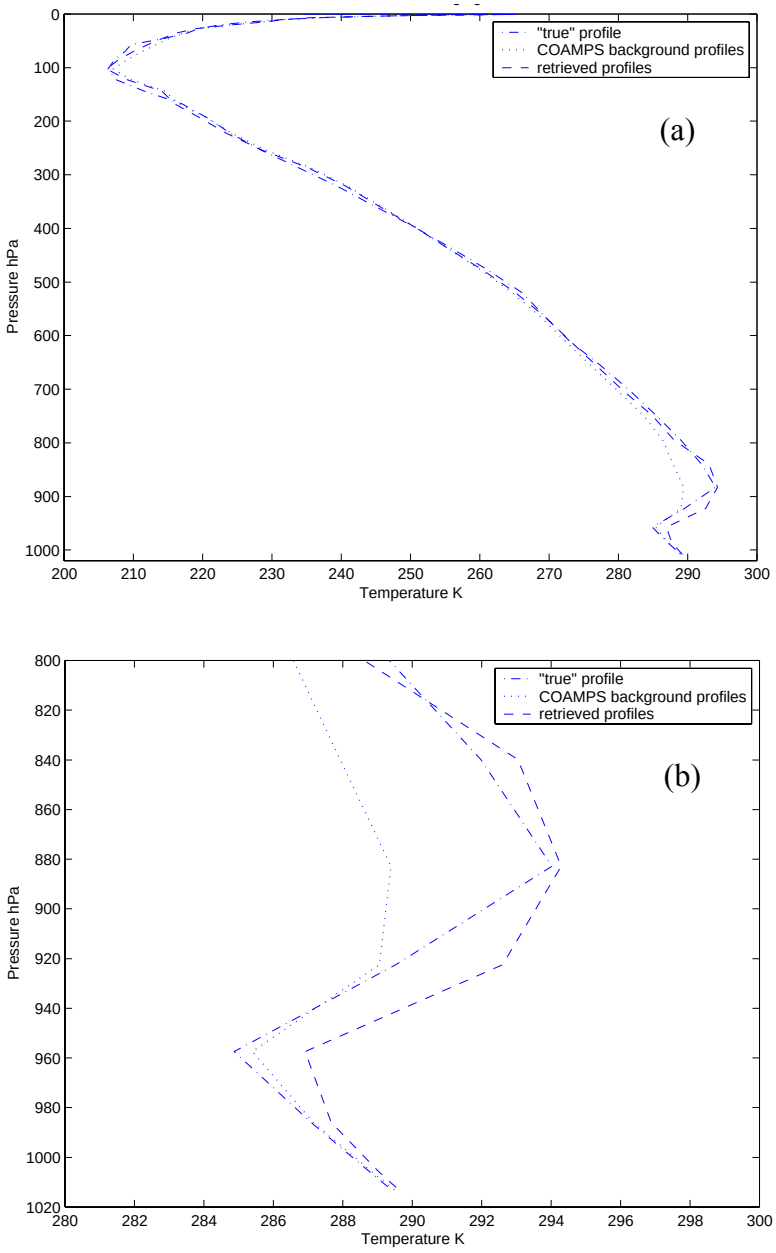

Figure 5.27. As in Figs. 5.26a-b, except for P_{CT} background error of 60 hPa and *T* errors within the lowest seven RTTOV-6 pressure levels (839.95 – 1013.25 hPa) set to 5.00 K.

c. 1DVAR Retrievals with Modified CLW Profiles

The ECMWF *CLW* forecast in $\mathbf{x}^t$ was modified for the following 1DVAR retrieval simulations by substituting a linearly increasing profile with a maximum value of 0.25 g kg^{-1} at the cloud top. The *CLW* forecasts in $\mathbf{x}^b$ were increased by a factor of ten, but no attempt was made to alter the vertical cloud distribution within the profiles. This change increased the cloud field (see Fig. 5.19) from near 0.02 to 0.20 g kg^{-1}.

Figs. 5.28a-b show the theoretical retrieval errors and theoretical retrieval performance calculated with P_{CT}, C_{FC}, and *CLW* background errors set to 20 hPa, 0.20, and 0.10 g kg^{-1}, respectively. The C_{FC} in $\mathbf{x}^t$ was set to 1.00. With respect to the previous "cloudy" case, there is a larger reduction (increase) in theoretical retrieval error (performance) near the cloud top and the theoretical $\log_e Q$ retrieval performance is slightly improved above the cloud top.

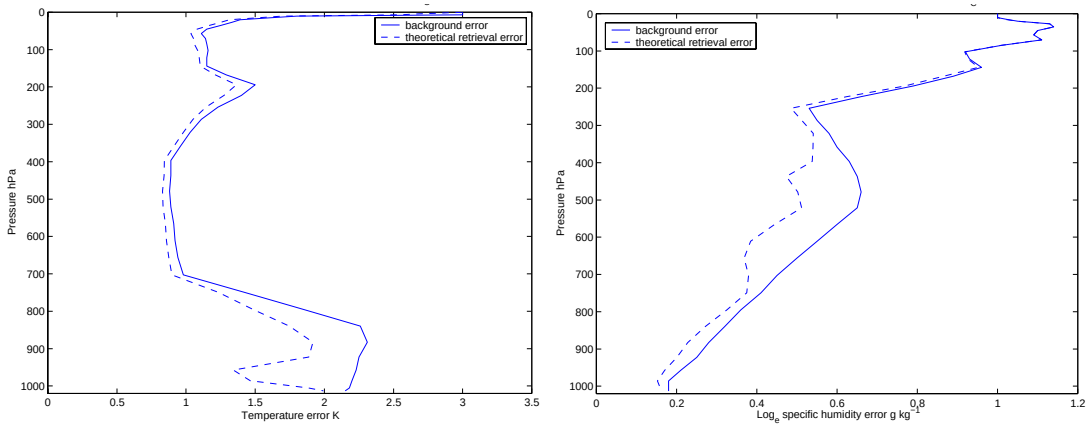

Figure 5.28a. Background, and theoretical retrieval *T* (left panel) and $\log_e Q$ (right panel) errors for cloudy sky 1DVAR simulated retrievals calculated using modified $\mathbf{x}^t$ and $\mathbf{x}^b$ *CLW* profiles. Cloud background errors are 20 hPa, 0.00, and 0.10 g kg^{-1} for P_{CT}, C_{FC} and *CLW*, respectively.

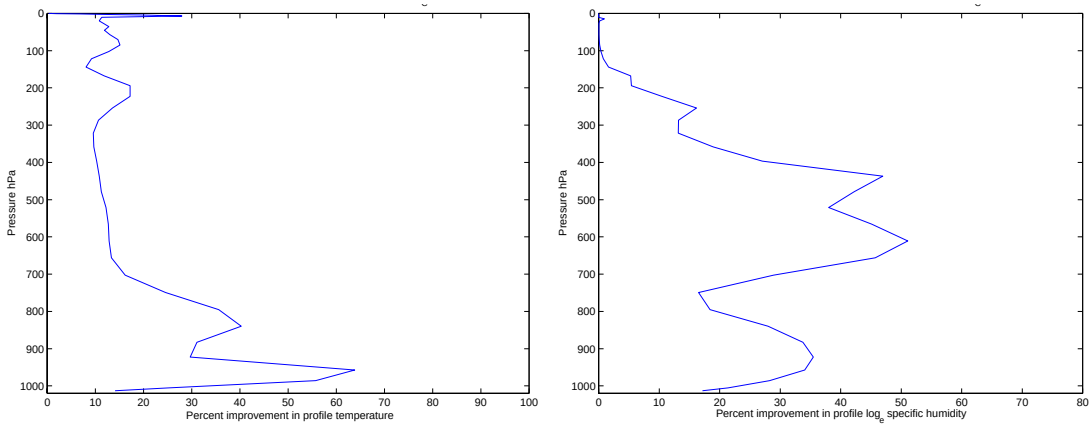

Figure 5.28b. As in Fig. 5.28a, except for theoretical T and $\log_e Q$ retrieval performance.

The T and $\log_e Q$ 1DVAR simulated retrievals presented in Fig. 5.29 were first calculated with cloud background errors described above. In this case, the averaged T retrieval is much closer to $\mathbf{x}^t$ at the inversion base and within the inversion itself. The retrieved product also more closely matches the inversion strength of $\mathbf{x}^t$. A closer match to the $\mathbf{x}^t$ temperature at the inversion top is possible if the low-level T background errors are increased (see Fig. 5.27).

The averaged T retrieval within the MABL (below 960 hPa) is colder than $\mathbf{x}^b$ or $\mathbf{x}^t$ by approximately 1 K due to relatively small P_{CT} a prior error. As shown in Fig. 5.30, there is a closer match for T within the MABL if P_{CT} error is increased to 60 hPa. Since most of the humidity information is derived from the MW channels, the retrieved $\log_e Q$ profiles (Figs 5.29c-d) are fairly similar to the previous "cloudy" sky case (Figs. 5.23c-d).

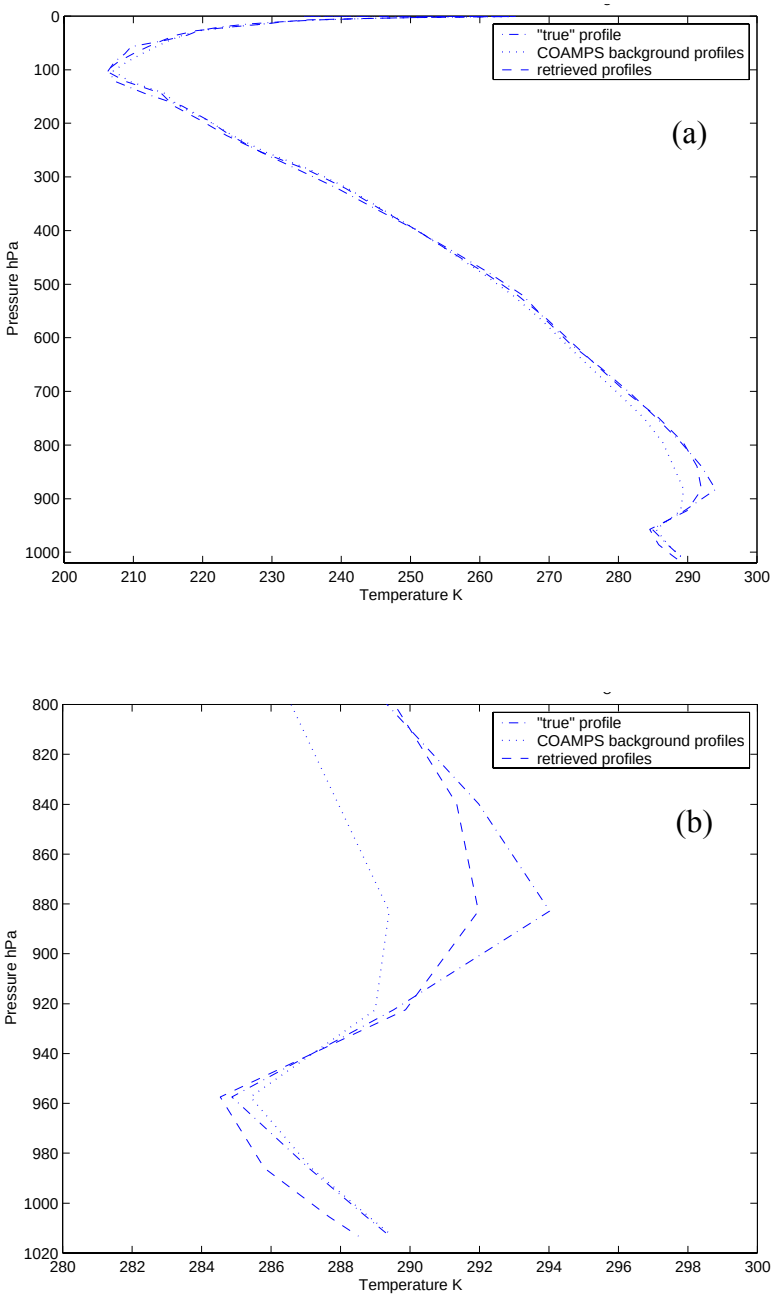

Figure 5.29. As in Fig. 5.23, except for cloudy sky simulated retrievals with modified *CLW* profiles. P_{CT}, C_{FC} and *CLW* errors are 20 hPa, 0.00, and 0.10 g kg^{-1}, respectively.

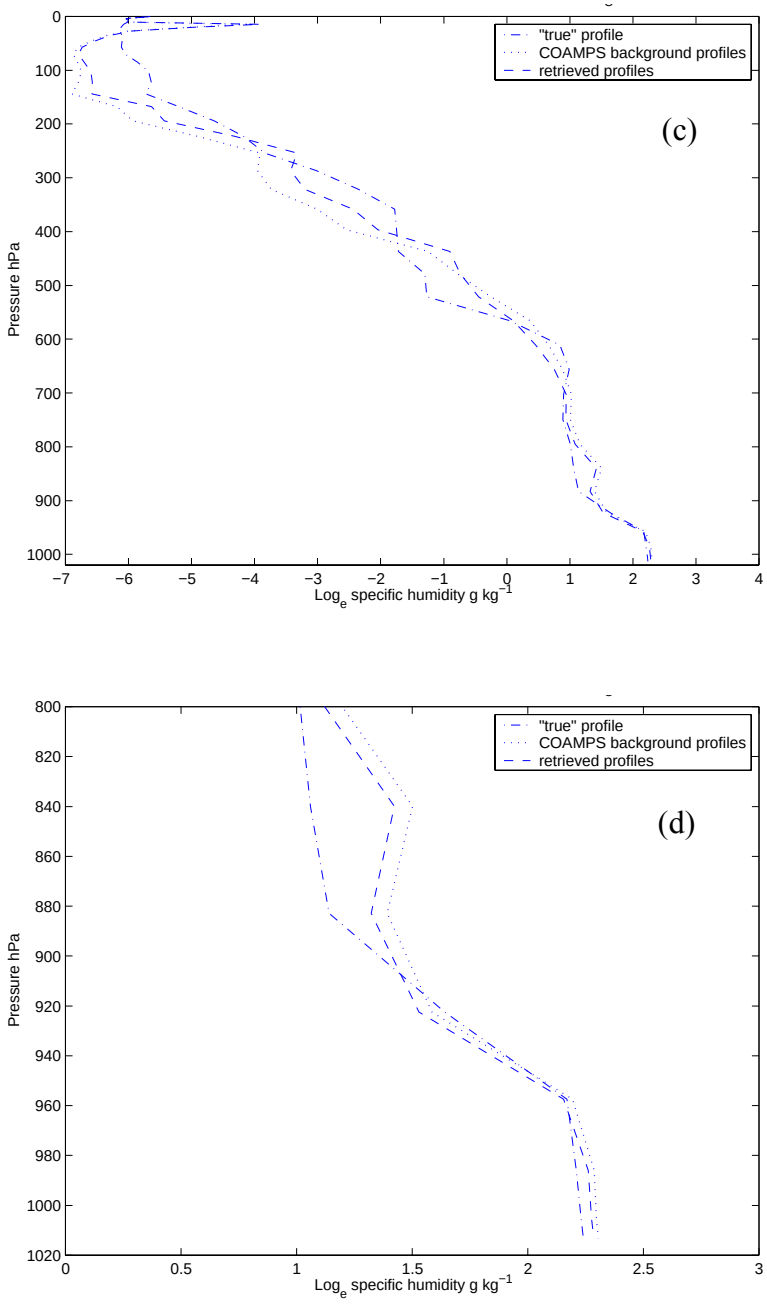

Figure 5.29. Continued.

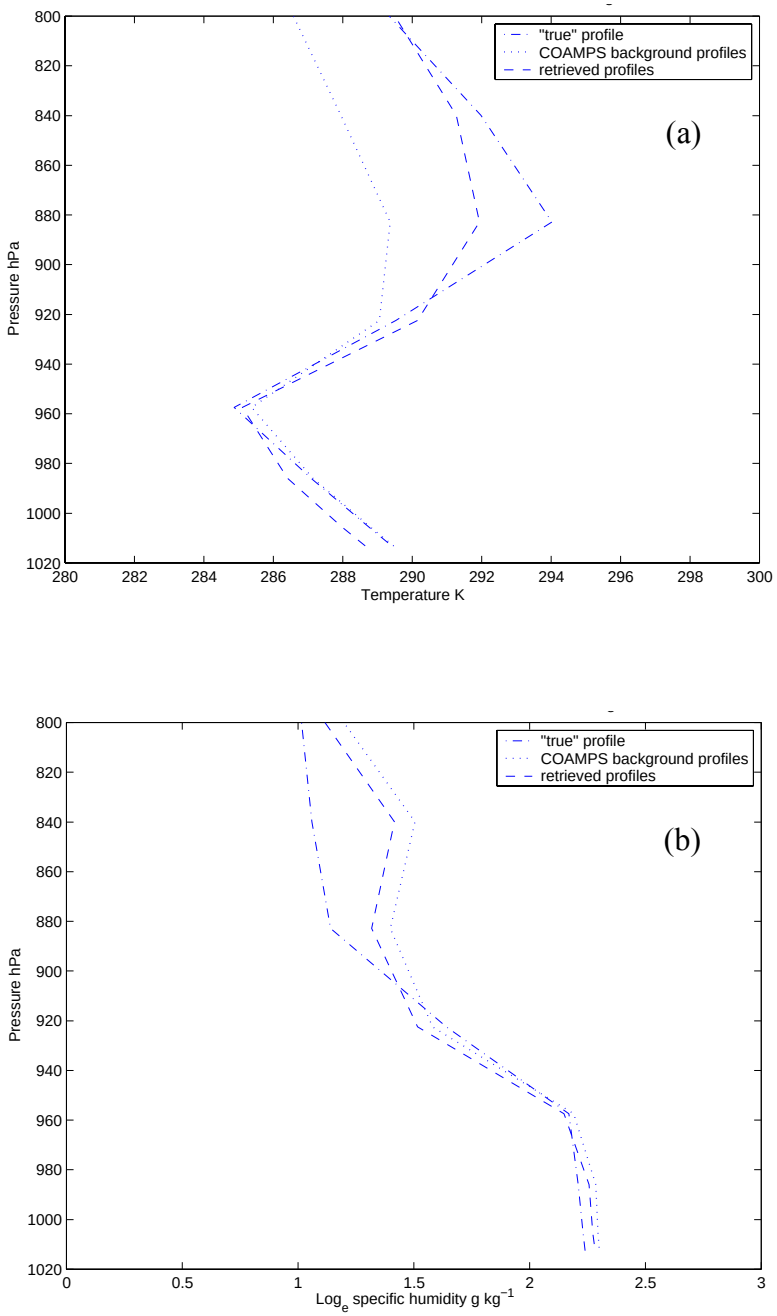

Figure 5.30. As in Fig. 5.29a and Fig. 5.29d, except P_{CT} background error set to 60 hPa.

2. Case Study: 1800Z 15 July 2001

This second 1DVAR retrieval case study was conducted using COAMPS 6-hr forecasts and the collocated averaged ECMWF 6-hr forecast with valid time for $\mathbf{x}^b$ and $\mathbf{x}^t$ of 15 July 2001 at 1800Z. It is included here since both the COAMPS and ECMWF forecast fields contain up to an order of magnitude more cloud liquid water than in the previous case study (Fig. 5.19) This case also provides an interesting test of whether the NRL 1DVAR retrieval scheme can adjust the upper-level $\log_e Q$ profile toward the designated "true" atmospheric state. The COAMPS water vapor forecasts provided by UCAR/JOSS for this date were very dry above approximately 600 hPa. The corresponding GOES-10 channel 1 satellite image is shown in Fig. 5.31.

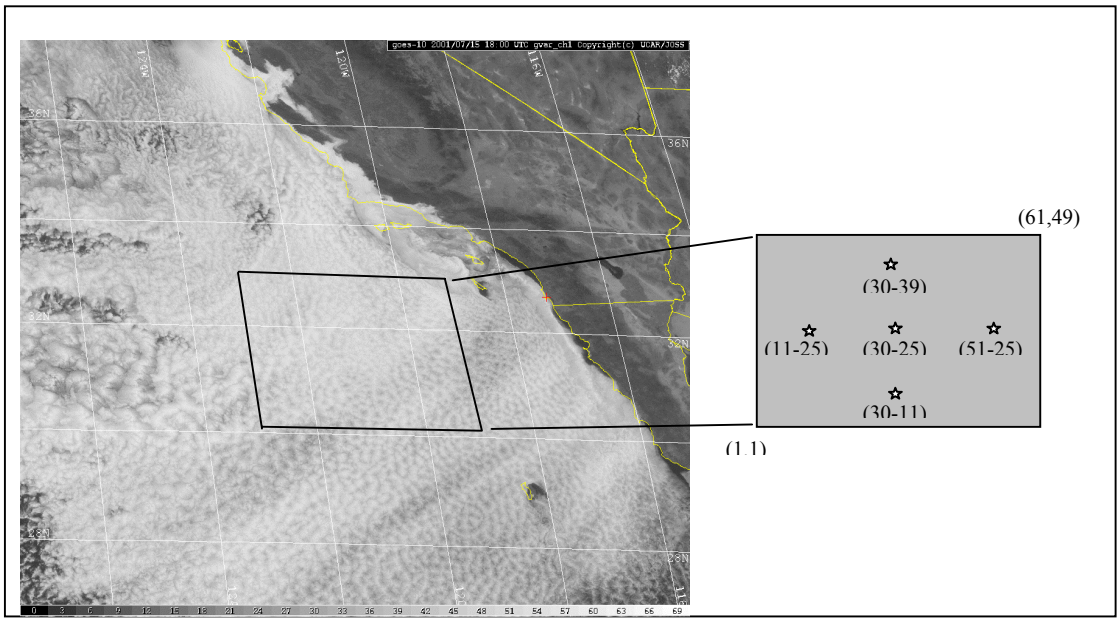

Figure 5.31. As in Fig. 5.18, except for GOES-10 channel 1 image for 1800Z 15 July 2001.

The "true" profile ($\mathbf{x}^t$) and five representative COAMPS background profiles ($\mathbf{x}^b$) for T, $\log_e Q$ and CLW are shown in Fig. 5.32. The CLW profiles are used directly for these 1DVAR simulated retrievals. Again, these COAMPS profiles are shown here only to demonstrate the horizontal variations within the area of interest. In-situ observations were not available from the DYCOMS II data set for this day.

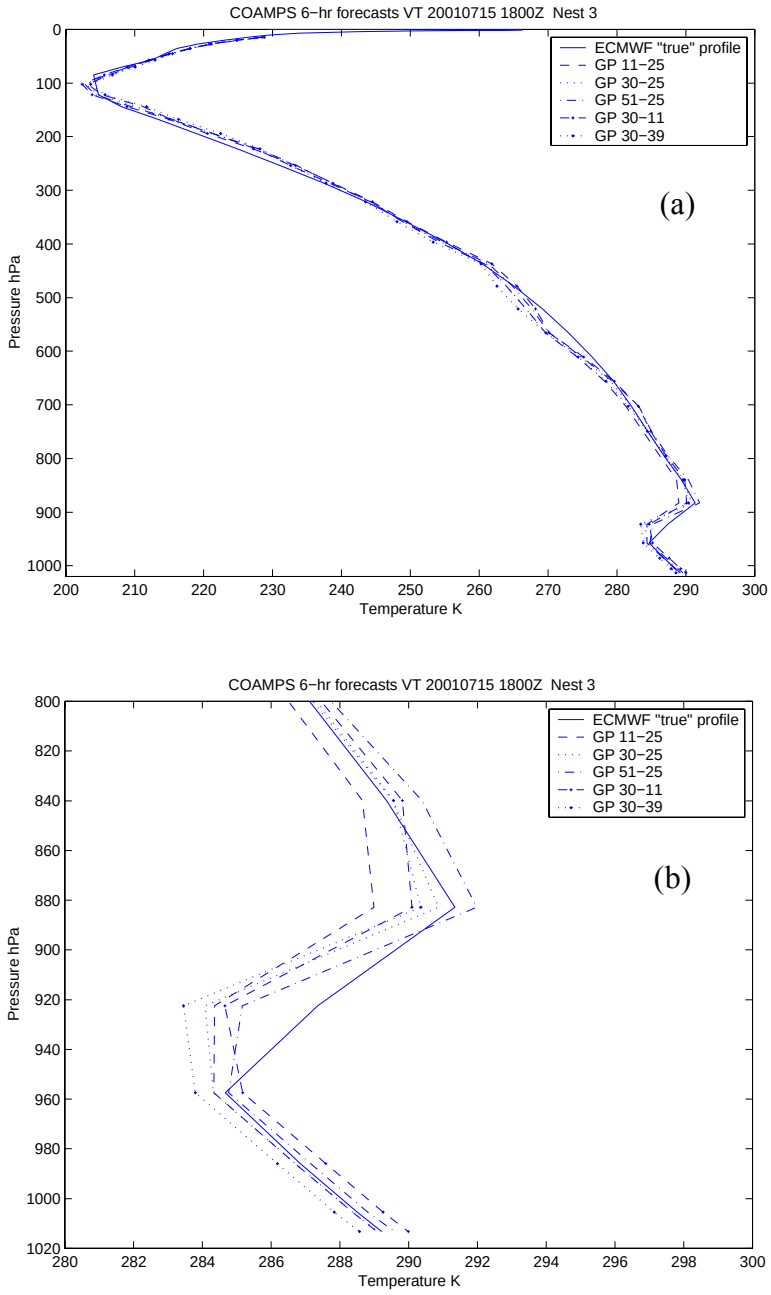

Figure 5.32. As in Fig. 5.19, except for 6-hr forecast valid time of 1800Z 15 July 2001.

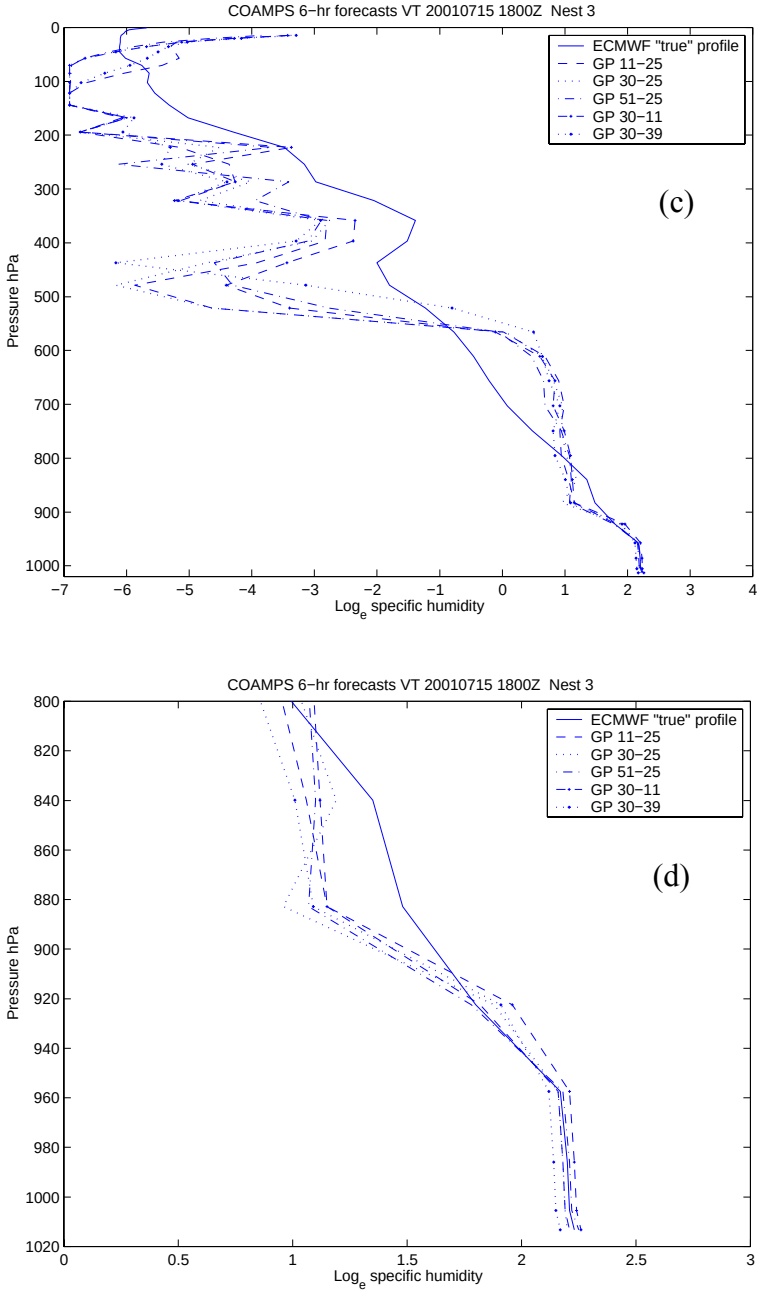

Figure 5.32. Continued.

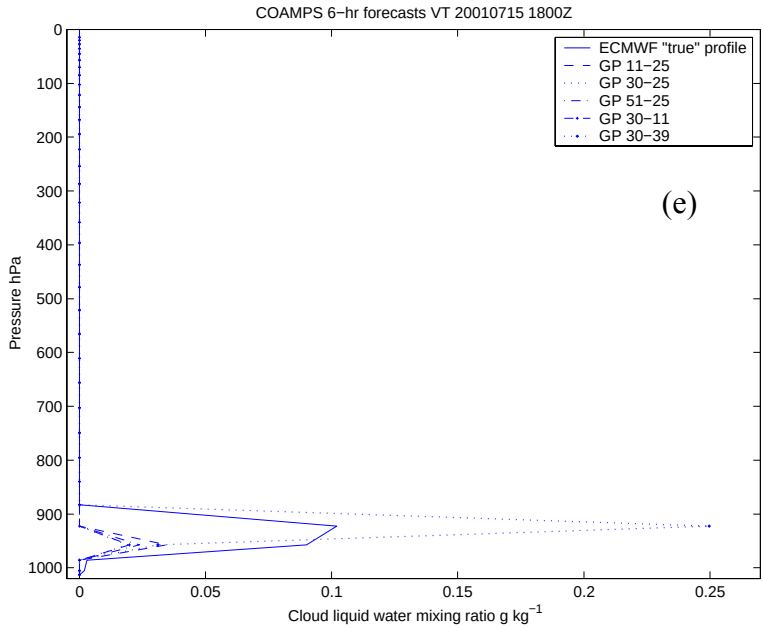

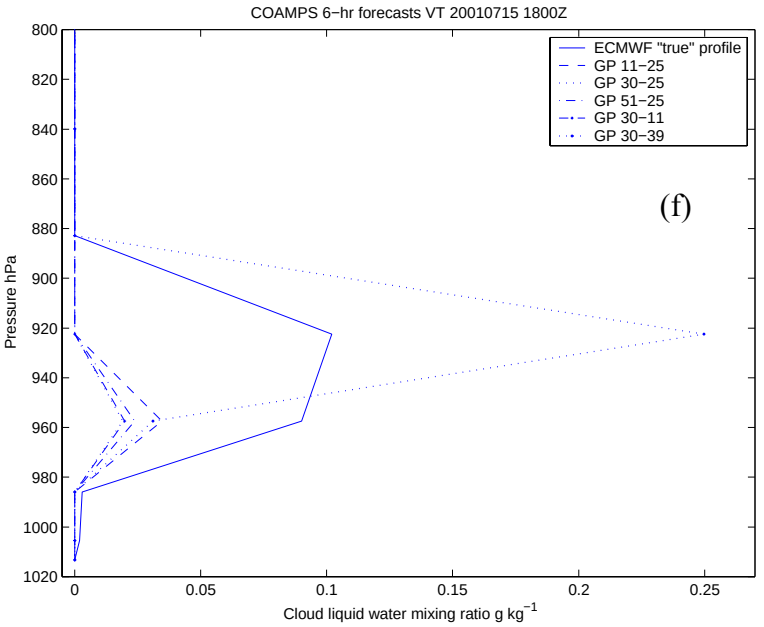

Figure 5.32. Continued.

For this simulation, $\mathbf{x}^t$ is very close to the representative background temperature profiles except at the base of the inversion. Interpolating to the fixed RTTOV-6 pressure levels could cause some of these differences. The $\log_e Q$ profiles agree well near the surface but soon diverge with height. Between approximately 100 and 600 hPa, the set of $\mathbf{x}^b$ contains very little water vapor. *CLW* in $\mathbf{x}^t$ is much larger than in the 11 July case study and is approximately 0.1 g kg^{-1}. Except for the northern reference profile (GP 30-39) with approximately 0.25 g kg^{-1} *CLW*, the set of $\mathbf{x}^b$ is well below 0.05 g kg^{-1}. The magnitudes of *CLW* derived from the COAMPS sigma level were in close agreement with the vertically interpolated values. The corresponding COAMPS 6-hr forecast 500 m *CLW* cross-section is shown in Fig. 5.33, and as in the 11 July cases study *CLW* at this altitude are very small (e.g., 0.02 g kg^{-1}). Surface elements for $\mathbf{x}^t$ and averaged $\mathbf{x}^b$ compared very closely (Table 5.4).

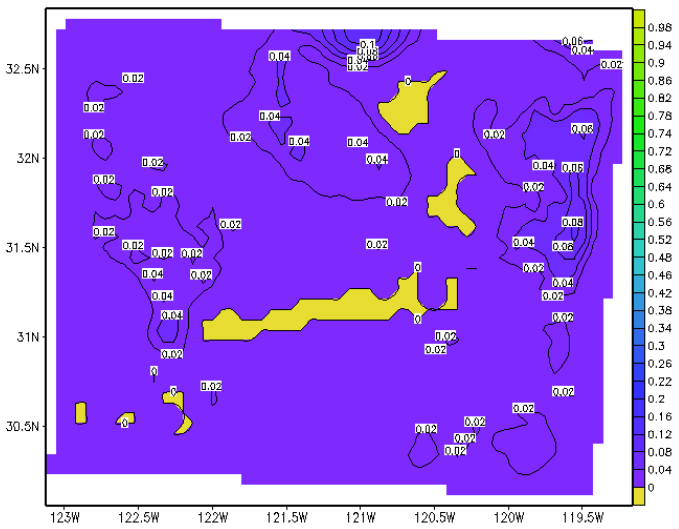

Figure 5.33. Horizontal cross-section at 500 m of cloud mixing ratio (g kg^{-1}) for DYCOMS II COAMPS 6 km grid. The 6-hr forecast valid time is 1800Z 15 July 2001. [From http://www.joss.ucar.edu.]

Table 5.4. As in Table 5.3, except for 6-hr forecast valid time of 1800Z 15 July 2001.

	$\mathbf{x}^t$	$\overline{\mathbf{x}^b}$
T_{2m} (K)	289.90	289.34
Q_{2m} (g kg^{-1})	2.23	2.23
U_{10m} (m s^{-1})	3.31	4.30
V_{10m} (m s^{-1})	-6.56	-6.92
P_s (hPa)	1015.50	1013.98

Figs. 5.34a-b show the theoretical retrieval errors and theoretical retrieval performance calculated with P_{CT}, C_{FC}, and *CLW* background errors set to 20 hPa, 0.20, and 0.10 g kg^{-1}, respectively. The C_{FC} in $\mathbf{x}^t$ was set to 1.00. All other background errors are per Tables 3.2 and 3.3 for $\mathbf{B_C}$. As observed for the 11 July modified cloud case, there is a reduction (increase) in theoretical retrieval error (performance) near the cloud top. The theoretical $\log_e Q$ retrieval performance peaks below 900 hPa, but is also relatively large near 600, 350, and 225 hPa, corresponding to the $\log_e Q$ gradients of $\mathbf{x}^b$ (see Fig. 5.32).

The T and $\log_e Q$ 1DVAR simulated retrievals were first calculated with cloud background errors described above and are shown in Fig. 5.35. In this case, the averaged T retrieval is closer to $\mathbf{x}^t$ at the inversion base and within the inversion itself. The averaged T and $\log_e Q$ retrievals below 960 hPa remain close to $\mathbf{x}^b$ and $\mathbf{x}^t$. Within the inversion the averaged T retrieval adjusts toward $\mathbf{x}^t$, but is warmer above the inversion top. The averaged $\log_e Q$ retrieval above 800 hPa adjusts toward $\mathbf{x}^t$ except where the difference between $\mathbf{x}^t$ and $\mathbf{x}^b$ is too large (e.g., ~ 500 hPa).

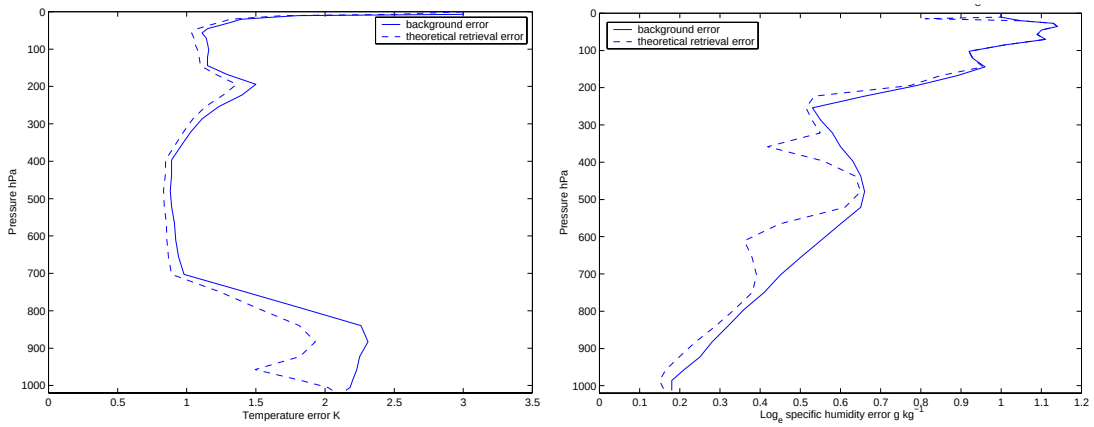

Figure 5.34a. Background, and theoretical retrieval T (left panel) and $\log_e Q$ (right panel) errors for cloudy sky 1DVAR simulated retrievals. Cloud background errors are 20 hPa, 0.20, and 0.10 g kg^{-1} for P_{CT}, C_{FC} and CLW, respectively.

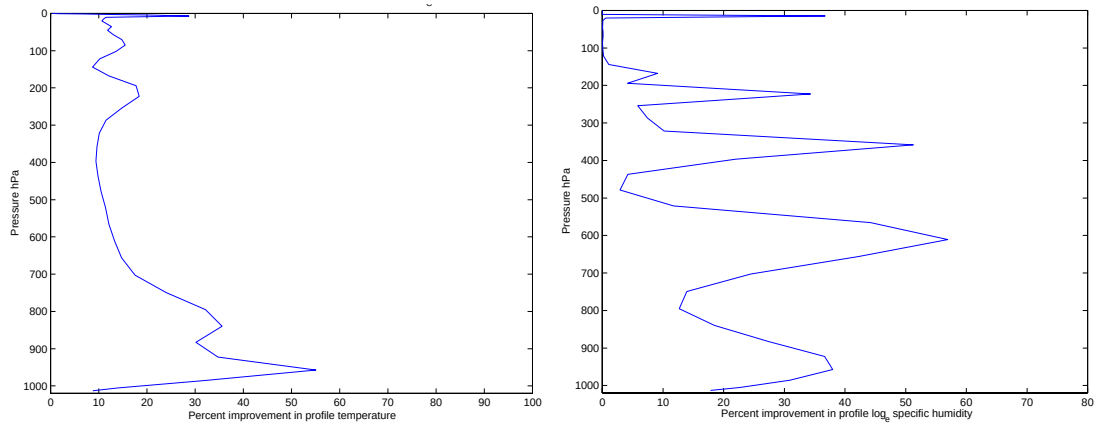

Figure 5.34b. As in Fig. 5.34a, except for theoretical T and $\log_e Q$ retrieval performance.

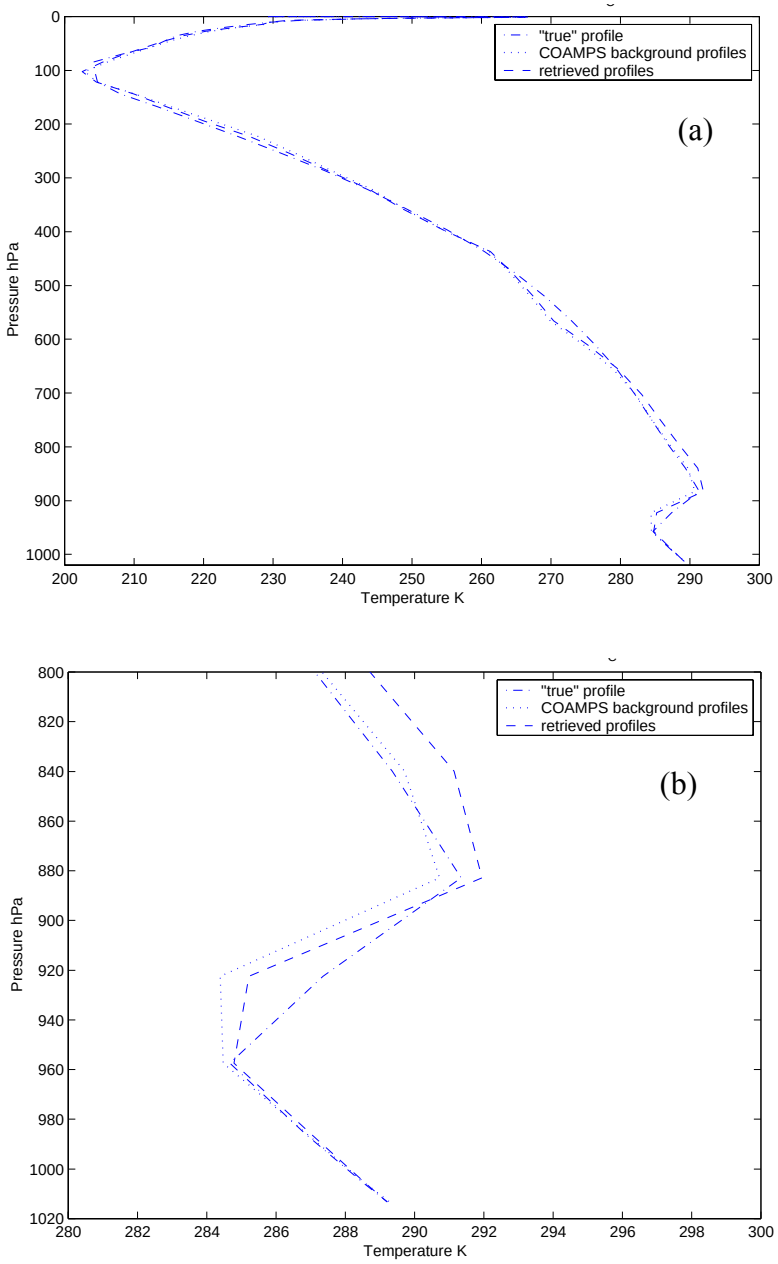

Figure 5.35. 1DVAR (a) T, and (c) $\log_e Q$ simulated cloudy sky retrievals using the DYCOMS II COAMPS 6-hr forecasts valid at 20010715 1800Z as background state vectors ($\mathbf{x}^b$) and simulated observations calculated from the collocated ECMWF "true" forecast profile. Cloud element background errors for P_{CT}, C_{FC}, and CLW set to 20 hPa, 0.20, and 0.10 g kg^{-1}, respectively. Background and retrieved profiles represent the averaged values over all successful retrievals. Expanded view of (a) and (c) provided in (b) and (d), respectively.

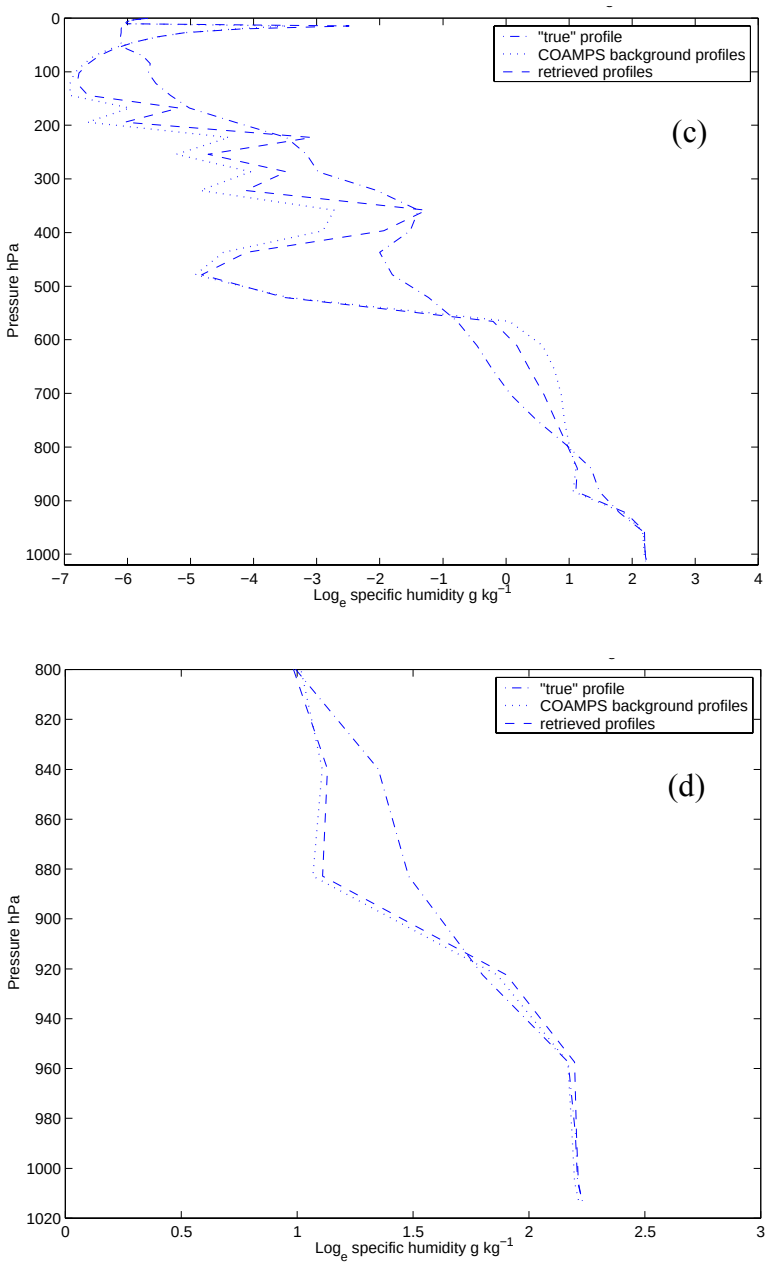

Figure 5.35. Continued.

3. Section Summary

The results of two case studies were presented in which 1DVAR retrievals were generated using COAMPS forecast fields and simulated ATOVS observations. The period of this study coincided with two days (11 and 15 July 2001) of the DYCOMS II field study. All model fields for this phase of study were obtained directly from the UCAR/JOSS data set. Simulated ATOVS observations were calculated using the collocated ECMWF forecast and the COAMPS 6-, and 9-hr forecast fields were used as the set of background state vectors.

For the first case study, the COAMPS and ECMWF model cloud liquid water profiles (*CLW*) were modified, since both models consistently under-forecast this cloud element. Simulations were conducted for three *CLW* cases. The first simulated clear sky conditions by eliminating *CLW* from the background and observation, while the second directly used the model forecasted *CLW*. The third simulation increased the model *CLW* values for both background and observation. Results from this case study showed that the ATOVS simulated IR and MW observations were able to adjust the existing structure of the background profile toward the designated "true" profile. The adjustment was most prominent for temperature directly above the low-level MABL temperature inversion. At these levels the retrieved temperature profile was adjusted by approximately 2 – 3 K toward "truth". The temperature retrieval directly above the cloud-topped MABL was improved by increasing the corresponding background errors to 5.00 K. This allowed the IR temperature information to better adjust the retrieval; however, the *T* retrieval was degraded within the MABL. Through the 1DVAR retrieval scheme, the observations were also able to adjust the $\log_e Q$ COAMPS background profiles toward "truth".

The second case study for 15 July 2001 also showed that the NRL 1DVAR retrieval scheme could adjust the low-level T and $\log_e Q$ retrievals toward "truth." Additionally, this case showed the limitation of the scheme in retrieving upper-level humidity. Specifically, if the difference between "truth" and background is too great, the retrieval scheme was unable to make the necessary adjustments.

C. 1DVAR RETRIEVALS WITH COAMPS BACKGROUND STATE VECTORS AND ATOVS MICROWAVE OBSERVATIONS

The first two sections of this chapter presented the results of 1DVAR retrievals using simulated ATOVS observations with either simulated backgrounds, or COAMPS short-term forecast fields from the DYCOMS II data set. Results of the simulated retrieval study demonstrated the consistency of the NRL 1DVAR retrieval scheme and that the simulated observations could adjust the background T and $\log_e Q$ toward the designated "true" profile, most notably near the EPAC MABL inversion.

This research also conducted 1DVAR retrievals using ATOVS microwave (MW) observations with the COAMPS forecast fields from the DYCOMS II data set. HIRS/3 observations were not included in this retrieval set due to the uncertainty in cloudy sky IR retrieval bias corrections. As discussed in Chapter II.A, a long-term monitoring program of observed and model generated brightness temperature is required in order to establish the proper bias corrections. NRL Monterey currently does not monitor HIRS/3 radiances and therefore, statistics were not available for the NRL bias correction scheme. Cloudy sky retrieval biases for the AMSU channels are also non-trivial (see Fig. 2.4). However, as a first order approximation to this near MW clear case, retrievals were conducted with no bias corrections. Exclusion of the IR channels will result in less available information, especially cloud-top temperature.

AMSU-A and B observations from the NOAA-16 satellite were obtained for this research directly from the calibrated level 1B data (K. Nielsen, personal communication). The satellite observations listed in Table 5.5 are for 11 July 2001 (orbit start time of 1010Z) and represent the averaged values over the area 30.0 – 33.0 N, 119.5 – 123.5 W. This area corresponds to the approximate geographical extent of the inner COAMPS nest from the DYCOMS II data set (see Fig. 5.18). Averaging the measured brightness temperatures from the numerous AMSU scan spots into a single observation clearly degrades the horizontal resolution of these microwave sounders. This was done as a matter of convenience and so the results would be consistent with those from the

simulated retrieval study. Multiple AMSU retrievals with the COAMPS / NAVDAS forecast / analysis system were also conducted for this dissertation and the results are presented in Section V.D.

Table 5.5. NOAA-16 AMSU-A and -B observations averaged over area 30.0 – 33.0 N, 119.5 – 123.5 W. Orbit start time is 1010Z 11 July 2001.

AMSU-A Channel	BT (K)	AMSU-B Channel	BT (K)
1	165.04	1	221.30
2	157.58	2	263.58
3	226.32	3	262.89
4	259.48	4	274.01
5	256.23	5	281.61
6	240.53		
7	226.52		
8	220.30		
9	213.56		
10	217.72		
11	225.75		
12	235.37		
13	245.07		
14	253.25		
15	228.52		

The 1DVAR retrievals presented in this section were constrained by the COAMPS 9-hr forecast fields (VT 0900Z 11 July 2001) described in Section B and the COAMPS EPAC background error covariance matrix, $\mathbf{B_C}$. Standard deviations of error for the cloud parameters are described in the following paragraphs. Retrievals were generated using both the under-predicted and modified cloud liquid water mixing ratio profile (*CLW*) values from the COAMPS output. As discussed in Section B, model output was modified by increasing *CLW* by an order of magnitude (e.g., 0.02 to 0.20 g kg^{-1}). Results are compared against the collocated in-situ temperature and humidity observation described in Section V.B.

1DVAR retrievals of profile temperature (T) and $\log_e$ specific humidity ($\log_e Q$) were generated using model *CLW* values and have been averaged over all successful retrievals. The retrievals were conducted using relatively large cloud-top pressure (P_{CT}) and cloud fractional coverage (C_{FC}) background error of 60 hPa and 0.50. From the findings presented in Chapter III, the AMSU surface channels are not sensitive to P_{CT} and C_{FC}. However, MW retrievals are sensitive to *CLW* error, surface MW emissivity (ε_m) error, and radiative skin temperature (T_s) error.

The AMSU retrievals of T and $\log_e Q$ generated with *CLW* background error set to 0.03 g kg^{-1} are shown in Fig. 5.36. All other background errors are those for $\mathbf{B}_C$ and as described in the above paragraph. Even with exclusion of the HIRS/3 surface

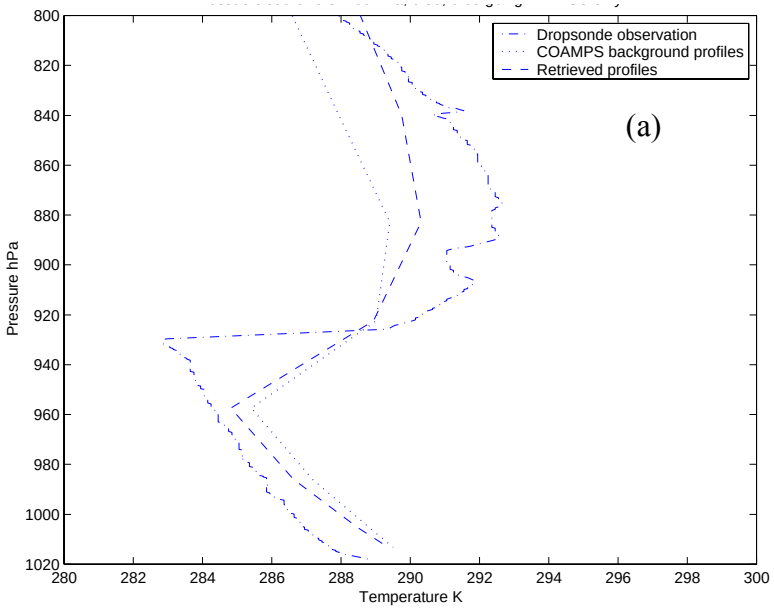

Figure 5.36. 1DVAR (a) T, and (b) $\log_e Q$ retrievals using the AMSU-A and B observations listed in Table 5.5 and COAMPS 9-hr forecast fields (valid at 0900Z 11 July 2001) from the DYCOMS II data set. Standard deviations of error for P_{CT}, C_{FC} and *CLW* set to 60 hPa, 0.50, and 0.03 g kg^{-1}. Retrievals are compared to collocated high-resolution dropsonde observation of 0815 Z and are shown for the lower atmosphere only.

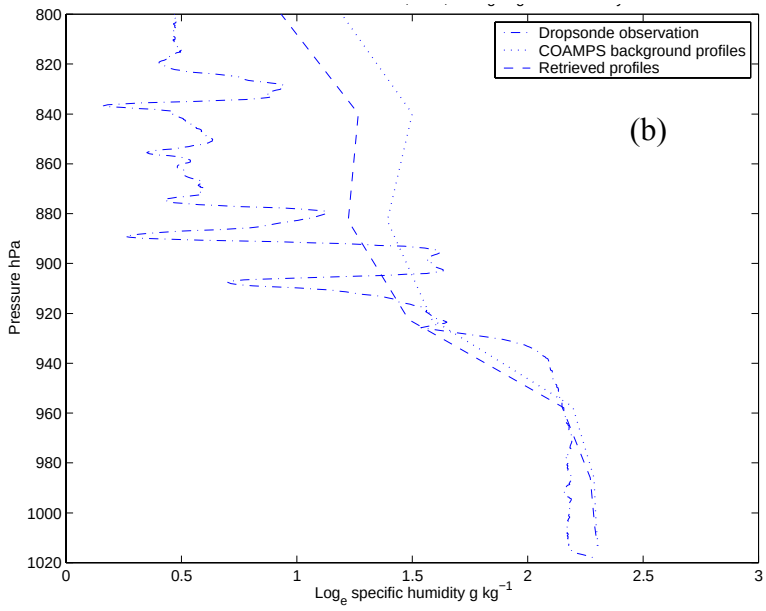

Figure 5.36. Continued.

channels, the 1DVAR retrieval is able to adjust the background profile toward the in-situ observation. Though there is not as much change in low-level *T* as observed using the 35-channel simulated observations (e.g., Fig. 5.29), this adjustment toward "truth" does occur both above and below the MABL inversion. The $\log_e Q$ retrieval also shows improvement over the background profile and is adjusted closer to the high-resolution dropsonde observation above the MABL inversion. Only minor adjustment from the background profile occurs near the surface.

Sensitivity of MW humidity retrievals to *CLW* error was further examined in this research by increasing the background error to 0.10 g kg^{-1}. Results confirm those found during the retrieval error sensitivity study (Chapter IV.C), specifically that increased *CLW* background error reduces $\log_e Q$ retrieval performance, but has little effect on *T*. As shown in Fig. 5.37 this relatively large *CLW* error produces a $\log_e Q$ retrieval that, in this case, is too dry within the MABL by approximately ($\log_e$) 0.5 g kg^{-1}. The retrieved low-level *T* retrieval (not shown) is similar to that shown in Fig. 5.36a with the exception that it remains closer to background below 980 hPa.

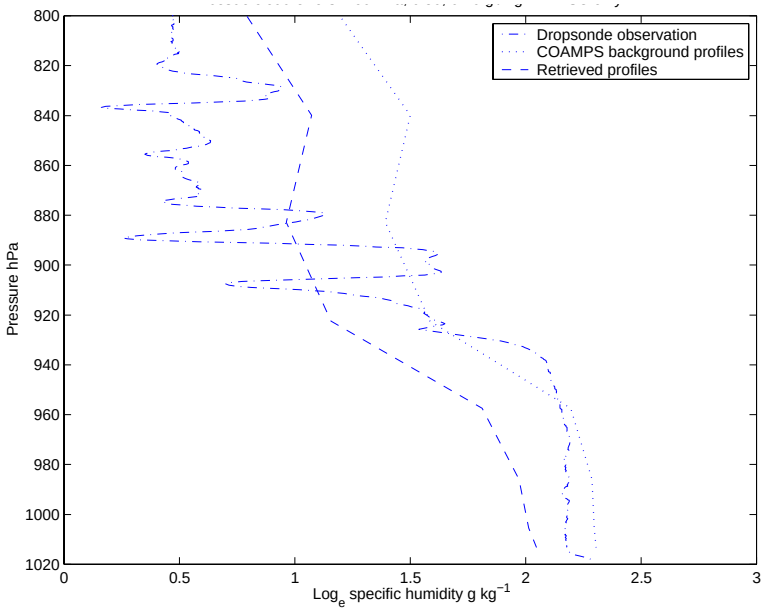

Figure 5.37. As in Fig. 5.36b, except for $\log_e Q$ with *CLW* background error increased to 0.10 g kg^{-1}.

The *CLW* error was reset to 0.03 g kg^{-1} and ε_m background error for the AMSU surface channels was increased from 0.02 to 0.05. From the retrieval error sensitivity study this increase in ε_m error reduced the low-level $\log_e Q$ retrieval performance (e.g., Fig. 4.16), but had negligible effect on *T* retrieval performance. The resulting 1DVAR retrieval shown in Fig. 5.37 is consistent with these previous findings and does adjust closer to the in-situ observation. The *T* retrieval (not shown) is similar to that shown in Fig. 5.36a.

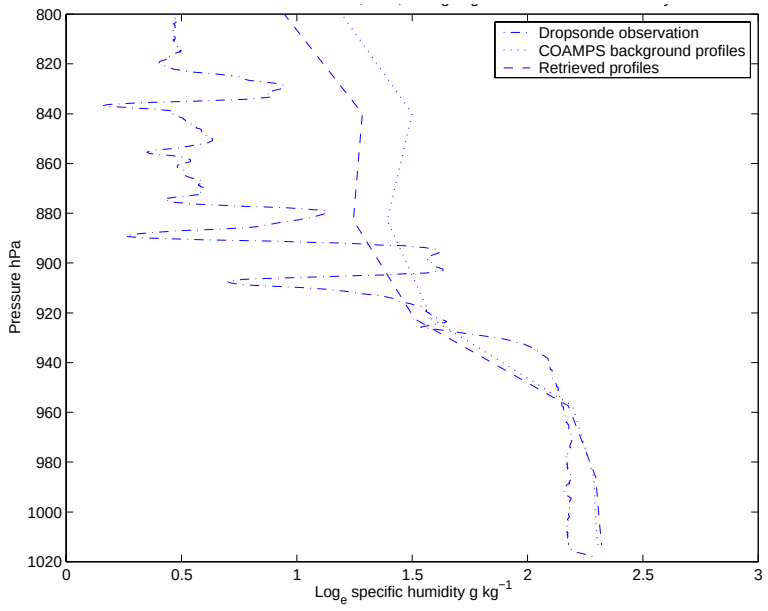

Figure 5.38. As in Fig. 5.36b, except for $\log_e Q$ with emissivity error of 0.05 for the AMSU surface sensitive channels.

Larger T_s error of 3.14 K (vice 1.57 K) was used for the 1DVAR retrievals shown in Fig. 5.39. In this case, the larger T_s error allowed the T retrieval near the surface to adjust closer to the in-situ observation. Additionally, the T retrieval was slightly improved above 920 hPa. This result may be slightly counterintuitive based upon the theoretical retrieval error sensitivity study, where the theoretical retrieval performance did not change greatly when T_s error was doubled to 3.14 K. However, this is a reasonable result considering that the surface and atmosphere errors are coupled in $\mathbf{B}_C$. Though this effect is more pronounced with strong surface and atmosphere correlations of error (e.g., Fig. 4.12), the larger T_s error should allow the satellite-derived information to have a greater freedom to adjust the low-level temperature profile. As expected, the $\log_e Q$ retrieval (not shown) is not sensitive to this T_s error and results are similar to that shown in Fig. 5.36b.

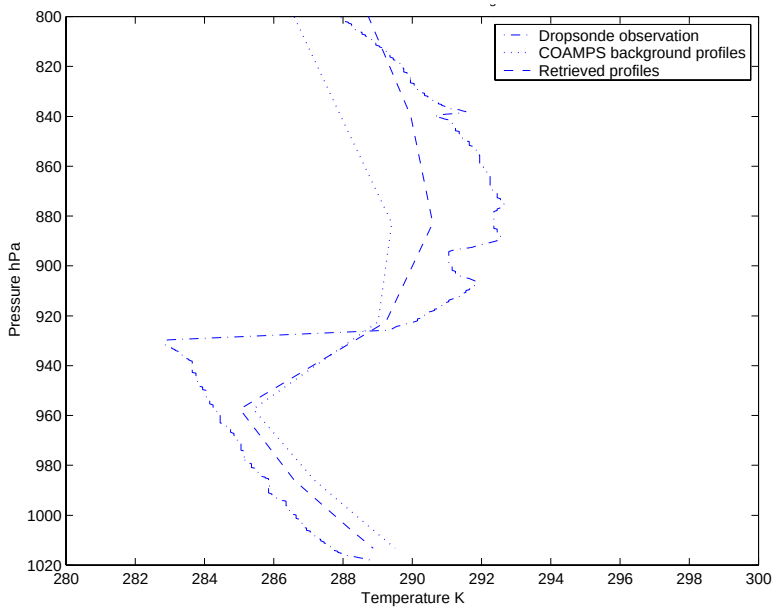

Figure 5.39. As in Fig. 5.36a, except T_s error increased from 1.57 to 3.14 K.

As previously discussed, the larger *CLW* values were used to bring the COAMPS model output closer to that observed during the DYCOMS II field experiment. 1DVAR *T* and $\log_e$ *Q* retrievals using this modified *CLW* background are shown in Fig. 5.40. Cloud errors for P_{CT}, C_{FC} and *CLW* are 60 hPa, 0.50, and 0.03 g kg^{-1}. As compared with the results shown in Fig. 5.36, this *T* retrieval is slightly closer to the in-situ observation near 960 hPa and 880 hPa. Otherwise the *T* retrievals are very similar. The $\log_e$ *Q* retrieval is closer to the in-situ observation except between adjacent RTTOV-6 levels 922.46 and 957.44 hPa where there is possibly a loss of detail due to vertical interpolation. Generally the results for $\log_e$ *Q* are consistent with the retrieval error sensitivity study. In this cloud case the background *CLW* error is much smaller in relation to the modified background *CLW*. 1DVAR retrievals were also generated using the modified *CLW* values with *CLW* errors of 0.10 g kg^{-1}, ε_m error of 0.05. and T_s error of 3.14 K (not shown). The effect of these cloud and surface errors on the 1DVAR retrievals was consistent with those shown in Fig. 5.39.

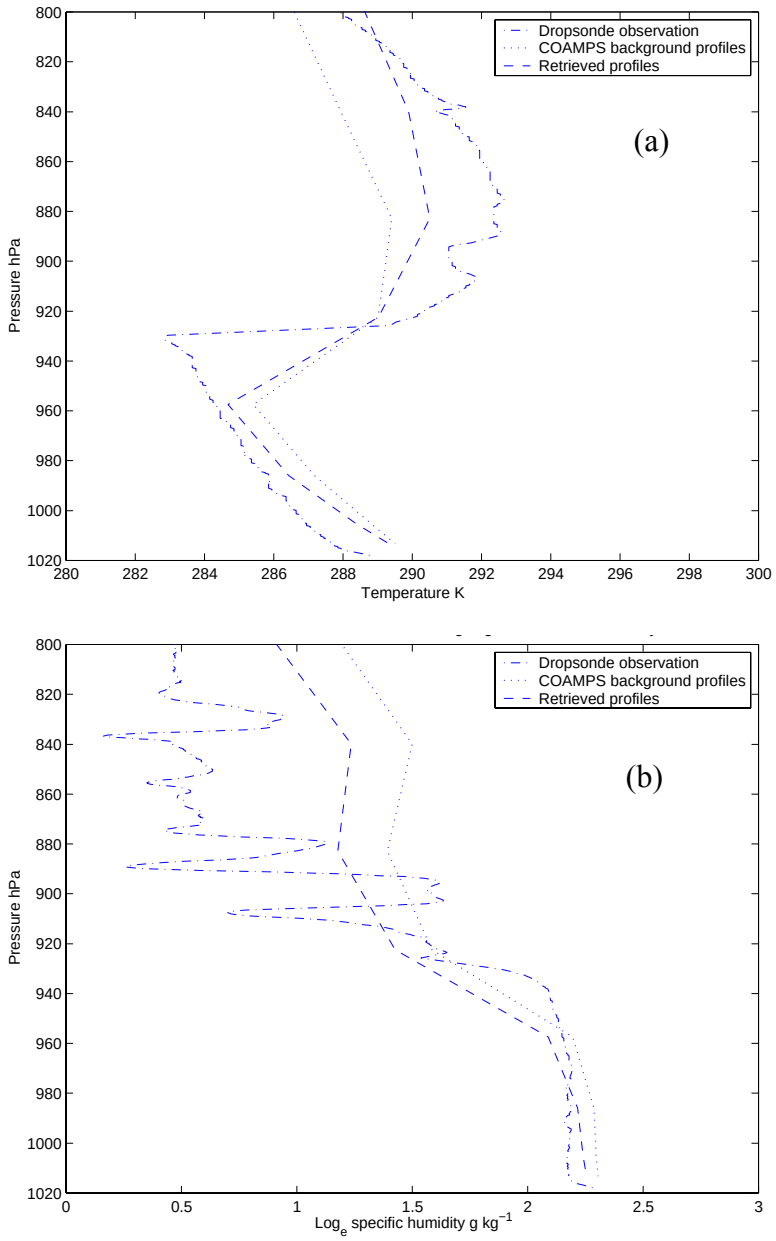

Figure 5.40. As in Fig. 5.36, except COAMPS *CLW* increased by a factor of ten.

D. 1DVAR RETRIEVALS USING THE COAMPS / NAVDAS FORECAST SYSTEM AND ATOVS MICROWAVE OBSERVATIONS

The profile temperature (T) and $\log_e$ specific humidity ($\log_e Q$) 1DVAR retrievals presented in Sections V.B and V.C were generated using simulated and actual ATOVS observations constrained by COAMPS short-term forecasts acquired from the DYCOMS II data set. The results of these 1DVAR retrieval studies showed that the temperature and humidity information from ATOVS was able to modify the low-level structure of the existing COAMPS background profile toward the designated "true" profile. Furthermore, the generally good agreement between theoretical retrieval errors and the error statistics calculated using optimal non-linear estimation demonstrated the consistency and reliability of this retrieval scheme (see Section V.A).

This section presents results of a preliminary 1DVAR retrieval study that used actual ATOVS microwave (MW) observations constrained by short-term forecast fields generated from the COAMPS / NAVDAS forecast system. A COAMPS domain corresponding to the outer DYCOMS II field study area was constructed for this research and the 1DVAR retrievals were based on the 6-hr forecast fields valid at 1200Z 11 July 2001. This retrieval case study did not include the model generated cloud liquid water mixing ratio (CLW) profiles in order to simulate microwave-clear conditions. The NRL 1DVAR retrieval scheme was modified to read the COAMPS forecast fields and to spatially match the AMSU-A and –B observations. At the time of this study, NRL Monterey was working to fully integrate 1DVAR retrievals into NAVDAS (N. Baker, personal communication). Therefore, the effect of these 1DVAR retrievals on the subsequent COAMPS analysis field could not be determined.

1. COAMPS Model

a. Model Domain

An 18 km, single nested COAMPS domain was constructed for this research at NRL Monterey (K. Sashegyi, personal communication). Grid (1,1) of the domain is located at approximately 22.5 N, 138.8 W with 136 grid points in E-W and 109 grid points in N-S. This relatively large geographic area corresponds to the outer DYCOMS II field study region and was selected in order to adequately model the area of

interest near 31.5 N 122.0 W. This position, within the Southern California bight region, is the approximate center point of the inner COAMPS nest for DYCOMS II (see Fig. 5.18). Vertical grid spacing followed the operational configuration of 30 sigma levels.

b. Model Configuration

This real data model simulation used the Comprehensive Ocean and Atmosphere Data (CODA) set sea surface temperature (SST) and Davies lateral boundary conditions. The model physics included the Kain-Fritsch convective parameterization, moisture, ice physics, radiation, surface fluxes. The turbulence closure scheme was Mellor and Yamada (1982) and the model run included sub-grid scale mixing and large eddy simulation.

The COAMPS model was initialized from NOGAPS at 0000Z 10 July 2001 and was run on a 6-hr update cycle. Data assimilation followed the operational NAVDAS configuration with incremental updates of standard observational data, such as land, aircraft, and National Environmental Satellite, Data, and Information Service (NESDIS) temperature retrievals.

c. Model Forecast Summary

Overall, the temperature and humidity structure of the Southern California bight region at 1200Z 11 July 2001 was reasonably well represented by the COAMPS 6-hr forecast fields. The model showed the strength of the low-level temperature inversion to be approximately 6 K and the near-surface specific humidity values were approximately 9.5 g kg^{-1}. Model generated SST (291.5 K), surface wind speed (6.9 ms^{-1}), and surface pressure (1016.1 hPa) were consistent with the local observations. The strength of the MABL temperature inversion decreased toward the west and south of the bight region.

2. AMSU Observations

a. Observation Selection and Scene Matching

NOAA-16 ATOVS MW level 1b data for the time period and location of interest were obtained from NESDIS via NRL Monterey (S. Swadley, personal communication). The AMSU observations over the model domain were included if they occurred within ± 3 hr of the model forecast valid time. In practice, a smaller time

window may be more appropriate, because of the large temporal variability of mesoscale features. For example, the UKMO uses a ±1.5 hr satellite data assimilation window for their limited area model (English et al. 2002).

The COAMPS forecast fields were horizontally interpolated to the center point of the nearest AMSU-B observation and the corresponding AMSU-A observation was then selected. From Chapter II.A, the size of the AMSU-B (A) scene resolution cells are approximately 16 (50) km in diameter at nadir with nine AMSU-B scenes per AMSU-A cell. Therefore, multiple AMSU-B observation vectors share the same AMSU-A observation vector.

For the six-hour data assimilation time window, there were 10,553 observation vectors available over the 2484 x 1944 km COAMPS domain. The observations were then screened for surface type and only those over ocean were included for study.

b. Bias Corrections

The HIRS/3 channels were also not included in this phase of study due to the uncertainty in the cloudy sky IR retrieval bias corrections. Their exclusion is an acknowledged limitation, since the majority of the low-level temperature information is derived from the HIRS/3 surface sensitive channels. In contrast to the previous 1DVAR retrieval study (Section V.C), bias corrections were applied to the AMSU-A channels. These bias corrections were generated from NRL Monterey's most comprehensive radiance assimilation run for the period 6 to 30 September 2001 (N. Baker, personal communication).

c. Quality Control Procedures

The NRL 1DVAR retrieval scheme performs a number of quality control checks on the satellite observations prior to minimization. The first is a gross departure check based upon the RTTOV-6 reference profiles and the second rejects the observation if the difference between the observed ($\mathbf{y}^o$) minus calculated ($H(\mathbf{x})$) brightness temperature for any channel is greater than 20 K. The observations are also rejected if too large a change in surface emissivity is required in order to fit the AMSU-A channels

1 – 3 brightness temperatures. For this study, only 280 observations were surface emissivity rejects. However, without the bias corrections, a large number of the AMSU brightness temperatures would have failed to pass the quality control checks.

To filter out signal that cannot be adequately handled by the radiative transfer model, the MW observations are screened for surface ice, scattering index, and *CLW*. The presence of ice, though not a concern to this study, is determined using AMSU-A channels 1 and 3. The scattering index is calculated using AMSU-A channels 1, 2 and 15, and *CLW* is determined using AMSU-A channels 1 and 2. For this research, the *CLW* limit was reduced 0.22 g kg^{-1} to ensure the observations were nearly clear for the MW frequencies.

Of the 10,553 available AMSU observations, approximately 3000 were rejected due to land and just over 3000 failed the quality control checks. Of those that failed the quality control phase, nearly 2000 were due to brightness temperature departures for AMSU-B channel 4. The large number of rejections for this channel may indicate the need for AMSU-B bias corrections.

3. 1DVAR Retrievals

1DVAR retrievals were generated using the appropriate 6-hr forecast fields valid at 1200Z 11 July 2001 and the collocated AMSU bias corrected observations. The background error covariance matrix $\mathbf{B_C}$ was used for this retrieval case study with the associated cloud element errors set to zero. All other background errors were those listed in Tables 3.2 and 3.3 and the AMSU observations errors were those listed in Table 3.4.

The total number of 1DVAR retrievals over the COAMPS domain that passed the quality control phase and then converged in 10 iterations or less was 4,550. The corresponding convergence rate was satisfactory when considering the large number of rejected observations.

a. Mean Effective Background Error

The mean effective background error ($\mathbf{H}\ \mathbf{B_C}\ \mathbf{H}^T$) based upon the 4,550 "successful" retrievals was calculated for each of the 20 AMSU channels. Fig. 5.41 compares the square root of the diagonal elements of the mean effective background error and the corresponding observation error matrix (**R**). As discussed in Chapter III.B, the effective background error projects $\mathbf{B_C}$ into m x m radiance space, and for channels with

large effective background error, the retrieval is determined primarily by the satellite-measured radiances. Since the COAMPS domain extends from approximately 23 to 40 N, a diverse set of EPAC atmospheric states are represented, through **H**, by this mean quantity. The mean effective background errors, and hence, information content, are generally similar to those representative clear sky EPAC profiles (see Fig. 4.3b). The notable exception is AMSU-B channel 2 (shown as ATOVS channel 32), where the mean effective background is reduced from approximately 6 to 4 K.

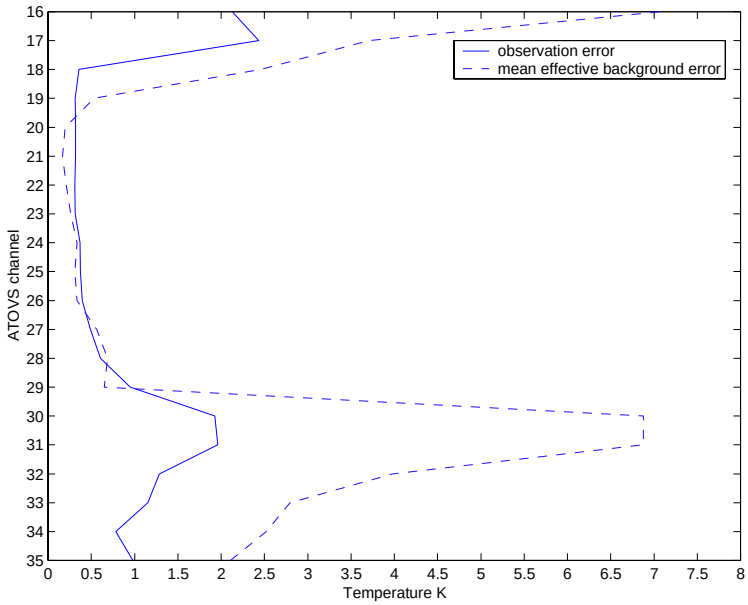

Figure 5.41. Square root of the diagonal elements of the mean effective background error ($\mathbf{H}\,\mathbf{B}_C\,\mathbf{H}^T$) and observation error (**R**) ATOVS channels 16 – 35 are AMSU-A channels 1 – 15 and ATOVS channels 31 –35 are AMSU-B channels 1 - 5. **H** was calculated at the final iteration for each of the 4,550 successful retrievals. $\mathbf{B}_C$ is the COAMPS specific background error covariance matrix.

b. T and $\log_e$ Q Retrievals within the COAMPS Domain

Overall, the 4,550 *T* and $\log_e$ *Q* 1DVAR retrievals generated using the AMSU observations were warmer and drier between 500 and 900 hPa than the corresponding COAMPS 6-hr forecast fields. In the vicinity of the Southern California bight, the *T* retrievals were generally warmer than the background near the top of the

MABL inversion and slightly colder below. Small adjustments to the temperature profile are expected in this case, since the majority of T information below 300 hPa is derived from the excluded HIRS/3 channels (see Fig. 4.7b). Also within the bight region, the $\log_e Q$ retrievals were drier than the COAMPS background above the MABL. The 1DVAR retrievals to the west and south of the bight region were consistent with the corresponding COAMPS background profiles, except for slightly larger near-surface $\log_e Q$ values (not shown). These results provide further evidence that satellite-derived information when constrained by a COAMPS background field is able to produce a solution that is consistent with the summertime EPAC environment.

c. Comparison with a Collocated Dropsonde Observation

Fig. 5.42 shows the 1430Z 11 July 2001 GOES channel 1 image of the Southern California bight region with the approximate release point of the 1432Z high-resolution dropsonde observation. This in-situ observation was obtained from the DYCOMS II data set and is compared with the adjacent 1200Z T and $\log_e Q$ retrieval.

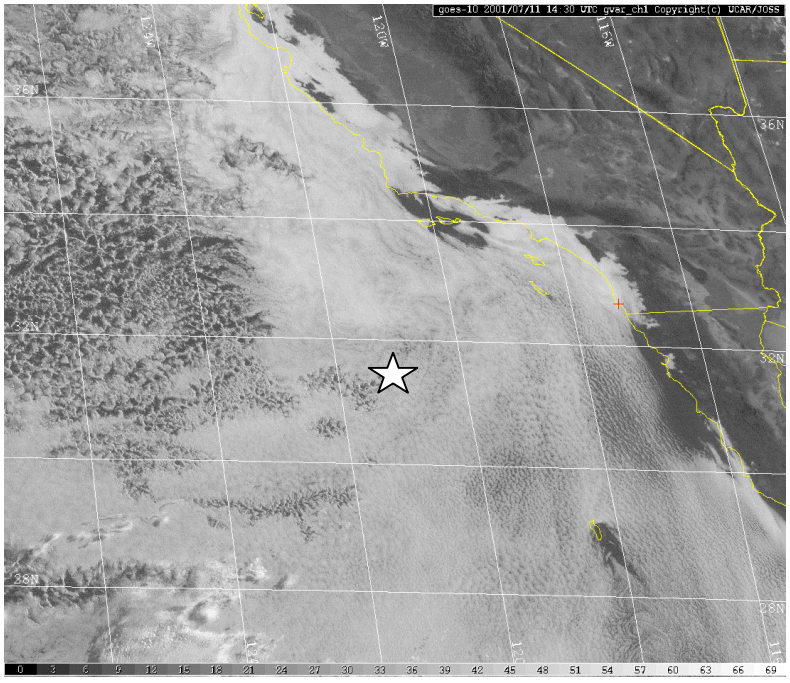

Figure 5.42. GOES-10 channel 1 satellite image for 1430Z 11 July 2001. [From http://www.joss.ucar.edu.] The star near 31.7 N 121.1 W indicates the approximate release position of the 1432Z high-resolution dropsonde observation.

The T and $\log_e Q$ 1DVAR retrieval closest to the 1432Z dropsonde observation is shown in Fig. 5.43. The T retrieval (Fig. 5.43a) is only slightly warmer than the COAMPS 6-hr forecast between 500 and 900 hPa, which is consistent with the general results described for the COAMPS domain. An expanded view of the T retrieval, plotted at the lowest 7 RTTOV-6 pressure levels, is shown in Fig. 5.43b and is compared with the COAMPS 6-hr forecast profile and the collocated dropsonde observation. The retrieved temperature profile is warmer (colder) than the COAMPS background profile above (below) the inversion. Again, the changes with respect to the background profile are minor, but the adjustments above and below the MABL inversion are toward the in-situ observation. This retrieval is consistent with the results shown Fig. 5.36a for the non-bias corrected observations, but the overall adjustment is much smaller. For this case, $\mathbf{x}^b$ starts closer to the dropsonde observation, but some of this difference might be due to the addition of the AMSU-A bias corrections.

The $\log_e Q$ retrieval shown in Fig. 5.43c is substantially drier at mid-, to upper-levels than the COAMPS 6-hr forecast. The retrieval appears to be reasonable and is consistent with the drying trend above the MABL observed in both the DYCOMS II dropsonde observation (Fig. 5.43d) and the 1200Z Vandenberg (VBG) sounding (not shown). This $\log_e Q$ retrieval is also similar to that shown in Fig. 5.36b, but with smaller corrections toward the true profile. This difference could again be due to the MW bias corrections.

The COAMPS forecast, and retrieved profiles shown in Figs. 5.43b and 5.43d demonstrate an important weakness of the RTTOV-6 with respect to mesoscale applications. The COAMPS forecast profile when vertically interpolated to the fixed RTTOV-6 pressure levels is unable to accurately represent the base of the MABL inversion at approximately 935 hPa. Therefore, the fixed pressure levels prevent the retrieval from taking full advantage of the *a priori* information contained within the COAMPS forecast profile (see Fig. 5.21).

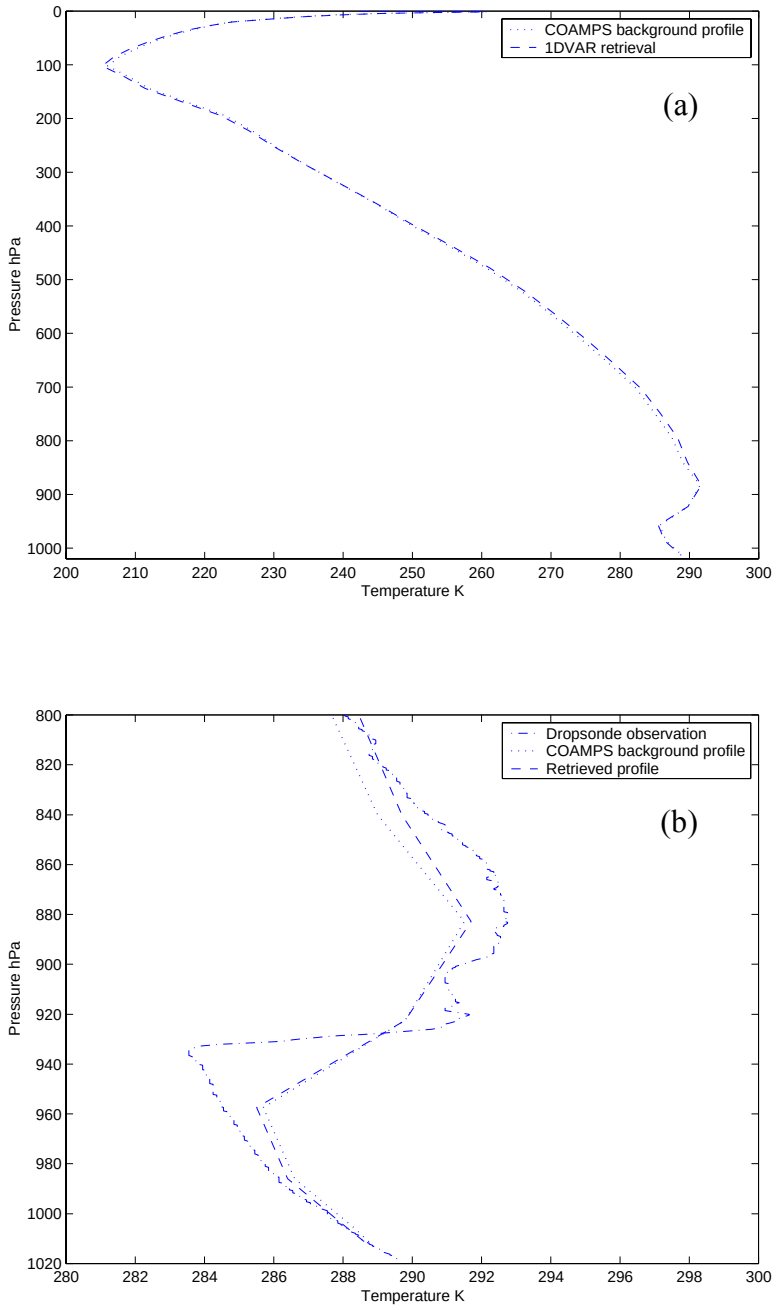

Figure 5.43. 1DVAR (a) T, and (c) $\log_e Q$ retrieval located near 31.7 N 121.1 W. These retrieval used AMSU-A and B observations and a COAMPS / NAVDAS 6-hr forecast valid at 12Z 11 July 2001. Expanded view of (a) and (c) from 800 hPa to the surface are shown in (b) and (c), respectively, along with the collocated 1423Z high-resolution dropsonde observation from the DYCOMS II data set. Release altitude for the in-situ observation was 2517 m.

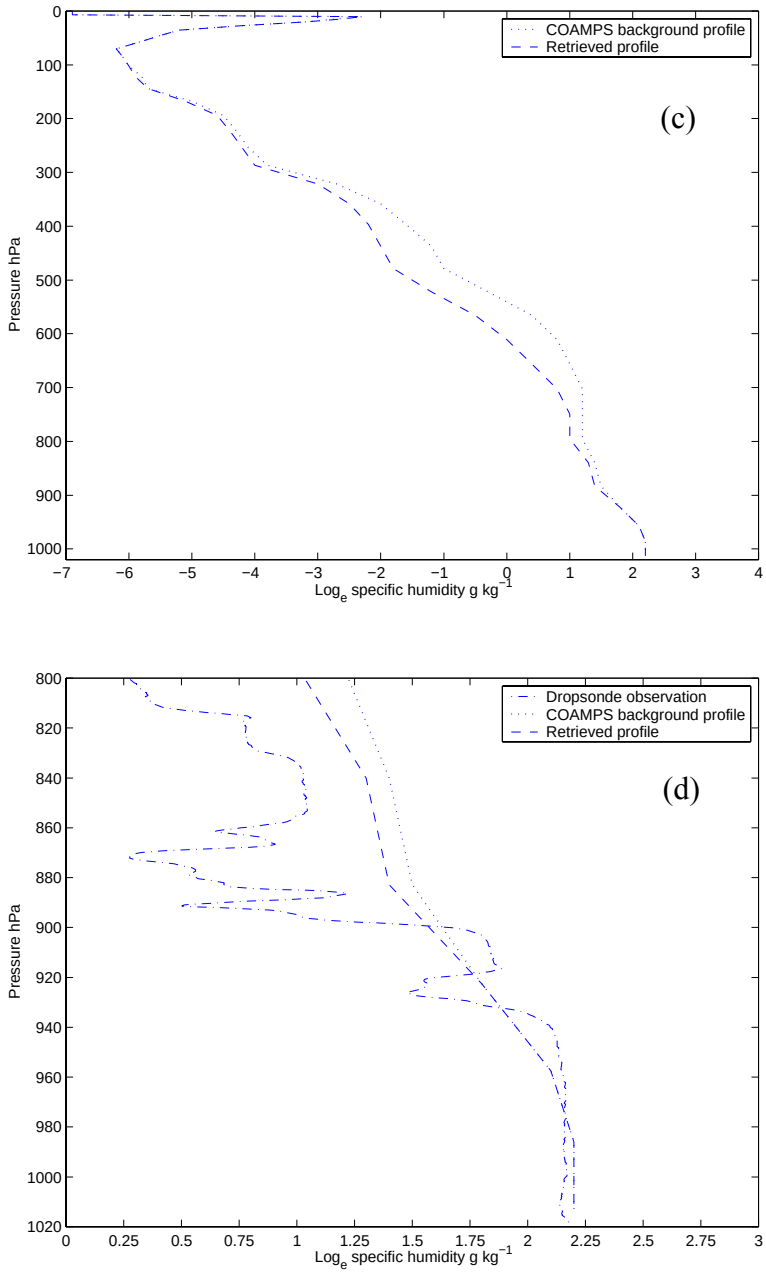

Figure 5.43. Continued.

d. Comparison with a Collocated NESDIS Retrieval

The T and $\log_e Q$ 1DVAR retrieval (Fig. 5.43) and the adjacent NESDIS retrieval for 1200Z 11 July 2001 are shown in Fig. 5.44. This comparison is made for a single forecast time and location and therefore, the results are case specific. However, the 1200Z NESDIS retrievals over the entire COAMPS domain exhibited similar structure with little to no MABL detail. The NESDIS T retrieval (Fig. 5.44a) does not include the low-level temperature inversion and the NESDIS level 40 (1000 hPa) temperature is approximately 5 K warmer than the DYCOMS II dropsonde observation. Low-level humidity is greater in the NESDIS retrieval (Fig. 5.44b) than observed and does not show the expected atmospheric drying above the MABL.

NESDIS retrievals are currently a part of the standard observation set for NAVDAS. However, this case provides an interesting example of how a 1DVAR retrieval constrained by a COAMPS forecast field would be more appropriate for mesoscale applications, such as satellite data assimilation and stand-alone temperature and humidity retrievals. These 1DVAR retrievals would adjust the MABL parameters toward truth at each model update cycle better than the corresponding NESDIS retrievals.

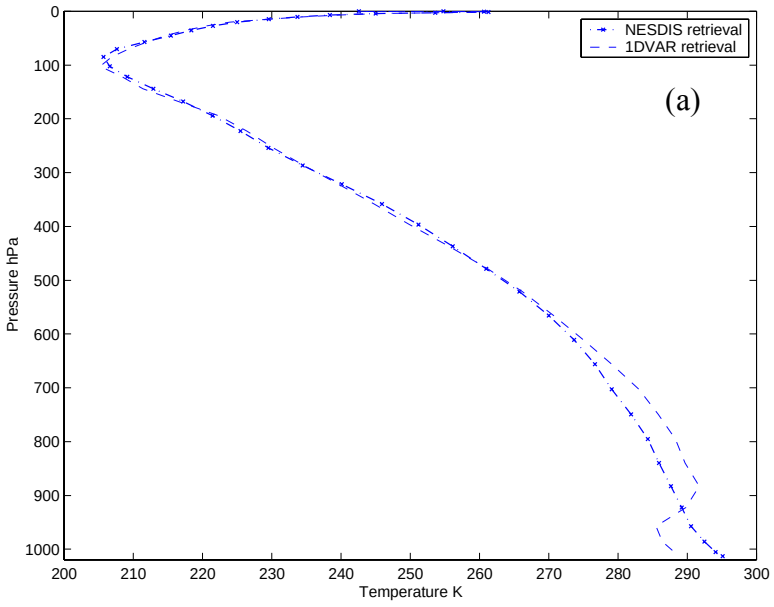

Figure 5.44. As in Figs. 5.43b and 5.43c, except the (a) T, and (b) $\log_e Q$ 1DVAR retrieval is compared with the adjacent NESDIS retrieval at 31.9N 121.0 W.

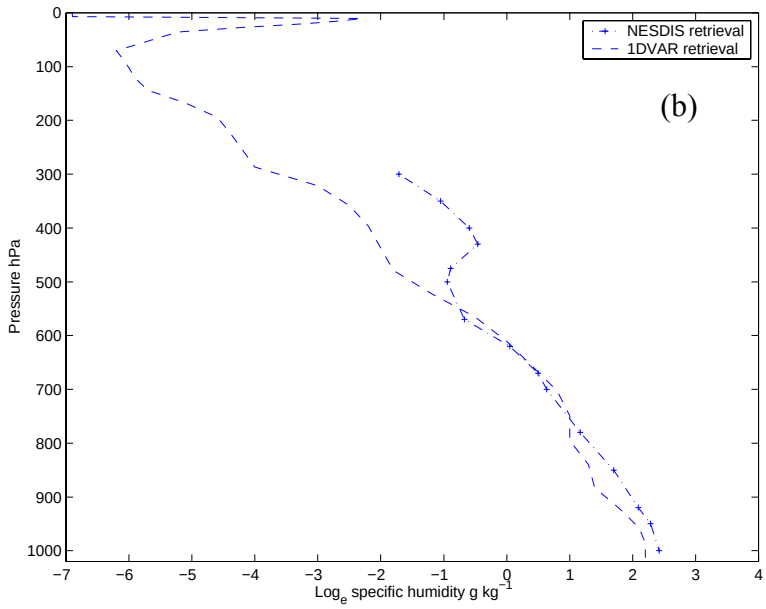

Figure 5.44. Continued.

E. SUMMARY OF CHAPTER RESULTS

Results presented in this chapter corroborate the findings of the theoretical information content study (Chapter IV), namely that significant humidity and temperature information can be derived from ATOVS IR and MW retrievals within the clear and cloudy sky summertime EPAC environment. Again, these finding do not imply that any one, or combinations of ATOVS instruments(s) can "resolve" fine scale boundary layer features. However, these satellite observations can provide information that, when used in concert with a reasonable first guess background, reduce the retrieval errors and result in a closer match to "truth".

1DVAR retrievals were calculated using a statistically significant number of simulated background state vectors and simulated ATOVS observation vectors. The generally good agreement between theoretical retrieval errors and the error statistics calculated vis-à-vis non-linear Newtonian iteration demonstrated the consistency and

reliability of the NRL 1DVAR retrieval scheme. Normalized retrieval biases were found to be generally small for most cases. However, there were relatively large *T* biases at cloud-top, but these were reduced by increasing the low-level *T* background errors.

1DVAR *T* and $\log_e Q$ retrievals were then calculated using simulated ATOVS observations and COAMPS 6-, and 9-hr forecasts derived from the Dynamics and Chemistry of Marine Stratocumulus (DYCOMS) Phase II data. Overall, the clear and cloudy sky retrievals were able to modify the structure of the existing background profiles toward the designated "true" profile, most notably at the low-level temperature inversion. Relatively large cloud background errors were used for these simulations since only one simulated ATOVS observation was used to represent the area of interest. Without the low-level MABL structure defined within the background state vector, the ATOVS observations alone cannot retrieve the low-level temperature inversion and humidity structure.

1DVAR retrievals were also generated using ATOVS microwave (MW) observations with the COAMPS forecast fields from the DYCOMS II data set. HIRS/3 observations were not included due to the uncertainty in retrieval bias corrections. AMSU-A and B observations from the NOAA-16 satellite were obtained for this research directly from the calibrated level 1B data. Retrievals were generated using both the under-predicted and modified cloud liquid water mixing ratio profile (*CLW*) values from the COAMPS output. Results were compared against a collocated dropsonde observation. Even without the IR surface channels, the 1DVAR retrieval was able to adjust the COAMPS background toward the in-situ observation. This adjustment toward "truth" occurred both above and below the MABL inversion.

This research generated *T* and $\log_e Q$ 1DVAR retrievals using AMSU-A bias corrected brightness temperatures constrained by 6-hr forecast fields from NRL Monterey's COAMPS / NAVDAS forecast system. The geographic area of the real data model simulation corresponded to the outer DYCOMS II field study region. Overall, the temperature and humidity of the Southern California bight region was reasonably well

represented by the COAMPS 6-hr forecast fields. The mean effective background errors for each of the 20 AMSU channels, and hence, information content, were similar to those calculated using the representative summertime EPAC profiles.

The 4,550 T and $\log_e Q$ 1DVAR retrievals generated using the AMSU brightness temperatures were warmer and drier between 500 and 900 hPa than the corresponding COAMPS 6-hr forecast fields. In the vicinity of the Southern California bight region, the T retrievals were generally warmer than the background near the top of the MABL inversion and slightly colder below. The 1DVAR retrievals from this region were also found to better represent the MABL temperature and humidity than the collocated NESDIS retrieval.

The results from this preliminary study show that the T and $\log_e Q$ 1DVAR retrievals constrained by COAMPS forecast fields could be used as a valid observation type for NAVDAS. However, the vertically interpolated COAMPS background, and hence, the retrieved profile was unable to accurately represent the base of the MABL temperature inversion. This is a distinct limitation of using the fixed RTTOV-6 pressure levels. Other RTE models, such as Optical Path Transmittance (OPTRAN; McMillan et al. 1995)), which do not interpolate to fixed pressure levels might be better suited for these mesoscale applications.

VI. DISCUSSION AND RECOMMENDATIONS

A. RESEARCH SUMMARY AND DISCUSSION

The theoretical and applied research conducted for this dissertation formed a rigorous investigation of the variational satellite retrieval problem within the summertime EPAC mesoscale environment. Specifically, the ability of ATOVS infrared and microwave sensors to provide information within the MABL to a mesoscale NWP system was studied. This work accelerated on-going research efforts at NRL Monterey by carrying out the prerequisite groundwork for operational satellite data assimilation using the COAMPS / NAVDAS mesoscale prediction system. From a larger Navy perspective, this dissertation focused on a top Fleet METOC priority for more accurate remote sensing and modeling capabilities for data sparse / denied areas. This research is also relevant to on-going efforts by other Department of Defense research groups working to improve sensing and modeling of refractivity parameters within the MABL for EM / EO weapon and sensor performance analyses and predictions.

The methodology employed in this research followed a logical sequence from analyses of satellite-derived theoretical information content to the demonstration of actual retrievals using the COAMPS / NAVDAS mesoscale prediction system. First, analyses of information content and retrieval performance of ATOVS with respect to representative clear and cloudy sky EPAC background state vectors and associated background errors were conducted. These EPAC profiles included clear and cloudy sky cases with varying MABL depth and LWP. Background error covariance matrices were constructed based on global scale NOGAPS forecast errors and the summertime forecast error statistics for COAMPS EPAC. This theoretical study quantified the total satellite-derived information with respect to background and established the *a priori* elements critical for T and $\log_e Q$ retrievals within the MABL. A statistically significant number of 1DVAR simulated retrievals were then generated based upon the representative EPAC background state vectors. The utility of the 1DVAR scheme for this mesoscale application was assessed through the comparison of theoretically derived retrieval errors and the error statistics calculated by non-linear Newtonian iteration. 1DVAR simulated T

and $\log_e Q$ retrievals, using the COAMPS short-term forecast fields from the DYCOMS II data set as background, were produced and compared for various sets of *a priori* cloud error. Actual AMSU observations were then used along with these COAMPS short-term forecast fields to generate 1DVAR T and $\log_e Q$ retrievals. Finally, a 1DVAR study retrieval was conducted using AMSU-A bias corrected, and AMSU-B non-bias observations constrained by 6-hr forecast fields from NRL Monterey's COAMPS / NAVDAS forecast system.

Various established methods (e.g., Prunet et al. 1998; Garand 2000; Rodgers 2000) were used to quantify the information content of ATOVS retrievals with respect to representative background state vectors and associated errors. These analyses showed that, when treated optimally, significant humidity and temperature information could be derived from ATOVS observations within the clear and cloudy sky summertime EPAC environment. As anticipated from previous PCA / SVD studies, the total quantity of information available from ATOVS is virtually independent of synoptic situation; however, this research suggests that significant low-level humidity information can be obtained within the summertime EPAC MABL. The relative magnitude of the effective background error to observation error for the AMSU window channels showed there is a large amount of humidity information available from these channels, most notably AMSU-B channel 2 (150.0 GHz).

The sensitivity of theoretical retrieval (analysis) errors to representative EPAC background state vector elements and their associated errors established the critical *a priori* elements necessary for successful 1DVAR retrievals. This sensitivity study showed that HIRS/3 infrared surface channel 8 provides a large amount of information on cloud-top temperature and established the importance of AMSU channels 1 – 4, and 15 - 17 in supplying low-level humidity information within the MABL. These results confirmed previous research (e.g., English 1999) that showed low-level clear sky T theoretical retrieval performance can be improved by prior knowledge of T_s and that T retrieval performance for all clear sky background state vectors is virtually insensitive to ε_m error. Cloudy sky profiles with large amounts of *CLW* were found to be slightly sensitive below cloud-top to ε_m error. Low-level $\log_e Q$ retrieval performance was found

to be sensitive to ε_m error. However, small ε_m errors ($\leq 2\%$) were found to not greatly affect $\log_e Q$ retrieval performance for the clear sky EPAC profiles. Temperature profile (T) retrieval performance was found to rapidly decrease as the uncertainty in P_{CT} and/or C_{FC} increases; however, $\log_e Q$ retrieval performance was found to be insensitive to these cloud errors. Prior knowledge of P_{CT} and C_{FC} was found to be necessary for improved retrieval of T. Overall, T retrieval errors were found to remain relatively unaffected by changes in *CLW* error. Cloudy sky $\log_e Q$ theoretical retrieval performance, however, was found to decrease as *CLW* error increases. A notable point is that clear sky $\log_e Q$ retrieval performance is degraded when non-zero *CLW* errors are included in background error covariance matrix. This situation would arise if a cloudy-sky background error covariance matrix were used for clear sky retrievals.

The generally good agreement between theoretical retrieval errors and the error statistics calculated from the statistically significant number of simulated retrievals demonstrated the consistency and reliability of the NRL 1DVAR retrieval scheme. This comparison also showed that this non-linear optimal estimation scheme is appropriate for mesoscale applications within the summertime EPAC environment.

1DVAR T and $\log_e Q$ retrievals using the COAMPS short-term forecast fields from the DYCOMS II data set were shown to adjust the background toward the designated true profile. These retrievals were also based on simulated ATOVS observations, but in this case a collocated global model background profile served as truth. Due to uncertainty in infrared bias corrections, only observations from AMSU-A, and -B were used for the retrieval case study. These passive microwave observations were constrained by the same COAMPS short-term forecast fields and model specific background errors. The resulting 1DVAR T and $\log_e Q$ retrievals compared well with in-situ observations, which showed improvement over background above and below the MABL inversion. This research suggests larger improvements, or adjustment toward the in-situ observation, would be observed if the corrected HIRS/3 surface channels had been included.

This research generated T and $\log_e Q$ 1DVAR retrievals using AMSU-A bias corrected, and AMSU-B non-bias corrected brightness temperatures constrained by 6-hr forecast fields from NRL Monterey's COAMPS / NAVDAS forecast system. The geographic area of the real data model simulation corresponded to the outer DYCOMS II field study region. The T and $\log_e Q$ 1DVAR retrievals generated using the AMSU brightness temperatures were warmer and drier between 500 and 900 hPa than the corresponding COAMPS 6-hr forecast fields. In the vicinity of the Southern California bight region, the T retrievals were generally warmer than the background near the top of the MABL inversion and slightly colder below. The 1DVAR retrievals from this region were also found to better represent the MABL temperature and humidity than the collocated NESDIS retrieval. The results from this preliminary study show that the T and $\log_e Q$ 1DVAR retrievals constrained by COAMPS forecast fields could be used as a valid observation type for NAVDAS. However, the vertically interpolated COAMPS background, and hence, the retrieved profile was unable to accurately represent the base of the MABL temperature inversion. This is a distinct limitation of using the fixed RTTOV-6 pressure levels.

These findings do not, however, imply that any one, or combinations of ATOVS instrument(s) can independently "resolve" fine scale boundary layer features. A principal result of this research is that ATOVS observations can provide information that, when used with a reasonable first-guess background field, i.e., COAMPS, reduce the retrieval error and adjust the temperature and humidity retrieval within the shallow boundary layer toward the designated "true" profile (see Appendix A). Results of the information content and retrieval error sensitivity study are by definition optimistic. To obtain these promising results and exploit the full potential of these sensors the bias computations must be precisely known and forward model errors including emissivity must be minimized.

The implications for mesoscale forecast improvements are clear, especially with respect to the problem of obtaining in-situ observations within data sparse / denied areas. This research demonstrated that ATOVS with its relatively broad weighting functions and limited vertical resolution could provide enough temperature and humidity

information to a 1DVAR retrieval scheme to improve a mesoscale first-guess profile. High-resolution infrared sounders such as AIRS or IASI are expected to provide significantly more temperature information (e.g. Pruent et al. 1998) for clear sky retrievals. However, the role of passive microwave systems should not be underestimated. This research demonstrated the importance of AMSU-A and AMSU-B in providing significant temperature and low-level humidity information. Also, many applications within the summertime EPAC environment are cloudy in infrared, but may be "microwave-clear" due to the enhanced transmissivity of clouds at MW frequencies.

Though this research did not explicitly make use of complementary satellite information, it did show how such observations could improve variational retrievals. Prior knowledge of various MABL specific background state vector elements was found to be important for gaining relatively large reductions in ATOVS retrieval error. As previously mentioned, for clear sky retrievals these parameters include T_s and ε_m, and for cloudy-sky retrievals, P_{CT} and C_{FC}. Reduction in *a priori* error associated with each of these elements can only be accomplished through higher confidence in the background state vector. Such confidence could be gained of course through accurate COAMPS forecasts of cloud liquid water and surface skin temperature. Another method would be to include collocated satellite observations directly in the minimization process. As discussed in Chapter II.C, information derived from collocated satellite imagery can be used to accurately determine cloud fraction and liquid water content, sea surface temperature, and boundary layer (cloud-top) height. However, the proper method of how to use these externally derived observations in a variational scheme must still be addressed.

B. RECOMMENDATIONS FOR FUTURE RESEARCH

This dissertation addressed many important theoretical and Navy relevant research issues. It has also provided the groundwork for operational satellite data assimilation, especially for the COAMPS / NAVDAS mesoscale prediction system. As with all complex scientific problems, more research is needed to realize the full potential of satellite-derived information with respect to the mesoscale MABL environment. The following are suggested research topics.

- **Run additional COAMPS / NAVDAS forecasts updated with ATOVS data**

The capability to conduct satellite retrievals with COAMPS / NAVDAS was not available until the end this dissertation process and hence, only one case study example was generated. More case studies are required in order to validate the results presented in this dissertation and to further explore the ability of satellite-derived information to improve mesoscale forecasts.

- **Exploit collocated satellite data and MABL retrieval techniques**

This research showed how externally derived MABL information derived from collocated satellites and thermodynamic models could be used to improve variational retrievals within the summertime EPAC environment. Further research is needed to determine the proper method of how to exploit these externally derived observations in a 3DVAR retrieval scheme.

- **Construct COAMPS specific background error covariance matrices**

Long-term records of regionally specific COAMPS forecast error statistics are required in order to generate a functional set of background error covariance matrices. The background errors derived from global models (e.g., NOGAPS) are appropriate only as a first-order approximation. Therefore, resources should be focused on collecting these data for multiple operational COAMPS areas. These error statistics should be tailored to the profile, surface, and cloud elements of the background state vector.

Another issue relating to the background error covariance matrix is the structure of the inter-level correlations of error. Vertical correlations calculated for global model may not be appropriate for mesoscale applications. Though not expressly addressed by this research, the error correlation functions should be studied, and possibility modified for MABL environments under strong subsidence inversions. The errors that are presumably coupled with respect to a global model may not necessarily be coupled across a strong boundary layer inversion.

- **Establish bias monitoring program for COAMPS operational areas**

All major NWP centers have an active satellite bias monitoring program for their respective global models. The derived corrections are most likely an appropriate first order approximation, but in some cases may not be directly applicable to mesoscale applications, specifically, the cloudy MABL retrieval problem.

The establishment of a long-term bias monitoring program for operational COAMPS areas is required in order to fully exploit satellite sensor information. This effort should begin with the COAMPS EPAC area and then be expanded to other operationally sensitive regions, e.g., the North Arabian Sea.

- **Minimize forward model errors**

Gains in satellite-derived information are derived from aggressively minimizing forward model errors, including emissivity. Forward model errors values are based upon the characteristics of the particular "broadband" radiative transfer model and on-going improvements with respect to line-by-line models are promising. Values used by NWP centers for global data assimilation may be different than required for mesoscale applications. As previously discussed, the U.K. Meteorological Office reduced the AMSU global observation errors from 4 to 2 K for mesoscale data assimilation (see English et al. 2002). Appropriate forward model errors are also dependent upon knowledge of cloud conditions and surface emissivity, which might be more accurately defined in a mesoscale area.

- **Determine information content of next generation satellite sounders**

This study only considered the information content of ATOVS, a relatively low vertical resolution sounding system. Though this research demonstrated that ATOVS could provide significant temperature and humidity information, the next generation infrared atmospheric sounders, such as GIFTS-IOMI and AIRS, are expected to dramatically increase the available atmospheric temperature and constituent information. As discussed in this dissertation, several information content studies have been completed for these high vertical resolution sensors. However, they are all based upon global scale background profiles and do not specifically address the mesoscale MABL retrieval problem.

Following the methods outlined in this dissertation, research is needed to determine the information content and retrieval error sensitivity of these next generation infrared sounders with respect to the clear and cloudy sky MABL regime. An interesting approach would be to include the AMSU channels to simulate collocated infrared hyperspectral / interferometer, and passive microwave observations.

APPENDIX A

The 1DVAR profile temperature (T) and $\log_e$ specific humidity ($\log_e Q$) retrievals presented in Chapter V were generated using both simulated and actual ATOVS observations constrained by COAMPS short-term forecasts and a synoptically relevant background error covariance matrix. A key result of this 1DVAR retrieval study is that ATOVS observations can provide information that, when used with a reasonable COAMPS background field, reduce the retrieval error and adjust the temperature and humidity retrieval within the shallow boundary layer toward the designated "true" profile (see Fig. 5.23). However, the findings presented in this dissertation do not imply that any one, or combination of ATOVS instrument(s) can independently "resolve" fine scale boundary layer features.

This appendix further explores the role of *a priori* temperature information in the variational retrieval process. To demonstrate this relationship, three clear sky 1DVAR T retrievals were generated using a smoothed T background profile and simulated observations for the 35 ATOVS channels based upon the 0900Z 11 July 2001 ECMWF forecast profile described in Chapter V.B. As shown in Fig. 5.19, this "true" profile ($\mathbf{x}^t$) has a well-defined temperature inversion of approximately 10 K at the top of the MABL. The background profile ($\mathbf{x}^b$) was created by removing the low-level temperature and humidity gradient from $\mathbf{x}^t$. Three different **B** matrices were constructed to represent various assumptions regarding the background error standard deviations and inter-level correlations of error. The first is a diagonal **B** matrix with large T errors, and the second **B** matrix includes the surface and atmosphere coupled inter-level correlations of error. The third retrieval case uses the COAMPS EPAC specific background error covariance ($\mathbf{B}_C$).

Fig. A.1 shows the 1DVAR T simulated retrieval calculated with respect to the diagonal **B** matrix with standard deviations of error for T of 10.00 K. The background errors for the surface array elements T_{2m} and T_s were also set to the relatively large value of 10.00 K. This scenario might arise if climatology were used instead of a more

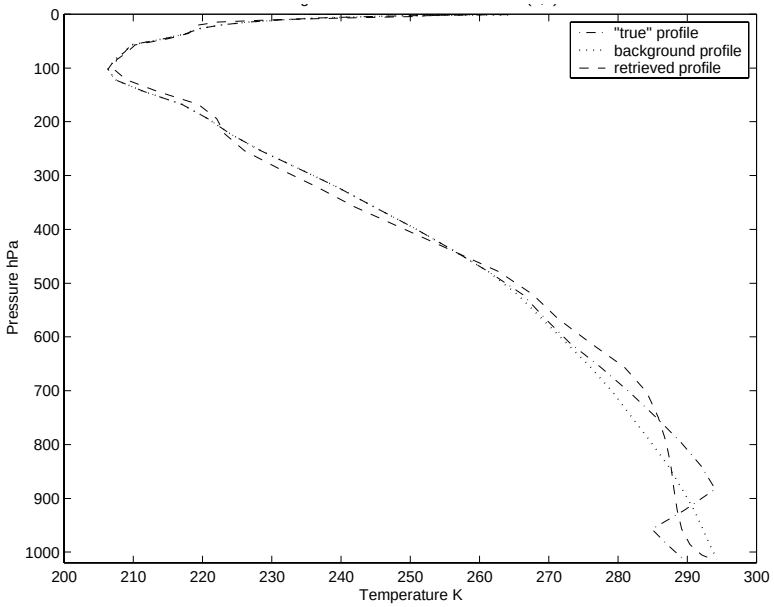

Figure A.1. Simulated 1DVAR *T* retrieval (dashed line) calculated with respect to diagonal **B** matrix with *T* background standard deviations of error set to 10 K. The background standard deviations of error for T_{2m} and T_s were set to 10 K. Simulated clear sky ATOVS observations were calculated from the 0900Z 11 July 2001 ECMWF "true" ($\mathbf{x}^t$) forecast profile (dashed-dotted line) shown in Fig. 5.19. The background profile (dotted line) is a representation of $\mathbf{x}^t$ without the MABL temperature inversion.

representative NWP background. As the uncorrelated errors are increased, the retrieval becomes unconstrained by the background profile and the limited ATOVS-derived temperature information can only make minor adjustments to the smoothed $\mathbf{x}^b$ near the top of the MABL. The second *T* retrieval case, shown in Fig. A.2, uses the large background errors described above, but includes the inter-level correlations of error listed in Table 3.1. The coupled surface and atmosphere error correlations allow the ATOVS-derived surface temperature information to adjust $\mathbf{x}^b$ closer to $\mathbf{x}^t$ near the surface. However, the retrieval is still unable to accurately represent the MABL temperature inversion. As shown in Fig. A.3, if the retrieval is generated using $\mathbf{B_C}$ with its smaller, more representative standard deviations of error, the *T* retrieval is tightly constrained by background profile and only minor adjustments are observed above and below the top of MABL inversion.

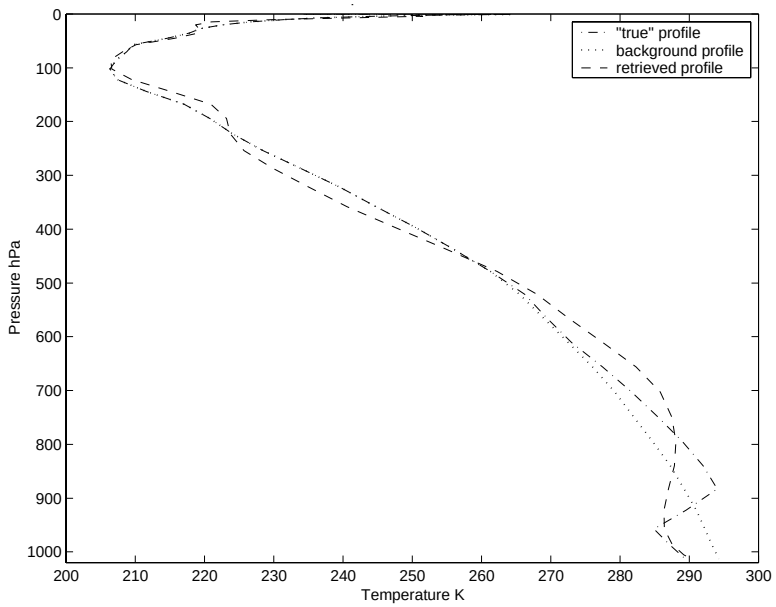

Figure A.2. As in Fig. A.1, except the retrieval was calculated using the diagonal **B** matrix with surface and atmosphere coupled inter-level correlations of error listed Table 3.1.

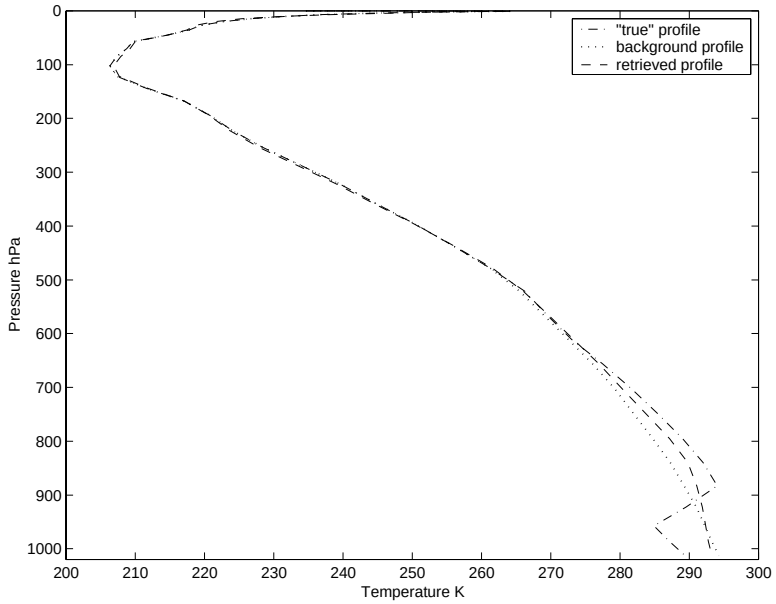

Figure A.3. As in Fig. A.1, except the retrieval was calculated using the COAMPS EPAC specific background error covariance ($\mathbf{B}_C$).

Simulated $\log_e Q$ retrievals were generated (not shown) using similar techniques and a smoothed low-level humidity background profile. The results were consistent with the *T* retrievals in that the low-level MABL humidity gradient was not well represented. However, the larger correlated surface errors did allow the retrieved $\log_e Q$ profile to adjust toward $\mathbf{x}^t$ below 900 hPa.

The U.S. Standard Atmosphere (see Fig. 3.2) was also used as a background state vector and T and loge Q retrievals were generated using the **B** matrices described above. The retrieval (not shown) failed converge in 10 iterations or less when calculated with respect to the $\mathbf{B}_C$ matrix. When the background errors were increased, the retrieval (not shown) converged to an unrealistic solution. The findings presented here and throughout this dissertation demonstrate the importance of accurate *a priori* background information for successful ATOVS 1DVAR retrievals within the summertime EPAC environment.

LIST OF REFERENCES

Baker, N., 1992: Quality control for the U.S. Navy operational database. *Wea. Forecasting*, **7**, 250-261.

Betts, A.K., P. Minnis, W. Ridgway, and D.F. Young, 1992: Integration of satellite and surface data using a radiative-convective oceanic boundary-layer model. *J. Appl. Meteor*., **31**, 340-350.

Bouttier, F., and P. Courtier, 1999: Data assimilation concepts and methods. European Centre for Medium Range Forecasting (ECMWF). [Available online from http://www.ecmwf.int /services/training/rcouse_notes].

Burk, S.D. and W.T. Thompson, 1982: Operational evaluation of a turbulence closure model forecast system. *Mon. Wea. Rev*., **110**, 1535-1543.

_____, and _____, 1996: The summertime low-level jet and marine boundary layer structure along the California coast. *Mon. Wea. Rev*. **124**, 668-686.

_____, and _____, 1997: Mesoscale modeling of summertime refractive conditions in the Southern California Bight. *J. Appl. Meteor*., **36**, 22-31.

Chesters, D.L., L. Uccelline, and W. Robinson, 1983: Low-level water fields from the VISSR Atmospheric Sounder (VAS) "split window" Channels. *J. Climate Appl. Meteor*., **23**, 725-743.

Cook, J., J. McCarthy, and T. Tsui, 2000: Nowcast for the Next Generation Navy, 8pp. [Available from Naval Research Laboratory Marine Meteorology Division, Monterey, CA. 93943-5502.]

Courtier, P., J. Derber, R. Errico, J.F. Louis, and T. Vukicevic, 1993: Important literature on the use of adjoint, variational methods and the Kalman filter in meteorology. *Tellus*, **45A**, 342-357.

Cram, J.M., and M.L. Kaplan, 1985: Variational assimilation of VAS data into a mesoscale model: Assimilation method and sensitivity experiments. *Mon. Wea. Rev*., **113**, 467-484.

Daley, R., 1991: *Atmospheric Data Analysis*. Cambridge University Press, 420pp.

_____, and E. Barker, 2000: *NRL Atmospheric Variational Data Assimilation System (NAVDAS) Source Book 2000*. NRL/PU/7530—00-418, Naval Research Laboratory Marine Meteorology Division, Monterey, CA, 155pp.

Dalu, G., 1986: Satellite remote sensing of atmospheric water vapor. *International Journal of Remote Sensing*, **7**, 1089-1097.

Deblonde, G., 1999: Variational assimilation of SSM/I total precipitable water retrievals in the CMC analysis system. *Mon. Wea. Rev*., **127**, 1458-1474.

_____, 2000: Variational retrievals using SSM/I and SSM/T-2 brightness temperatures in clear and cloudy situations. [Available from Data Assimilation and Satellite Meteorology Division, Meteorological Service of Canada, Dorval, Quebec, Canada.]

Dorman, C.E., and C.D. Winant, 2000: The structure and variability of the marine atmosphere around the Santa Barbara Channel. *Mon. Wea. Rev*., **128**, 261-282.

_____, T. Holt, D.P. Rodgers, K. Edwards, 2000: Large-scale structure of the June-July 1996 marine boundary layer along California and Oregon. *Mon. Wea. Rev*., **128**, 1632-1652.

Durkee, P.A., D.R. Jensen, E.E. Hindman, and T.H. Vonder Haar, 1986: The relationship between marine aerosol particles and satellite-derived radiance. *J. Geophys. Res.*, **91**, 4063-4072.

_____, F. Pheil, E. Frost, and R. Shema, 1991: Global analysis of aerosols and their effects on climate. *Atmos. Environ.*, **25A**, 2457.

English, S.J., 1999: Estimation of temperature and humidity profile information from microwave radiances over different surface types. *J. Appl. Meteor.*, **38**, 1526-1541.

_____, R.J. Renshaw, P.C. Dibben, A.J. Smith, P.J. Rayer, C. Poulsen, F.W. Saunders, and J.R. Eyre, 2000: A comparison of the impact of TOVS and ATOVS satellite sounding data on the accuracy of numerical weather forecasts. *Quart. J. Roy. Meteor. Soc.*, **126**, 2911-2931.

_____, D. Jones, A. Smith, F. Hilton, and K. Whyte, 2002: ATOVS and SSM/I assimilation as the Met Office. *The 12th International TOVS Study Conference, ITSC XII*, 26 Feb – 5 Mar, Lorne, Victoria, Austrailia. [Available online at: http://cimss.ssec.wisc.edu/itwg/itsc/itsc12.].

Errico, R.M., 1997: What is an adjoint model? *Bull. Amer. Meteor. Soc*., **78**, 2577-2591.

_____, T. Vukicevic, and K. Raeder, 1993: Examination of the accuracy of a tangent linear model. *Tellus*, **45A**, 462-477.

Eyre, J.R., 1989a: Inversion of cloudy satellite sounding radiances by nonlinear optimal estimation. I: Theory and simulation for TOVS. *Quart. J. Roy. Meteor. Soc*., **115**, 1001-1026.

_____, 1989b: Inversion of cloudy satellite sounding radiances by nonlinear optimal estimation. II: Application to TOVS data. *Quart. J. Roy. Meteor. Soc*., **115**, 1027-1037.

_____, 1990: The information content of data from satellite sounding systems: A simulation study. *Quart. J. Roy. Meteor. Soc.*, **116**, 401-434.

_____, 1991: Inversion methods for satellite sounding data. European Centre for Medium Range Forecasting (ECMWF). [Available online from http://www.ecmwf.int /services/training/rcouse_notes.]

_____, J.R., G.A. Kelly, A.P. McNally, E. Andersson, and A. Persson, 1993: Assimilation of TOVS radiance information through one-dimensional variational analysis. *Quart. J. Roy. Meteor. Soc.*, **119**, 1427-1463.

Filiberti, M.A., and L. Eymard, 1994: Assimilation of satellite precipitable water in a meteorological forecast model. *Mon. Wea. Rev.*, **122**, 486-506.

Franke, R., 1999: Vertical correlation functions for temperature and relative humidity errors. NRL/MR/7531—99-7240, 78pp. [Available from Naval Research Laboratory, Marine Meteorology Division, Monterey, CA, 93943-5502.]

Garand, L., 2000: Sensitivity of retrieved atmospheric profiles from infrared radiances to physical and statistical parameters of the data assimilation system. *Atmos-Ocean*, **38**, 431-455.

_____, D.S. Turner, M. Larocque, and Co-authors, 2001: Radiance and jacobian inter-comparison of radiative transfer models applied to HIRS and AMSU channels. [Available from Meteorological Service of Canada, 2121 Trans-Canada Highway, Dorval, Qc, Canada, H9P1J3, or online at http://www.cmc.ec.gc.ca.]

Ghil, M., M. Harem, and R. Atlas, 1979: Time-continuous assimilation of remote-sounding data and its effect on weather forecasting. *Mon. Wea. Rev*., **107**, 140-171.

Golub, G.H., and C.F. Van Loan, 1996: *Matrix Computations*. Johns Hopkins University Press, Baltimore, MD., 694pp.

Haltiner, G.J., and F.L. Martin, 1957: *Dynamical and Physical Meteorology*. McGraw-Hill, New York, NY., 470pp.

Harshvardhan, R.D., D. Randall, and T. Corsetti, 1987: A fast radiation parameterization for atmospheric circulation models. *J. Geophy. Res*., **92**, 1009-1015.

Haack, T., and S.D. Burk, 2000: Summertime marine refractivity conditions along coastal California. Submitted to *J. Appl. Meteor*.

Hansen, J.E., and L.D. Travis, 1974: Light scattering in planetary atmospheres. *Space Sci. Rev*., **16**, 527-610.

Healy, S.B., and J.R. Eyre, 2000: Retrieving temperature, water vapor and surface pressure information from refractive-index profiles derived by radio occultation: A simulation study. *Quart. J. Roy. Meteor. Soc*. **126**, 1661-1683.

Hodur, R.M., 1987: Evaluation of a regional model with an update cycle. *Mon. Wea. Rev*., **115**, 2702-2718.

_____, 1997: The Naval Research Laboratory's coupled ocean / atmosphere mesoscale prediction system (COAMPS*). Mon. Wea. Rev*., **125**, 1414-1430.

Hogan, T.F., and T.E. Rosmond, 1991: The description of the U.S. Navy Operational Global Atmospheric Prediction System's spectral forecast model. *Mon. Wea. Rev*., **119**, 1786-1815.

Joiner, J., and A.M. da Silva, 1998: Efficient methods to assimilate remotely sensed data based on information content. *Quart. J. Roy. Meteor. Soc*., **124**, 1669-1694.

Kain, J.S, and J.M. Fritsch, 1993: Convective parameterization for mesoscale models: The Kain-Fritsch scheme. *The Representation of Cumulus Convection in Numerical Models, Meteor. Monogr.,* No. 46. Amer. Meteor. Soc., 165-170.

Kidder, S.Q., and T.H. Vonder Haar, 1995: *Satellite Meteorology an Introduction.* Academic Press, San Diego, CA, 466pp.

Kohn, D.J., 1995: Refinement of a semi-empirical model for the microwave emissivity of the sea surface as a function of wind speed. M.S. Thesis, Meteorology Dept., Texas A&M University.

Kuji, M., T. Hayaska, N. Kikuchi, T. Nakajima, and M. Tanaka, 2000: The retrieval of effective particle radius and liquid water path of low-level marine clouds from NOAA AVHRR data. *J. Appl. Meteor.*, **39**, 999-1016.

Kren, R.J., 1987: Estimation of marine boundary layer depth and relative humidity with

multispectral satellite measurements. M.S. Thesis, Dept. of Meteorology, Naval Postgraduate School, Monterey, CA, 70pp.

Lerner, J.A., E. Weisz, and G. Kirchengast, 2001: Temperature and humidity retrieval from simulated Infrared Atmospheric Sounding Interferometer (IASI) measurements. Submitted to *J. Geophys. Res.*

Li, J., W.W. Wolf, W.P. Menzel, W. Zhang, H. Hunag, and T.H. Achtor, 2000: Global Soundings of the Atmosphere from ATOVS measurements: The algorithm and validation. *J. Appl. Meteor*., **39**, 1248-1268.

Lipton, A.E., and T.H. Vonder Haar, 1990: Mesoscale analysis by numerical modeling coupled with sounding retrieval from satellites. *Mon. Wea. Rev.*, **118**, 1308-1329.

Lorenc, A.C., 1986: Analysis methods for numerical weather prediction. *Quart. J. Roy. Meteor. Soc*., **112**, 1177-1194.

Louis, J.F., 1979: A parametric model of vertical eddy fluxes in the atmosphere. *Bound. – Layer Meteor*., **17**, 187-202.

McBride, M.B., 2000: Estimation of stratocumulus-topped boundary layer depth using sea surface and remotely sensed cloud-top temperatures. M.S. Thesis, Dept. of Meteorology, Naval Postgraduate School, Monterey, CA, 80pp.

McNally, A.P., and M. Vesperini, 1996: Variational analysis of humidity information from TOVS radiances. *Quart. J. Roy. Meteor. Soc*., **122**, 1521-1544.

McMillin L.M., and D.S. Crosby, 1984: Theory and validation of the multiple window sea surface temperature technique. *J. Geophys. Res.*, **89**,3655-3661.

_____, L.J. Crone, M.D. Goldberg, and T.J. Kleespies, 1995: Atmospheric Transmittance of an Absorbing Gas .4. OPTRAN - A Computationally Fast and Accurate Transmittance Model for Absorbing Gases with Fixed and with Variable Mixing Ratios at Variable Viewing Angles. *App. Opt.*, **34** (**27**), 6269-6274.

Mellor,G., 1982: Development of a turbulence closure for geophysical fluid problems. *Rev. Geophys and Space Phys*., **20**, 851-875.

_____, and T. Yamada, 1974: A hierarchy of turbulence closure models for planetary boundary layers. *J. Atmos. Sci*., **31**, 1791-1806.

Minnis, P., P.W. Heck, D.F. Young, C.W. Fairall, and J.B. Snider, 1992: Stratocumulus cloud properties derived from simultaneous satellite and island-based instrumentation during FIRE. *J. Appl. Meteor*., **31**, 317-339.

Mozer, J.B., and S.M. Ayer, 1998: Objective techniques for fusion and analysis of mesoscale NWP and satellite-derived cloud data. Preprint, *Proceedings of the Battlespace Atmospheric and Cloud Impacts on Military Operations (BACIMO) Conference, 1-3 December 1998*, Hanscom, AFB, MA, 57-64.

Nachamkin, J.E, and R.M. Hodur, 2001: Sensitivity of short-term forecasts from the Navy COAMPS to grid configuration and data assimilation. Preprints, *18th Conference on Weather Analysis and Forecasting*, Ft. Lauderdale, FL., Amer. Meteor. Soc.

National Oceanic and Atmospheric Administration (NOAA) KLM User's Guide, 2001. [Available online at http://www2.ncdc.noaa.gov/docs/klm.]

Palmer, P.I., J.J. Barnett, J.R. Eyre, and S.B. Healy, 2000: A nonlinear optimal estimation inverse method for radio occultation measurements of temperature, humidity and surface pressure. *J. Geophys. Res.*, **105**, 17513-17526.

Peckham, G.E., and M. Grippa, 2000: Improved retrieval of tropospheric temperatures from remote measurements of thermal radiation using the adiabatic lapse rate as a constraint. *Quart. J. Roy. Meteor. Soc*., **126**, 749-760.

Phalippou, L., 1996: Variational retrieval of humidity profile, wind speed and cloud liquid-water path with the SSM/I: Potential for numerical weather prediction. *Quart. J. Roy. Meteor. Soc*., **122**, 327-355.

Powers, J.G., and K. Gao, 2000: Assimilation of DMSP and TOVS Satellite Soundings in a Mesoscale Model. *J. Appl. Meteor.*, **39**, 1727-1741.

Prunet, P., J. Thepaut, and V. Casse, 1998: The information content of clear sky IASI radiances and their potential for numerical weather prediction. *Quart. J. Roy. Meteor. Soc*., **124**, 211-241.

Purser, R.J., and H.-L. Huang, 1993: Estimating effective data density in a satellite retrieval or an objective analysis. *J. Appl. Meteor.*, **32**, 1092-1107.

Rodgers, C.D., 1976: Retrieval of atmospheric temperature and composition from remote measurements of thermal radiation. *Rev. Geophys. Space Phys.*, **14**, 609-624.

_____, 2000: *Inverse Methods for Atmospheric Sounding: Theory and Practice*. World Scientific, Singapore, 238pp.

Rodgers, R.R., and M.K. Yau 1989: *A Short Course in Cloud Physics*, 3d ed. Butterworth-Heinemann, 74-75.

Rosenthal, J., R. Helvey, T. Battalino, L. Eddinton, C. Fisk, and P. Greiman, 1997: Predicting the EM/EO environment from satellite, synoptic and in-situ data sources. *Proceedings: Electromagnetic/Electo-Optics Prediction Requirements & Products Symposium 1997*, 77-86.

Ruggiero, F., K. Sashegyi, A. Lipton, R. Madala, and S. Raman, 1999: Coupled assimilation of geostationary satellite sounder data into a mesoscale model using the Bratseth analysis approach. *Mon. Wea. Rev*., **127**, 802-821.

Rutledge, S.A., and P.V. Hobbs, 1983: The mesoscale and microscale structure of organization of clouds and precipitation in midlatitude cyclones. VIII: A model for the "seeder-feeder" process in warm-frontal rainbands. *J. Atmos. Sci*., **40**, 1185-1206.

Saunders, R.W., 1993: A note on the Advanced Microwave Sounding Unit. *Bull. Amer. Meteor. Soc.*, **74**, 2211-2212.

_____, 2000: NWP-SAF 4 year plan for RT development and RTTOV-6 science and validation report. [Available online at http://www.met-office.gov.uk.]

_____, M. Matricardi, and P. Brunel, 1999: An improved radiative transfer model for assimilation of satellite radiances. *Quart. J. Roy. Meteor. Soc*., **125**, 1407-1426.

Simpson, J.J., T. McIntire, J. Zhonghai, and J.R. Stitt, 2000: Improved cloud top height retrieval under arbitrary viewing and illumination conditions using AVHRR data. *Rem. Sen. Environ*., **72**, 95-110.

Smith, W.L., and H. Woolf, 1978: Use of eigenvectors of statistical covariance matricies for interpreting satellite sounding observations. *J. Atmos. Sci*., **33**, 1127-1140.

_____, _____, and H.E. Fleming, 1972: Retrieval of atmospheric temperature profiles from satellite measurements for dynamical forecasting. *J. Appl. Meteor*., **11**, 113 - 122.

Stephens, G.L., 1978: Radiation profiles in extended water clouds. Part II: Parameterization schemes. *J. Atmos. Sci.*, **35**, 2123-2132.

Stevens, B., D.H. Lenschow, G. Vali, and Co-authors, 2002: Dynamics and Chemistry of Marine Stratocumulus – DYCOMS II. Submitted to *Bull. Amer. Meteor. Soc.*

Stull, R.B., 1997: *An Introduction to Boundary Layer Meteorology*. Kluwer Academic Publishers, Dordrecht, 670pp.

Thepaut, J.-N, and P. Moll, 1990: Variational inversion of simulated TOVS radiances using the adjoint technique. *Quart. J. Roy. Meteor. Soc*., **116**, 1425-1448.

Thompson, O.E, and Y. Hou, 1990: Coupling of horizontal, vertical, and temporal resolving power of a satellite temperature sounder. *J. Atmos. Oceanic. Tech.*, **7**, 454-463.

_____, and M.T. Tripputi, 1994: NWP-initialized satellite temperature retrievals using statistical regularization and singular value decomposition methods. *Mon. Wea. Rev.,* **122**, 897–926.

_____, D.D. Dazlich, and Y. Hou, 1986: The ill-posed nature of the satellite temperature retrieval problem and the limits of retrievability. *J. Atmos. Oceanic. Tech*., **3**, 643-649.

University Corporation for Atmospheric Research / Joint Office for Science Support (UCAR / JOSS), cited 2002. Dynamics and Chemistry of Marine Stratocumulus (DYCOMS) Phase II data set. [Available online at: http://www.joss.ucar.edu.]

Uddstrom, M.J., and L.M. McMillin, 1994a: System noise in the NESDIS TOVS forward model. Part I: Specification. *J. Appl. Meteor.*, **33**, 919-938.

_____, 1994b: System noise in the NESDIS TOVS forward model. Part I: Consequences. *J. Appl. Meteor.*, **33**, 939-947.

Van Tuyl, A.H., and R. Daley, 1999: Estimation of forecast error covariances over an oceanic region using NORPEX data. Preprint, *13th Converence on Numerical Weather Prediction*, 13-17 September 1999, Denver, CO, 15-19.

Wetzel, M.A., and T.H. Vonder Haar, 1991: Theoretical development and sensitivity tests of stratus cloud droplet size retrieval method for AVHRR-K/L/M. *Remote Sens. Environ*., **36**, 105-119.

_____, W.T. Thompson, G. Vali, S.K. Chai, T. Haack, M.J. Szumowski, and R. Kelly, 2001: Evaluation of COAMPS forecasts of coastal stratus using satellite microphysical retrievals and aircraft measurements. *Wea. Forecasting*, **16**, 588-599.

INITIAL DISTRIBUTION LIST

1. Defense Technical Information Center
   Ft. Belvoir, Virginia

2. Dudley Knox Library
   Naval Postgraduate School
   Monterey, California

3. Chairman, Code MR
   Department of Meteorology
   Naval Postgraduate School
   Monterey, CA 93943-5101

4. Dr. Nancy L. Baker
   Naval Research Laboratory
   Marine Meteorology Division
   Monterey, CA 93943-5502

5. Prof. Philip A. Durkee
   Department of Meteorology
   Naval Postgraduate School
   Monterey, CA 93943-5101

6. Prof. Carlyle H. Wash
   Department of Meteorology
   Naval Postgraduate School
   Monterey, CA 93943-5101

7. Prof. Qing Wang
   Department of Meteorology
   Naval Postgraduate School
   Monterey, CA 93943-5101

8. Prof. Douglas K. Miller
   Department of Meteorology
   Naval Postgraduate School
   Monterey, CA 93943-5101

9. Prof. Carlos F. Borges
Department of Mathematics
Naval Postgraduate School
Monterey, CA 93943-5101

10. CDR Grant A. Cooper, USN
Naval Research Laboratory
Marine Meteorology Division
Monterey, CA 93943-5502